Institute for Automation and Control
Graz University of Technology

Stefan Kaltenbacher, B.Sc.

Model Based Control of Regenerative Thermal Oxidizers

Master's Thesis

to achieve the university degree of
Master of Science

Master's degree program
Electrical Engineering

Under the Supervision of
Dipl.-Ing. Dr.techn. Martin Steinberger
Univ.-Prof. Dipl.-Ing. Dr.techn. Martin Horn

In collaboration with
Chemisch Thermische Prozesstechnik GmbH

Graz, December 2015

AFFIDAVIT

STATUTORY DECLARATION

I declare that I have authored this thesis independently, that I have not used other than the declared sources / resources and that I have explicitly marked all material which has been quoted either literally or by content from the used sources.

Ich erkläre an Eides statt, dass ich die vorliegende Arbeit selbstständig verfasst, andere als die angegebenen Quellen/Hilfsmittel nicht benutzt und die den benutzten Quellen wörtlich und inhaltlich entnommenen Stellen als solche kenntlich gemacht habe.

…… ……..

Date / Datum Signature / Unterschrift

Abstract

Regenerative Thermal Oxidizers (RTOs) are widely used in industry for the purification of exhaust gases and waste airflow partially consisting of combustible elements. The gas portions affected by contamination, mainly *volatile organic compounds* (VOCs), are almost entirely decomposed to water and carbon dioxide by oxidation at high temperatures. The enthalpy of the hot purified gas is buffered in heat accumulators, e.g. in ceramic beds to heat the incoming raw gas in order to save energy and gain process efficiency.

This thesis delivers on the one hand sophisticated models for the simulation of these plants, including all relevant components for a two-bed configuration and presents optimized solutions for the implementation in *Matlab Simulink* as partial differential equations and complex system properties have to be taken into account and demand the application of developed methods.

On the other hand this thesis provides a model based control of the gas temperature in the combustion chamber by fuel injection, aiming to minimize the portion of VOCs in the gas composition by spending as less fuel as possible. It thereby represents a proper fundament for the design of further control loops, e.g. for the control of the RTO half cycle period and for the modelling of additional systems of the plant. The developed control concept is not restricted to the two-bed configuration, it can be applied to all RTOs using some sort of fuel injection for combusting exhaust gases.

Furthermore, the monitoring of the dynamic behavior of temperature sensors in the combustion chamber pointed out that the quality of measured signals needs to be doubted. As a result, the developed mathematical models of these sensors could be exploited to find accurate values for the real gas temperature.

Kurzfassung

Anlagen zur *regenerativen thermischen Oxidation* (RTOs) finden breite Anwendung in der Industrie zur Reinigung von Abgas- und Abluftströmen, die zum Teil aus brennbaren Bestandteilen bestehen. Das verunreinigte Rohgas beinhaltet oft flüchtige organische Verbindungen (VOCs), die bei hohen Temperaturen oxidieren und dadurch fast vollständig zu Wasser und Kohlendioxid umgewandelt werden. Der Enthalpiestrom des gereinigten Gases wird in Wärmespeichern, wie zum Beispiel in Keramikbetten zwischengespeichert, um das eintretende Rohgas zu erhitzen und den Prozess möglichst energieeffizient und wirtschaftlich zu gestalten.

Die Arbeit liefert zum einen anspruchsvolle Modelle für die Simulation solcher Anlagen unter Berücksichtigung aller wesentlichen Komponenten für eine zwei-Bett Konfiguration und präsentiert optimierte Methoden zur Implementierung in *Matlab Simulink*. Das Zusammenspiel von komplexen Systemeigenschaften und partiellen Differentialgleichungen erfordert die Verwendung der Methoden im Simulationsaufbau.

Zum anderen liefert die Arbeit ein modellbasiertes Konzept zur Regelung der Gastemperatur in der Brennkammer durch Brennstoffzufuhr. Das Konzept gewährleistet durch die Schaffung der richtigen thermischen Bedingungen den gezielten Abbau von Schadstoffen bei möglichst geringem Brennstoffverbrauch. Dabei stellt es ein robustes Fundament für die Entwicklung weiterer Regelschleifen dar, wie zum Beispiel für die Regelung der Periodendauer von RTO Zyklen, aber auch für die Modellierung weiterer Systeme und Effekte der Anlage. Das entwickelte Konzept ist nicht an die betrachtete zwei-Bett Konfiguration gebunden, sondern kann an allen RTOs angewandt werden, solange sie unter Brennstoffzufuhr Abgase oxidieren.

Weiters zeigte die Untersuchung des dynamischen Verhaltens der Temperatursensoren in der Brennkammer, dass die Qualität der gemessenen Signale angezweifelt werden muss. Die entwickelten mathematischen Modelle dieser Sensoren werden daher ausgenutzt, um wesentlich genauere Werte der tatsächlichen Gastemperatur zu berechnen.

Contents

1 Introduction

This thesis combines very different subjects in the areas of process, chemical, as well as control engineering. Due to the interaction of various disciplines and the complexity of the applied mathematical models for describing *Regenerative Thermal Oxidizers* (RTOs), the modelling of plant components was only paid little attention as this issue would readily fill further scientific papers.

The focus is set on control, which involves the processing of these models for simulation. With the presumption that model based approaches could possibly improve process stability of the plant in the operating phase, the potential in terms of fuel consumption and purification performance of the raw gas should have been analyzed.
However, the complexity of the system soon required to place the focus on a specific aspect. The control of the gas temperature in the combustion chamber was favored, whereas e.g. the controlling of the fan, which forces the gas to flow through the plant, or the controlling of the half cycle periods remains open for future research and developments.

In the course of this thesis it became evident that the signals of the two temperature sensors in the combustion chamber can not be used for proper control, as long as they do not recognize fluctuation in temperatures, e.g. as a reason of changing input parameters. Significantly long time responses and deviations to the real gas temperature required to model these sensors, whereas in a second step this model is used for calculating more accurate values of the real gas temperature during run time.

1.1 Machine Assembly

In order to design an appropriate control concept adapted to real conditions it was necessary to integrate the main components of the RTO in the control loop. The valve boxes (VB A & VB B), the ceramic beds (Bed A & Bed B), the combustion chamber (CC) with integrated burner (B) and the two temperature sensors (S1 & S2) form the considered system configuration as shown in figures 1.1.1 and 1.1.2.
The burner in the combustion chamber mainly undertakes the task of heating the raw gas, which should establish the right thermal conditions to decompose harmful substances such as *volatile organic compounds* (VOCs).

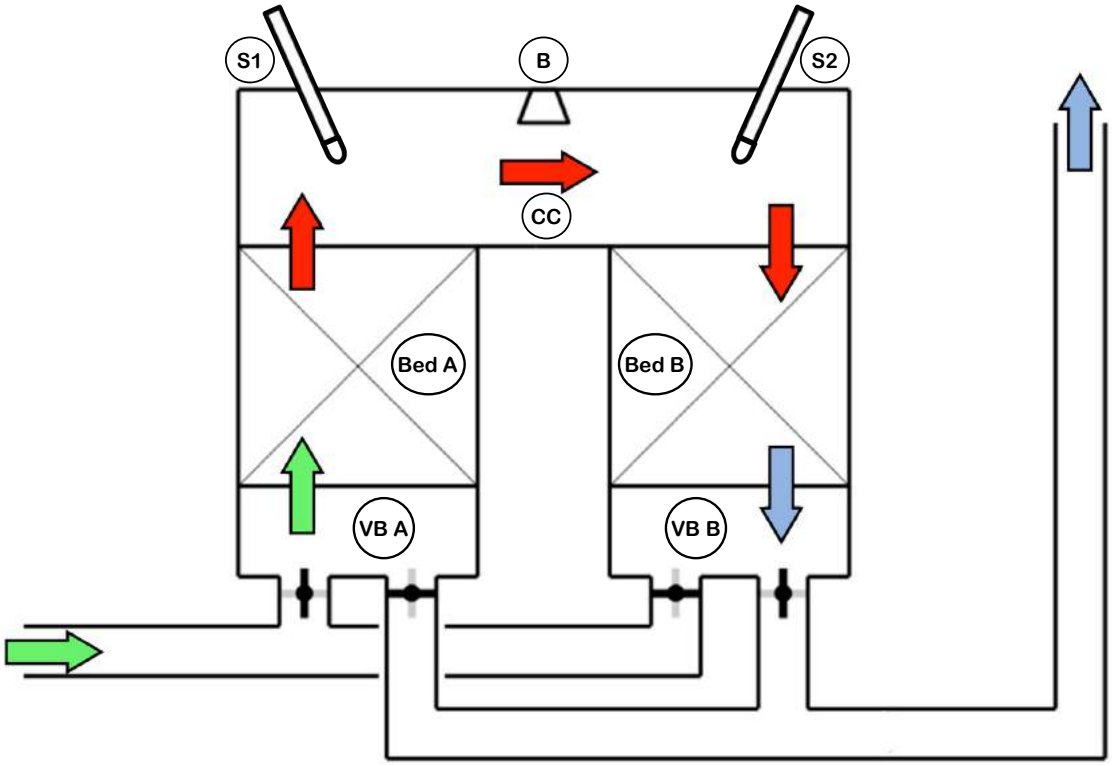

Figure 1.1.1: First half cycle of the RTO.

In the first half cycle of the RTO the contaminated raw gas enters the plant on the left side (as shown in figure 1.1.1) and passes via the valve box A (VB A) the ceramic bed A (Bed A). At the beginning of the start-up phase of the plant the ceramic beds are cold (in the range of the ambient temperature) and consequentially do not heat the incoming raw gas, which will be also in the range of ambient temperatures or insignificantly higher. In this case the raw gas is first heated in the combustion chamber, where the reaction heat by the release of energy (due to the decomposition of VOCs) should also contribute to reach the desired temperature range. The ceramic bed B (Bed B) serves the purpose of buffering the supplied energy and simultaneously cools down the hot purified gas, which leaves the plant via valve box B (VB B) and through the chimney.

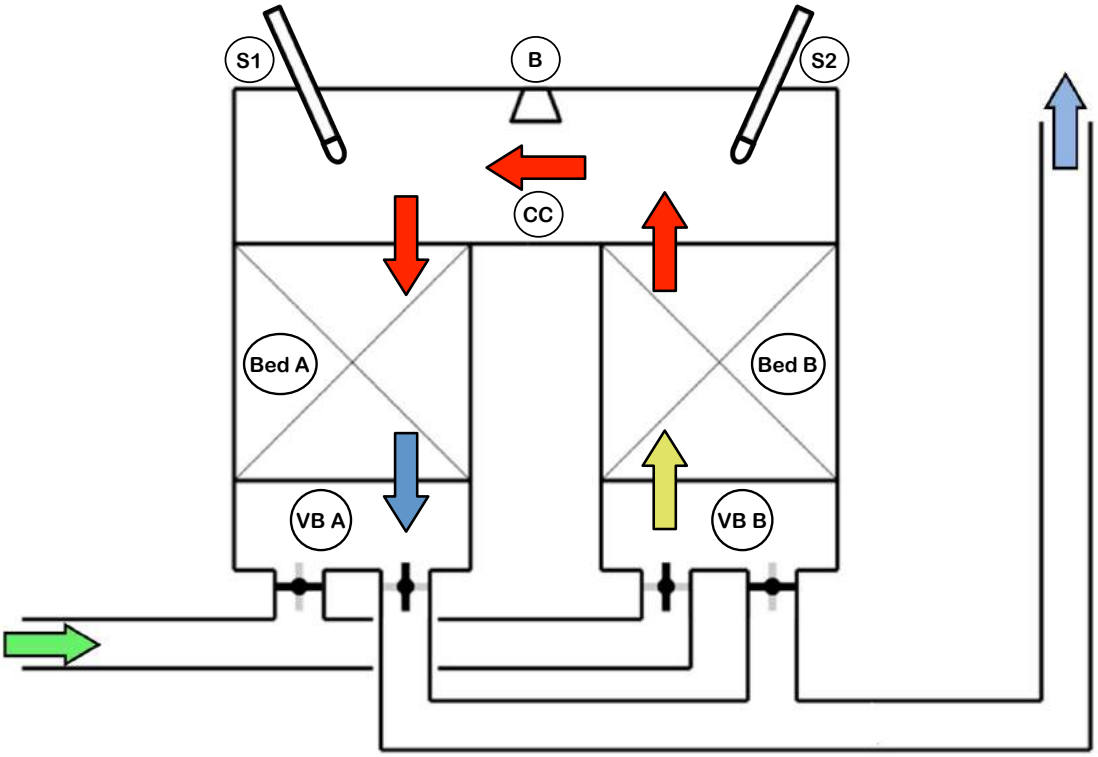

Figure 1.1.2: Second half cycle of the RTO.

After switching the valve positions in the valve boxes A and B (VB A & VB B) the flow through the plant reverses. Via valve box B (VB B) the raw gas enters the preheated ceramic bed B (Bed B) and absorbs a part of the buffered energy through heat transfer between solid and gas phase. This means that the gas has already reached higher temperatures before entering the combustion chamber (CC). Nevertheless, the hot purified gas delivers heat to the ceramic bed A (Bed A) before leaving the plant via valve box A (VB A). As a result, temperatures gradually increase in the start-up phase of the plant until the temperature sensors (S1 & S2) (should) recognize that the required temperature range for ensuring the favored chemical reaction has been reached, which would allow the reduction of the supplied fuel to the burner.
The ceramic beds play a key role as they retain the heat inside the closed system, which makes it possible to reach quite high temperatures at a moderate fuel consumption level.

1.2 State of the Art

Until now the situation for controlling the gas temperature in the combustion chamber is considered substantially simplified by applying PID (proportional-integral-derivative) controllers, whose parameters are empirically determined. Research on the model based control of *Regenerative Thermal Oxidizers* with regard to these subjects remained without results.

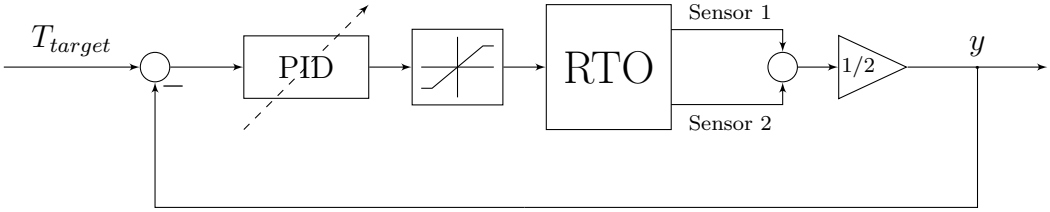

Figure 1.2.1: State of the art.

The average of two signals from the two temperature sensors is simply used as output quantity y, whereas the error between the reference temperature T_{target} and y feeds the PID controller. The maximal amount of supplied fuel is certainly fixed by the geometric dimensions of the valve in charge of the fuel injection.
The description displayed in figure 1.2.1 lacks the blocks for sampling and for digital processing in between the measurement of temperatures and the controlling of the valve feeding fuel to the burner, but it properly demonstrates the simplified approach for the complex problem.

With the aim to develop a model based control concept, it was necessary to model the considered components of the pilot plant and in a second step to install these models in the control loop.

2 Mathematical Description of Components

In order to simulate the behavior of a two-bed *Regenerative Thermal Oxidizer*, the currently applied mathematical models rely on valid, but also required assumptions and simplifications. Most of the equations and identified parameters in the model are built up on the research of *Thomas Rieger*, employed at CTP-Air Pollution Control [1] [2].
The equations describing the different components are not only connected by the temperature of the flowing gas T_g and the volume fraction Φ of volatile organic compounds (VOCs), but also by additional input variables such as the mass flow $\dot{m}(t)$, the pressure $p(t)$, the ambient temperature $T_{amb}(t)$ and the reference temperature in the combustion chamber $T_{target}(t)$, which can be time variant.

2.1 General Parameters

The simulation predominantly deals with *SI units* (Système international d'unités), therefore all functions require temperature arguments in *Kelvin* [K], the volume fraction of VOCs Φ in [m^3/m^3], the pressure in *Pascal* [Pa], the mass flow in *kilogram* per *seconds* [kg/s], however the molar mass in *kilogram* per *kilomole* [kg/kmol]. This means that the ideal gas constant $R_{id} = 8314.4621 \left[\frac{\mathrm{J}}{\mathrm{kmol\ K}}\right]$ is also adapted to [kmol].

Density
The density of the solid phase ρ_s is treated as a constant inside of the ceramic layers of the bed (cf. figure 2.3.1) due to the low thermal expansion of ceramic, unlike the density of the gas phase ρ_g, which satisfies the ideal gas law

$$M_{mix} = \sum_{k=1}^{N} x_k M_k \tag{2.1.1}$$

$$\rho_g(T_g, p) = \frac{p M_{mix}}{R_{id} T_g} \tag{2.1.2}$$

consisting of the pressure p, the ideal gas constant R_{id}, the gas temperature T_g and a mix of N molar masses M_k of the gas mixture. x_k stands for the appropriate molar volume fractions in the gas mixture, which are assumed constant during simulation.

Viscosity
The dynamic viscosity of pure gases is defined by fourth-order polynomials (Kleiber and Joh in 2013 [4]). The specific coefficients $A_\eta, B_\eta, \ldots, E_\eta$ for corresponding materials are

listed in the Appendix. In good approximation the viscosity of the gas mixture

$$\eta_g(T_g) = \sum_{k=1}^{N} x_k \left(A_{\eta,k} + B_{\eta,k} T_g + C_{\eta,k} T_g^2 + D_{\eta,k} T_g^3 + E_{\eta,k} T_g^4 \right) \tag{2.1.3}$$

is calculated by the weighted sum of the gas components.

Heat Conductivity

The heat conductivity of the solid phase λ_s is also treated as a constant inside of ceramic layers, unless the heat conductivity of pure gas λ_g, which is defined by fourth-order polynomials (Kleiber and Joh in 2013 [4]). The specific coefficients for corresponding materials are listed in the Appendix. In good approximation the heat conductivity of the gas mixture is defined as follows:

$$\lambda_g(T_g) = \sum_{k=1}^{N} x_k \left(A_{\lambda,k} + B_{\lambda,k} T_g + C_{\lambda,k} T_g^2 + D_{\lambda,k} T_g^3 + E_{\lambda,k} T_g^4 \right) \tag{2.1.4}$$

Heat Capacity

The heat capacity c_s of the ceramic layers are available in form of third-order polynomials [5], whose coefficients (attached) were determined by measurements. i characterizes the corresponding ceramic layer.

$$c_{s,i}(T_s) = A_{c_s,i} + B_{c_s,i}(T_s - 273.15) + C_{c_s,i}(T_s - 273.15)^2 + D_{c_s,i}(T_s - 273.15)^3 \tag{2.1.5}$$

The heat capacity of pure gas is calculated with the PDDS-equation (Physical Properties Data Service) [6]. The parameters $A_{c_g,k}, B_{c_g,k}, \ldots, G_{c_g,k}$ of the broken rational function are provided in the Appendix.

$$\begin{aligned} c_g(T_g) = \sum_{k=1}^{N} w_k R_{s,k} \Bigg\{ & B_{c_g,k} + (C_{c_g,k} - B_{c_g,k}) \left(\frac{T_g}{A_{c_g,k} + T_g} \right)^2 \Bigg[1 - \frac{A_{c_g,k}}{A_{c_g,k} - T_g} \\ & \left(D_{c_g,k} + E_{c_g,k} \frac{T_g}{A_{c_g,k} + T_g} + F_k \left(\frac{T_g}{A_{c_g,k} + T_g} \right)^2 + G_{c_g,k} \left(\frac{T_g}{A_{c_g,k} + T_g} \right)^3 \right) \Bigg] \Bigg\} \end{aligned} \tag{2.1.6}$$

Each portion of the gas mixture in c_g is weighted by its mass fraction w_k and its specific gas constant $R_{s,k} = \frac{R_{id}}{M_k}$, applying the ideal gas constant to the molar mass M_k.

Mean Heat Capacity

In order to provide correct values for the heat capacity within a temperature range, the integral mean of c_g

$$c_{g,m}(T_g) = \frac{1}{T_g} \int_0^{T_g} c_g(T) dT \tag{2.1.7}$$

will be taken into account. As one can see from the definition of $c_g(T_g)$ in equation (2.1.6), it would be quite challenging to determine an explicit solution of this integral. Therefore the numerical approximation by using the *Matlab* function *trapz*(.) and applying *polyfit*(.) for interpolation afterwards, helped to obtain a polynomial featuring 6^{th} degree, which approximates $c_{g,m}$ with sufficient accuracy.

Chemical Reaction
The Arrhenius law

$$C(T_g, p) = \frac{p}{R_{id} T_g} \tag{2.1.8}$$

$$r_g(T_g, \Phi, p) = -C(T_g, p)\Phi A_{kin} \exp\left(\frac{-E_a}{R_{id} T_g}\right) \tag{2.1.9}$$

consisting of the gas temperature T_g, the volume fraction of VOCs Φ and the concentration C describes the chemical reaction in each component of the RTO. The material for chemical reaction, e.g. methane, can be adjusted via the activation energy E_a and the kinetic parameter A_{kin}. The reaction enthalpy $\Delta H_R \left[\frac{\mathrm{J}}{\mathrm{kmol}}\right]$ has to be adapted as well, it appears in the gradient of the gas temperature as part of the term describing the reaction heat.

Gas Composition
Involved materials of the gas composition, which are considered in parameters like ρ_g in equation (2.1.2), M_{mix} (2.1.1), λ_g (2.1.4) and c_g (2.1.6) will not be modified with the addition of VOCs during simulation, since it is presumed that their fractions are very small and consequentially would lead to a negligible change in these parameters [2]. For better understanding it has proved preferable to highlight this distinguishing feature by applying the notation x_k for volume fractions (w_k for mass fractions), which have to be chosen in preprocessing and Φ for the volume fraction of VOCs, which constantly changes in all submodels.

At this early stage of the mathematical description of the two-bed RTO it needs to be mentioned that the state variable Φ actually represents the volume fraction of one material of *volatile organic compounds* as the *Arrhenius* law adjusts the reaction rate r_g (see equation (2.1.9)) to one specific material by parameters A_{kin} and E_a. Nevertheless, Φ still remains representative for the entire VOCs mixture in the gas.

2.2 Valve Box

In terms of the propagation of the incoming gas flow, the volumes of the valve boxes can be divided into laminar and turbulent areas depending on their geometry. In this thesis it has been assumed that a simplified model by means of a continuous stirred tank reactor describes reality to sufficient level of detail, concerning the gas temperature T_g and the portion of VOCs Φ (respectively the concentration) [2].

The two differential equations (2.2.1) are connected by the heat of chemical reaction in the box. To put it simply, one could say that gas flow encounters a delay passing the valve boxes specified by (for better readability function arguments are rendered as a subscript)

$$\frac{dT_g}{dt} = \frac{\frac{|\dot{m}_{(t)}|}{V_{vb}}\left(c_{g,m(T_{g,in})}T_{g,in(t)} - c_{g,m(T_g)}T_g\right) + \Delta H_R\, r_{g(T_g,\Phi,p_{in})} - k_{loss}a^{vb}_{V,loss}(T_g - T_{amb(t)})}{c_{g(T_g)}\rho_{g(T_g,p_{in})}} \tag{2.2.1a}$$

$$\frac{d\Phi}{dt} = \frac{\frac{|\dot{m}_{(t)}|}{M_{mix}V_{vb}}\left(\Phi_{in(t)} - \Phi\right) + r_{g(T_g,\Phi,p_{in})}}{C_{(T_g,p_{in})}} \tag{2.2.1b}$$

whereas its behavior resembles the one of a PT1-element (proportional time) in good approximation. Since parameters such as the heat capacity c_g and the mixed heat capacity $c_{g,m}$ depend on the gas temperature by higher order polynomials (see section 2.1), the ordinary differential equations, related to the initial conditions $T_g(t = t_0) = T_{g,t_0}$ and $\Phi(t = t_0) = \Phi_{t_0}$, become nonlinear. Regarding parameter values such as the volume V_{vb} or the profile A_{vb} of the valve box see Appendix.

Switching Inputs/Outputs

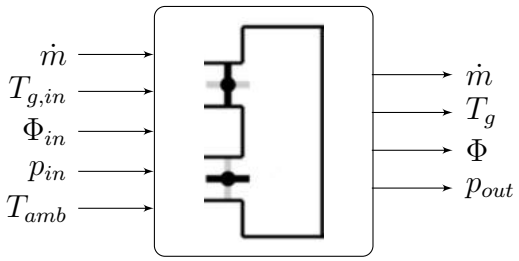

Figure 2.2.1: Block diagram of the valve box.

Parameters of the input stream characterized by the subscript "in" such as the gas temperature $T_{g,in}$, the inlet volume fraction of VOCs Φ_{in} and the inlet pressure p_{in} arrive as inputs of the RTO in the **cold gas cycle** $\rightarrow \operatorname{sign}(\dot{m}) = 1$, though they come from the ceramic bed at $x_{bed} = H_{N_l}$ (see section 2.3.1.1 and 2.3.1.4) in the **hot gas cycle** $\rightarrow \operatorname{sign}(\dot{m}) = -1$.

2.2.1 Pressure Drop in the Valve Box

The calculation ensues with the pressure drop, which should be considered dynamically in the inlet absolute pressure p_{in} of the ceramic beds in cold gas cycles (cf. equation (2.3.1)). For simplification it is assumed that the pressure drop

$$\Delta p_{vb} = \frac{\zeta_{vb}}{2\rho_g(T_g, p_{in})}\left(\frac{\dot{m}}{A_{basis}}\right)^2 \tag{2.2.2}$$

is exclusively caused by the turbulent flow, which is of course not entirely correct (see [1] at page 18-21 and 49 for more information). Equation (2.2.2) applies the coefficient $\zeta_{vb} = 213$ (in reference to the pilot plant), which was determined by measurements, the input parameters $\dot{m}$, p_{in} and the output gas temperature T_g of the valve box, provided by the solution of the differential equations in (2.2.1).

2.3 Ceramic Bed

The early identification of the bed equations can be found in [1]. The considered basis model ([1] page 39, equation 4-2 and 4-3) deals with a thermal description only. Among others, a chemical reaction in the bed was added by now, so that the three coupled partial differential equations (cf. [1], equations 4-2, 4-3, 4-36, 4-37 and 2-91)

$$\frac{\partial T_s}{\partial t} = \overbrace{\frac{\lambda_{s(x)}}{\rho_{s(x)} c_{s(x,T_s)}}}^{\text{Ia}} \frac{\partial^2 T_s}{\partial x^2} + \overbrace{\frac{h_{(x,T_g,\dot{m}_{bed})} a_{V(x)}}{(1-\epsilon_{B(x)})\rho_{s(x)} c_{s(x,T_s)}}}^{\text{IIIa}} (T_g - T_s) - \overbrace{\frac{k_{loss} a^{\text{bed}}_{V,loss}}{(1-\epsilon_{B(x)})\rho_{s(x)} c_{s(x,T_s)}}}^{\text{IVa}} (T_s - T_{amb(t)}) \tag{2.3.1a}$$

$$\begin{aligned}\frac{\partial T_g}{\partial t} = {} & \overbrace{a_{\text{eff}(x,T_g,\dot{m}_{bed},p_{in})}}^{\text{Ib}} \frac{\partial^2 T_g}{\partial x^2} - \overbrace{\frac{\dot{m}_{bed(t)}}{\epsilon_{B(x)} A_{bed}\, \rho_{g(T_g,p_{in})}}}^{\text{IIb}} \frac{\partial T_g}{\partial x} + \overbrace{\frac{h_{(x,T_g,\dot{m}_{bed})} a_{V(x)}}{\epsilon_{B(x)} \rho_{g(T_g,p_{in})} c_{g(T_g)}}}^{\text{IIIb}} (T_s - T_g) \\ & + \underbrace{\varphi_{shape} \frac{64}{2} \frac{\eta_{g(T_g)}}{d^2_{h(x)} \rho_{g(T_g,p_{in})} c_{g(T_g)}} \left(\frac{\dot{m}_{bed}}{\epsilon_{B(x)}\, A_{bed}\, \rho_{g(T_g,p_{in})}} \right)^2}_{\text{IVb}} + \underbrace{\frac{\Delta H_R\, r_{g(T_g,\Phi,p_{in})}}{\rho_{g(T_g,p_{in})} c_{g(T_g)}}}_{\text{Vb}}\end{aligned} \tag{2.3.1b}$$

$$\frac{\partial \Phi}{\partial t} = \underbrace{D_{ax(x,T_g,\dot{m}_{bed},p_{in})}}_{\text{Ic}} \frac{\partial^2 \Phi}{\partial x^2} - \underbrace{\frac{\dot{m}_{bed(t)}}{\epsilon_{B(x)} A_{bed}\, \rho_{g(T_g,p_{in})}}}_{\text{IIc}} \frac{\partial \Phi}{\partial x} + \underbrace{\frac{r_{g(T_g,\Phi,p_{in})}}{C_{(T_g,p_{in})}}}_{\text{Vc}} \tag{2.3.1c}$$

with *Neumann* **boundary conditions in the hot gas cycle** $\rightarrow \text{sign}\,(\dot{m}_{bed}) = 1$:

at $x = 0$

$$\frac{\partial T_s}{\partial x} = 0 \tag{2.3.2a}$$

$$\frac{\partial T_g}{\partial x} = \frac{1}{a_{\text{eff}(0,T_g,\dot{m}_{bed},p_{in})}} \frac{\dot{m}_{bed(t)}}{\epsilon_{B(0)} A_{bed}\, \rho_{g(T_g,p_{in})}} \left(T_g - T_{g,in(t)}\right) \tag{2.3.2b}$$

$$\frac{\partial \Phi}{\partial x} = \frac{1}{D_{ax(0,T_g,\dot{m}_{bed},p_{in})}} \frac{\dot{m}_{bed(t)}}{\epsilon_{B(0)} A_{bed}\, \rho_{g(T_g,p_{in})}} \left(\Phi - \Phi_{in(t)}\right) \tag{2.3.2c}$$

at $x = H_{N_l}$

$$\frac{\partial T_s}{\partial x} = 0 \tag{2.3.3a}$$

$$\frac{\partial T_g}{\partial x} = 0 \tag{2.3.3b}$$

$$\frac{\partial \Phi}{\partial x} = 0 \tag{2.3.3c}$$

and *Neumann* **boundary conditions in the cold gas cycle** $\rightarrow \operatorname{sign}(\dot{m}_{bed}) = -1$:
at $x = 0$

$$\frac{\partial T_s}{\partial x} = 0 \tag{2.3.4a}$$

$$\frac{\partial T_g}{\partial x} = 0 \tag{2.3.4b}$$

$$\frac{\partial \Phi}{\partial x} = 0 \tag{2.3.4c}$$

at $x = H_{N_l}$

$$\frac{\partial T_s}{\partial x} = 0 \tag{2.3.5a}$$

$$\frac{\partial T_g}{\partial x} = \frac{1}{a_{\text{eff}(H_{N_l}, T_g, \dot{m}_{bed}, p_{in})}} \frac{\dot{m}_{bed(t)}}{\epsilon_{B(H_{N_l})} A_{bed}\, \rho_{g(T_g, p_{in})}} \left(T_g - T_{g,in(t)}\right) \tag{2.3.5b}$$

$$\frac{\partial \Phi}{\partial x} = \frac{1}{D_{ax(H_{N_l}, T_g, \dot{m}_{bed}, p_{in})}} \frac{\dot{m}_{bed(t)}}{\epsilon_{B(H_{N_l})} A_{bed}\, \rho_{g(T_g, p_{in})}} \left(\Phi - \Phi_{in(t)}\right) \tag{2.3.5c}$$

specify the distribution of the gas temperature T_g, the temperature of solid phase T_s and the volume fraction of VOCs Φ over time t and space x. At the starting time $t = t_0$ initial distributions

$$T_s(x, t_0) = T_{s,t_0}(x) \qquad T_g(x, t_0) = T_{g,t_0}(x) \qquad \Phi(x, t_0) = \Phi_{t_0}(x) \tag{2.3.6}$$

over space have to be chosen. Since this thesis merely focuses on a bed with honeycomb structures made of ceramic, the meaning of the solid phase temperature T_s is equivalent to the temperature of the ceramic in the bed. Using a single dimension in space assumes that the behavior over the horizontal bed profile is constant, which is of course not entirely correct. This assumption was made in favor for implementation effort in *Matlab Simulink* and to ensure bearable computation times. A more detailed description of the equation can be found in section 2.3.1.5. For further information on the PDEs and its boundary conditions see [2].

2.3.1 Parameters

The parameters in the equation (2.3.1) deal with strongly nonlinear dependencies, however it should be pointed out that the dependency on space x is piecewise constant in most cases. More details on bed parameters for the pilot plant at CTP can be found in the Appendix.

2.3.1.1 Space Dependencies

The count direction of space x starts at the top of the bed (cf. figure 2.3.1). The ceramic is constructed by layers, in which parameters of the solid phase (characterized by the subscript "s"), such as the heat conductivity $\lambda_{s,i} = \lambda_s(x)$, the density $\rho_{s,i} = \rho_s(x)$, the specific surface $a_{V,i} = a_V(x)$, the porosity $\epsilon_{B,i} = \epsilon_B(x)$, the hydraulic diameter $d_{h,i} = d_h(x)$, the layer boundaries of the ceramic height $H_i = H(x)$ and the heat capacity $c_{s,i}(T_g) = c_s(x, T_g)$ are constant in the current layer $i \in [1, \ldots, N_l]$.

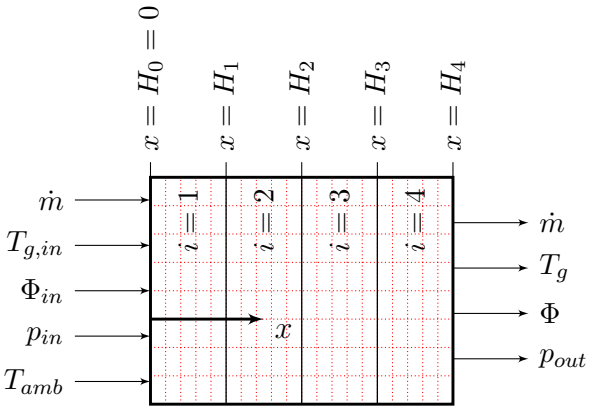

Figure 2.3.1: Overview of bed B in the first half cycle or bed A in the second half cycle.

This leads to their piecewise constant distribution in x. For instance, both beds of the implemented pilot plant, which stands at CTP consist of four layers, whereas only the one at the top ($x \in [0, H_1)$) differs from the other ones.

2.3.1.2 Heat Transfer Coefficient

An explicit dependency on space is given in the heat transfer coefficient h. The coefficient is a function of the heat conductivity of gas $\lambda_g(T_g)$ and the Nusselt number Nu, which relies on an empiric mathematical relation according to Muzychka and Yovanovich (1998) (2004) [7]. Nu is treated as a function of the Reynolds number Re, the Prandtl number Pr and the proportion of the hydraulic diameter $d_{h,i} = d_h(x)$ over space x applied to the height $\tilde{x}_i = x - H_{i-1}$ for $i = 1, \ldots, N_l$.

$$\mathrm{Nu} = \frac{h\, d_{h,i}}{\lambda_g(T_g)} \qquad \mathrm{Re}_i = \frac{|\dot{m}_{bed}|\, d_{h,i}}{\epsilon_{B,i}\, A_{bed}\, \eta_g(T_g)} \qquad \mathrm{Pr} = \frac{\eta_g(T_g) c_g(T_g)}{\lambda_g(T_g)} \tag{2.3.7}$$

The Reynolds number has to be checked, since the Nu relation is limited up to $\mathrm{Re} < 2300$. Therefore exceeding Re values are set to 2300 in the simulation. The following empiric relation adapted to quadratic channels of the honeycomb ceramic bed is used to calculate the Nusselt number

$$\tilde{m} = 2.27 + 1.65\mathrm{Pr}^{1/3}$$

$$\mathrm{Nu} = \left\{ \left(\frac{0.886}{\left[1 + (1.909\mathrm{Pr}^{1/6})^{9/2}\right]^{2/9}} \sqrt{\frac{d_{h,i}}{\tilde{x}_i}\, \mathrm{Re}_i\, \mathrm{Pr}} \right)^{\tilde{m}} + \left(\left(1.7831 \frac{d_{h,i}}{\tilde{x}_i}\, \mathrm{Re}_i\, \mathrm{Pr} \right)^{5/3} + 3.61^5 \right)^{\tilde{m}/5} \right\}^{1/\tilde{m}} \tag{2.3.8}$$

under state dependencies regarding the gas temperature T_g, a certain point x in the layer i and considering the input parameter $\dot{m}_{bed}$, which can be time variant.

2.3.1.3 Diffusion and Dispersion Coefficients

Diffusion and dispersion coefficients are initially used for the propagation of mass and temperature [2]. The absolute or effective diffusion coefficient

$$D_{abs}(T_g, p_{in}) = 10^{-5} \left(\frac{T_g}{273.15} \right)^{1.75} \frac{1.01325 \cdot 10^5}{p_{in}(t)} \tag{2.3.9}$$

and the axial dispersion coefficient for mass transfer

$$D_{ax}(x, T_g, \dot{m}_{bed}, p_{in}) = D_{abs}(T_g, p_{in}) + \left(\frac{\dot{m}_{bed}(t)}{\epsilon_{B,i}\, A_{bed}\, \rho_g(T_g, p_{in})} \right)^2 \frac{d_{h,i}^2}{192\, D_{abs}(T_g, p_{in})} \tag{2.3.10}$$

and the dispersion coefficient for the gas temperature

$$a_{\text{eff}}(x, T_g, \dot{m}_{bed}, p_{in}) = \frac{\lambda_g(T_g)}{\rho_g(T_g, p_{in}) c_g(T_g)} + \left(\frac{\dot{m}_{bed}(t)\, d_{h,i}}{\epsilon_{B,i}\, A_{bed}} \right)^2 \frac{c_g(T_g)}{192\, \rho_g(T_g, p_{in})\, \lambda_g(T_g)} \tag{2.3.11}$$

occur at the second space derivatives in the partial differential equations (2.3.1).

2.3.1.4 Switching Inputs/Outputs

Incoming physical quantities, such as the input gas temperature $T_{g,in}$, the inlet volume fraction of VOCs Φ_{in} and the inlet pressure p_{in} arrive from the valve box in the **cold gas cycle** $\rightarrow \text{sign}\,(\dot{m}_{bed}) = 1$ and from the combustion chamber in the **hot gas cycle** $\rightarrow \text{sign}\,(\dot{m}_{bed}) = -1$. The subscript "*bed*" is added to clarify the count direction of x.

$$\dot{m}_{bed} = -\dot{m} \tag{2.3.12}$$

$T_{g,in}$ and Φ_{in} (cf. figure 2.3.1) can be interpreted as input sources due to the relation to the state variables T_g and Φ, which attract attention by the (global) appearance in all model's differential equations of the RTO. Alternatively, there are input parameters p_{in}, $\dot{m}$ as well as T_{amb} (cf. figure 2.3.1), which could be potential control variables for a global control strategy of the entire flue gas cleaning system.

2.3.1.5 Mathematical Terms in the PDEs

This paragraph refers to the mathematical terms (Ia) to (Vc) in the partial differential equations of the ceramic bed (2.3.1). The equation has been brought to a consistent form with time derivatives on the left hand side. Originally the equation goes back to the one dimensional description of thermal distribution of heat in a given region over time (*heat equation* [3]).

$$\frac{\partial T}{\partial t} = a \frac{\partial^2 T}{\partial x^2}$$

The parameter $a = \lambda/(\rho c)$ (SI unit m^2/s), equivalent to the term (Ia), describes the thermal conductivity, characterizing the shape of the thermal propagation in the ceramic, but also of the gas temperature. The coefficient a_{eff} at the second order space derivative in (2.3.1b) can also be interpreted as a function of the thermal conductivity

$$\frac{\lambda_g}{\rho_g c_g}$$

applied to the mass flow $\dot{m}_{bed}$ and geometric dimensions. Similar to temperatures the axial diffusion coefficient D_{ax} characterizes the shape of the propagation of the volume fraction of VOCs in the bed. The figures 2.3.2 to 2.3.4 assume a linear distribution of the ceramic temperature T_s and the gas temperature T_g between 0°C and 1100°C over space x. Parameters like c_g and λ_g were adapted to air, with the usual gas composition (table 6.1.1 and 6.1.2) at an atmospheric pressure of $p_{in} = 1.01325 \cdot 10^5$ Pa.

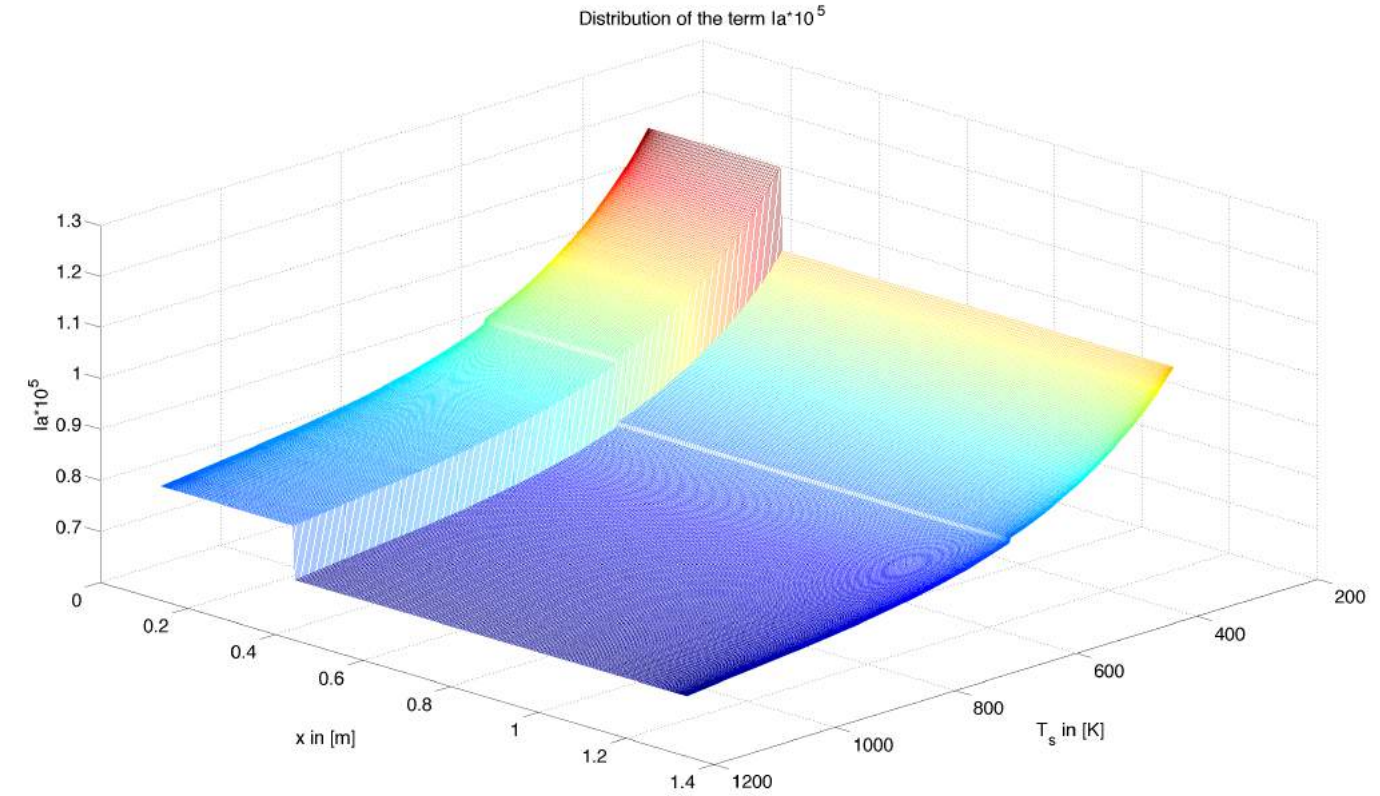

Figure 2.3.2: Distribution of term Ia.

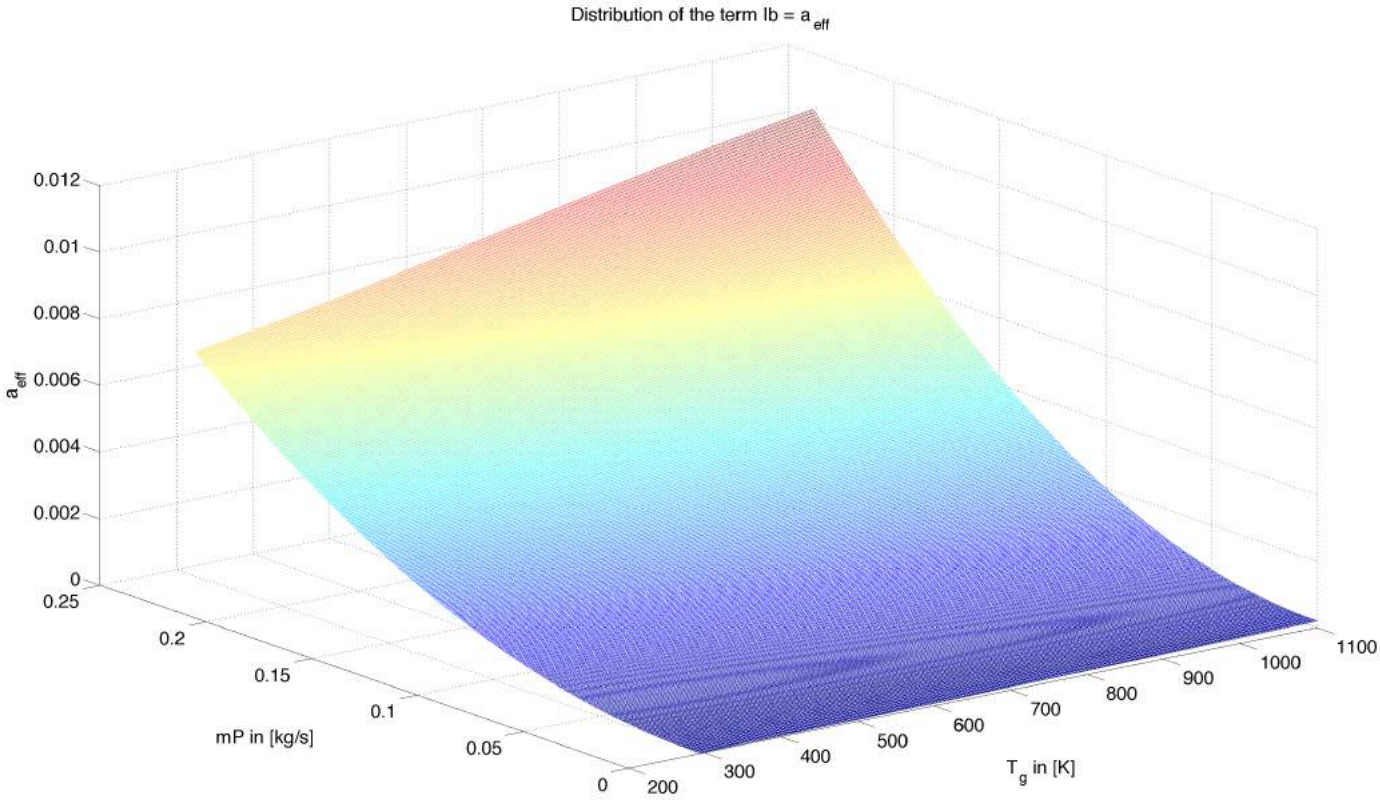

Figure 2.3.3: Distribution of term Ib = a_{eff}, which is constant over x in the pilot plant.

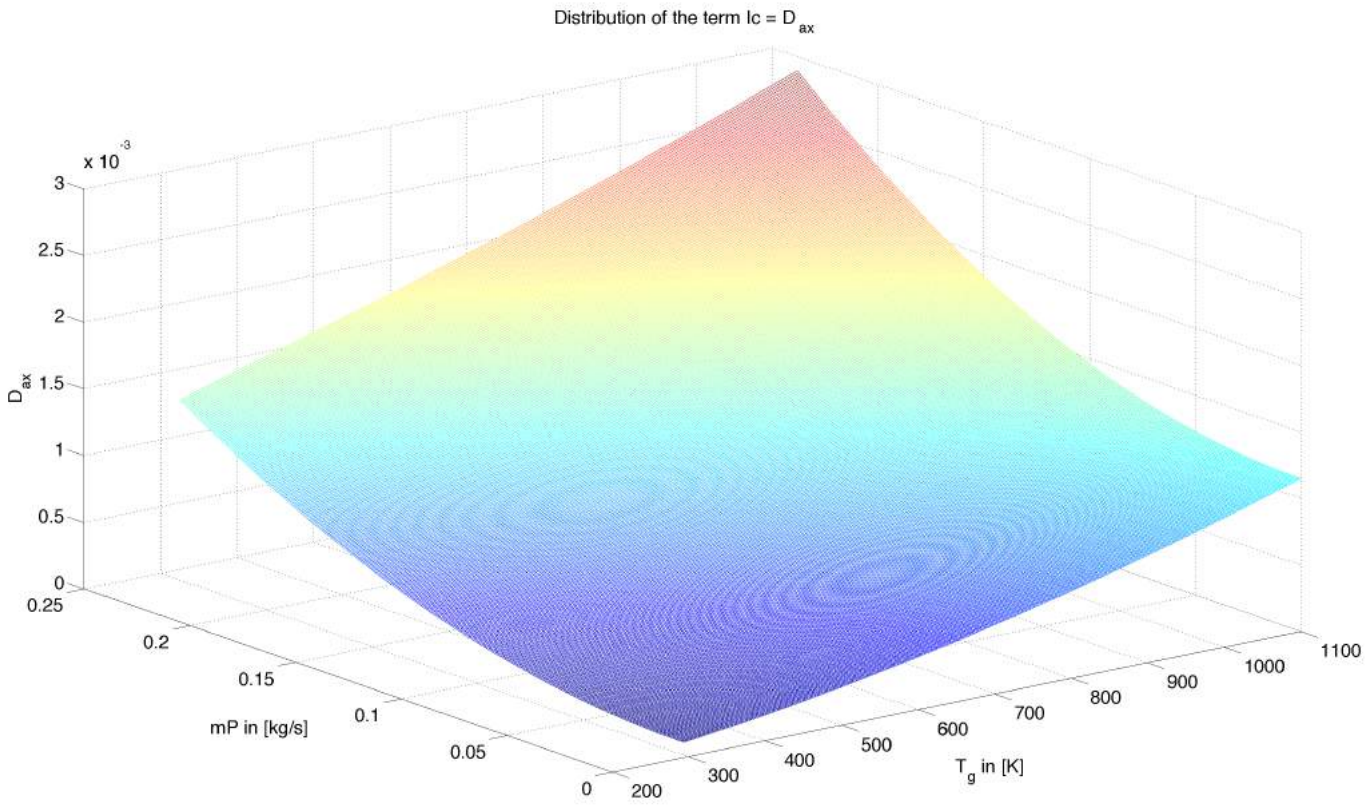

Figure 2.3.4: Distribution of term Ic = D_{ax}, which is constant over x in the pilot plant.

When looking at figure 2.3.3 and 2.3.4 smooth distributions over the input parameter $\dot{m}_{bed}$ and the state variable T_g can be seen, whereas in figure 2.3.2 the discontinuous jump at $x = 0.3$m visualizes the transition between ceramic layers. This can be attributed to the change in density ρ_s of the layers, which occupy a height of 0.3m each in the pilot plant.
In order to understand the small jump in the distribution of Ⓘa at around $T_g \approx 600$K remember that the heat capacity $c_s(x, T_s) = c_{s,i}(T_s)$ is continuous in T_s, but again a discontinuous jump of polynomials occurs at $x = 0.3\text{m} = H_1$. Due to the fact that the temperature profile of the solid phase changes over space, the parameters $T_s(x, t)$ and x are no longer independent from each other.

The term Ⓘ = ⒾⅠb = ⒾⅠc describes the thermal convection and is equivalent to the velocity u of the incoming gas through the bed. (Keep in mind that $\dot{m} = -\dot{m}_{bed}$.)

$$u = \frac{\dot{m}(t)}{\epsilon_{B,i}\, A_{bed}\, \rho_g(T_g, p_{in})}$$

This certainly explains its appearance at the first order space derivative in the PDEs (2.3.1). Since the gas density ρ_g depends on T_g reciprocally, the term Ⓘ is linear in $\dot{m}_{bed}$ and T_g.

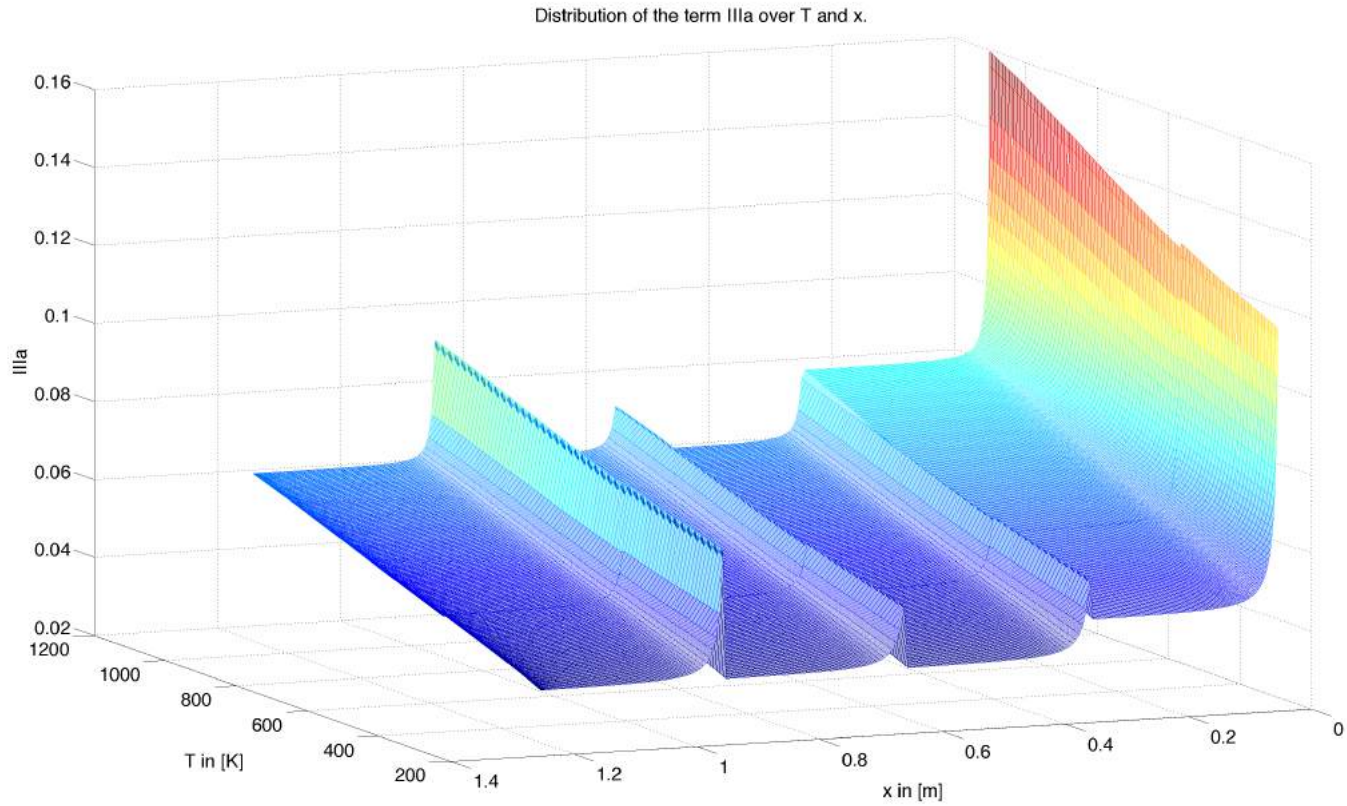

Figure 2.3.5: Distribution of term IIIa over T and x.

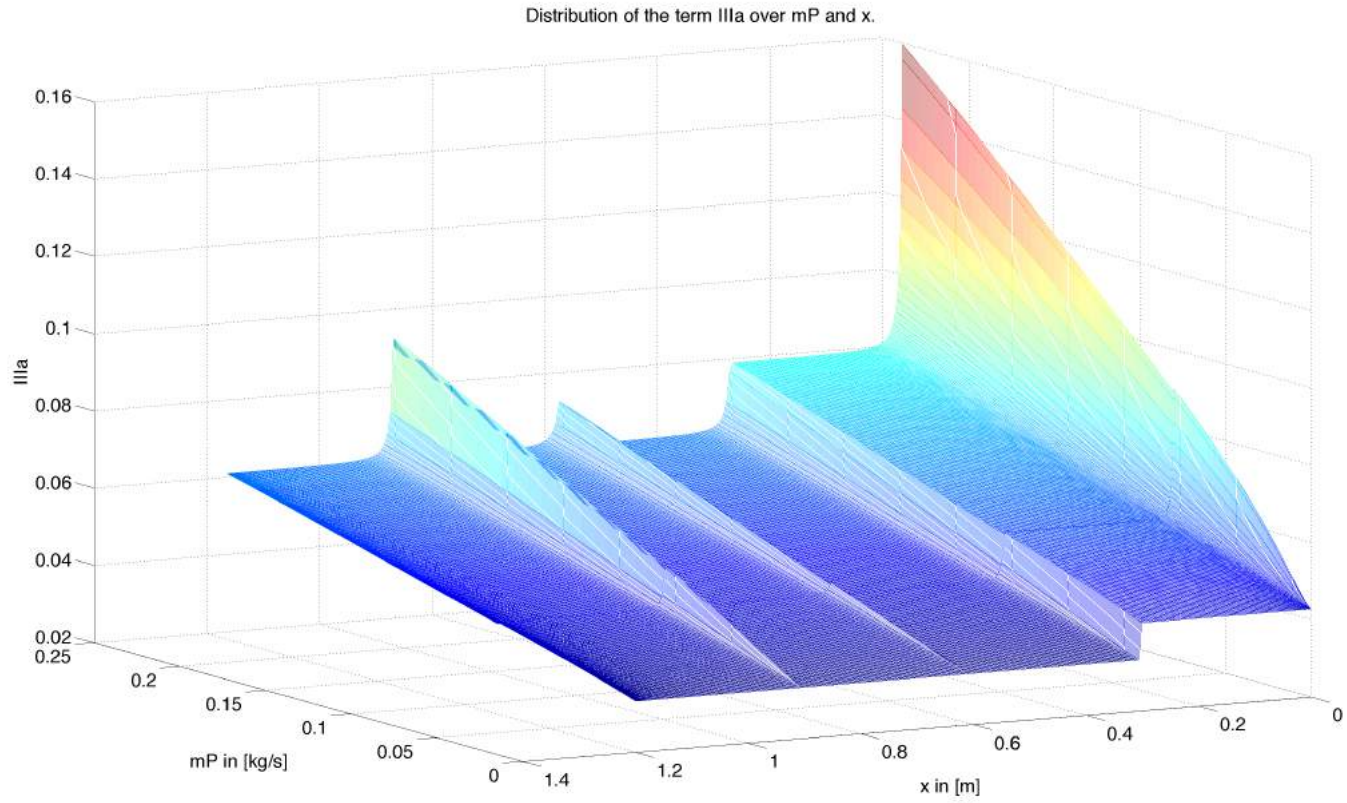

Figure 2.3.6: Distribution of term IIIa over $\dot{m}_{bed}$ and x.

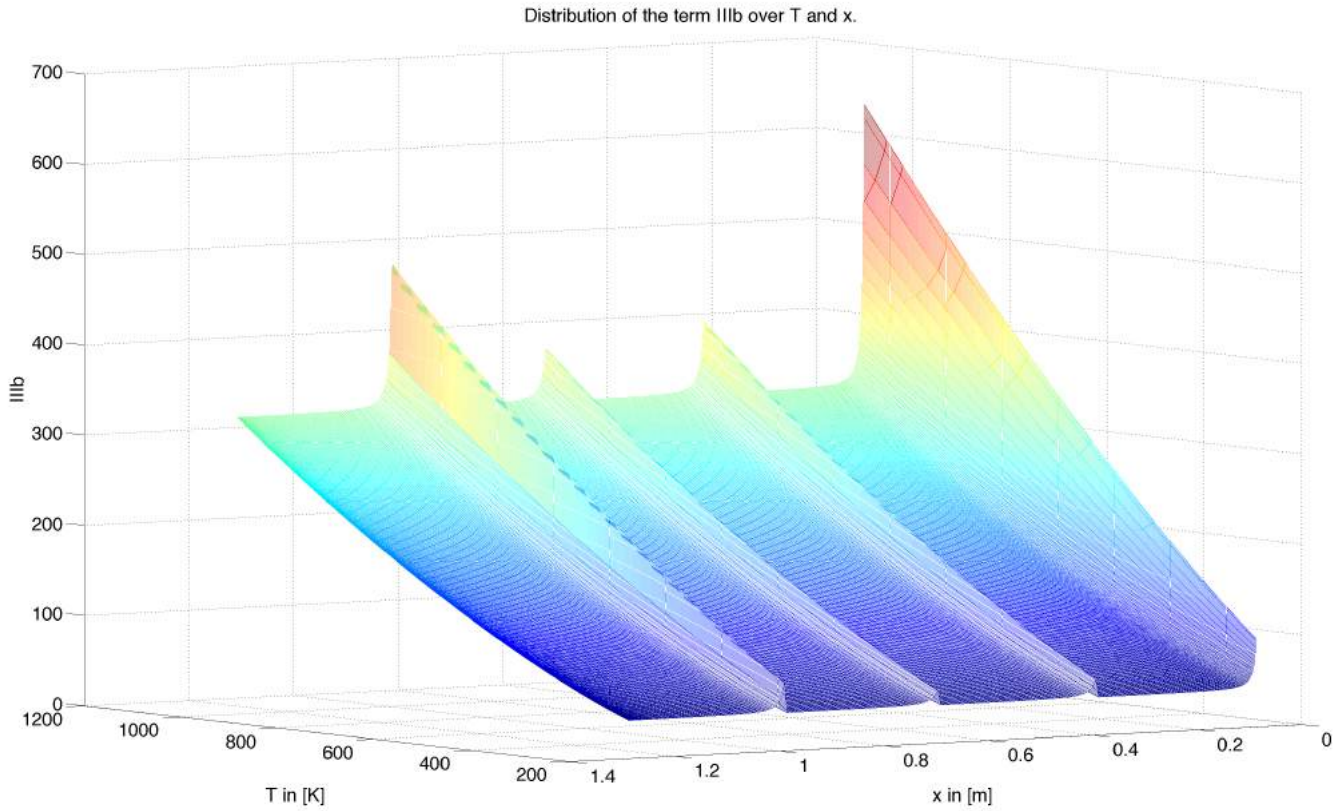

Figure 2.3.7: Distribution of term IIIb over T and x.

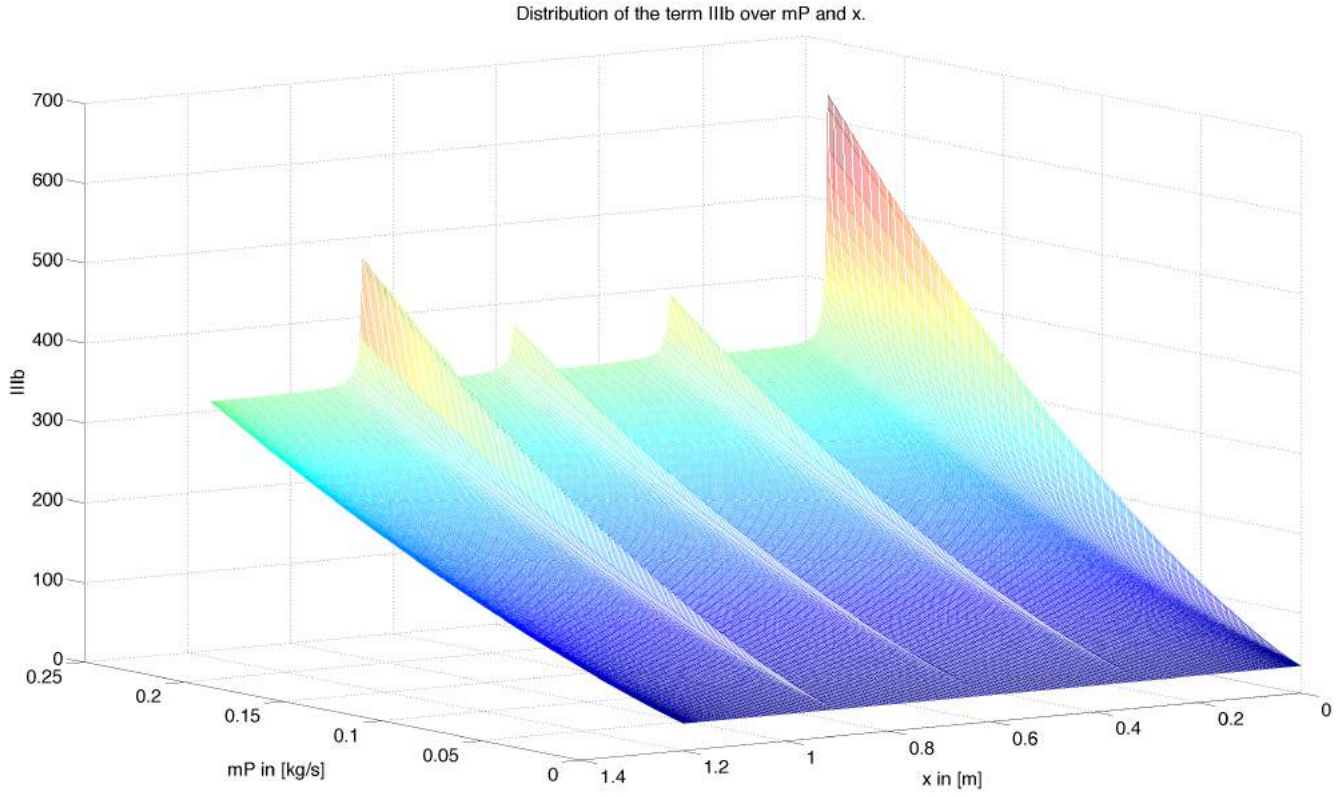

Figure 2.3.8: Distribution of term IIIb over $\dot{m}_{bed}$ and x.

The terms (III) characterize the heat transfer between the gas temperature and the ceramic temperature. When looking at figures 2.3.5 to 2.3.8 it has been assumed that the temperature profile of the solid and the gas phase are equivalent $T = T_s = T_g$ and linearly distributed between 0°C and 1100°C over space x. The heat capacity c_g was adjusted to air, with the usual gas composition (table 6.1.1 and 6.1.2) at an atmospheric pressure of $p_{in} = 1.01325 \cdot 10^5$ Pa.

The gain of the heat transfer coefficient (IIIa) for T_s in (2.3.1b) in the top ceramic layer (cf. figures 2.3.5 and 2.3.6 at $x \in [0, 0.3)$m) provides a better absorption of heat coming from the combustion chamber. This also points out that a tightening of the honeycomb channels (by reducing ϵ_B) in the top ceramic layer would also increase the heat transfer near the combustion chamber.
The coefficient is discontinuous, since it increases rapidly at the layer inlet points $x = H_{i-1}$ for $i = 1, \ldots, N_l$ as a reason of the Nusselt equation (2.3.8). The visibly sharper increases at $x = 0$m $= H_0$ and also at $x = 0.9$m $= H_3$ compared to $x = H_1, H_2$ occurred due to the choice of grid points in space x (cf. figure 3.3.1). As a reason of the switching boundary conditions, the gaps between grid points will be much tighter at the boundaries of the bed.

The coefficient (IVa) describes the behavior of heat loss to the surrounding area, considering the specific surface of the bed $a_{V,loss}^{bed}$ and a coefficient k_{loss}, determined by measurements. The dissipation term (IVb) will provoke an increase of the gas temperature because of the pressure drop. Due to the chemical reaction the release of heat will also increase the gas temperature, characterized by the term (Vb). And again this leads to the reduction of the volume fraction of VOCs, described by (Vc).

2.3.2 Pressure Drop in the Bed

Three different areas for the pressure drop in the ceramic bed have to be considered [1]. The pressure drop at the layer inlet points $\mathbf{x}_{in} = [x_0^{in}\ x_1^{in}\ \dots\ x_{N_l-1}^{in}]^T$ (whereas $x_0^{in} = 0$) with the corresponding coefficient $\zeta_{in} = 0.67$

$$\Delta p_{in}(t) = \sum_{i=0}^{N_l-1} \frac{\zeta_{in}}{2\rho_g(T_{g(x_i^{in},t)}, p_{in(t)})} \left(\frac{\dot{m}_{bed}(t)}{\epsilon_{B,i}\, A_{bed}}\right)^2, \tag{2.3.13}$$

at the layer outlet points $\mathbf{x}_{out} = [x_1^{out}\ x_2^{out}\ \dots\ x_{N_l}^{out}]^T$ with the coefficient $\zeta_{out} = 1.08$

$$\Delta p_{out}(t) = \sum_{i=1}^{N_l} \frac{\zeta_{out}}{2\rho_g(T_{g(x_i^{out},t)}, p_{in(t)})} \left(\frac{\dot{m}_{bed}(t)}{\epsilon_{B,i}\, A_{bed}}\right)^2 \tag{2.3.14}$$

and inside each of the N_l layers.

$$\zeta_{pipe,i}(T_{g(x,t)}) = \varphi_{shape} \frac{64}{\mathrm{Re}_i(T_{g(x,t)})} \tag{2.3.15}$$

$$\begin{aligned}
\Delta p_{pipe}(t) &= \left(\frac{\dot{m}_{bed}(t)}{\epsilon_{B,i}\, A_{bed}}\right)^2 \sum_{i=1}^{N_l} \int_{x_{i-1}^{in}}^{x_i^{out}} \frac{\zeta_{pipe,i}(T_{g(x,t)})}{2\, d_{h,i}\, \rho_g(T_{g(x,t)}, p_{in(t)})} dx \\
&= \varphi_{shape} \frac{64}{2} \sum_{i=1}^{N_l} \int_{x_{i-1}^{in}}^{x_i^{out}} \frac{\eta_g(T_g)}{d_{h,i}^2} \frac{|\dot{m}_{bed}(t)|}{\epsilon_{B,i}\, A_{bed}\, \rho_g(T_{g(x,t)}, p_{in})} dx \\
&= \varphi_{shape} \frac{64}{2} \frac{R_{id}|\dot{m}_{bed}(t)|}{A_{bed}\, p_{in}(t)\, M_{mix}} \sum_{i=1}^{N_l} \frac{1}{d_{h,i}^2 \epsilon_{B,i}} \left(\int_{x_{i-1}^{in}}^{x_i^{out}} \eta_g(T_{g(x,t)}) T_g(x,t) dx\right)
\end{aligned} \tag{2.3.16}$$

The distribution of the gas temperature T_g in the equations from (2.3.13) to (2.3.16) has to be provided as a solution of the partial differential equations (2.3.1). The length (one dimensional view), respectively the height (three dimensional view) of each layer is characterized by $L_i = x_i^{out} - x_{i-1}^{in}$ for $i = 1, \dots, N_l$ (whereas $x_0^{in} = 0$). For required discretization, there will be a substitution of space x by a grid of $N_x + 1$ points later on. As a result, the integral will be replaced by the sum of $N_x + 1 - 2N_l$ points with corresponding grid gaps Δx_l for $l = 1, \dots, N_x$.

profile	shape coefficient φ_{shape}
circle	1
square	0.89

Table 2.3.1: Shape coefficient (Kast & Nirschl, 2013 [8]).

place	pressure coefficient ζ
inlet	0.67
outlet	1.08

Table 2.3.2: Pressure coefficient (Kast & Nirschl, 2013 [8]).

2.4 Combustion Chamber

The equations for the combustion chamber resemble the ones of the ceramic bed (2.3.1). Since the chamber does not consist of any porous layers inside, almost no parameters with space dependencies have to be taken into account in the first place. The partial differential equations (for better readability function arguments are rendered as a subscript)

$$\frac{\partial T_g}{\partial t} = \overbrace{D_{cc(T_g,\dot{m},p_{in})}\frac{\partial^2 T_g}{\partial x^2}}^{\text{conduction}} - \overbrace{\frac{\dot{m}_{(x,t)}}{A_{cc}\,\rho_{g(T_g,p_{in})}}\frac{\partial T_g}{\partial x}}^{\text{convection}} - \overbrace{\frac{k_{loss}\,a^{cc}_{V,loss}}{\rho_{g(T_g,p_{in})}\,c_{g(T_g)}}(T_g - T_{amb(t)})}^{\text{ambient loss}} + \underbrace{\frac{\Delta H_R\, r_{g(T_g,\Phi,p_{in})}}{\rho_{g(T_g,p_{in})} c_{g(T_g)}}}_{\text{reaction heat}} \tag{2.4.1a}$$

$$\frac{\partial \Phi}{\partial t} = \underbrace{D_{cc(T_g,\dot{m},p_{in})}\frac{\partial^2 \Phi}{\partial x^2}}_{\text{conduction}} - \underbrace{\frac{\dot{m}_{(x,t)}}{A_{cc}\,\rho_{g(T_g,p_{in})}}\frac{\partial \Phi}{\partial x}}_{\text{convection}} + \underbrace{\frac{r_{g(T_g,\Phi,p_{in})}}{C_{(T_g)}}}_{\text{reduction}} \tag{2.4.1b}$$

describe the distribution of the state variables T_g and Φ over time t and over space x of the combustion chamber in single dimension. The equations are related to the initial distributions

$$T_g(x,t_0) = T_{g,t_0}(x) \qquad \Phi(x,t_0) = \Phi_{t_0}(x) \tag{2.4.2}$$

at the time $t = t_0$, which have to be chosen. If the **mass flow arrives from the bed A** ($\rightarrow \operatorname{sign}(\dot{m}) = 1 \ \forall x$) *Neumann* **boundary conditions** are given by:
at $x = 0$

$$\frac{\partial T_g}{\partial x} = \frac{1}{D_{cc(T_g,\dot{m},p_{in})}}\frac{\dot{m}_{(0,t)}}{A_{cc}\,\rho_{g(T_g,p_{in})}}\big(T_g - T_{g,in(t)}\big) \tag{2.4.3a}$$

$$\frac{\partial \Phi}{\partial x} = \frac{1}{D_{cc(T_g,\dot{m},p_{in})}}\frac{\dot{m}_{(0,t)}}{A_{cc}\,\rho_{g(T_g,p_{in})}}\big(\Phi - \Phi_{in(t)}\big) \tag{2.4.3b}$$

at $x = L_{cc}$

$$\frac{\partial T_g}{\partial x} = 0 \tag{2.4.4a}$$

$$\frac{\partial \Phi}{\partial x} = 0 \tag{2.4.4b}$$

If the **mass flow arrives from the bed B** ($\rightarrow \operatorname{sign}(\dot{m}) = -1 \ \forall x$) *Neumann* **boundary conditions** are given by:
at $x = 0$

$$\frac{\partial T_g}{\partial x} = 0 \tag{2.4.5a}$$

$$\frac{\partial \Phi}{\partial x} = 0 \tag{2.4.5b}$$

at $x = L_{cc}$

$$\frac{\partial T_g}{\partial x} = \frac{1}{D_{cc(T_g,\dot{m},p_{in})}} \frac{\dot{m}_{(L_{cc},t)}}{A_{cc}\,\rho_{g(T_g,p_{in})}} \left(T_g - T_{g,in(t)}\right) \tag{2.4.6a}$$

$$\frac{\partial \Phi}{\partial x} = \frac{1}{D_{cc(T_g,\dot{m},p_{in})}} \frac{\dot{m}_{(L_{cc},t)}}{A_{cc}\,\rho_{g(T_g,p_{in})}} \left(\Phi - \Phi_{in(t)}\right) \tag{2.4.6b}$$

Diffusion Coefficient
Similar to the dispersion in the bed (cf. equations (2.3.9) and (2.3.10)), the axial diffusion coefficient for mass propagation (more information can be obtained in [2]) in the ceramic-free combustion chamber

$$D_{cc}(T_g, \dot{m}, p_{in}) = 0.04 \frac{|\dot{m}|}{\rho_g(T_g, p_{in})} L_{cc} \tag{2.4.7}$$

occurs at the second space derivatives in the partial differential equations (2.4.1).

Switching Inputs/Outputs

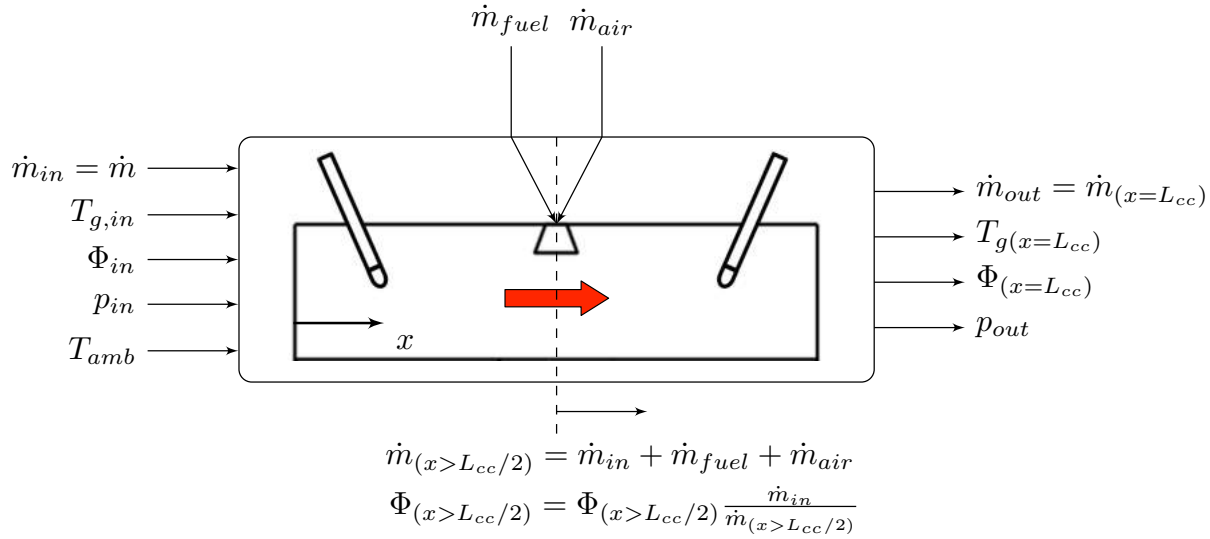

Figure 2.4.1: Overview of the combustion chamber in the first half cycle.

The input gas temperature $T_{g,in}$ and the inlet volume fraction of VOCs Φ come from the ceramic bed A at $x_{bedA} = 0$m in the first half cycle ($\rightarrow \text{sign}(\dot{m}) = 1$) and from the ceramic bed B at $x_{bedB} = 0$m in the second half cycle ($\rightarrow \text{sign}(\dot{m}) = -1$), assuming that the heating by the burner is already considered in the PDEs (2.4.1) (see section 2.5.2). One would advise to be cautious with the contrary count directions of space in the combustion chamber x_{cc} and the bed x_{bed}. The subscripted "*cc*" for the combustion chamber or the "*bed*" for the ceramic bed is only added if clarification about the count direction is needed.

2.4.1 Increase of the Mass Flow

The volume fraction of VOCs

$$\begin{aligned} \Phi(x > L_{cc}/2) &= \Phi(x > L_{cc}/2)\,\frac{\dot{m}_{in}}{\dot{m}_{in} + \dot{m}_{fuel} + \dot{m}_{air}} \qquad \text{if} \qquad \dot{m} > 0 \\ \Phi(x < L_{cc}/2) &= \Phi(x < L_{cc}/2)\,\frac{\dot{m}_{in}}{\dot{m}_{in} + \dot{m}_{fuel} + \dot{m}_{air}} \qquad \text{if} \qquad \dot{m} < 0 \end{aligned} \tag{2.4.8}$$

located in one half of the combustion chamber (depends on the sign of the mass flow $\dot{m}$) has to be adapted to the proportion of inlet, respectively outlet mass flow, as a result of the addition of the air-fuel gas mixture consisting of no VOCs (cf. figure 2.4.1).

2.4.2 Pressure Drop in the Combustion Chamber

Analogous to the previous equations another coefficient ζ_{cc} is required. Due to the lack of honeycomb structures inside the chamber it is sufficient to take the mean value of the gas temperature (as solution of (2.4.1)) over x

$$\overline{T}_{g,cc}(t) = \frac{1}{L_{cc}} \int_{x=0}^{L_{cc}} T_g(x,t)dx \tag{2.4.9}$$

for calculation of the pressure drop in the combustion chamber.

$$\Delta p_{cc}(t) = \frac{\zeta_{cc}}{2\rho_g(\overline{T}_{g,cc(t)}, p_{in(t)})} \left(\frac{\dot{m}(t)}{A_{basis}}\right)^2 \tag{2.4.10}$$

More details on parameter values are provided in the Appendix.

2.5 Burner and Fuel Injection

The burner, located in the center of the combustion chamber $x_{cc} = L_{cc}/2$ (referring to the pilot plant), not only heats the surrounding gas, but also adds a mixture of fuel gas (natural gas) and air to the mass flow, which explains the dependency on space $\dot{m} = \dot{m}(x,t)$ in the PDEs (2.4.1) (cf. figure 2.4.1). The temperature of the flowing gas T_g located in the area of the burner in the combustion chamber should match the reference temperature T_{target}. The portion of air added to the mass flow at $x_{cc} = L_{cc}/2$ is fixed in the pilot plant, which means that the target air–fuel equivalence ratio $\lambda_{\text{af-ratio}}$ will not be satisfied (status October 2015). Thus the fuel mass flow $\dot{m}_{fuel}$ currently serves as control variable for a PID controller, whose parameters were empirically determined. $\dot{m}_{fuel}$ varies according to sensor signals, respectively with the reference signal T_{target} (see chapter 5).

A throttle valve controls the quantity of the fuel substance added, which will be limited if the valve end position is reached. This certainly is the case if the desired jump between measured temperatures and T_{target} is too high.

The integration of the burner in the simulation was achieved by two different concepts. Either the combustion chamber has to be divided into two independent parts with the burner in between, or the heating of the gas by the burner has to be considered to some extent in the partial differential equations (2.4.1), facing additional implementation efforts due to space dependencies.

2.5.1 Separation of Combustion Chamber through the Burner

If the burner is implemented as independent function between two separated (in space) parts of the combustion chamber, the gas temperature increases isolated at the separation point. This does not represent the natural increase of temperature properly due to its discontinuous distribution. Although not only computation time seems to benefit from this concept, it is also easier to modify the burner equations, since one does not have to deal with the partial differential equations. The challenge with this concept is, that the gas temperature, which will feed (as input) the second half of the combustion chamber, has to be calculated via enthalpy relations. The problem can be reduced to the finding of zero points of a polynomial. The calculation ensues iteratively so far. Starting with the temperature $T_{out,0} = T_{in}$ and the relative error $\Delta T_0 = 1$

$$\begin{aligned} &\text{while} \quad |\Delta T_j| > \epsilon_R \\ &\qquad T_{out,j+1} = \frac{\dot{m}_{in} c_{g,m}(T_{g,in}) T_{g,in} + \frac{\dot{m}_{fuel}}{M_{fuel}} HV}{\dot{m}_{out} c_{g,m}(T_{out,j})} \\ &\qquad \Delta T_{j+1} = \frac{T_{out,j+1} - T_{out,j}}{T_{out,j}} \end{aligned} \tag{2.5.1}$$

(for more information see [2]) the output gas temperature $T_{g,out} = T_{out,N}$ can be provided after N_{iter} iterations with a relative error smaller than e.g. $\epsilon_R = 10^{-4}$. $HV \left[\frac{\text{J}}{\text{kmol}}\right]$

describes the heating value (or energy value or calorific value) of the fuel substance. Tests have shown that in most cases a few iterations $N_{iter} < 10$ are sufficient.

Switching Inputs/Outputs
The input parameters $T_{g,in}$ and Φ_{in} (assuming that the mass flow $\dot{m}$ does not change in the valve box, in the ceramic bed and in the combustion chamber) switch with the same sequence like the inputs of the other components. The burner represents the binding element between the two symmetrical sides (A and B) of the RTO. Each side consists of a valve box, a ceramic bed and one part of the combustion chamber characterized by a capital A or B. So the mass flow enters the RTO in side A but leaves in side B and vice versa. The inputs of the burner come from the same side, in which the mass flow enters the plant.

2.5.2 Integration in Combustion Chamber

The integration of the burner in the combustion chamber can be described through the increase of the time-gradient of the gas temperature in the equation (2.4.1a) by the power term

$$\frac{\dot{m}_{fuel} HV}{\rho_g(T_g) c_g(T_g) M_{fuel} A_{cc} L_{flame}}. \tag{2.5.2}$$

The length (one dimensional view) of the flame L_{flame} and the sign of the mass flow $\text{sign}(\dot{m})$ specify the position of the integration. The power term (2.5.2) occurs at subspace $x_{cc} \in \mathbb{B}$

$$\begin{aligned} \mathbb{B} &= \left\{ x_{cc} \in \mathbb{R} \,\middle|\, L_{cc}/2 \leq x_{cc} < L_{cc}/2 + L_{flame} \right\} \quad \text{if} \quad \text{sign}(\dot{m}) = 1 \\ \mathbb{B} &= \left\{ x_{cc} \in \mathbb{R} \,\middle|\, L_{cc}/2 - L_{flame} < x_{cc} \leq L_{cc}/2 \right\} \quad \text{if} \quad \text{sign}(\dot{m}) = -1 \end{aligned} \tag{2.5.3}$$

on the length L_{flame} adjusting to the direction of the mass flow through the plant. This ensures an almost linear increase of the gas temperature over subspace $\mathbb{B}$.
This concept models the real process more properly compared to the method, described in section 2.5.1. Tests have shown that $T_g(x_{cc}, t)$ and as a solution of equation (2.4.1) shows little change over space. Due to the integration of the power term (2.5.2) a fundamental change of state variables appears in $x_{cc} \in \mathbb{B}$. In other words, because of the significant difference of the space-gradient, smaller step sizes in time t might be necessary to meet solver tolerances, which probably explains the additional computation time.

3 Preconditions for implementing

In order to develop control concepts for the plant and to perform accurate testing, a transparent implementation should not only facilitate the modification of equations and the modelling of additional effects, but also provide a proper fundament for future developments.
System properties, particularly referring to the switch between cycles of the RTO, provoke unpleasant effects in the solution and force the step size to become significantly small periodically. As a result, the computation time will be negatively affected and long simulation times carry additional weight.
The system including all mathematical models described in section 2 was implemented in *Matlab Simulink* 2013a. One major issue was the handling of the coupled partial differential equations in the ceramic bed (2.3.1) and the combustion chamber (2.4.1), since *Simulink* does not support PDE-solvers. The appearance of algebraic loops also complicates the implementation and slows down the simulation. Furthermore, emerging stability and numerical problems have required to take further appropriate preventive actions.

3.1 Strategy

The merging of all mathematical models (see section 2) to one united system for simulation occupies a central position for preparing model based control concepts for the RTO (section 3.2). The aim was to implement the system with maximum accuracy, considering all dependencies of state variables, space and input parameters in the first place and then let the model undergo simplifications for control purposes.
Taking a closer look at the four, respectively three different mathematical models (combined burner and combustion chamber equations), a single solver had to be chosen to determine step sizes in time t for the united system. First attempts to convert the partial differential equations to algebraic ones by discretizing space and time pointed out that the system is very sensitive during cycle switches. A relatively large step size in t can be admitted inside cycles, whereas it has to be reduced to its numerical minimum during switches. So there commonly arises a step size of $t \pmod{\tau} \approx 10^{-12}$s (depending on solver tolerances), which highlights the high stiffness of the system.
As it turned out, it is advisable to convert all partial differential equations to ordinary ones by approximating space derivatives by differential quotients. Therefore all mathematical models manage to have the same time basis, chosen by the solver. The comparison of solutions with small and large numbers of grid points in space confirmed that the establishment of non-equidistant meshes delivers a significant higher accuracy.

3.2 Linkage of Models

State of the Art
The implementation of the entire, constantly evolving system in *Matlab*, without using *Simulink* has been achieved by *Thomas Rieger* [2]. He started implementing all models independently from each other by using functions, wherein (differential) equations can be solved by calling *Matlab* intern solvers. This allows the usage of different solvers. Specified input and output parameters of those functions connect all subsystems to one simulation model of *Regenerative Thermal Oxidizers* with two, three, even five bed configurations. For other configurations, in particular for more-bed ones, the system description in section 2 has to be extended by additional components such as cold and warm bypass. During simulation the submodels are processed one after another by calling the appropriate functions for each interval (function call interval).
The communication (the overall exchange of input and output values) between submodels is therefore clearly specified by the function call intervals. This interval has been modified by now, so that input and output parameters are refreshed every second in simulation time (status September 2015). This certainly corresponds with the PLC (programmable logic controller) sample time of one second.
This form of linkage between models represents one decisive aspect in terms of simulation time, accuracy and therefore of the overall performance of the implementation. It turned out that as a result of stability issues and the high stiffness of the system, which becomes apparent during cycle switches, some models (f.i. the ceramic bed) have to undergo small time steps (chosen by the solver) to converge. Computation time presumably benefits from the fact that input parameters remain constant within function call intervals, which supports convergence of the solver algorithm of the current submodel. It has to be noted that this form of communication between submodels will provoke an error, which carries weight if the input parameters change rapidly within function intervals (referring to cycle switches).

New Approach
Since control laws require the feedback of measured quantities, the implementation of the system had to be somehow processed, so that desired quantities can be fed back, at least each second (PLC sample time). At the beginning of this thesis (status March 2015) the function call interval was equivalent to the cycle interval (about 120 seconds) of the RTO, whereas input and output parameters were handled as (time) vectors. So input values were interpolated linearly in case the solver (of the current model) required time steps, which have not been provided from the previous function, respectively from the solver in the previous model.
Together with the possibilities to abstract models to blocks this motivated the application of *Simulink*. The challenge was the implementation of partial differential equations, since no *Simulink* PDE-solvers are available. *Michael Wieser* processed *Simulink* models in the way that they are compatible with the functions of *Thomas Rieger* using *Interpreted MATLAB Function* blocks. The problem of solving PDEs was shifted outside *Simulink* and therefore the *Matlab* intern *pdepe*-solver could have been used. In *Simulink* a discrete *fixed-step* solver with one second sample time allowed the call of all

desired functions every second in simulation time. The drawback of this form of implementation is the use of the significantly slower *Interpreted MATLAB Function* blocks for calling external functions and again the *discretized* communication (explained in the first paragraph of section 3.2) between blocks.
In favor of accuracy and computation time the discretization of the PDEs in space was established in the way that a global *variable-step* solver can determine step sizes in time for all grid points, respectively for all submodels at once. So the differential equations are basically solved by the *Integrator* block in *Simulink*. It turned out that the amount of grid points, the method of approximating first and second space derivatives and especially the handling of boundary conditions have significant impact on the solution and the computation time. The drawback of this method is that only one single solver can be chosen to solve all coupled differential equations. Stability issues made it even more difficult to chose a proper solver with appropriate tolerances and settings.

3.3 Discretization of Space

The finite difference method for discretization of space will be applied to the partial differential equations (2.3.1) and (2.4.1) to convert them into ordinary differential equations. Initially $N_x + 1$ grid points

$$x_l = x_0 + \sum_{j=1}^{l} \Delta x_j \quad \text{for} \quad l = 0, \ldots, N_x \tag{3.3.1}$$

starting with $x_0 = 0$ and corresponding N_x grid gaps

$$\Delta x_j \quad \text{for} \quad j = 1, \ldots, N_x \tag{3.3.2}$$

have to be chosen. The consideration of boundary conditions requires special treatment of the grid points at the borders $l = 0$ and $l = N_x$. The substitution of first order space derivatives by the *Neumann* boundary conditions should provide a proper approximation of the continuous solution (see section 3.3.3).
The choice of these points turned out to be decisive for accuracy of the numerical approximation of the PDEs solutions. Early simulation results highlighted that borders required higher resolution. Think of a cold ceramic bed with an equally distributed temperature $T_s(x_l, t_0) = T_g(x_l, t_0) = 20°\text{C}$ for $l = 0, \ldots, N_x$ in the solid phase, as well as in the gas phase. Once the burner starts firing, bed B will be warmed up continuously, but with the RTO cycle switch bed A will encounter a significant jump in temperature (cf. figure 3.3.12), since one assumes that the incoming gas temperature of the RTO is also in the range of the ambient temperature $\approx 20°\text{C}$. Therefore the derivatives on the boundary of the bed B $x_{bedB} = 0$ to the combustion chamber will increase rapidly in an almost infinitesimal small time period.
In order to represent the space derivatives more accurately, one needs to tighten the grid gaps, at least on the boundaries. To keep the computation times in a tolerable time range, non equidistant meshes were established. For distribution either a trigonometric function

$$x_l = L\frac{1 - \cos(\tilde{l})}{2} \quad \text{for} \quad \tilde{l} \in [0, \pi] \tag{3.3.3}$$

or a third order polynomial

$$x_l(\tilde{l}) = a_3\tilde{l}^3 + \ldots + a_1\tilde{l} + a_0 \quad \text{for} \quad \tilde{l} \in [0, L] \tag{3.3.4}$$

had been used. The range between $\tilde{l} \in [0, \pi]$ in equation (3.3.3) and between $\tilde{l} \in [0, L]$ in equation (3.3.4) has to be represented with $N_x + 1$ equally distributed points (function *linspace*). The coefficient of the polynomial can be provided by solving a linear equation system. The conditions

$$\begin{aligned} x_l(\tilde{l} = 0) &= 0 & x_l(\tilde{l} = L) &= L \\ \left.\frac{dx_l}{d\tilde{l}}\right|_{\tilde{l}=0} &= 0 & \left.\frac{dx_l}{d\tilde{l}}\right|_{\tilde{l}=L} &= 0 \end{aligned} \tag{3.3.5}$$

lead to the following system

$$\begin{bmatrix} 1 & 0 & 0 & 0 \\ 0 & 1 & 0 & 0 \\ 0 & 1 & 2L & 3L^2 \\ 1 & L & L^2 & L^3 \end{bmatrix} \begin{bmatrix} a_0 \\ a_1 \\ a_2 \\ a_3 \end{bmatrix} = \begin{bmatrix} 0 \\ 0 \\ 0 \\ L \end{bmatrix} \tag{3.3.6}$$

which can be uniquely solved by inverting the matrix on the left hand side. This matrix is non singular if $L \neq 0$. L characterizes either the length of the combustion chamber $L = L_{cc}$, or the height of the ceramic bed $L = H_{N_l}$.

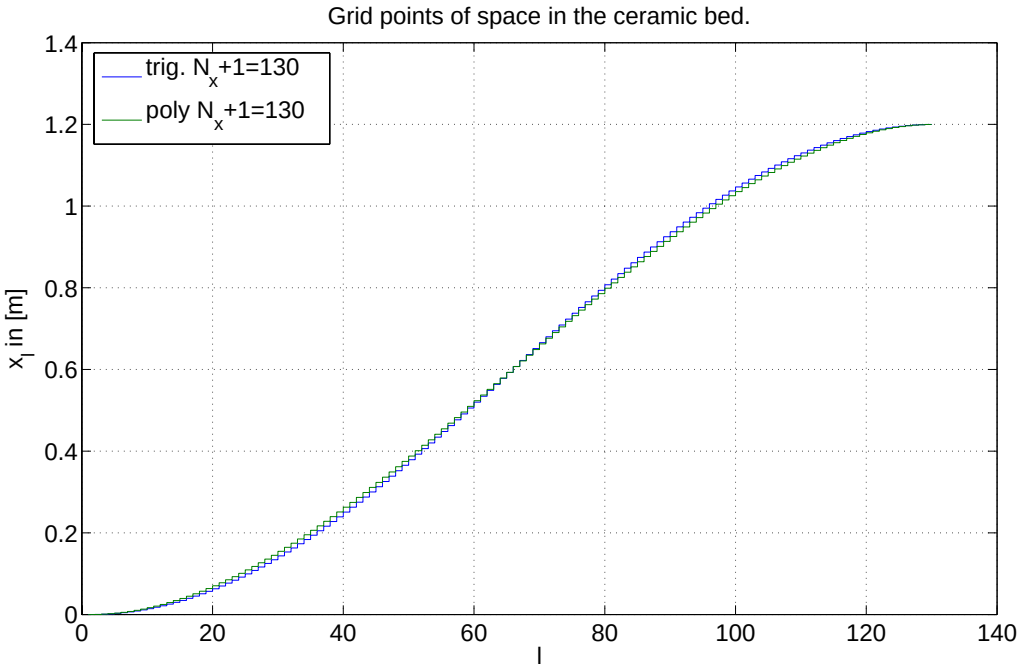

Figure 3.3.1: Distribution of grid points in both ceramic beds with a trigonometric (blue) and a polynomial (green) approach.

Figure 3.3.1 illustrates that the trigonometric approach ensures slightly smaller grid gaps on the boundaries, therefore it will be applied to both ceramic beds. Additionally, the

polynomial approach turned out to work efficiently with the space x_{cc} of the combustion chamber. Initial attempts of using different linear functions for the distribution of space with higher slopes at the boundaries, produced inappropriate effects in the solution at the transition points of these linear functions.
For further considerations the integration of the burner will be achieved by the addition of the power term in equation (2.5.2) to the time derivative of the gas temperature in the PDEs of the combustion chamber (2.4.1a). This addition of energy will lead to significant change of the state variables at subspace $\mathbb{B}$ (see section 2.5.2), which motivated the tightening of grid gaps in the area of the burner flame.

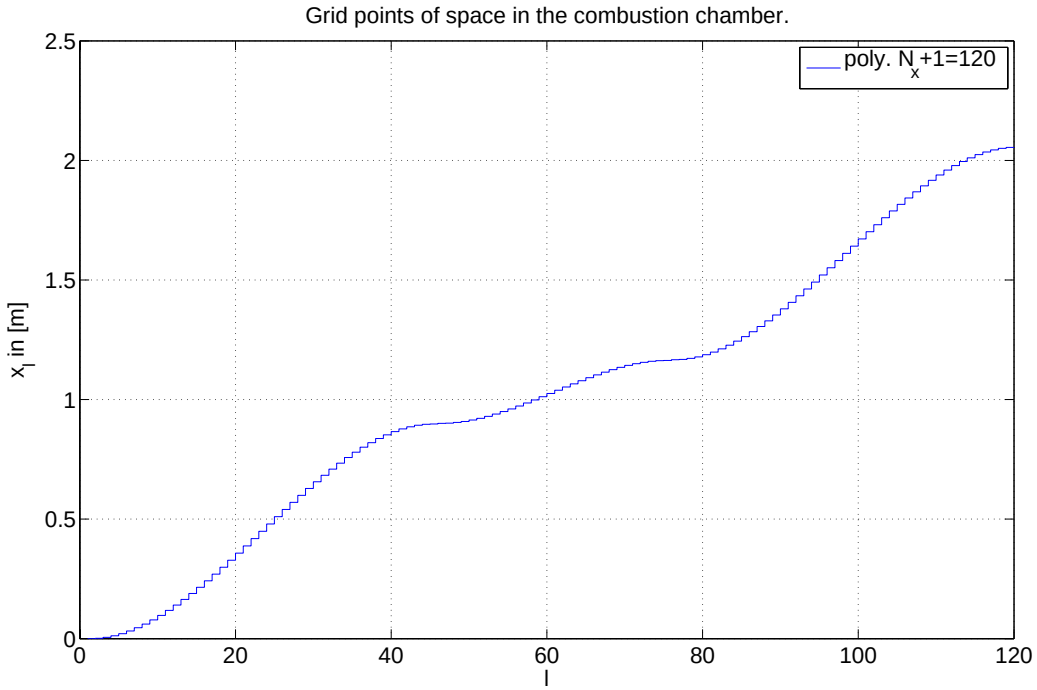

Figure 3.3.2: Distribution of grid points in the combustion chamber with a polynomial approach.

The combination of three polynomials, as shown in figure 3.3.2 has been used for the distribution of grid points in the combustion chamber.
The construction of the ceramic bed by layers would also demand the use of smaller grid gaps at the area of transition. This is one issue, which remains open for future developments.

3.3.1 First Order Derivative

The methods for approximating first order derivatives are decisive for stability, consequentially for computation time and even for convergence. The classical approach with a central differential quotient (CDQ) (cf. [9]), also called symmetric differential quotient, assuming an arbitrary, continuous function $y(x,t)$ at a fixed time $t = t^*$ (notation: $y_l := y(x_l, t^*)$)

$$\text{CDQ:} \quad \left.\frac{\partial y}{\partial x}\right|_{x=x_l} \approx \frac{y_{l+1} - y_{l-1}}{\Delta x_l + \Delta x_{l+1}} \quad \text{for} \quad l = 1, \ldots, N_x - 1 \tag{3.3.7}$$

tends to provoke numerical oscillations, which are indeed non-physical. So backward differential quotients (BDQ)

$$\text{BDQ:} \quad \left.\frac{\partial y}{\partial x}\right|_{x=x_l} \approx \frac{y_l - y_{l-1}}{\Delta x_l} \quad \text{for} \quad l = 1, \ldots, N_x \tag{3.3.8}$$

as well as forward differential quotients (FDQ)

$$\text{FDQ:} \quad \left.\frac{\partial y}{\partial x}\right|_{x=x_l} \approx \frac{y_{l+1} - y_l}{\Delta x_{l+1}} \quad \text{for} \quad l = 0, \ldots, N_x - 1 \tag{3.3.9}$$

were tested. Variable y can be replaced by the state variables T_g, T_s and Φ. A combination between FDQ and BDQ depending on the (sign of the) mass flow $\dot{m}$ turned out to be the most robust, which gives a nice physical meaning to the problem. Whereas the mathematical explanation can be presumably found (again) in the switching boundary conditions on the one hand, but on the other hand in the missing interconnection of the CDQ to the current grid point y_l (see [11] and [12]). The RTO cycle switch forces homogenous Neumann boundary conditions (equation (2.3.3), (2.3.4), (2.4.4) and (2.4.5)) to become inhomogeneous ones (equation (2.3.2), (2.3.5), (2.4.3) and (2.4.6)) or vice versa. This might be the reason why the following method

$\dot{m} \geq 0$	$\dot{m} < 0$
BDQ	FDQ

$\dot{m}_{bed} \geq 0$	$\dot{m}_{bed} < 0$
BDQ	FDQ

Table 3.3.1: Most robust method for approximating the first order derivatives.

outperforms all kinds of central differential quotients in terms of robustness. In case the mass flow $\dot{m} = 0$ equals zero, the appropriate coefficients at the first order derivatives, f.i. (II) in equation (2.3.1) (similar in the equation (2.4.1)) ensure that convection terms equal zero. Since the sign of the mass flow was adapted to the count direction of the space in the ceramic beds, the definition in table 3.3.1 holds in reference to $\dot{m}_{bed}$.
The drawback of differential quotients explicitly using two neighboring grid points (BDQ & FDQ) becomes visible by approximating sharp edges, which will occur after the RTO cycle switches in the gas temperature and particularly in the volume fraction of VOCs.

3.3.1.1 Test Configuration in terms of Stability

For demonstration purposes, a cold ceramic bed $T_g(x_l, t_0) = T_s(x_l, t_0) = 20°\text{C} \ \forall l$ with no VOCs $\Phi(x_l, t_0) = 0 \ \forall l$ at starting time $t_0 = 0$ is assumed. All parameters depending on the composition of gas were adapted to air considering the main components (see table 6.1.1 and 6.1.2) at an atmospheric pressure $p_{in} = 1.01325 \cdot 10^5\text{Pa}$. The gas composition for parameters like λ_g and c_g will not be modified with the addition of VOCs during simulation, since their fractions are negligibly small. At time $t = t_0$ a hot gas $T_{g,in} =$

850°C and a volume fraction of VOCs $\Phi_{in} = 5 \cdot 10^{-4}$ cause quite interesting effects in the solution, considering transient reactions in a very small time window.

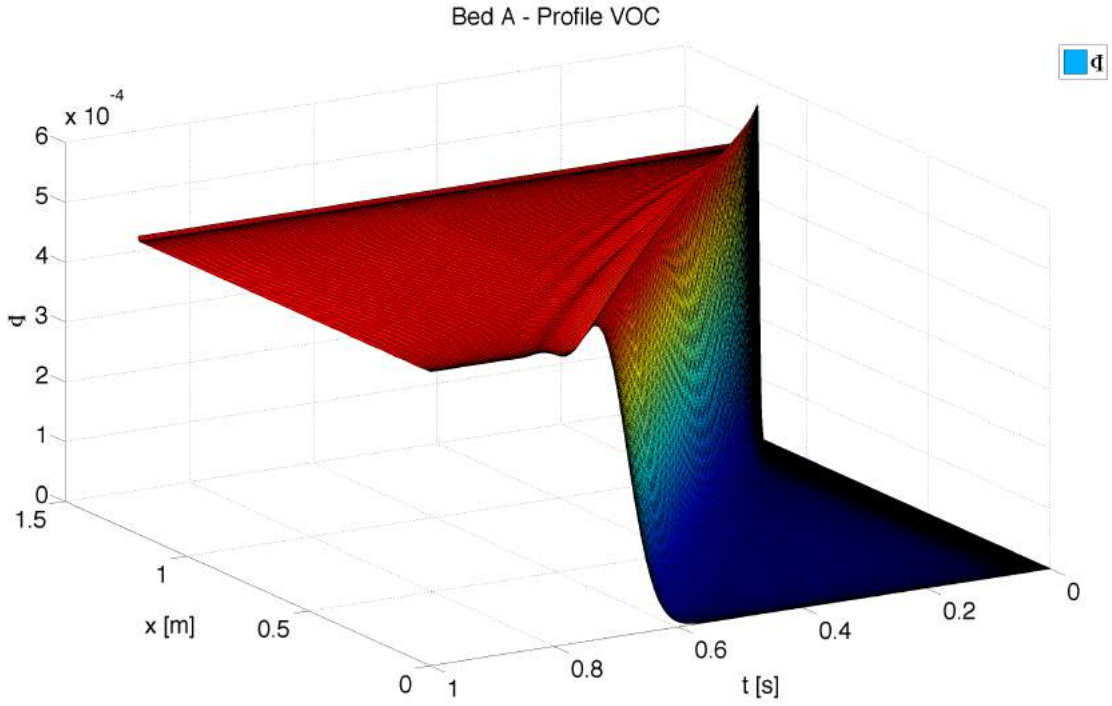

Figure 3.3.3: Distribution of Φ in the test configuration with input parameters, coming from $x_{bed} = H_{N_l}$ applying **Central Differential Quotients** (CDQ) with $N_x + 1 = 130$.

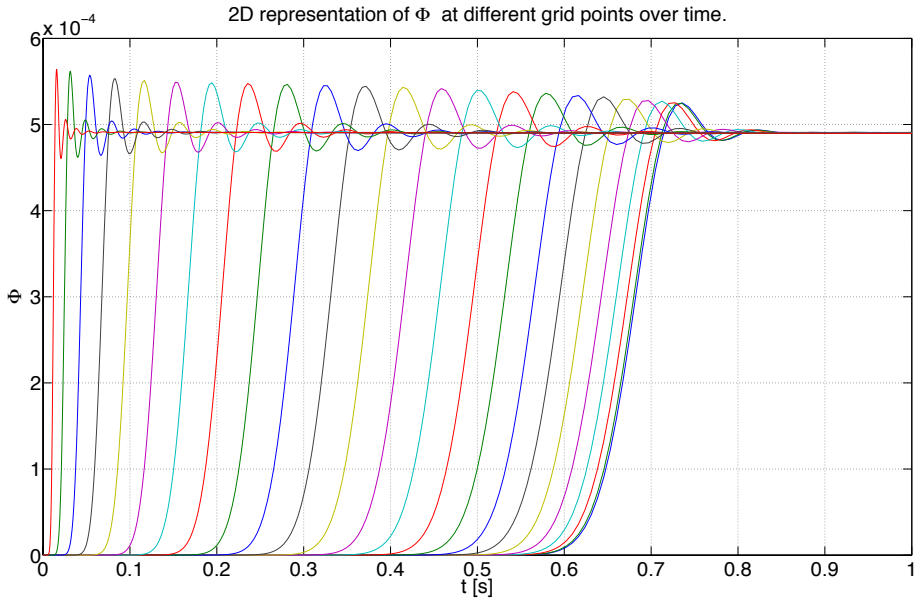

Figure 3.3.4: 2D representation of $\Phi(x_l, t)$ at different grid points l, applying **Central Differential Quotients** (CDQ) with $N_x + 1 = 130$.

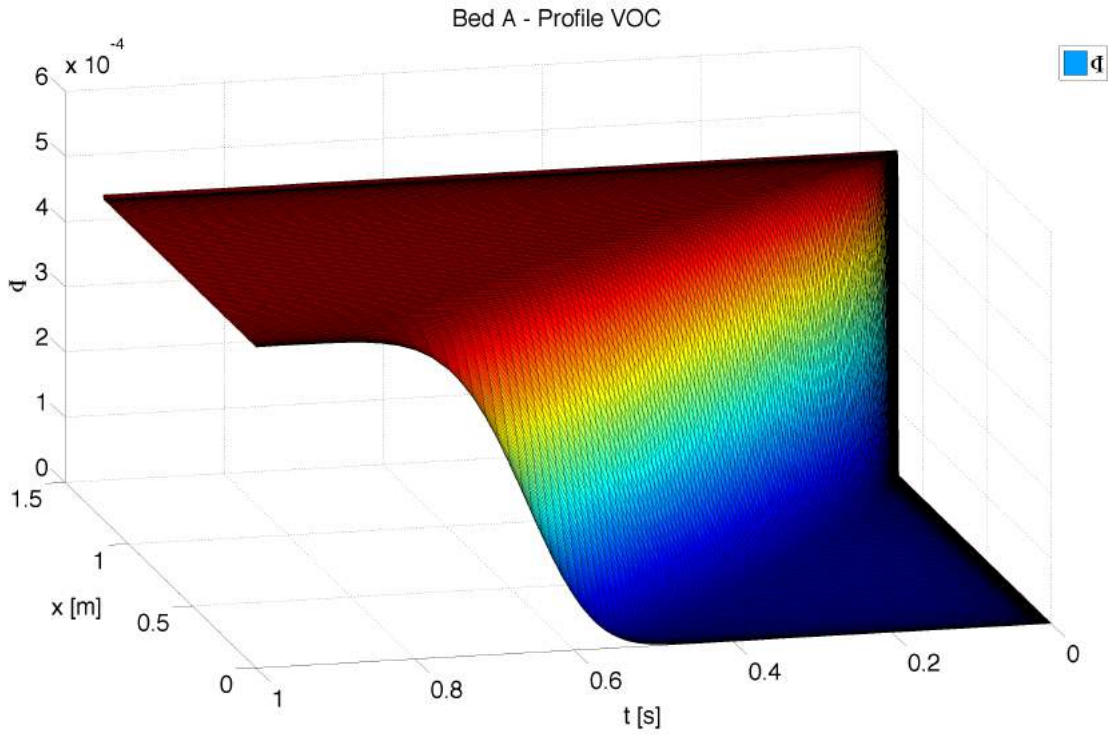

Figure 3.3.5: Distribution of Φ in the test configuration with input parameters, coming from $x_{bed} = H_{N_l}$ applying BDQ and FDQ with $N_x + 1 = 130$ points according to table 3.3.1.

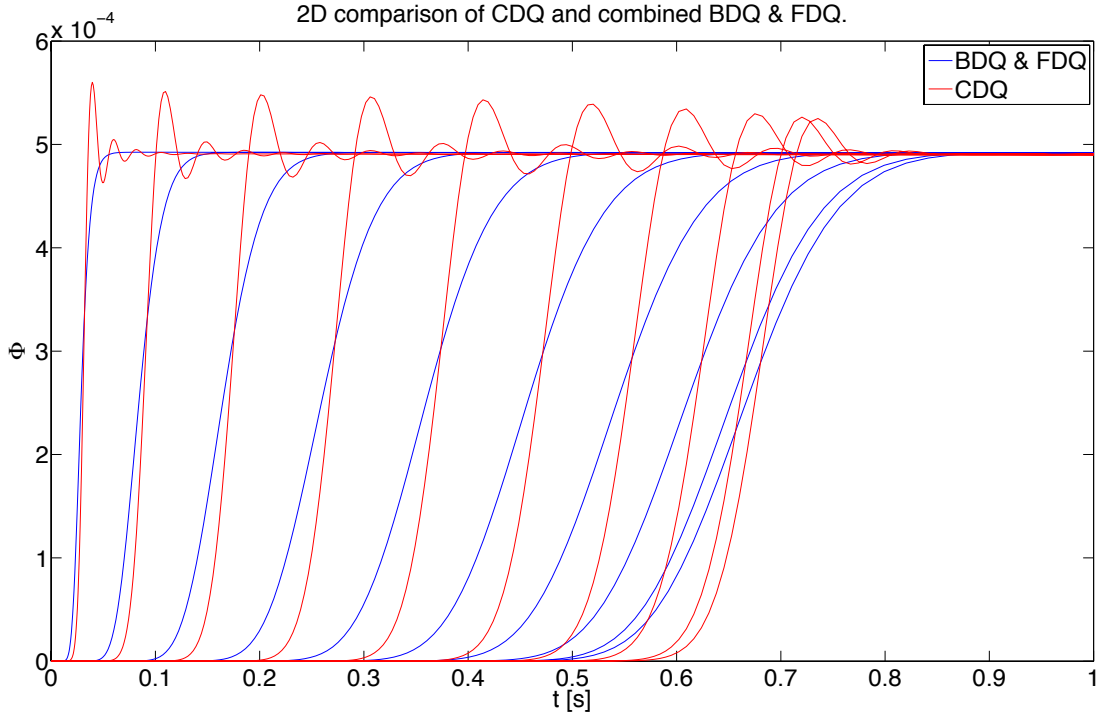

Figure 3.3.6: Comparison of the two methods approximating first order derivatives at different grid points x_l over time with $N_x + 1 = 130$ in total.

As figure 3.3.6 illustrates, there definitively will be a problem when using CDQ. The real solution probably lies somewhere in between red and blue curves, whereas the red curves obviously have serious issues due to numerical oscillations and the blue ones probably flatten the edges substantially.
The distribution of Φ for demonstrating stability issues has been chosen on purpose. Analyzing the transport equations (2.3.1c) and (2.4.1b), one can recognize the missing coupling of the equation to the current grid point y_l, which is provided by the heat transfer terms in the PDEs (cf. (III) in equation (2.3.1b)) and by the term describing ambient losses (cf. equation (2.4.1a) and (IVa) in equation (2.3.1a)). In finite difference literature (see [11] and [12]) there are mathematical conditions, which guarantee stability, arguing with the coefficient (at state variables) at the current grid point y_l and those in its neighborhood used for approximating derivatives. Numerical oscillations also appear in the approximated solution of the gas temperature T_g when using CDQ, though their impact might be less visible.
The crucial point was seen when linking all subsystems (see section 3.2) to one simulation model for the two-bed RTO. When using CDQ, it was impossible to adjust solver settings at a moderate number of grid points (cue: computation time), so that solver algorithms safely converge during RTO cycle switches.

At this point, the use of the method in table 3.3.1 has to be recommended when using the finite difference method for discretizing space. In case the model should be fed with highly time invariant quantities, for instance with sensor signals, robustness will be substantial for convergence.

Since the *Matlab* intern *pdepe* solver uses some sort of central differential quotient, without the inclusion of the approximated solution at the current grid point y_l (up to current versions 2015 of this solver, discovered by code analysis), there have been major differences to existing simulation results. Therefore a method for approximating first order derivatives was developed, which relies on the basis of central differential quotients, but provokes less numerical oscillations.

3.3.1.2 Modified Central Differential Quotient

The classical CDQ (equation (3.3.7)) can be interpreted as backward, respectively forward differential quotient of inner mesh points

$$z_l = \frac{x_l + x_{l-1}}{2} \quad \text{for} \quad l = 1, \ldots, N_x \tag{3.3.10}$$

which are located in the center between original grid points x_l.

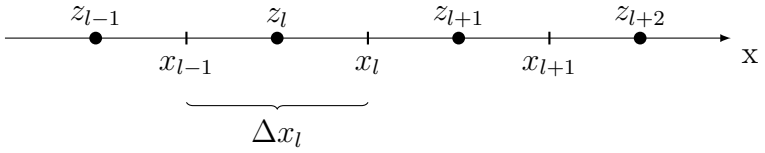

Figure 3.3.7: Original and inner mesh points for $l > 1$.

The linear average of two neighboring solutions (notation: $y_{z_l} := y(z_l, t^*)$)

$$y_{z_l} \approx \frac{y_l + y_{l-1}}{2} \quad \text{for} \quad l = 1, \ldots, N_x \tag{3.3.11}$$

provides

$$\left.\frac{\partial y}{\partial x}\right|_{x=x_l} \approx \frac{y_{z_{l+1}} - y_{z_l}}{\left(\frac{\Delta x_l + \Delta x_{l+1}}{2}\right)} \approx \frac{y_{l+1} + y_l - y_l - y_{l-1}}{\Delta x_l + \Delta x_{l+1}} = \frac{y_{l+1} - y_{l-1}}{\Delta x_l + \Delta x_{l+1}} \quad \text{for} \quad l = 1, \ldots, N_x - 1 \tag{3.3.12}$$

CDQ according to equation (3.3.7). Due to the application of a linear average in equation (3.3.11) the connection to y_l got lost. The idea was to represent y_l with a second order polynomial using three points in space x and then interpolate y_{z_l} so that the difference of the values $y_{z_{l+1}} - y_{z_l}$ would not entirely compensate the coupling to the point y_l. Since three points for interpolation are used, one has to decide the direction of inclination of the polynomial approach. Facing the two possibilities

$$\begin{aligned} y_{z_l} &\overset{\text{from}}{\rightarrow} y_{l-1}, y_l, y_{l+1} \\ y_{z_l} &\overset{\text{from}}{\rightarrow} y_{l-2}, y_{l-1}, y_l \end{aligned} \tag{3.3.13}$$

(cf. figure 3.3.7) the interpolation was adjusted to the boundary where the mass flow arrives. In case of a **positive mass flow** $\operatorname{sign}(\dot{m}) = 1$ the ansatz

$$\begin{aligned} a_l + b_l x_{l-2} + c_l x_{l-2}^2 &= y_{l-2} \\ a_l + b_l x_{l-1} + c_l x_{l-1}^2 &= y_{l-1} \qquad \text{for} \quad l = 2, \ldots, N_x \\ a_l + b_l x_l + c_l x_l^2 &= y_l \end{aligned} \tag{3.3.14}$$

leads to the linear equation system

$$\begin{bmatrix} 1 & x_{l-2} & x_{l-2}^2 \\ 1 & x_{l-1} & x_{l-1}^2 \\ 1 & x_l & x_l^2 \end{bmatrix} \begin{bmatrix} a_l \\ b_l \\ c_l \end{bmatrix} = \begin{bmatrix} y_{l-2} \\ y_{l-1} \\ y_l \end{bmatrix} \quad \text{for} \quad l = 2, \ldots, N_x \tag{3.3.15}$$

by adjusting the interpolation to $x = 0$. For the following consideration one pardons the mathematical incorrectness when equating y_{z_l} with the interpolated value.

$$\begin{aligned} \begin{bmatrix} 1 & z_l & z_l^2 \end{bmatrix} \begin{bmatrix} a_l \\ b_l \\ c_l \end{bmatrix} &= y_{z_l} \quad \text{for} \quad l = 2, \ldots, N_x \\ \underbrace{\begin{bmatrix} 1 & z_l & z_l^2 \end{bmatrix} \begin{bmatrix} 1 & x_{l-2} & x_{l-2}^2 \\ 1 & x_{l-1} & x_{l-1}^2 \\ 1 & x_l & x_l^2 \end{bmatrix}^{-1}}_{=:\mathbf{d}_{l,+}^T} \begin{bmatrix} y_{l-2} \\ y_{l-1} \\ y_l \end{bmatrix} &= y_{z_l} \quad \text{for} \quad l = 2, \ldots, N_x \end{aligned} \tag{3.3.16}$$

When comparing equation (3.3.11) with (3.3.16), one may notice the absence of one equation at $l = 1$ as a result of the inclination to one boundary. Intuitively the first three points are used to interpolate the value y_{z_1}.

$$\underbrace{\begin{bmatrix}1 & z_1 & z_1^2\end{bmatrix}\begin{bmatrix}1 & x_0 & x_0^2\\ 1 & x_1 & x_1^2\\ 1 & x_2 & x_2^2\end{bmatrix}^{-1}}_{=:\mathbf{d}_{1,+}^T}\begin{bmatrix}y_0\\ y_1\\ y_2\end{bmatrix} = y_{z_1} \tag{3.3.17}$$

After applying the differential quotient according to equation (3.3.12) to the interpolated values, one can define the modified backward differential quotient (MBDQ).

$$\text{MBDQ:}\begin{cases}\left.\dfrac{\partial y}{\partial x}\right|_{x=x_l} \approx \frac{2}{\Delta x_{l-1}+\Delta x_l}\left(\mathbf{d}_{l+1,+}^T\begin{bmatrix}y_{l-1}\\ y_l\\ y_{l+1}\end{bmatrix} - \mathbf{d}_{l,+}^T\begin{bmatrix}y_{l-2}\\ y_{l-1}\\ y_l\end{bmatrix}\right) & \text{for} \quad l = 2,\dots,N_x-1\\ \left.\dfrac{\partial y}{\partial x}\right|_{x=x_1} \approx \frac{2}{\Delta x_1+\Delta x_2}\left(\mathbf{d}_{2,+}^T - \mathbf{d}_{1,+}^T\right)\begin{bmatrix}y_0\\ y_1\\ y_2\end{bmatrix} & \text{for} \quad l = 1\end{cases} \tag{3.3.18}$$

In case of a **negative mass flow** $\operatorname{sign}(\dot{m}) = -1$ the polynomial interpolation needs to be adjusted to the boundary $x = x_{N_x}$. The linear equation system

$$\begin{bmatrix}1 & x_{l-1} & x_{l-1}^2\\ 1 & x_l & x_l^2\\ 1 & x_{l+1} & x_{l+1}^2\end{bmatrix}\begin{bmatrix}a_l\\ b_l\\ c_l\end{bmatrix} = \begin{bmatrix}y_{l-1}\\ y_l\\ y_{l+1}\end{bmatrix} \quad \text{for} \quad l = 1\dots,N_x-1 \tag{3.3.19}$$

leads to $N_x - 1$ values of y_{z_l}

$$\underbrace{\begin{bmatrix}1 & z_l & z_l^2\end{bmatrix}\begin{bmatrix}1 & x_{l-1} & x_{l-1}^2\\ 1 & x_l & x_l^2\\ 1 & x_{l+1} & x_{l+1}^2\end{bmatrix}^{-1}}_{=:\mathbf{d}_{l,-}^T}\begin{bmatrix}y_{l-1}\\ y_l\\ y_{l+1}\end{bmatrix} = y_{z_l} \quad \text{for} \quad l = 1,\dots,N_x-1 \tag{3.3.20}$$

whereas the last point for interpolation $y_{z_{N_x}}$ can be provided by

$$\underbrace{\begin{bmatrix}1 & z_{N_x} & z_{N_x}^2\end{bmatrix}\begin{bmatrix}1 & x_{N_x-2} & x_{N_x-2}^2\\ 1 & x_{N_x-1} & x_{N_x-1}^2\\ 1 & x_{N_x} & x_{N_x}^2\end{bmatrix}^{-1}}_{=:\mathbf{d}_{N_x,-}^T}\begin{bmatrix}y_{N_x-2}\\ y_{N_x-1}\\ y_{N_x}\end{bmatrix} = y_{z_{N_x}}. \tag{3.3.21}$$

After applying the differential quotient according to equation (3.3.12) to the interpolated values, the modified forward differential quotient (MFDQ) can be defined.

$$\text{MFDQ:}\begin{cases}\left.\dfrac{\partial y}{\partial x}\right|_{x=x_l} \approx \frac{2}{\Delta x_l+\Delta x_{l+1}}\left(\mathbf{d}_{l+1,-}^T\begin{bmatrix}y_l\\ y_{l+1}\\ y_{l+2}\end{bmatrix} - \mathbf{d}_{l,-}^T\begin{bmatrix}y_{l-1}\\ y_l\\ y_{l+1}\end{bmatrix}\right) & \text{for} \quad l = 1,\dots,N_x-2\\ \left.\dfrac{\partial y}{\partial x}\right|_{x=x_{N_x}} \approx \frac{2}{\Delta x_{N_x-1}+\Delta x_{N_x}}\left(\mathbf{d}_{N_x,-}^T - \mathbf{d}_{N_x-1,-}^T\right)\begin{bmatrix}y_{N_x-2}\\ y_{N_x-1}\\ y_{N_x}\end{bmatrix} & \text{for} \quad l = N_x-1\end{cases} \tag{3.3.22}$$

Remark (Solvability)**.** *The invertibility of the matrices appearing in the vectors* $\boldsymbol{d}_{l,+}^T$*, as well as in* $\boldsymbol{d}_{l,-}^T$ *is guaranteed, since the points* $l = 0, \ldots, N_x$ *in space* x *are strictly monotonically increasing and strictly positive.*

Finally, one can sum up the modified method for approximating first derivatives on the basis of the central differential quotient.

$\dot{m} \geq 0$	$\dot{m} < 0$
MBDQ	MFDQ

$\dot{m}_{bed} \geq 0$	$\dot{m}_{bed} < 0$
MBDQ	MFDQ

Table 3.3.2: Modified method for approximating the first order derivatives.

In case the mass flow $\dot{m} = 0$ equals zero, the appropriate coefficients at the first order derivatives, f.i. (II) in equation (2.3.1) (similar in the equation (2.4.1)) ensure that convection terms equal zero. As one may noticed, the vectors $\mathbf{d}_{l,+}^T$, as well as $\mathbf{d}_{l,-}^T$ can be calculated in advance $\forall l$, which saves quite a lot of computation time during simulation. In addition, one should avoid the application of loops, which are indeed significantly slow compared to vector operations in *Matlab*.

3.3.1.3 Beneficial Matrix Representations

In order to combine the equations for all mesh points the *Hadamard Matrix Product* [10] will be introduced.

Definition: Hadamard Product. *Let* $\boldsymbol{A}$ *and* $\boldsymbol{B}$ *be* $m \times n$ *matrices with entries in* $\mathbb{C}$*. The Hadamard product of* $\boldsymbol{A}$ *and* $\boldsymbol{B}$ *is defined by* $[\boldsymbol{A} \circ \boldsymbol{B}]_{ij} = \boldsymbol{A}_{ij}\boldsymbol{B}_{ij}$ *for all* $1 \leq i \leq m, 1 \leq j \leq n$*.*

As one can see, the Hadamard product is simply the element-wise multiplication of matrices, which can be easily applied in *Matlab* using the element-wise operator $(.*)$. Introducing the notations $\mathbf{y}_z \in \mathbb{R}^{N_x \times 1}$ and $\mathbf{D}_+$, $\mathbf{D}_-$, $\mathbf{Y}_+$, $\mathbf{Y}_- \in \mathbb{R}^{N_x \times 3}$

$$\mathbf{y}_z = \begin{bmatrix} y_{z_1} \\ \vdots \\ y_{z_{N_x}} \end{bmatrix}, \quad \mathbf{D}_+ := \begin{bmatrix} \mathbf{d}_{1,+}^T \\ \mathbf{d}_{2,+}^T \\ \vdots \\ \mathbf{d}_{N_x-1,+}^T \\ \mathbf{d}_{N_x,+}^T \end{bmatrix}, \quad \mathbf{Y}_+ := \begin{bmatrix} y_0 & y_1 & y_2 \\ y_0 & y_1 & y_2 \\ y_1 & y_2 & y_3 \\ \vdots & \vdots & \vdots \\ y_{N_x-2} & y_{N_x-1} & y_{N_x} \end{bmatrix}$$
$$\mathbf{D}_- := \begin{bmatrix} \mathbf{d}_{1,-}^T \\ \mathbf{d}_{2,-}^T \\ \vdots \\ \mathbf{d}_{N_x-1,-}^T \\ \mathbf{d}_{N_x,-}^T \end{bmatrix}, \quad \mathbf{Y}_- := \begin{bmatrix} y_0 & y_1 & y_2 \\ y_1 & y_2 & y_3 \\ \vdots & \vdots & \vdots \\ y_{N_x-2} & y_{N_x-1} & y_{N_x} \\ y_{N_x-2} & y_{N_x-1} & y_{N_x} \end{bmatrix} \tag{3.3.23}$$

the interpolated values $\mathbf{y}_z$ can be provided by the sum over columns

$$\begin{aligned} \mathbf{y}_z &= \sum_{j=1}^{3} [\mathbf{D}_+ \circ \mathbf{Y}_+]_{ij} \quad \text{if} \quad \dot{m} > 0 \quad \text{or} \quad \dot{m}_{bed} > 0 \\ \mathbf{y}_z &= \sum_{j=1}^{3} [\mathbf{D}_- \circ \mathbf{Y}_-]_{ij} \quad \text{if} \quad \dot{m} < 0 \quad \text{or} \quad \dot{m}_{bed} < 0 \end{aligned} \tag{3.3.24}$$

with the *Matlab* equivalents: sum($\mathbf{D}_+$.*$\mathbf{Y}_+$,2) and sum($\mathbf{D}_-$.*$\mathbf{Y}_-$,2). The use of element-wise operations could minimize the number of arithmetic operations and therefore is preferable in comparison to block diagonal representations.
The matrices $\mathbf{Y}_+$ and $\mathbf{Y}_-$ have to be evaluated during run time certainly, but their indices can be set up in preprocessing as *Matlab* allows the application of matrix indices. Introducing

$$\mathbf{y} = \begin{bmatrix} y_0 \\ y_1 \\ \vdots \\ y_{N_x} \end{bmatrix}, \quad \mathbf{I}_+ = \begin{bmatrix} 0 & 1 & 2 \\ 0 & 1 & 2 \\ 1 & 2 & 3 \\ \vdots & \vdots & \vdots \\ N_x - 2 & N_x - 1 & N_x \end{bmatrix} \tag{3.3.25}$$

the interpolated values $\mathbf{y}_z$ can be evaluated for instance in one line *Matlab* code: $\mathbf{y}_z$ = sum($\mathbf{D}_+$.*$\mathbf{y}(\mathbf{I}_+), 2$). However, one may not forget that *Matlab* indices have to start with one corresponding with the *Matlab* code: $\mathbf{y}_z$ = sum($\mathbf{D}_+$.*$\mathbf{y}(\mathbf{I}_+ + 1), 2$) and that the matrices $\mathbf{D}_+$, as well as $\mathbf{D}_-$ should be computed in preprocessing.

3.3.1.4 Results of Test Configuration

The method described in section 3.3.1.2 was implemented considering the aspects in section 3.3.1.3 and then tested by applying the configurations of section 3.3.1.1.

It was no surprise when the method described in table 3.3.1 outperforms CDQ and the method described in table 3.3.2 in terms of computation time, whereas the simulation applying CDQ was most time consuming, as a result of stability issues.
Referring to figure 3.3.9 it becomes evident, that numerical oscillations were reduced in comparison to CDQ. Although one has to be cautious, when zooming to $\Phi \approx 0$ it can be recognized that the green curves tend to go slightly negative, which is of course incorrect in physical terms. This problem will also occur when using CDQ in case of an appropriate negative jump, for instance from $\Phi_{in} = 5 \cdot 10^{-4}$ to $\Phi_{in} = 0$.

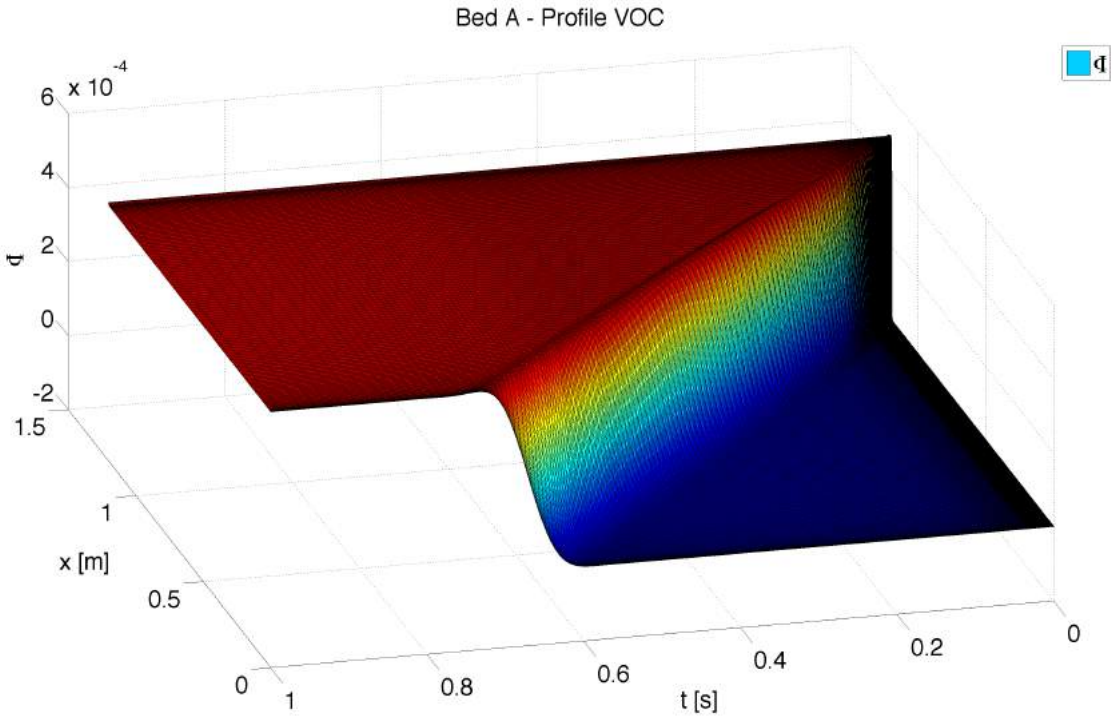

Figure 3.3.8: Distribution of Φ in the test configuration with input parameters, coming from $x_{bed} = H_{N_l}$ applying MBDQ and MFDQ with $N_x + 1 = 130$ points according to table 3.3.2.

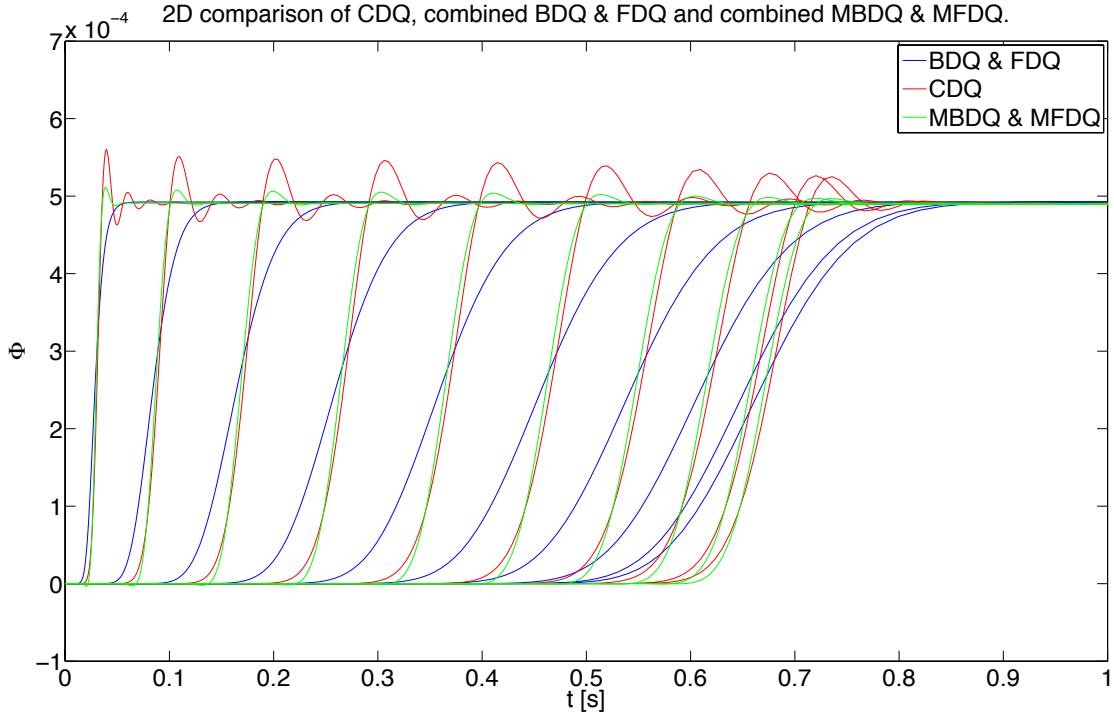

Figure 3.3.9: Comparison of the methods approximating first order derivatives at different grid points x_l over time, with $N_x + 1 = 130$ in total.

Not only three methods for approximating the first order derivatives in PDEs (2.3.1) and (2.4.1), moreover, mixed versions were implemented, applying CDQ for the state variables T_g and T_s (hence equations (2.3.1a), (2.3.1b) and (2.4.1a)) and combined BDQ and FDQ for the state variable Φ (equations (2.3.1c) and (2.4.1b)). Once again emphasizing on the connection between for instance BDQ and MBDQ

$$\left.\frac{\partial y}{\partial x}\right|_{x=z_l} \approx \frac{y_l - y_{l-1}}{\Delta x_l} \quad \text{for} \quad l = 1, \ldots, N_x \tag{3.3.26}$$

the defined backward differential quotient (cf. equation (3.3.8)) actually represents the derivative at $x = z_l$ more accurately than the derivative at $x = x_l$. As a result, a method, which interpolates the derivative

$$\left.\frac{\partial y}{\partial x}\right|_{x=x_l}$$

at $x = x_l$ with a second order polynomial, using three points of

$$\begin{aligned} \left.\frac{\partial y}{\partial x}\right|_{x=x_l} &\overset{\text{from}}{\rightarrow} \frac{\partial y}{\partial x} \quad \text{at} \quad x = z_{l-1}, z_l, z_{l+1} \quad \text{if} \quad \dot{m} < 0 \\ \left.\frac{\partial y}{\partial x}\right|_{x=x_l} &\overset{\text{from}}{\rightarrow} \frac{\partial y}{\partial x} \quad \text{at} \quad x = z_{l-2}, z_{l-1}, z_l \quad \text{if} \quad \dot{m} > 0 \end{aligned} \tag{3.3.27}$$

the derivative in z_l (interpolated central differential quotient - ICDQ), was also implemented. The procedure of setting up the equations is quite analogous to the one described in section 3.3.1.2. Since the results are almost identical to the method using combined MBDQ and MFDQ, the formulation of equations will be no longer an area of concerns.

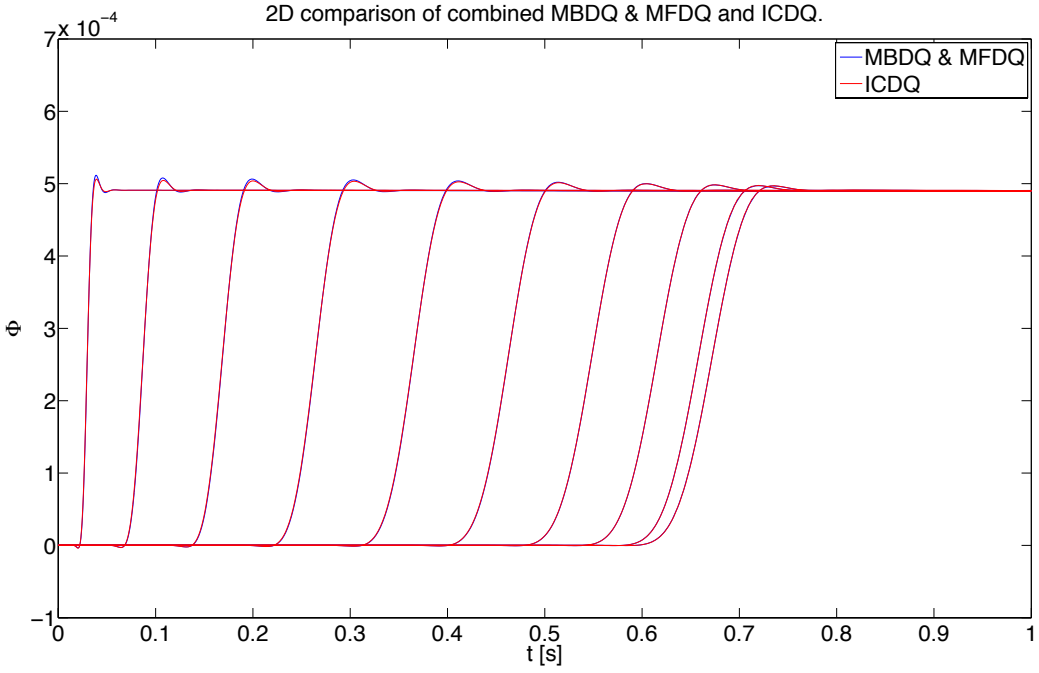

Figure 3.3.10: Comparison of MBDQ & MFDQ and ICDQ at different grid points x_l over time, with $N_x + 1 = 130$ in total.

However, if one zooms in figure 3.3.10 it can be recognized that at least a slight improvement (referring to $t < 0.5$s) could have been achieved.
The testing of higher order polynomials as candidates for interpolation confirmed that the problem only gains complexity, whereas numerical oscillations accumulate with the growing degree of polynomials. This might be the reason of the decreasing coefficient of the solution at the current mesh point y_l.

3.3.2 Second Order Derivative

There are various methods for calculating second order derivatives using differential quotients. A method which relies on *Taylor* series [9], considering

$$\begin{aligned} y_{l+1} &= y_l + \Delta x_{l+1} \left.\frac{\partial y}{\partial x}\right|_{x_l} + \frac{\Delta x_{l+1}^2}{2} \left.\frac{\partial^2 y}{\partial x^2}\right|_{x_l} + O(\Delta x_{l+1}^3) \\ y_{l-1} &= y_l - \Delta x_l \left.\frac{\partial y}{\partial x}\right|_{x_l} + \frac{\Delta x_l^2}{2} \left.\frac{\partial^2 y}{\partial x^2}\right|_{x_l} + O(\Delta x_l^3) \end{aligned} \tag{3.3.28}$$

two series at $l+1$ and $l-1$ up to the second order term was established. The first order derivative can be expressed using the first equation, while the second one

$$\begin{aligned} \left.\frac{\partial^2 y}{\partial x^2}\right|_{x_l} &\approx 2\left(\frac{y_{l+1}-y_l}{\Delta x_{l+1}(\Delta x_l + \Delta x_{l+1})} - \frac{y_l - y_{l-1}}{\Delta x_l(\Delta x_l + \Delta x_{l+1})}\right) \quad \text{for} \quad l = 1, \ldots, N_x - 1 \\ &= 2\frac{\Delta x_l(y_{l+1}-y_l) - \Delta x_{l+1}(y_l - y_{l-1})}{\Delta x_l \Delta x_{l+1}(\Delta x_l + \Delta x_{l+1})} \quad \text{for} \quad l = 1, \ldots, N_x - 1 \end{aligned} \tag{3.3.29}$$

serves for the approximation.

3.3.3 Boundary Conditions

At this point it has to be mentioned that the following application of the finite difference method will only work properly, if there are sufficient small grid gaps at the boundaries. The interconnection between grid points is guaranteed by the first and second order space derivatives. Since the grid points at the borders $l = 0$ and $l = N_x$ are represented exactly, the first derivatives will be replaced by *Neumann* boundary conditions (2.3.2) to (2.3.5) and (2.4.3) to (2.4.6) corresponding with sign of the mass flow. So the second order derivatives *only* are responsible for keeping connection between grid points at the boundaries. As a consequence, the infinitesimally small coefficient (f.i. (1a) in the ceramic bed, figure 2.3.2) at the second order space derivatives in the PDEs (2.3.1) and (2.4.1) can provoke the connection loss between grid points. However, a gain of these coefficients can be provided if small grid gaps appear in the dominator.
For demonstration, the simulation of a ceramic bed with the configuration from section 3.3.1.1 applying an equidistant distributed mesh grid (figure 3.3.11) and a non-equidistant distributed mesh grid (figure 3.3.12) using a trigonometric approach (cf. equation 3.3.3) are compared. The switch of the RTO cycle was accomplished by the time variant decrease of the mass flow, which changes its sign at $t = 120$s.

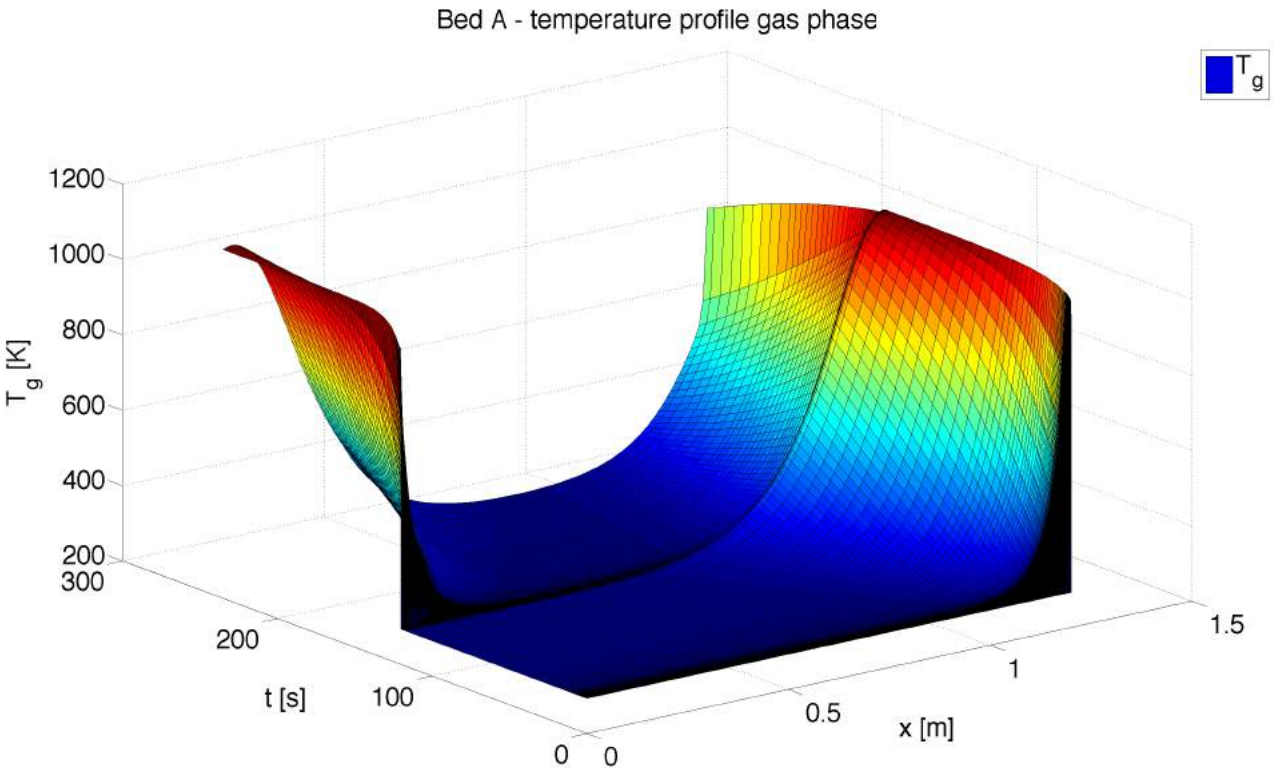

Figure 3.3.11: Distribution of T_g after one RTO cycle switch applying an equidistant mesh with $N_x + 1 = 120$ points.

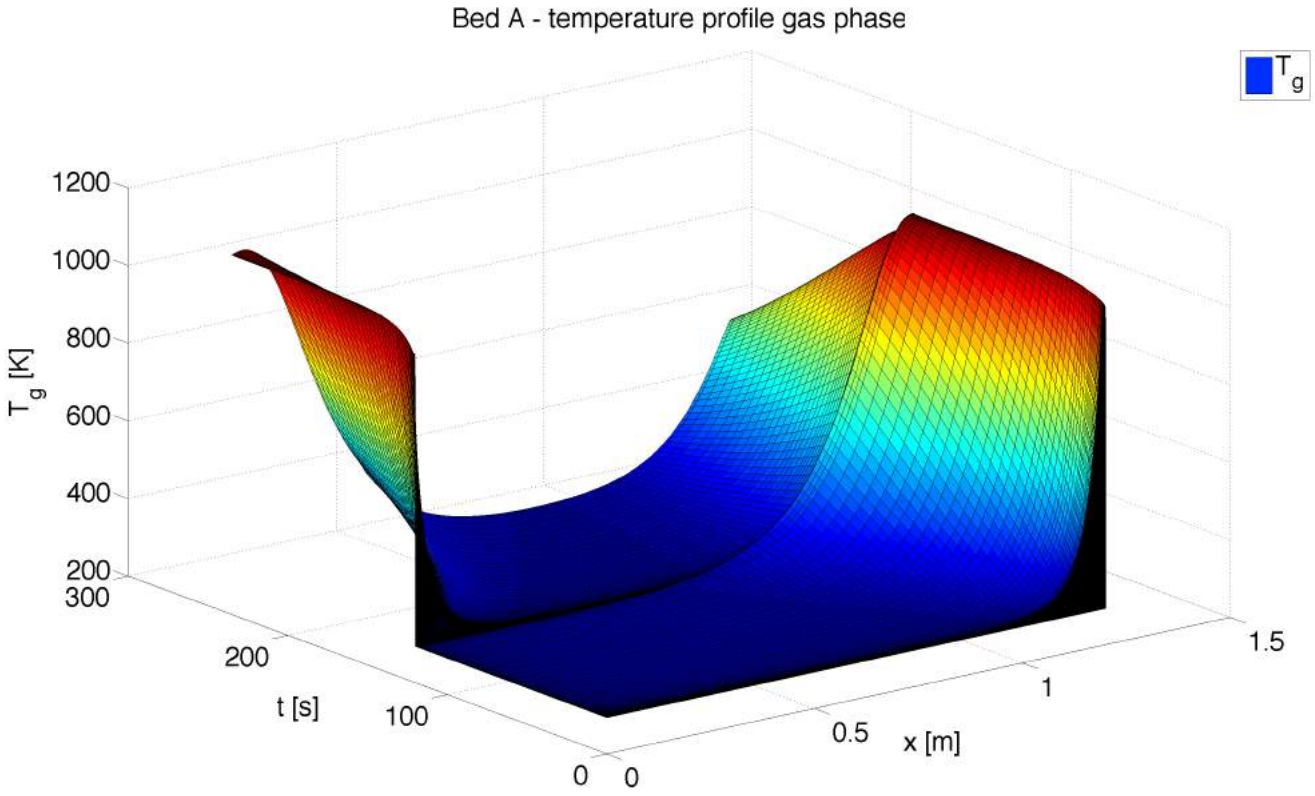

Figure 3.3.12: Distribution of T_g after one RTO cycle switch applying a non-equidistant mesh with $N_x + 1 = 120$ points.

As one can see in figure 3.3.11, the loss of connection in between points expresses after the first RTO cycle switch at the boundary $x = x_{N_x} = 1.2\text{m}$, where the gas temperature should cool down almost linearly (cf. figure 3.3.12). The second order derivatives can be written as follows:

$$\left.\frac{\partial^2 y}{\partial x^2}\right|_{x_{N_x}} \approx \frac{\overbrace{\left.\frac{\partial y}{\partial x}\right|_{x_{N_x}}}^{\text{BC}_{N_x}} - \left.\frac{\partial y}{\partial x}\right|_{x_{N_x-1}}}{\Delta x_{N_x}} \tag{3.3.30a}$$

$$\approx \frac{2}{(\Delta x_{N_x-1} + \Delta x_{N_x})}\left(\overbrace{\frac{y_{N_x} - y_{N_x-1}}{\Delta x_{N_x}}}^{\text{BC}_{N_x}} - \frac{y_{N_x-1} - y_{N_x-2}}{\Delta x_{N_x-1}}\right) \tag{3.3.30b}$$

$$\left.\frac{\partial^2 y}{\partial x^2}\right|_{x_0} \approx \frac{\left.\frac{\partial y}{\partial x}\right|_{x_1} - \overbrace{\left.\frac{\partial y}{\partial x}\right|_{x_0}}^{\text{BC}_0}}{\Delta x_{N_x}} \tag{3.3.30c}$$

$$\approx \frac{2}{(\Delta x_1 + \Delta x_2)}\left(\frac{y_2 - y_1}{\Delta x_2} - \overbrace{\frac{y_1 - y_0}{\Delta x_1}}^{\text{BC}_0}\right) \tag{3.3.30d}$$

The first order derivatives, characterized by BC_{N_x} and BC_0, appearing as part of the second order derivative have to be replaced by the *Neumann* boundary conditions (2.3.2) to (2.3.5) and (2.4.3) to (2.4.6) corresponding with sign of the mass flow. In order to minimize the number of arithmetic operations, the calculation of the first order derivatives of the ceramic temperature T_s can be avoided, since equation (2.3.1a) does not include convection terms. Therefore the methods in reference to equation (3.3.30b) and (3.3.30d) for approximating the second order derivative at the boundaries are used. Simulation results show that there is almost no visible difference between the method used in equations (3.3.30a) & (3.3.30c) and the one used in (3.3.30b) & (3.3.30d), assuming the first order derivatives are approximated by the methods in section 3.3.1.

3.3.4 Pressure

This section should clarify the issue how the pressure drop in the valve boxes 2.2.1, in the ceramic beds 2.3.2 and in the combustion chamber 2.4.2 can be considered dynamically in the simulation.

The absolute pressure as input of the RTO will certainly be in the range of the atmospheric pressure at around 101325 Pa and will be decreased by the appropriate subsystems. For instance, under the assumption that the mass flow enters the plant in side A and leaves in side B, the pressure drop of the valve box A should lead to a decrease of the input pressure p_{in} of bed A and so on. Along with the next half cycle switch this sequence will be changed and the pressure drop of the ceramic bed A should be considered in the decrease of the input pressure p_{in} of the valve box A. So the inputs and outputs of valve boxes and the inputs and outputs of the ceramic beds, as well the ones of the combustion chamber have to be connected with each other, since *Simulink*

does not allow the dynamic linking of blocks during simulation. As a consequence, the appearance of algebraic loops complicates the processing of *Simulink* models and may possibly demand significantly longer computation times, presuming that the algebraic loops can be solved. However, the solvability of the algebraic loops can not be guaranteed at cycle switches. In case of the connection between state variables and input sources like $T_{g,in}$ or Φ_{in} this will be no problem, because the *Integrator* block in between explicitly breaks the loop. The issue with these *algebraic differential equations* should have been made more comprehensible, since their calculation demands the explicit use of the state variable T_g and not of its derivative.

3.3.4.1 Approximation of Integrals

Initially, the discretization of space will lead to the necessity of approximating integrals in the relation of the pressure drop inside of the $i = 1, \ldots, N_l$ ceramic layers (cf. equation (2.3.16)), considering the layer inlet points $l = l_0^{in}, l_1^{in}, \ldots, l_{N_l-1}^{in}$ and the layer outlet $l = l_1^{out}, l_2^{out}, \ldots, l_{N_l}^{out}$ points (space x_{bed} of the ceramic bed)

$$\int_{x_{i-1}^{in}}^{x_i^{out}} \eta_g(T_{g(x,t)}) T_g(x,t) dx \approx \sum_{l=l_{i-1}^{in}+1}^{l_i^{out}-1} \frac{\eta_g(T_{g(x_l,t)}) T_g(x_l,t) + \eta_g(T_{g(x_{l-1},t)}) T_g(x_{l-1},t)}{2} \Delta x_l \tag{3.3.31}$$

as well as the integral in the calculation of the mean gas temperature (cf. equation (2.4.9)).

$$T_{g,mean}(t) \approx \frac{1}{L_{cc}} \sum_{l=1}^{N_{x_{cc}}} \frac{T_g(x_{cc,l},t) + T_g(x_{cc,l-1},t)}{2} \Delta x_{cc,l} \tag{3.3.32}$$

Considering the two different half cycles of the two-bed RTO, the following relations concerning the input parameter p_{in} can be determined.

	Input	**Output**
VB A	$p_{in} = 101325\text{Pa}$	$p_{A,out}^{vb}$
BED A	$p_{in} = p_{A,out}^{vb} - \Delta p_{A,vb}$	$p_{A,out}^{bed}$
CC	$p_{in} = p_{A,out}^{bed} - \Delta p_{A,in} - \Delta p_{A,pipe} - \Delta p_{A,out}$	p_{out}^{cc}
BED B	$p_{in} = p_{out}^{cc} - \Delta p_{cc}$	$p_{B,out}^{bed}$
VB B	$p_{in} = p_{B,out}^{bed} - \Delta p_{B,in} - \Delta p_{B,pipe} - \Delta p_{B,out}$	p_{out}

Table 3.3.3: Pressure input parameter p_{in} in the first half cycle of the RTO.

	Input	**Output**
VB B	$p_{in} = 101325\text{Pa}$	$p_{B,out}^{vb}$
BED B	$p_{in} = p_{B,out}^{vb} - \Delta p_{B,vb}$	$p_{B,out}^{bed}$
CC	$p_{in} = p_{B,out}^{bed} - \Delta p_{B,in} - \Delta p_{B,pipe} - \Delta p_{B,out}$	p_{out}^{cc}
BED A	$p_{in} = p_{out}^{cc} - \Delta p_{cc}$	$p_{A,out}^{bed}$
VB A	$p_{in} = p_{A,out}^{bed} - \Delta p_{A,in} - \Delta p_{A,pipe} - \Delta p_{A,out}$	p_{out}

Table 3.3.4: Pressure input parameter p_{in} in the second half cycle of the RTO.

The calculation of the sum of the pressure drop at the layer inlet points Δp_{in} (equation (2.3.13)), as well as at the layer outlet points Δp_{out} (equation (2.3.14)) of the ceramic bed is covered in section 2.3.2, whereas the calculation of the pressure drop in the combustion chamber can be found in section 2.4.2.

3.3.4.2 Algebraic Loops

The appearance of algebraic loops can be attributed to the linkage of inputs and outputs of submodels concerning the absolute pressure. Although the loops are not closed inside of the cycles, *Simulink* discovers mutual dependencies due to the physical connection in the block diagram. The switch between inputs/outputs was implemented using *Switch* blocks, which are controlled by the sign of the mass flow.
These dependencies can be entirely suppressed if *Simulink* models are processed for each cycle, which demands the need of four valve boxes, four ceramic beds and two combustion chamber models as far as a two-bed configuration is concerned. In other words, the implementation of n different RTO models will be necessary for simulating the behavior of a n-bed RTO configuration, whereas only one single RTO model needs to be enabled in the appropriate cycle. One of the challenges of this method is the establishment of the communication between these different RTO models, since e.g. the states of integrators have to be exchanged. *Michael Wieser* set the focus on this method of implementing due to the application of *Interpreted MATLAB Functions*, which do not break algebraic loops like *Integrator* blocks in *Simulink*.
Attempts of replacing *Switch* blocks by more advanced combinations of other blocks failed, but in order to establish a proper connection without using delay elements another approach was made.

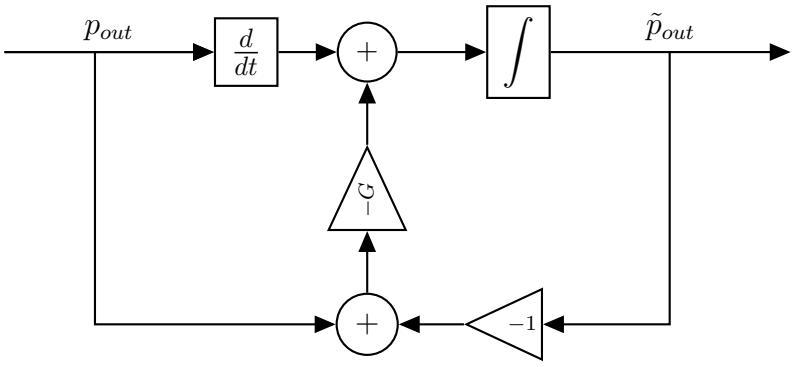

Figure 3.3.13: Method for breaking algebraic loops concerning the pressure.

Taking the derivative of the outlet pressure p_{out} and integrating afterwards produces an explicit break point in the algebraic loop. The error made by the approximation of the derivative, as well as by the approximation of the integration will be asymptotically stable, since a negative gain of this error will be fed back. Almost no visible difference between p_{out} and $\tilde{p}_{out}$ can be seen when using a gain of e.g. $G = 10^3$. The addition of the derivatives of the equations for the output pressure as a coupled one to the model's differential equations would be another possibility, whereas consequentially the derivatives of input parameters such as p_{in} would have to be approximated as well.

3.4 Numerical Precaution

This section briefly introduces a simple action in order to reduce numerical oscillations, which will be provoked due to the quite high range difference $\sim 10^6$ between the volume fraction of VOCs and temperatures. The application of a numerical factor e.g. $\alpha_\Phi = 10^7$ in models' differential equations (2.2.1), (2.3.1) and (2.4.1), considering a function $f(.)$ describing the time derivative in dependence of Φ

$$\frac{\partial\left(\alpha_\Phi \Phi\right)}{\partial t} = f\left(\alpha_\Phi \Phi_{in}, \alpha_\Phi \Phi, \frac{\partial(\alpha_\Phi \Phi)}{\partial x}, \frac{\partial^2(\alpha_\Phi \Phi)}{\partial x^2}\right) \tag{3.4.1}$$

effectively suppresses numerical issues. If one analyzes the mentioned equations in more detail, it can be seen that the function $f(.)$ applied on these equations is *linear* in Φ and in the input parameter Φ_{in}.

$$\begin{aligned}
\Phi &= \frac{1}{\alpha_\Phi} \int_t f\left(\alpha_\Phi \Phi_{in}, \alpha_\Phi \Phi, \frac{\partial(\alpha_\Phi \Phi)}{\partial x}, \frac{\partial^2(\alpha_\Phi \Phi)}{\partial x^2}\right) dt \\
&= \frac{1}{\alpha_\Phi} \int_t \alpha_\Phi f\left(\Phi_{in}, \Phi, \frac{\partial \Phi}{\partial x}, \frac{\partial^2 \Phi}{\partial x^2}\right) dt \\
&= \int_t f\left(\Phi_{in}, \Phi, \frac{\partial \Phi}{\partial x}, \frac{\partial^2 \Phi}{\partial x^2}\right) dt
\end{aligned} \tag{3.4.2}$$

The applied *Integrator* and *Embedded MATLAB Function* blocks for processing gradients exclusively deal with the quantity $\alpha_\Phi \Phi$, whereas outside of these blocks the real Φ can be provided by the appropriate gain $1/\alpha_\Phi$. As a result, the reaction heat in the derivatives of the gas temperature also need to be divided by α_Φ.

3.5 RTO Cycle Switch

RTO cycle switches are controlled by the sign of the mass flow $\dot{m}$, which certainly appears as input parameter in all submodels of the plant. At the beginning of this thesis simulation was terminated at the end of one cycle and then continued by the start with the opposite sign of the mass flow. The modification of the function call interval (see section 3.2) to one second did not change this method of switching.
The merging of all submodels to one united system for simulation facilitated the establishment of a continuous change in the mass flow from positive to negative sign or vice versa. So the switches in between RTO cycles ensues dynamically without terminating the simulation. It turned out that the sharp edges in $\dot{m}$ force the step sizes in time to become infinitesimally small and occasionally the solver algorithm does not converge. As a result, the application of the central differential quotient (CDQ in equation (3.3.7)) for approximating first order derivatives particularly endangers convergence and thus will not be used. Early attempts of using a square signal for the mass flow with a half

period of $\tau = 120$s pointed out that most computation time is spent for switches. So not only convergence benefits from a continuous change in $\dot{m}$, also computation time.

The modelling of the change in the mass flow during the switches was accomplished by a polynomial

$$p_{\dot{m}}(\tilde{t}) = a_{p_3}\tilde{t}^3 + a_{p_2}\tilde{t}^2 + a_{p_1}\tilde{t} + a_{p_0} \tag{3.5.1}$$

almost identical to the one used for the distribution of space (cf. equation (3.3.4)). Since the absolute value $|\dot{m}|$ eventually varies due to model intern characteristics, the polynomial moves between $p_{\dot{m}} \in [-1, 1]$ considering a transition time t_{trans} in $\tilde{t} \in [0, t_{\text{trans}}]$. The following conditions

$$\begin{aligned} p_{\dot{m}}(\tilde{t}=0) &= -1 & p_{\dot{m}}(\tilde{t}=t_{\text{trans}}) &= 1 \\ \left.\frac{dp_{\dot{m}}}{d\tilde{t}}\right|_{\tilde{t}=0} &= 0 & \left.\frac{dp_{\dot{m}}}{d\tilde{t}}\right|_{\tilde{t}=t_{\text{trans}}} &= 0 \end{aligned} \tag{3.5.2}$$

lead to the system:

$$\begin{bmatrix} 1 & 0 & 0 & 0 \\ 0 & 1 & 0 & 0 \\ 0 & 1 & 2t_{\text{trans}} & 3t_{\text{trans}}^2 \\ 1 & t_{\text{trans}} & t_{\text{trans}}^2 & t_{\text{trans}}^3 \end{bmatrix} \begin{bmatrix} a_{p_0} \\ a_{p_1} \\ a_{p_2} \\ a_{p_3} \end{bmatrix} = \begin{bmatrix} -1 \\ 0 \\ 0 \\ 1 \end{bmatrix} \tag{3.5.3}$$

The transition time highly depends on the characteristics of the valves in the valve boxes. According to product specifications the transition can be guaranteed within $t_{\text{trans}} = 3$s with an average of about two seconds.
The more challenging part was to accomplish the periodical change of the mass flow, whereas the period of one half cycle can also depend on inner system quantities and therefore can be understood as control variable. Therefore the RTO half cycle period has to be interpreted as $\tau(t)$ time function, or even dependent on sensor signals. Considering the modified time

$$\tilde{t}(t, \tau) \coloneqq \left(t + \frac{t_{\text{trans}}}{2}\right) \pmod{\tau} \tag{3.5.4}$$

(the addition of $t_{\text{trans}}/2$ is required if $p_{\dot{m}}$ should affect both half cycles) for the polynomial approach and the square function $s(t, \tau)$ for generating cycle switches, the mass flow can be specified by:

$$s(t, \tau) \coloneqq \operatorname{sign}\left(\sin\left(\frac{\pi}{\tau}t\right)\right)$$

$$\dot{m} = \dot{m}_{abs}(t) \begin{cases} s\left(t + \frac{t_{\text{trans}}}{2}, \tau\right) p_{\dot{m}}(\tilde{t}) & \text{for} \quad 0 \le \tilde{t} < t_{\text{trans}} \\ s(t, \tau) & \text{for} \quad \frac{t_{\text{trans}}}{2} \le t \pmod{\tau} < \tau - \frac{t_{\text{trans}}}{2} \end{cases} \tag{3.5.5}$$

On the one hand the absolute mass flow $\dot{m}_{abs}$ characterizes the input parameter of the overall plant, on the other hand it can actually change in submodels. For instance the fuel mass flow $\dot{m}_{fuel}$ and the more or less corresponding portion of air $\dot{m}_{air}$ are added at the location of the burner in the system, or the consideration of bypasses would also require the modification of the mass flow $\dot{m}$ at the appropriate locations in the model.

Therefore the modification of $\dot{m}_{abs}$, referring to the definition in equation (3.5.5) would be sufficient. For demonstration, a small half cycle period of $\tau = 10$s, a transition time of $t_{\text{trans}} = 3$s and a constant absolute mass flow of $\dot{m}_{abs} = 0.2383$kg/s are considered in figure 3.5.1.

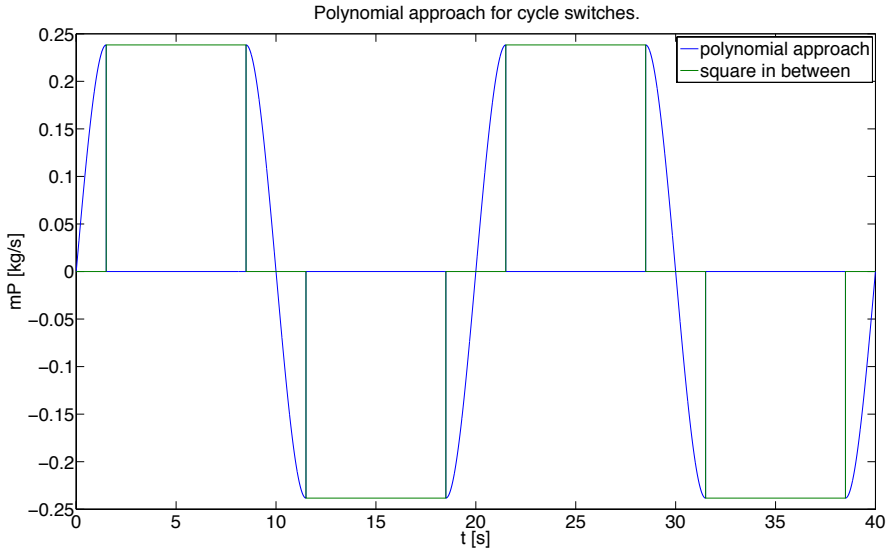

Figure 3.5.1: Modelling of the mass flow for a continuous RTO cycle switch.

Due to discontinuities (figure 3.5.2) for small $|\dot{m}| < 10^{-3}$ in the Nusselt equation (2.3.8)

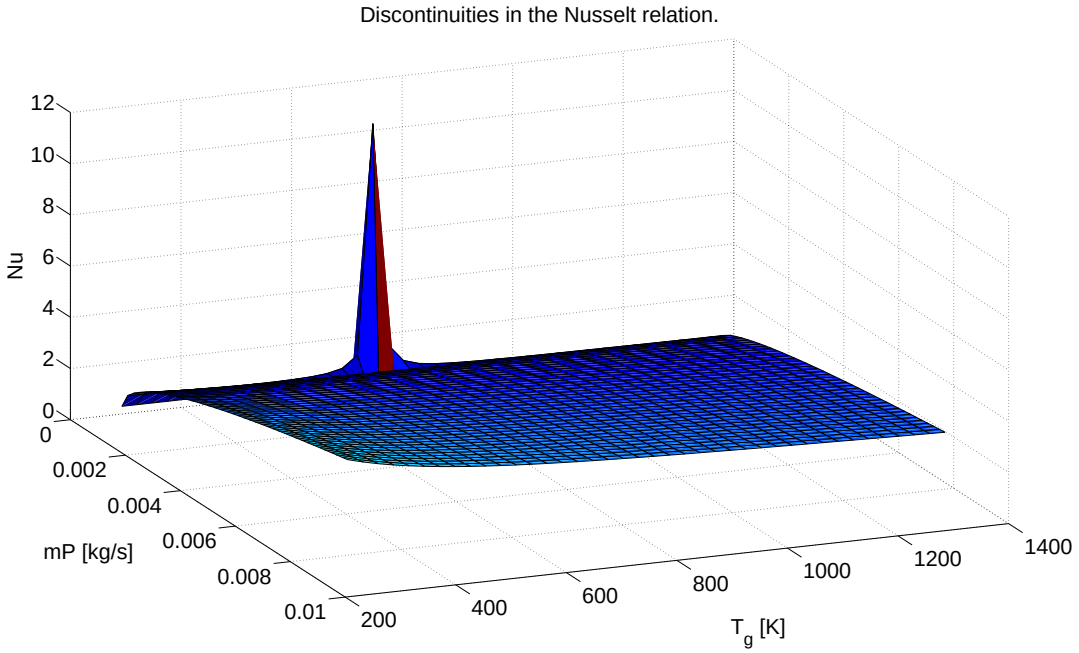

Figure 3.5.2: Discontinuities for small $|\dot{m}| < 10^{-3}$ in the Nusselt equation.

and numerical advantages, values smaller than $|\dot{m}| < \dot{m}_{min} = 10^{-3}$ are set to $\text{sign}(\dot{m}) \cdot \dot{m}_{min}$ with the appropriate sign during cycle switches in the polynomial $p_{\dot{m}}$.

It will be seen later on, it is highly recommended to replace the polynomial $p_{\dot{m}}$ with a function, which is based on measurements. This function should describe the dynamic decrease of the mass flow specified by the valve boxes during switches.

3.6 Résumé and Thoughts on Improvement

Computation Time
In direct comparison between the *Matlab* intern *pdepe* solver and the processed *Simulink* models using the stiff *ode15s* solver, a significant boost concerning subsystems e.g. at the calculation of the ceramic bed could have been achieved, whereas same principles are used. So the *pdepe* solver also discretizes the PDEs in space and then assigns the *ode15s* solver as well to determine step sizes in t.
The main cause for this boost can be attributed to the fact, that the *pdepe* solver iterates through the points in space $l = 0, \ldots, N_x$ (up to versions 2015), whereas the space-gradients were processed by taking advantage of matrix and vector operations. However, this aspect motivated the modification of *pdepe* solver and as a consequence the performance of the simulation of *Thomas Rieger* and *Michael Wieser* could be improved as well.
After linking all submodels to one large model for the two-bed RTO a large amount of coupled differential equations demand intensive computational power. Recapitulating, there are two times three ODEs for the valve boxes, two times three times 130 (amount of grid points) ODEs for the ceramic bed and two times 120 (amount of grid points) ODEs for the combustion chamber, which leads to 1146 coupled differential equations for a two-bed RTO without any consideration of preprocessing, sensors, control feedback loops, sampling, and additional systems such as fans, which control the volume flow through the plant, or hot, respectively cold bypass, etc. Under common circumstances this would not be a problem, but the request of simulation times of up to 30 hours as a result of the inertial thermal processes, places high demands on the processor, the memory and the overall hardware architecture.
Again, this would not be a big deal when using stiff solvers like *ode15s*, but as already mentioned, the RTO cycle switches cause substantial changes in the solution at an almost infinitesimal small period of time. Thus the solver algorithm is forced to tighten step sizes periodically corresponding with the RTO half cycles. Furthermore, the continuous communication between blocks/models (see section 3.2) sensitizes the situation due to stability issues.
In hindsight, it might be advantageous to keep the discretized communication between the blocks (see section 3.2) and the separated calculation of submodels, since convergence probably benefits. Although one might have to compare these two concepts of implementing in detail, in order to determine the origins of the major differences in the solution, whereas implementation errors can never be completely excluded. The suppression of the change of inputs inside function call intervals (see section 3.2) presumably causes errors, in particular during cycle switches, which remains a substantial aspect worth to analyze. Since this thesis focuses on control, there was no time left to pay further attention to these issues.

Applied Software
The intense use of matrix and vector operations in order to process gradients for the PDEs stimulated the application of *Embedded MATLAB Function* blocks in *Simulink*. These blocks significantly outperform the *Interpreted MATLAB Function* blocks in terms of speed, although their (programming) syntax needs to be more restrictive, since they are interpreted in C code. This form of implementation has facilitated the application of the *Rapid Accelerator Mode*, which produces a standalone executable program of the model. Although the gain in speed is quite modest, this can be considered the first step towards the establishment of an embedded system operating on a real time capable OS. Allowing a more differentiated view, it might be advisable to consider the possibility of using another programming environment, since there presumably is high potential in terms of speed, as long as one is aware of the high implementation effort.

Thoughts on Improvement
The code analysis of the *pdepe* solver pointed out that the application of *ode15s* solver settings like the predefined *JPattern*, the Jacobian pattern, which describes the mutual dependencies of the state variable vector by means of a block diagonal matrix, would help to avoid iterations through the grid points in space, when using the solver intern *odenumjac*(.) or *numjac*(.) function. Along with the *ode15s* setting *Vectorized 'on'*, performance could be improved rapidly, at least when using *Matlab* without *Simulink*. However, this option would demand the handling of multiple state vector inputs in the time derivative function $F(.)$ at once

$$\frac{d}{dt}\begin{bmatrix} y_{0,1} & y_{0,2} & \cdots & y_{0,n} \\ \vdots & \vdots & & \vdots \\ y_{N_x,1} & y_{N_x,2} & \cdots & y_{N_x,n} \end{bmatrix} = \frac{d}{dt}\begin{pmatrix} \mathbf{y}_1 & \mathbf{y}_2 & \cdots & \mathbf{y}_n \end{pmatrix} = F\left(\begin{bmatrix} \mathbf{y}_1 & \mathbf{y}_2 & \cdots & \mathbf{y}_n \end{bmatrix}\right)$$

which is quite challenging considering all parameter dependencies of the differential equations. The bad news is that *Simulink* and *Matlab* use different versions of the stiff *ode15s* solver and as a consequence these options are not available in *Simulink*, as far as I have experienced. Research in *Mathworks* forums remained unsuccessful, only a comment on the *Mass* option [13] rises the hope, that there eventually exists an undocumented solution.

4 Sensor Systems

At the moment the amount of available sensor data, which can be used for control purposes, is quite limited, whereas the quality of these signals has to be questioned. Restricted to the measurement of temperatures the aim to control, respectively to minimize the portion of VOCs, spending as few energy as possible results in a challenging task for engineers.
This thesis sets focus on the temperatures in the combustion chamber and hence the sensors located in this area have received adequate attention. The presumption, based on experience and scientific knowledge, that temperature sensors designed for the combustion chamber feature significant long response times, could be verified by mathematical models. The almost complete lack of measurement data endangers the quality of the informative value, given by these models.

4.1 Temperature Sensors in the Combustion Chamber

In the pilot plant two temperature sensors consisting of straight thermocouples with the following type

straight thermocouple AMK 1 × NlCr-Ni
nominal length 400mm
protective steel tube WNr. 1,4762 ∅ 22 × 2mm
inner ceramic tube of type KER710 (C799), ∅ 16 × 2mm
connector head form type AUSH, protection class IP 54
silicone sealant
DIN IEC 584-2 type K, class 1
CTP-Nr. AU.20.01.04.01

Table 4.1.1: Characteristics of the temperature sensors in the pilot plant.

are installed next to the burner, whereas the construction of temperature sensors in combustion chambers in general, in all *Regenerative Thermal Oxidizers*, is quite identical. Research on the modelling of sensors in harsh environments and high temperatures leads to a paper about temperature sensors in biomass furnaces [14], featuring the almost identical construction.

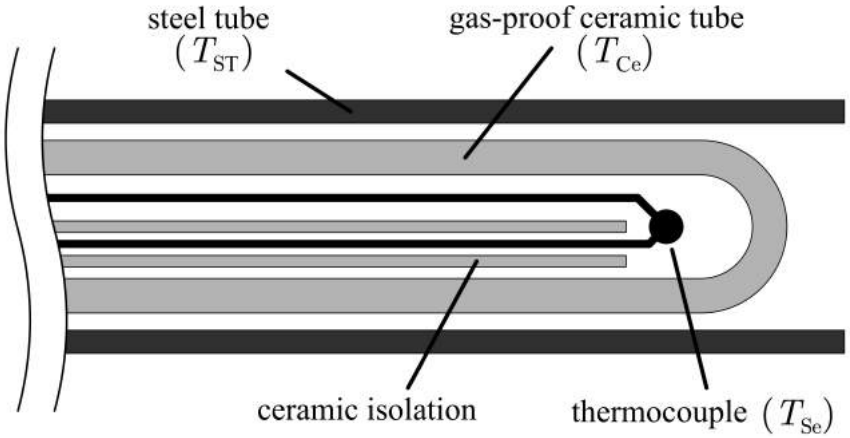

Figure 4.1.1: Construction of the temperature sensors in the combustion chamber (source: [14], figure 7).

4.1.1 Modelling

The modelling of the two temperature sensors located next to the burner in the combustion chamber is based on the sections 2 to 4 in the paper *What Is Really Measured by Temperature Sensors in a Biomass Furnace ?* [14]. See Appendix for more information regarding parameter values of the sensors.

4.1.1.1 Theoretical Basis on Heat Flow and Radiation

Considering the exchange of energy by the release or absorption of heat of an isothermal body with the temperature T, the differential equation

$$\frac{dT}{dt} = \frac{1}{mc} \sum \dot{Q} \tag{4.1.1}$$

involving the mass m, the heat capacity c and the sum of all incoming heat flows $\dot{Q}$, describes the dynamic behavior of the temperature.

Regarding the modelling of exchanging energy by radiation in between two isothermal bodies 1 and 2 with surfaces A_1 and A_2, emissivity ϵ_1 and ϵ_2 and temperatures T_1 and T_2, a simple configuration is considered, assuming that surface of body 2 will entirely cover the surface of body 1. As a consequence, the heat flow $\dot{Q}_{12}$ by radiation from body 1 to body to 2 can be described by [14]

$$\dot{Q}_{12} = A_1 \epsilon_{12} \sigma (T_1^4 - T_2^4) \tag{4.1.2}$$

applying the Stefan-Boltzmann-constant σ and the radiational exchange number

$$\epsilon_{12} = \left(\frac{1}{\epsilon_1} + \frac{A_1}{A_2} \left(\frac{1}{\epsilon_2} - 1 \right) \right)^{-1}. \tag{4.1.3}$$

In case the surface of body 2 is considerably much larger than the surface of body 1 ($A_2 \gg A_1$), the heat flow caused by radiation can be specified in good approximation by:

$$\dot{Q}_{12} = A_1 \epsilon_1 \sigma (T_1^4 - T_2^4) \tag{4.1.4}$$

4.1.1.2 Heat Transfer between Steel tube and Gas

The exchange of energy, respectively the heat flow $\dot{Q}$ between the flowing flue gas (T_g) and the protective steel tube (T_{ST}) can be specified by conductive heat transfer

$$\dot{Q}_{\mathrm{conv,ST\text{-}g}} = m_{\mathrm{ST}} c_{\mathrm{ST}} \frac{dT_{\mathrm{ST}}}{dt} = h_{\mathrm{ST}} A_{\mathrm{ST}} (T_g - T_{\mathrm{ST}}) \tag{4.1.5}$$

introducing the heat transfer coefficient h_{ST}, the effective surface A_{ST}, the mass m_{ST} and the specific, constant heat capacity c_{ST} of the steel tube. The calculation of the heat transfer coefficient ensues similar to the one for the ceramic bed (2.3.7)

$$h_{\mathrm{ST}} = \mathrm{Nu}_{\mathrm{ST}}(\dot{m}, T_g) \frac{\lambda_g(T_g)}{d_{h,\mathrm{ST}}} \tag{4.1.6}$$

considering the empiric Nusselt number $\mathrm{Nu}_{\mathrm{ST}}$, the heat conductivity λ_g and the constant parameter $d_{h,\mathrm{ST}}$, describing the hydraulic diameter of the steel tube. The empiric relation of the Nusselt number resembles the one used for the ceramic bed (cf. equation (2.3.8)), depending on the dimensionless Prandtl Pr and Reynolds $\mathrm{Re}_{\mathrm{ST}}$ number, considering the borders $10 < \mathrm{Re} < 10^7$ and $0.6 < \mathrm{Pr} < 1000$.

$$\mathrm{Re}_{\mathrm{ST}} = \frac{|\dot{m}|\, d_{h,\mathrm{ST}}}{A_{cc}\, \eta_g(T_g)} \qquad \mathrm{Pr} = \frac{\eta_g(T_g) c_g(T_g)}{\lambda_g(T_g)} \tag{4.1.7}$$

$$\mathrm{Nu}_{\mathrm{ST}} = 0.3 + \sqrt{\underbrace{\left(0.664\sqrt{\mathrm{Re}_{\mathrm{ST}}}\sqrt[3]{\mathrm{Pr}}\right)^2}_{\text{laminar part}} + \underbrace{\left(\frac{0.037\mathrm{Re}_{\mathrm{ST}}^{0.8}\mathrm{Pr}}{1 + 2.443\mathrm{Re}_{\mathrm{ST}}^{-0.1}(\mathrm{Pr}^{2/3} - 1)}\right)^2}_{\text{turbulent part}}} \tag{4.1.8}$$

Taking a closer look at equation (4.1.8), one may notice that the Nusselt number can be interpreted as a function of the gas temperature and the mass flow only, which will be helpful for further considerations.

4.1.1.3 Heat Transfer between Thermocouple and Ceramic Tube

The difference $|T_{\mathrm{Ce}} - T_{\mathrm{Se}}|$, considering the convective heat flow $\dot{Q}_{\mathrm{conv,Se\text{-}Ce}}$ between the temperature of the thermocouple and the ceramic tube

$$\begin{aligned} \dot{Q}_{\mathrm{conv,Se\text{-}Ce}} &= m_{\mathrm{Se}} c_{\mathrm{Se}} \frac{dT_{\mathrm{Se}}}{dt} = h_{\mathrm{Se}} A_{\mathrm{Se}} (T_{\mathrm{Ce}} - T_{\mathrm{Se}}) \\ \curvearrowright \frac{dT_{\mathrm{Se}}}{dt} &= \frac{1}{m_{\mathrm{Se}} c_{\mathrm{Se}}} \dot{Q}_{\mathrm{conv,Se\text{-}Ce}} \end{aligned} \tag{4.1.9}$$

or vice versa, will decrease rapidly in comparison to the difference $|T_{\mathrm{ST}} - T_{\mathrm{Se}}|$, as the mass of the thermocouple m_{Se} will be significantly small. As a result, the temperature

of the thermocouple can be equated to the temperature of the ceramic tube in good approximation (cf. section 3 and 4 in [14]).

$$T_{\mathrm{Se}} \approx T_{\mathrm{Ce}} \tag{4.1.10}$$

4.1.1.4 Heat Transfer between Thermocouple and Steel Tube

Analogous to above, the convective heat transfer between the thermocouple and the ceramic tube can be specified as follows:

$$m_{\mathrm{ST}} c_{\mathrm{ST}} \frac{dT_{\mathrm{ST}}}{dt} = h_{\mathrm{Ce}} A_{\mathrm{Ce}} (T_{\mathrm{Se}} - T_{\mathrm{ST}}) \tag{4.1.11}$$

whereas the temperature of the ceramic tube T_{Ce} was replaced by the temperature of the thermocouple T_{Se}. The heat transfer coefficient in terms of equation (4.1.11) can be assumed constant, since no gas mixture will reach the inside of the sensor.
In addition to the convective part, the radiation between the surface of the steel and the ceramic tube has to be taken into account

$$\begin{aligned} m_{\mathrm{ST}} c_{\mathrm{ST}} \frac{dT_{\mathrm{ST}}}{dt} &= A_{\mathrm{Ce}} \epsilon_{\mathrm{ST,Ce}} \sigma (T_{\mathrm{ST}}^4 - T_{\mathrm{Ce}}^4) \\ &\approx A_{\mathrm{Ce}} \epsilon_{\mathrm{ST,Ce}} \sigma (T_{\mathrm{ST}}^4 - T_{\mathrm{Se}}^4) \end{aligned} \tag{4.1.12}$$

whereas the temperature of the ceramic tube T_{Ce} will be replaced by T_{Se} in a second step. The emissivity

$$\epsilon_{\mathrm{ST,Ce}} = \left(\frac{1}{\epsilon_{\mathrm{ST}}} + \frac{A_{\mathrm{ST}}}{A_{\mathrm{Ce}}} \left(\frac{1}{\epsilon_{\mathrm{Ce}}} - 1 \right) \right)^{-1} \tag{4.1.13}$$

referring to equation (4.1.3) applies the emissivity of both bodies to their surface ratio.

4.1.1.5 Radiation between Steel Tube and Wall

The radiation between the protective steel tube of the sensor and the wall of the combustion chamber must not be neglected due to high temperatures near the burner. The temperature of the combustion chamber wall remains one decisive aspect being uncertain, since the form of consideration in the differential equations demands the usage of a single temperature $T_{cc,\mathrm{wall}}$, representative for the distribution of the temperature over the entire inner surface of the combustion chamber. In a first approximation the assumption was made, that $T_{cc,\mathrm{wall}}$ depends linearly on the gas temperature T_g and the ambient temperature T_{amb}

$$T_{cc,\mathrm{wall}} = \frac{\alpha_{cc,\mathrm{wall}} T_g + k_{ss,\mathrm{loss}} T_{amb}}{\alpha_{cc,\mathrm{wall}} + k_{ss,\mathrm{loss}}} \tag{4.1.14}$$

whereas the linear parameters were determined by empiric knowledge. As one can see in section 4.1 in [14], the modelling of this temperature demands further attention and highly depends on the geometric characteristics, as well as on the gas composition and on the reaction of VOCs and consequentially, on the exact position of the sensors in the combustion chamber. The usage of a dynamic model similar to the one in [14] could

probably improve accuracy, although the model in equation (4.1.14) might be sufficient in case the parameters $\alpha_{cc,\text{wall}}$ and $k_{ss,\text{loss}}$ will be verified and eventually adjusted to measurement data.

Since the inner surface of the combustion chamber can certainly be considered much larger than the effective surface of the protective steel tube of one of the sensors, the equation

$$m_{\text{ST}} c_{\text{ST}} \frac{dT_{\text{ST}}}{dt} = A_{\text{ST}} \epsilon_{\text{ST}} \sigma (T_{\text{ST}}^4 - T_{cc,\text{wall}}^4) \tag{4.1.15}$$

presumably identifies radiation to a sufficient level of detail, as long as one is aware of the issue regarding $T_{cc,\text{wall}}$.

4.1.1.6 Final Model

Introducing the definitions

$$\begin{aligned} c_{ss,1} &:= \frac{h_{\text{ST}} A_{\text{ST}}}{m_{\text{ST}} c_{\text{ST}}} & c_{ss,2} &:= \frac{A_{\text{ST}} \epsilon_{\text{ST}}}{m_{\text{ST}} c_{\text{ST}}} \sigma \\ c_{ss,3} &:= \frac{h_{\text{Ce}} A_{\text{Ce}}}{m_{\text{ST}} c_{\text{ST}}} & c_{ss,4} &:= \frac{A_{\text{Ce}} \epsilon_{\text{ST,Ce}}}{m_{\text{ST}} c_{\text{ST}}} \sigma \\ c_{ss,5} &:= \frac{h_{\text{Ce}} A_{\text{Ce}}}{m_{\text{Ce}} c_{\text{Ce}}} & c_{ss,6} &:= \frac{A_{\text{Ce}} \epsilon_{\text{ST,Ce}}}{m_{\text{Ce}} c_{\text{Ce}}} \sigma \end{aligned} \tag{4.1.16}$$

the second order mathematical model [14]

$$\begin{aligned} \frac{dT_{\text{ST}}}{dt} &= c_{ss,1}(T_g - T_{\text{ST}}) + c_{ss,2}\left(T_{cc,\text{wall}}^4 - T_{\text{ST}}^4\right) \\ &\quad + c_{ss,3}(T_{\text{Se}} - T_{\text{ST}}) + c_{ss,4}\left(T_{\text{Se}}^4 - T_{\text{ST}}^4\right) \end{aligned} \tag{4.1.17a}$$

$$\frac{dT_{\text{Se}}}{dt} = c_{ss,5}(T_{\text{ST}} - T_{\text{Se}}) + c_{ss,6}\left(T_{\text{ST}}^4 - T_{\text{Se}}^4\right) \tag{4.1.17b}$$

describes the dynamic behavior of the temperature of the protective steel tube, coupled to the temperature of the thermocouple of the sensors, located in the combustion chamber. It will be noted that the condition as a result of the definitions (4.1.16)

$$c_{ss,3} c_{ss,6} = c_{ss,4} c_{ss,5} \tag{4.1.18}$$

might facilitate the determination of the coefficients $c_{ss,j}\ \forall j$.

4.1.2 Restoring of the Original Gas Temperature

Analyzing the equation (4.1.17), the determination of the original gas temperature T_g by the sensor signal T_{Se} can not be considered trivial. T_g obviously appears as input parameter in the ordinary differential equation, hence the application of observers becomes problematic.
The restoring of the original gas temperature by taking advantage of the knowledge provided by the mathematical model in equation (4.1.17) is therefore separated in two steps. At first the temperature of the steel tube has to be calculated and then the gas temperature. The method of recalculating T_g is simply based on the search of zero points of polynomials, which feature 4^{th} degree as a result of thermal radiation. Since this method solves algebraic equations only, the derivatives

$$\frac{dT_{\mathrm{ST}}}{dt} \quad \text{and} \quad \frac{dT_{\mathrm{Se}}}{dt}$$

need to be somehow approximated, whereas the quality of their approximation substantially affects the accuracy of the restored gas temperature. The dependency of the thermal coefficient h_{ST} on T_g, as well as on $\dot{m}$ additionally aggravates the determination of T_g.

4.1.2.1 Restoring T_{ST} from T_{Se}

In order to calculate the temperature of the steel tube T_{ST} from the actually measured temperature (of the thermocouple) T_{Se}, the equation (4.1.17b) receives the form (cf. equation (36) and (37) in [14])

$$0 = T_{\mathrm{ST}}^4 + \underbrace{\frac{c_{ss,5}}{c_{ss,6}}}_{=d} T_{\mathrm{ST}} + \underbrace{\frac{1}{c_{ss,6}} \left(-c_{ss,5} T_{\mathrm{Se}} - c_{ss,6} T_{\mathrm{Se}}^4 - \frac{dT_{\mathrm{Se}}}{dt} \right)}_{=e} \tag{4.1.19}$$

of a 4^{th} order polynomial with coefficients e and d, assuming that the derivative $\frac{dT_{\mathrm{Se}}}{dt}$ is known. For determining T_{ST} in each time step, an analytical solution for the appropriate real and positive zero point is preferable in terms of computational effort. It is worth mentioning, that thanks to the definitions (4.1.16) and the physical meanings of the parameters, the coefficient $d > 0$ remains strictly positive.
There certainly exist four zero points, whereas two will be complex and one negative, which leads to one remaining possibility for T_{ST}. As a consequence of the strictly positive coefficient d and the missing coefficients at T_{ST} to the power of two and three, the real and positive solution will not change its position among the zero points. *Lodovico Ferrari* could reduce the problem, so it requires the zero points of a third order polynomial (*cubic resolvent*) to be found, which was achieved by *Gerolamo Cardano* [14].

$$w = \sqrt[3]{\frac{d^2}{16} + \sqrt{\left(\frac{d^2}{16}\right)^2 - \left(\frac{e}{3}\right)^3}} + \sqrt[3]{\frac{d^2}{16} - \sqrt{\left(\frac{d^2}{16}\right)^2 - \left(\frac{e}{3}\right)^3}}$$

$$T_{\mathrm{ST}} = \sqrt{\frac{d}{2\sqrt{2w}} - \frac{w}{2}} - \frac{\sqrt{2w}}{2} \tag{4.1.20}$$

The appropriate solution remains positive and real, even in the case of a negative discriminant as a reason of the structure.

4.1.2.2 Restoring T_g from T_{Se} and T_{ST}

The method of restoring the original gas temperature turns out to be more complicated, whereas the same principle is used. Again, a polynomial form

$$\begin{aligned} 0 = & T_{cc,\text{wall}}^4 + \frac{c_{ss,1}}{c_{ss,2}} T_g - \frac{c_{ss,1}}{c_{ss,2}} T_{\text{ST}} \\ & + \frac{1}{c_{ss,2}} \left(-c_{ss,2} T_{\text{ST}}^4 + c_{ss,3}(T_{\text{Se}} - T_{\text{ST}}) + c_{ss,4} \left(T_{\text{Se}}^4 - T_{\text{ST}}^4 \right) - \frac{dT_{\text{ST}}}{dt} \right) \end{aligned} \tag{4.1.21}$$

will help to reduce the problem to the search of zeros points. Assuming that the temperature $T_{cc,\text{wall}}$ depends linearly on T_g, it will be beneficial to solve the polynomial for $T_{cc,\text{wall}}$ (equation (4.1.14))

$$\begin{aligned} 0 = & T_{cc,\text{wall}}^4 + \frac{c_{ss,1}}{c_{ss,2}} \left(1 + \frac{k_{ss,\text{loss}}}{\alpha_{cc,\text{wall}}} \right) T_{cc,\text{wall}} - \frac{c_{ss,1}}{c_{ss,2}} \left(T_{\text{ST}} - \frac{k_{ss,\text{loss}}}{\alpha_{cc,\text{wall}}} T_{amb} \right) \\ & + \frac{1}{c_{ss,2}} \left(-c_{ss,2} T_{\text{ST}}^4 + c_{ss,3}(T_{\text{Se}} - T_{\text{ST}}) + c_{ss,4} \left(T_{\text{Se}}^4 - T_{\text{ST}}^4 \right) - \frac{dT_{\text{ST}}}{dt} \right) \end{aligned} \tag{4.1.22}$$

in the first place and recalculate T_g after the desired zero point has been determined. The aim will be to formulate a *depressed quartic polynomial* [15]

$$0 = T_{cc,\text{wall}}^4 + p T_{cc,\text{wall}}^2 + q T_{cc,\text{wall}} + r \tag{4.1.23}$$

in $T_{cc,\text{wall}}$ with the coefficients p, q and r. The dependency of coefficient $c_{ss,1}$, respectively of the transfer coefficient h_{ST} on T_g needs to be considered in more detail.

Heat Transfer Coefficient

In reference to equation (4.1.6), the heat transfer coefficient can explicitly be interpreted as function of the mass flow and the gas temperature, whereas the complex relations in equation (4.1.7) and (4.1.8) have to be somehow defused in mathematical terms. Analysis on the distribution of h_{ST} over the gas temperature in the area of interest $T_g \in [0, 1100]°\text{C}$ confirmed that the dependency can be considered linear in good approximation, particularly in that range.

Although one may not forget the additional dependency on the mass flow, which leads to a continuous distribution of parameter h_{ST} over $\dot{m}$ and T_g. In [14] the assumption was made that the gas velocity (in the biomass furnace)

$$u = \frac{\dot{m}}{A \rho_g(T_g, p_{in})}$$

is known and as a result the heat transfer coefficient could be parameterized by the velocity $h_{\text{ST}} \approx h_{\text{ST}}(u)$. Hence, the solution of equation (4.1.22) could be provided by the

same method used for calculating T_{ST} out of T_{Se} in section 4.1.2.1, considering

$$d = \frac{c_{ss,1}}{c_{ss,2}} \left(1 + \frac{k_{ss,\mathrm{loss}}}{\alpha_{cc,\mathrm{wall}}}\right)$$

$$e = -\frac{c_{ss,1}}{c_{ss,2}} \left(T_{\mathrm{ST}} - \frac{k_{ss,\mathrm{loss}}}{\alpha_{cc,\mathrm{wall}}} T_{amb}\right) + \frac{1}{c_{ss,2}} \left(-c_{ss,2} T_{\mathrm{ST}}^4 + c_{ss,3}(T_{\mathrm{Se}} - T_{\mathrm{ST}}) + c_{ss,4}\left(T_{\mathrm{Se}}^4 - T_{\mathrm{ST}}^4\right) - \frac{dT_{\mathrm{ST}}}{dt}\right)$$

for equation (4.1.20). In this thesis another, more accurate concept was developed, which requires the knowledge of the mass flow $\dot{m}$, instead of u. The idea was to interpolate the continuous surface of h_{ST} by another linear (in T_g) polynomial

$$h_{\mathrm{ST}}(\dot{m}, T_g) \approx p_{h_{\mathrm{ST}}}(\dot{m}, T_g) = a_1 T_g + a_2 \dot{m} T_g + a_3 \dot{m} + a_4 \dot{m}^2 + a_5 \tag{4.1.24}$$

with coefficients a_i for $i = 1, \ldots, 5$ to be determined. For the following consideration parameters were adapted to air (table 6.1.1 and 6.1.2), referring to λ_g, η_g and c_g. Using the free *polyfitn* toolbox [16] the parameters could be calculated in the way that the variance of the error (of a chosen set of values) between h_{ST} and $p_{h_{\mathrm{h}}}$ has been minimized.

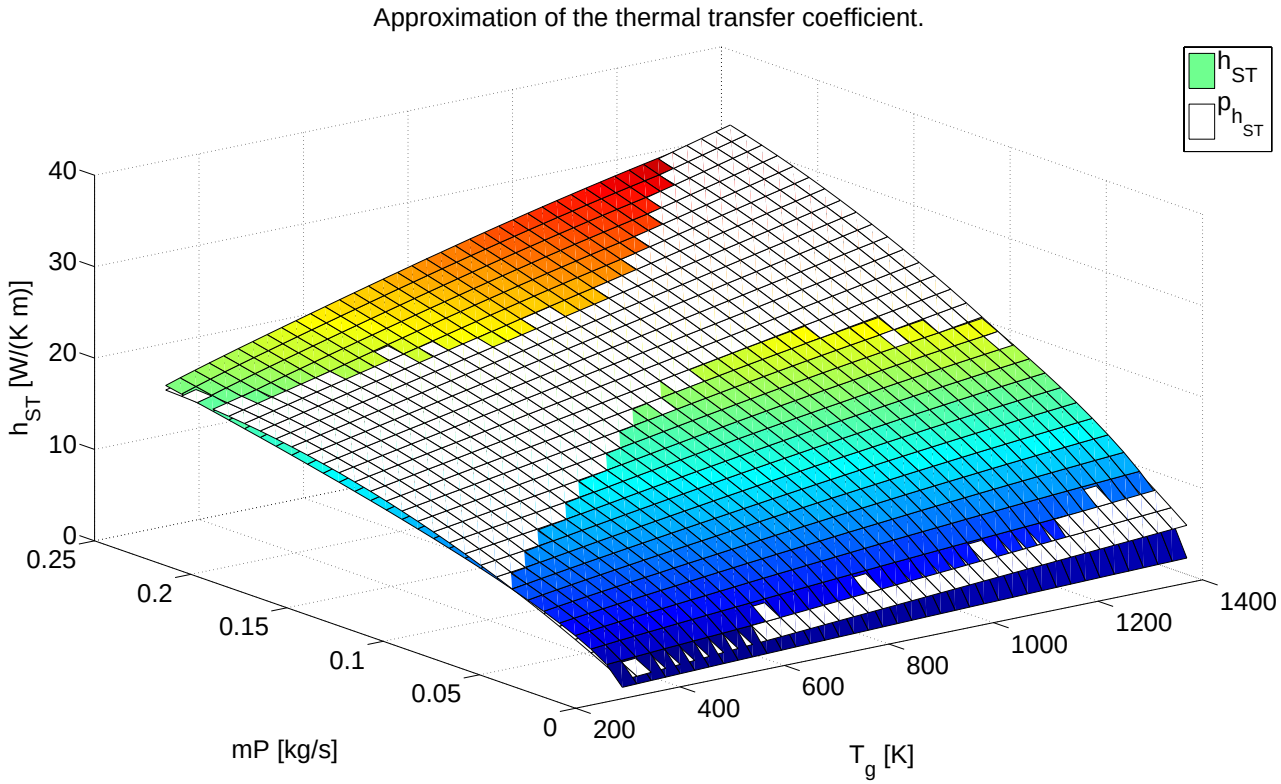

Figure 4.1.2: Approximation ($p_{h_{\mathrm{ST}}}$ - white mesh) of the heat transfer coefficient (h_{ST} - colored mesh).

In order to gain maximal accuracy this method was extended, which presumably will not be necessary due to the interference of the far less accurate approximation of the

derivatives of T_{Se} and T_{ST}. Nevertheless, the usage of n_p polynomials of form (4.1.24)

$$h_{\mathrm{ST}}(\dot{m}, T_g) \approx p_{j,h_{\mathrm{ST}}}(\dot{m}, T_g) = a_{j,1} T_g + a_{j,2} \dot{m} T_g + a_{j,3} \dot{m} + a_{j,4} \dot{m}^2 + a_{j,5} \quad \text{for} \quad j = 1, \ldots, n_p \tag{4.1.25}$$

corresponding with n_p regions $[\dot{m}_j, \dot{m}_{j-1})$ for $j = 1, \ldots, n_p$ between $n_p + 1$ borders $\mathbf{v}_{\dot{m}}^T = \begin{bmatrix} \dot{m}_0 & \ldots & \dot{m}_{n_p} \end{bmatrix}$ of $\dot{m}$ could help to improve the quality of the approximation. The distances between borders were chosen with equal length, depending on the number of regions.

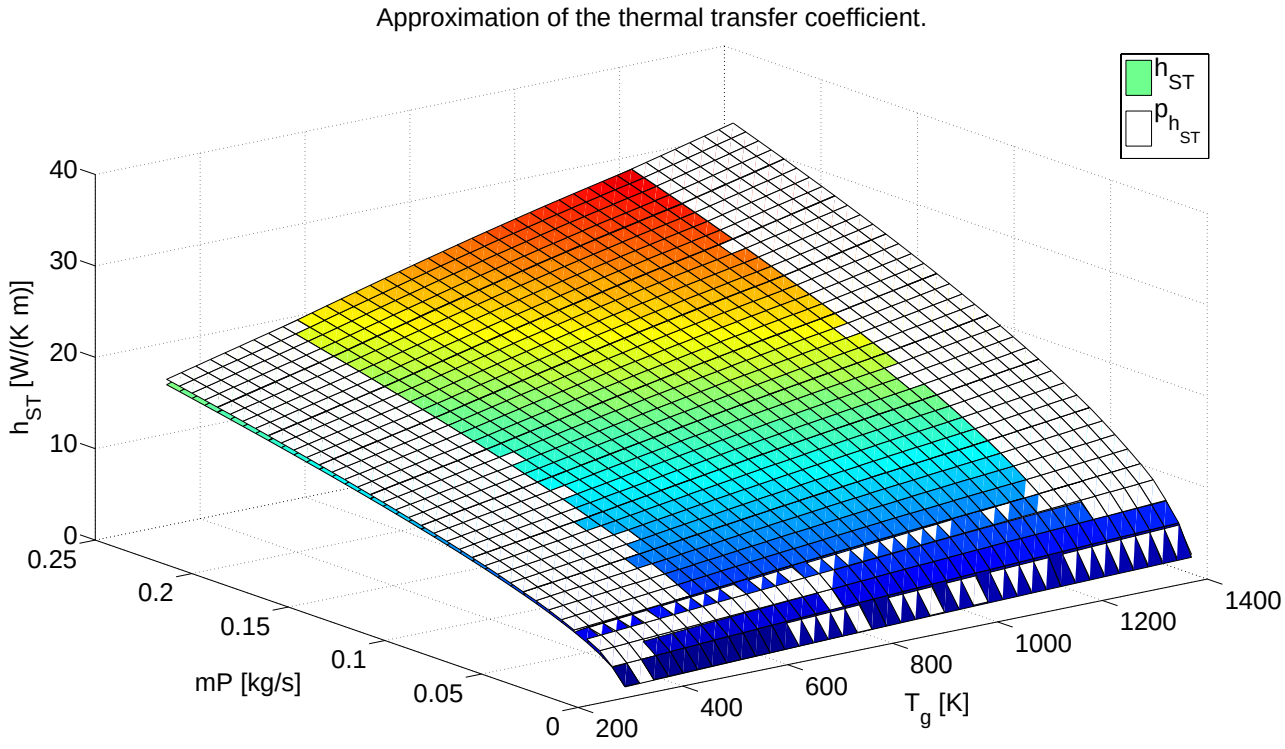

Figure 4.1.3: Approximation ($p_{h_{\mathrm{ST}}}$ - white mesh) of the heat transfer coefficient (h_{ST} - colored mesh) by $n_p = 10$ polynomials.

The processing in *Matlab* is comfortable to handle by taking advantage of matrix and logic operations. Introducing

$$\mathbf{A}_{h_{\mathrm{ST}}} := \begin{bmatrix} a_{1,1} & \ldots & a_{1,5} \\ \vdots & & \vdots \\ a_{n_p,1} & \ldots & a_{n_p,5} \end{bmatrix} \tag{4.1.26}$$

the appropriate polynomial coefficient vector $\mathbf{p}_{j,h}^T := \begin{bmatrix} a_{j,1} & \ldots & a_{j,5} \end{bmatrix}$ can be chosen by the *Matlab* code: $\mathbf{p}_h^T = \mathbf{A}_{h_{\mathrm{ST}}}(\mathrm{sum}(\mathbf{v}_{\dot{m}}^T < \mathrm{abs}(\dot{m})), :)$, assuming positive borders. $\mathbf{A}_{h_{\mathrm{ST}}}$, as well as $\mathbf{v}_{\dot{m}}^T$ should be calculated in preprocessing.

Solution
At first the split of the parameter according to the definition in (4.1.16)

$$\begin{aligned} c_{ss,1} &= h_{\mathrm{ST}}(\dot{m}, T_g)\tilde{c}_{ss,1} \\ &\approx p_{h_{\mathrm{ST}}}(\dot{m}, T_g)\tilde{c}_{ss,1} = T_g(a_1 + a_2\dot{m})\tilde{c}_{ss,1} + (a_3\dot{m} + a_4\dot{m}^2 + a_5)\tilde{c}_{ss,1} \end{aligned} \tag{4.1.27}$$

in one dependent and one independent part is required, replacing the gas temperature

$$\begin{aligned} c_{ss,1} \approx\ & T_{cc,\mathrm{wall}}\,\tilde{c}_{ss,1}\left(1 + \frac{k_{ss,\mathrm{loss}}}{\alpha_{cc,\mathrm{wall}}}\right)(a_1 + a_2\dot{m}) \\ & + \tilde{c}_{ss,1}\left((a_3\dot{m} + a_4\dot{m}^2 + a_5) - T_{amb}\frac{k_{ss,\mathrm{loss}}}{\alpha_{cc,\mathrm{wall}}}(a_1 + a_2\dot{m})\right) \end{aligned} \tag{4.1.28}$$

and thereafter reformulating equation (4.1.22)

$$\begin{aligned} 0 =\ & T_{cc,\mathrm{wall}}^4 + T_{cc,\mathrm{wall}}^2\frac{\tilde{c}_{ss,1}}{c_{ss,2}}\left(1 + \frac{k_{ss,\mathrm{loss}}}{\alpha_{cc,\mathrm{wall}}}\right)^2(a_1 + a_2\dot{m}) \\ & + T_{cc,\mathrm{wall}}\frac{\tilde{c}_{ss,1}}{c_{ss,2}}\left((a_3\dot{m} + a_4\dot{m}^2 + a_5) - T_{amb}\frac{k_{ss,\mathrm{loss}}}{\alpha_{cc,\mathrm{wall}}}(a_1 + a_2\dot{m})\right)\left(1 + \frac{k_{ss,\mathrm{loss}}}{\alpha_{cc,\mathrm{wall}}}\right) \\ & + T_{cc,\mathrm{wall}}\frac{\tilde{c}_{ss,1}}{c_{ss,2}}\left(\frac{k_{ss,\mathrm{loss}}}{\alpha_{cc,\mathrm{wall}}}T_{amb} - T_{\mathrm{ST}}\right)\left(1 + \frac{k_{ss,\mathrm{loss}}}{\alpha_{cc,\mathrm{wall}}}\right)(a_1 + a_2\dot{m}) \\ & + \frac{\tilde{c}_{ss,1}}{c_{ss,2}}\left(\frac{k_{ss,\mathrm{loss}}}{\alpha_{cc,\mathrm{wall}}}T_{amb} - T_{\mathrm{ST}}\right)\left((a_3\dot{m} + a_4\dot{m}^2 + a_5) - T_{amb}\frac{k_{ss,\mathrm{loss}}}{\alpha_{cc,\mathrm{wall}}}(a_1 + a_2\dot{m})\right) \\ & + \frac{1}{c_{ss,2}}\left(-c_{ss,2}T_{\mathrm{ST}}^4 + c_{ss,3}(T_{\mathrm{Se}} - T_{\mathrm{ST}}) + c_{ss,4}\left(T_{\mathrm{Se}}^4 - T_{\mathrm{ST}}^4\right) - \frac{dT_{\mathrm{ST}}}{dt}\right) \end{aligned} \tag{4.1.29}$$

so that the coefficients p, q and r of the *quartic* polynomial (4.1.23) can explicitly be determined and read off the equation (4.1.29). The solution can be provided by

$$\gamma = -\frac{p}{12} - r \qquad \delta = -\frac{p^3}{108} + \frac{pr}{3} - \frac{q^2}{8}$$

$$w = \sqrt[3]{-\frac{\delta}{2} + \sqrt{\left(\frac{\delta}{2}\right)^2 + \left(\frac{\gamma}{3}\right)^3}} + \sqrt[3]{-\frac{\delta}{2} - \sqrt{\left(\frac{\delta}{2}\right)^2 + \left(\frac{\gamma}{3}\right)^3}} - \frac{5}{6}p \tag{4.1.30}$$

$$T_{cc,\mathrm{wall}} = \begin{cases} \dfrac{\sqrt{p+2w} + \sqrt{-3p - 2w - \frac{2q}{\sqrt{p+2w}}}}{2} & \text{for} \quad \left(-3p - 2w - \frac{2q}{\sqrt{p+2w}}\right) \geq 0 \\ \dfrac{-\sqrt{p+2w} + \sqrt{-3p - 2w + \frac{2q}{\sqrt{p+2w}}}}{2} & \text{for} \quad \left(-3p - 2w + \frac{2q}{\sqrt{p+2w}}\right) > 0 \end{cases}$$

$$T_g = \frac{(\alpha_{cc,\mathrm{wall}} + k_{ss,\mathrm{loss}})T_{cc,\mathrm{wall}} - k_{ss,\mathrm{loss}}T_{amb}}{\alpha_{cc,\mathrm{wall}}} \tag{4.1.31}$$

assuming a positive discriminant $\left(\frac{\delta}{2}\right)^2+\left(\frac{\gamma}{3}\right)^3 \geq 0$ in equation (4.1.30), as well as a positive mass flow $\dot{m} > 0$ in equation (4.1.29) and more importantly a non zero coefficient $q \neq 0$. The condition $\left(\frac{\delta}{2}\right)^2 + \left(\frac{\gamma}{3}\right)^3 \geq 0$ assures that the two cases in equation (4.1.23) do not interfere, however one has to be cautious. Since the derivative of T_{Se} and T_{ST} has to be somehow approximated, it eventually occurs that the mentioned discriminant goes negative and as a result provokes complex solutions. This case needs to be intercepted by for instance taking the absolute value of the discriminant in equation (4.1.30). In case $q = 0$ the polynomial

$$0 = T_{cc,\mathrm{wall}}^4 + pT_{cc,\mathrm{wall}}^2 + r \tag{4.1.32}$$

can easily be solved by substitution of the quadratic temperature.

4.1.2.3 Mathematical Background on a *Depressed Quartic Polynomial*

This section briefly introduces a method for solving a *depressed quartic* polynomial

$$f(y) = y^4 + py^2 + qy + r$$

which can be traced back in history to the mathematician *Lodovico Ferrari* and his teacher *Gerolamo Cardano* in the 16$^{\mathrm{th}}$ century [17]. The aim will be to factorize function f, assuming $f(y)$ and the solutions to be rational numbers $\mathbb{Q}$ [15]. *Ferrari* considered the equation

$$y^4 + py^2 = -qy - r$$

and aimed a quadratic form

$$\begin{aligned} y^4 + 2py^2 + py^2 &= py^2 - qy - r + py^2 \\ (y^2 + p)^2 &= py^2 - qy - r + py^2 \end{aligned}$$

by introducing another variable w inside the square on the left hand side and complementing the right hand side.

$$\begin{aligned} (y^2 + p + w)^2 &= py^2 - qy - r + p^2 + 2(y^2 + p)w + w^2 \\ &= y^2(p + 2w) - qy + (p^2 - r + 2pw + w^2) \end{aligned}$$

This form can be accomplished if the discriminant of the right hand side disappears, hence the problem was reduced to the search of zero points of a 3$^{\mathrm{rd}}$ order polynomial, the cubic resolvent R.

$$\begin{aligned} 0 &= (-q)^2 - 4(p + 2w)(p^2 - r + 2pw + w^2) \\ R &= w^3 + \frac{5}{2}pw^2 + (2p^2 - r)w + \frac{1}{2}\left(p^3 - pr - \frac{1}{4}q^2\right) \end{aligned}$$

As a result, the right hand side of the original problem receives two zero points at $\frac{q}{2(p+2w)}$ and after taking the square root, one obtains

$$\pm_1(y^2 + p + w) = \pm_2\sqrt{p + 2w}\left(y - \frac{q}{2(p + 2w)}\right).$$

Considering the positive and negative sign of the square root

$$y^2 - \sqrt{p+2w}y + \frac{q}{2\sqrt{p+2w}} + p + w = 0$$
$$y^2 + \sqrt{p+2w}y - \frac{q}{2\sqrt{p+2w}} + p + w = 0$$

two quadratic equations finally lead to four solutions (cf. equation (4.1.31)).

$$y_{1,2} = \frac{1}{2}\left(\sqrt{p+2w} \pm \sqrt{-3p-2w-\frac{2q}{\sqrt{p+2w}}}\right)$$
$$y_{3,4} = \frac{1}{2}\left(-\sqrt{p+2w} \pm \sqrt{-3p-2w+\frac{2q}{\sqrt{p+2w}}}\right)$$

Furthermore one has to provide a value for the variable w as a solution of the *cubic resolvent* R. In order to gain a *depressed cubic* polynomial

$$g(t) = t^3 + \gamma t + \delta$$

to apply the method of *Cardano*, the *Tschirnhaus transformation* [17]

$$w = t - \frac{1}{3}\left(\frac{5}{2}p\right)$$

helps to reduce the resolvent R. Considering the new coefficients

$$\gamma = -\frac{p}{12} - r \qquad \delta = -\frac{p^3}{108} + \frac{pr}{3} - \frac{q^2}{8}$$

(cf. equation (4.1.30)), *Cardano* introduces two auxiliary variables u and v, so that the conditions [17]

$$\delta = v - u$$
$$uv = \left(\frac{\gamma}{3}\right)^3$$
$$t = \sqrt[3]{u} - \sqrt[3]{v}$$

in fact solve the *depressed cubic resolvent*. Consequentially, the first two conditions from above finally lead to

$$v^2 + v\delta - \left(\frac{\gamma}{3}\right)^3 = 0 \qquad v = u + \delta$$

a quadratic function to be solved. Now one is capable to sum up

$$t = \sqrt[3]{-\frac{\delta}{2} + \sqrt{\left(\frac{\delta}{2}\right)^2 + \left(\frac{\gamma}{3}\right)^3}} + \sqrt[3]{-\frac{\delta}{2} - \sqrt{\left(\frac{\delta}{2}\right)^2 + \left(\frac{\gamma}{3}\right)^3}}$$

(cf. equation (4.1.30)), whereas $w = t - \frac{5}{6}p$. This equation provides one real solution and two complex ones, in case $\left(\frac{\delta}{2}\right)^2 + \left(\frac{\gamma}{3}\right)^3 > 0$, a triple real solution if $\left(\frac{\delta}{2}\right)^2 + \left(\frac{\gamma}{3}\right)^3 = 0$ and quite fascinating three real solutions if $\left(\frac{\delta}{2}\right)^2 + \left(\frac{\gamma}{3}\right)^3 < 0$, which provokes the involvement of complex numbers. According to this last case ("casus irreducibilis"), no real solutions can be obtained using algebraic methods [17].

4.1.2.4 Approximation of Derivatives

The appearance of derivatives of the sensor signal, respectively the temperature of the thermocouple, as well as the one of the steel tube demands the application of approximations. Due to limited time and resources this aspect was paid little attention, so the use of a simple backward differential quotient

$$\frac{\partial y}{\partial t} \approx \frac{y(t) - y(t - t_s)}{t_s} \tag{4.1.33}$$

applying the *Discrete Derivative* block in *Simulink*, delivered sufficiently accurate results in the first place. $t_s = 1$s characterizes the sample time, corresponding with the PLC sample time. Since the accuracy of the restored original gas temperature almost explicitly depends on the quality of the approximation of derivatives, it is highly recommended to look into this issue more precisely. This certainly assumes that the mathematical model is verified and sufficiently represents the actual process. In literature can be found a large amount of papers and articles, which cover the issue of approximating derivatives of continuous sensor signals at a high level of detail.

4.1.3 Simulation

For demonstration purposes, one assumes cold initial states $T_g(t_0) = T_{\mathrm{Se}}(t_0) = T_{\mathrm{ST}}(t_0) = 20°\mathrm{C}$ at $t_0 = 0$s (and $T_{amb} = 20°\mathrm{C}\ \forall t$), the mass flow changes its sign every $\tau = 120$s with a transition time of $t_{\mathrm{trans}} = 30$s (see section 3.5) with an absolute value of $\dot{m}_{abs} = 0.2383$kg/s (figure 4.1.4) and all parameters depending on the gas composition are adapted to air (table 6.1.1 and 6.1.2) at an atmospheric pressure of $p_{in} = 101325$ Pa. Since the gas temperature occurs as input parameter, one has to assume its distribution over time. A polynomial for the increase of the gas temperature from 20°C to 850°C takes charge of the rapid, but smooth increase in the initial phase, whereas a sawtooth signal (*Signal Generator* block) with a period of 240s is added to imitate the cooling of the gas temperature at the location of the inlet points from the ceramic bed to the combustion chamber (cf. figure 3.3.12 at $t > 120$ and $x = 1.2$m). The temperature sensor only, without the consideration of any other RTO components is part of this simulation.

4.1.3.1 Configuration with Focus on the Mass Flow

For early considerations, one assumes that the derivative of the sensor signal $\frac{dT_{\mathrm{Se}}}{dt}$ and the one of the temperature of protective steel tube $\frac{dT_{\mathrm{ST}}}{dt}$ are available (figure 4.1.5 and 4.1.6), which certainly is not the case in reality. Furthermore, the simulation does not include sampling, hence no *Zero Order Hold* blocks are in use.

In figure 4.1.5 one can see that the restoring of the temperature of the steel tube T_{ST}, as well as the temperature of the original gas temperature T_g is almost perfect, expecting exact approximations of derivatives and that the mathematical model in equation (4.1.17) reflects reality to a sufficient level of detail.

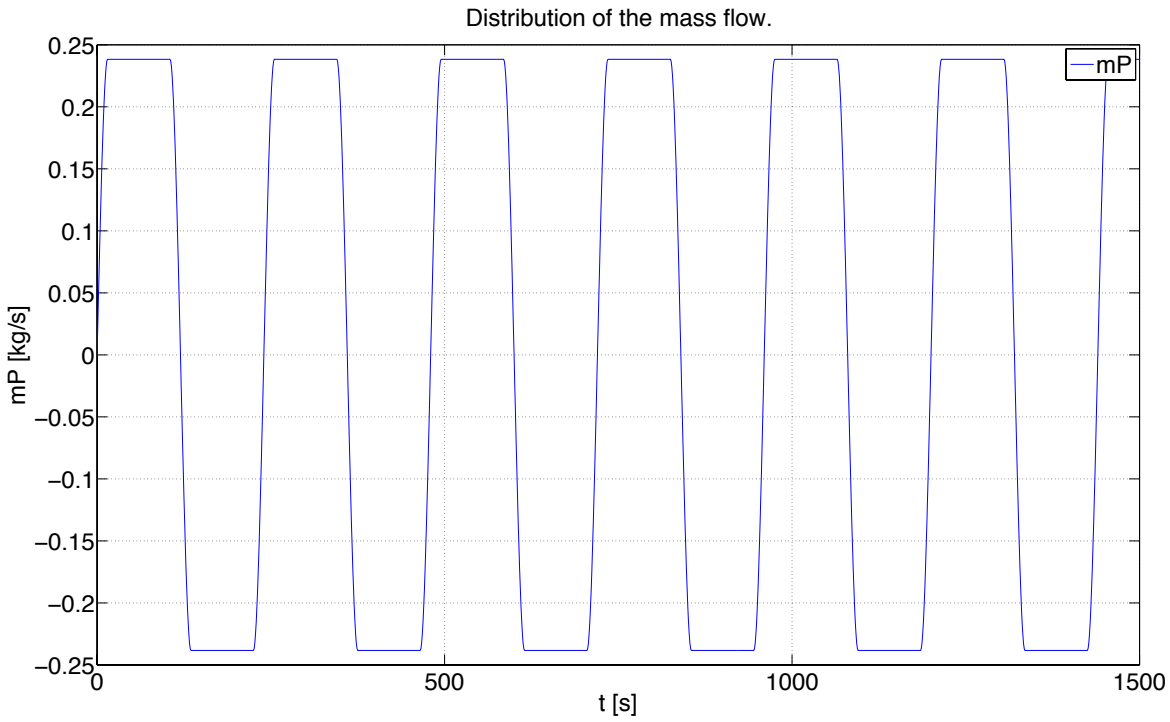

Figure 4.1.4: Distribution of the mass flow for the sensor simulation.

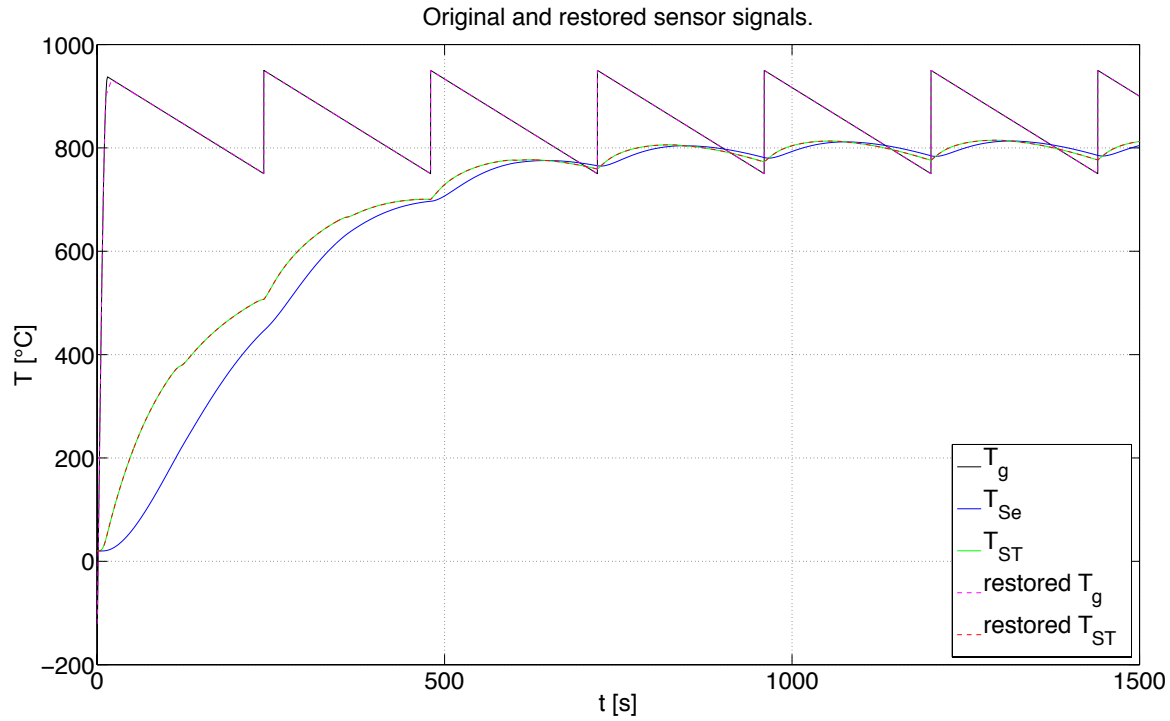

Figure 4.1.5: Distribution of original and restored temperature signals of the sensor model.

At the moment RTOs are not equipped with sensors, measuring the mass, respectively the volume flow through the plant. Under these circumstances one has to apply the heat transfer coefficient (see section 4.1.2.2) to a specific value of the absolute mass flow, e.g. $\dot{m} = 0.2383\text{kg/s}$ (cf. figure 4.1.3). As a result, the polynomial approach can be reduced to (e.g. by using *Matlab* function *polyfit*)

$$p_{h_{\text{ST}}} = a_1 T_g + a_5 \tag{4.1.34}$$

with coefficients $a_2 = a_3 = a_4 = 0$ (cf. equation (4.1.24)), as long as the mass flow is already considered in the coefficients a_1 and a_5.

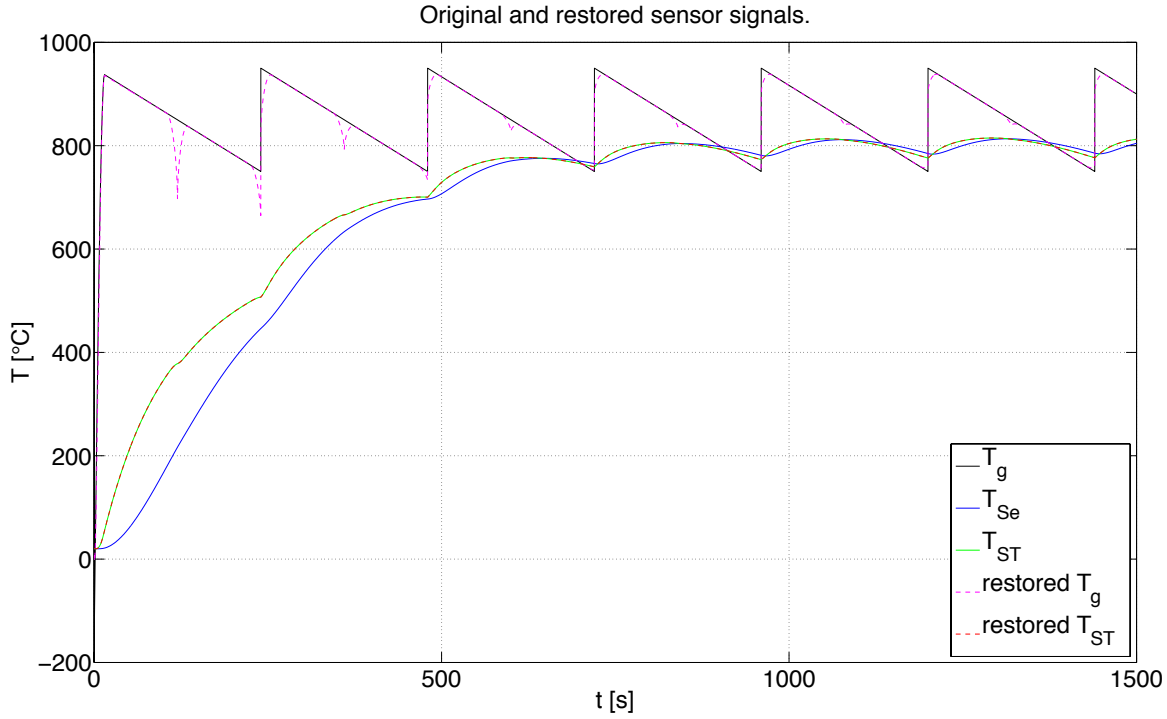

Figure 4.1.6: Distribution of original and restored temperature signals of the sensor model, whereas the approximation of the heat transfer coefficient h_{ST} was adapted to a single mass flow value of $\dot{m} = 0.2383\text{kg/s}$.

Figure 4.1.6 illustrates the error in the restoring of T_g at the time of the transition between RTO half cycles, as a consequence of the decreasing mass flow. Quite interesting is the fact that the peak, respectively the error at $t = 120\text{s}$ in the first half cycle is obviously more fatal than in the ongoing transition areas. Since the method for restoring signals is not dynamical, this phenomenon might be attributed to the rapidly changing values in the initial phase, as this can be seen in the temperature of the thermocouple T_{Se} and in the one of the steel tube T_{ST}.
In the (one might say) steady state of the plant (here t >1000s), where temperatures oscillate within small borders, corresponding with the cooling of the hot ceramic bed at $x_{\text{bed}} = 0$, the error of restoring ($< 15\text{K}$ in figure 4.1.7) is less fatal.

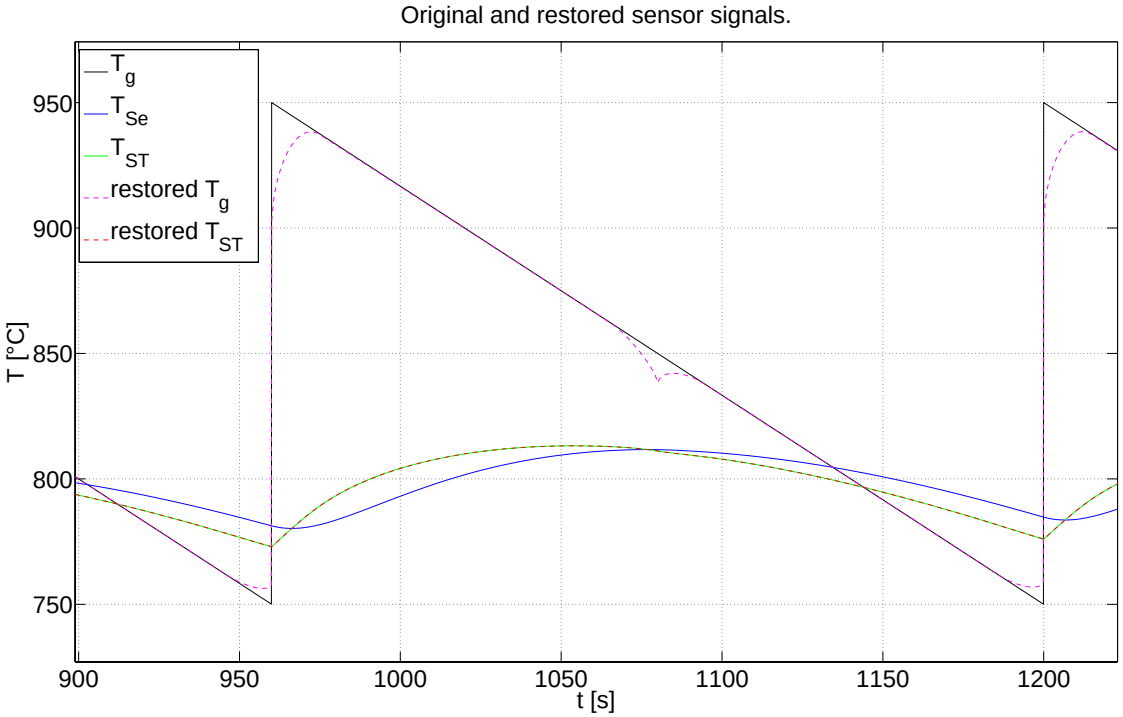

Figure 4.1.7: Zoom in figure 4.1.6 at one half cycle in imitated steady state of the RTO.

4.1.3.2 Configuration with Focus on the Approximation of Derivatives

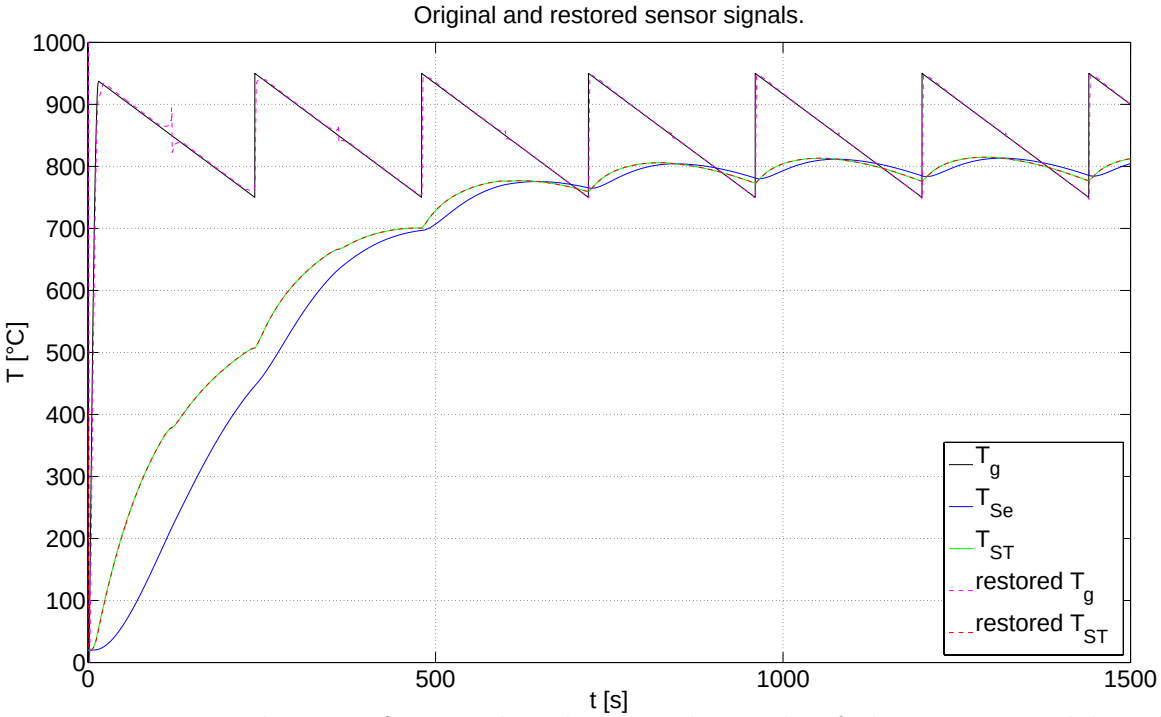

Figure 4.1.8: Distribution of original and restored signals of the sensor model with approximated derivatives (equation (4.1.33)), considering the change of the mass flow in the method of restoring.

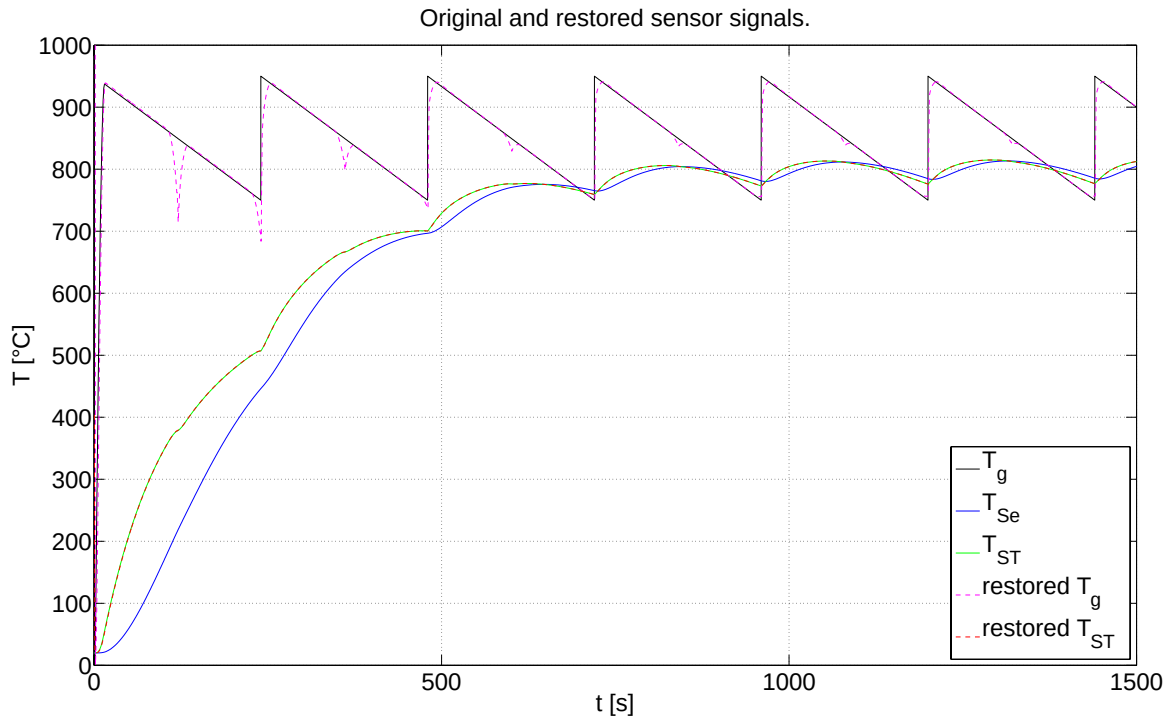

Figure 4.1.9: Distribution of original and restored signals of the sensor model with approximated derivatives (equation (4.1.33)), whereas the method of restoring (the heat transfer coefficient h_{ST}) was adapted to the mass flow $\dot{m} = 0.2383\mathrm{kg/s}$.

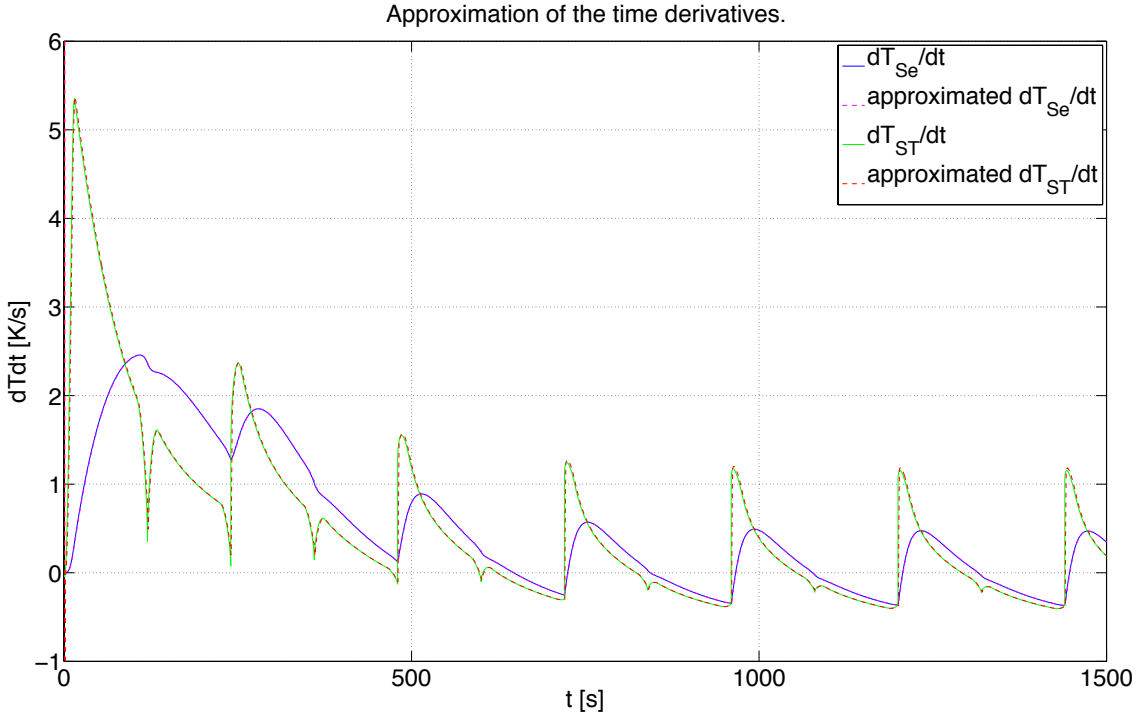

Figure 4.1.10: Approximation of the time derivatives of the temperatures according to equation (4.1.33).

In figures 4.1.8 and 4.1.9 the derivatives, occurring in the method of restoring (see section 4.1.2) are being approximated by a simple backward differential quotient (see section 4.1.2.4), whereas figure 4.1.10 illustrates the little difference between the exact and approximated derivatives, applying a sample time of $t_s = 1$s and using *Zero Order Hold* blocks for producing sampled inputs T_{Se} and $\dot{m}$ for the part, which is responsible for restoring.
Referring to figure 4.1.10, there only occurs a slight, almost invisible error between the red (approximated) and green (exact) distribution of the T_{ST}-derivative at the RTO half cycle switches (especially at $t = 120$s and $t = 240$s). This small deviations at $t = 120$s are sufficient for causing an error of $\sim$ 50K (figure 4.1.8) and $\sim$ 150K (figure 4.1.9), although one should be aware, that the error between the thermocouple and the real gas temperature is much more serious.
The reason for this sensitivity lies in the separated treatment of the restoring of T_{ST} in the first and T_g in the second step, whereas the derivative of T_{Se} appears in the calculation of T_{ST}. As the calculation of T_g demands the derivative of T_{ST}, the second order derivative of the thermocouple (of the actually measured quantity)

$$\frac{d^2 T_{\mathrm{Se}}}{dt^2} \rightarrow \frac{dT_{\mathrm{ST}}}{dt}$$

somehow occurs in the calculation of the gas temperature T_g. This is again a point where one has to indicate the need for caution, since the deriving of measured quantities, which certainly have some sort of high frequency background noise, can be seen to be quite problematic. This noise will undergo a significant gain, in particular in a second order derivative.

4.1.4 Résumé

The simulation results demonstrate that the real gas temperature can be restored out of the model of the temperature sensors somehow, although the knowledge of derivatives of the measured signals, as well as the knowledge of the mass flow is needed. The results should underline the effects of little deviations in these signals to the recalculated gas temperature.
If one should decide that the installation of sensors, which can measure the mass flow in the combustion chamber is too expensive, it may be sufficient to adapt the method of restoring (the heat transfer coefficient h_{ST}) to a reasonable value of $\dot{m}$ as shown (cf. figure 4.1.9). Furthermore, the approximation of derivatives occupies an even more significant position in the quality of the calculated gas temperature. Another important point remains the effect of radiation to these sensors, which seems to be the most uncertain in the sensor model (equation (4.1.17)) as the determination of the temperature $T_{cc,\mathrm{wall}}$, representative for the distribution of the temperature over the entire inner surface of the combustion chamber, is quite challenging.
To sum up, the need for measurement data and early test phases on the plant has been hopefully legitimated, otherwise further theoretical considerations are less advisable in this matter.

4.2 Further Sensors and Measurement Data

The temperature sensors in the ceramic bed presumably also feature a non-negligible response time and therefore a mathematical model could also be useful to determine more accurate values of the gas temperature near the bottom of the ceramic bed. The article [14] also presents a model for temperature sensors without the coverage of the thermocouple by a protective ceramic tube (cf. figure 4.1.1), which probably fits to the applied sensors in that area. Since this thesis focuses on control at the location of the combustion chamber, no other sensors are covered due to time and resource constraints.

As one will see in the following chapters dealing with control, it would be profitable to install sensors for measuring the concentration of the volatile organic compounds with the aim to be minimized. However, the demand of the knowledge of a decent value of the mass flow will be intensified by further considerations towards control purposes.
Again the necessity of verifying the mathematical model by measurement data should be emphasized. All values of the parameters were determined by research and empiric knowledge so far. I believe that with the optimization of a few parameters like $\alpha_{cc,\text{wall}}$ and $k_{ss,\text{loss}}$, adjusted to measurements by e.g. applying an objective function which minimizes the sum of least square errors, there is high potential in the model of the temperature sensors in equation (4.1.17). In many cases the use of a simple search algorithm, e.g. *Nelder and Mead* (function *fminsearch* in *Matlab*), without the need for the Jacobian of the objective function, leads to very useful parameter values.

5 Control

This thesis puts focus on the control of the gas temperature in the combustion chamber by adjusting the amount, more precisely the mass flow of the injected fuel substance, this means natural gas in case of the pilot plant. In order to take advantage of identified models for control, some sort of simplification had to be done, since the complexity of the entire model system hardly guarantees real-time capability.
The reduction to the submodel of the combustion chamber in terms of the simplification is obvious, whereas the two temperature sensors next to the burner (see section 4) should provide information of the current distribution of the gas temperature over space (of the combustion chamber). Simulation results have shown that the average of the two signals delivers a proper estimate for the real mean gas temperature $\overline{T}_{g,cc}$ over space x_{cc} (cf. equation (2.4.9)) due to the fact that the contribution of energy leads to a strictly monotonically increasing distribution of the gas temperature over subspace $\mathbb{B}$ of the combustion chamber (see section 2.5.2). This certainly implies that these signals deliver accurate values for the temperature at their location. Furthermore, it has shown that it might be a good idea to put some distance between these temperature sensors and the burner flame as radiation presumably most heavily affects the quality of the measurement data in that area.

5.1 Model Simplification for Control Purposes

The application of a stirring-tank reactor model, almost identical to the one used for the description of the valve boxes (see section 2.2) will provide a good approximation of the more sophisticated model using PDEs (2.4.1). Nevertheless, one should not entirely exclude the possibility to use PDEs for control, since modern RTOs feature fuel injections at various location points in the combustion chamber. This would demand the installation of additional temperature sensors to measure and to control (in a second step) the real distribution of the gas temperature over the space of the combustion chamber. *Panagiotis D. Christofides* as an example covers the issue of using models consisting of PDEs for the control of transport-reaction processes [18].

5.1.1 Combustion Chamber as Stirring-Tank Model

The way of representing the continuous stirred-tank model (cf. equation (2.2.1)) should help to distinguish between variables. There are input parameters, such as $\dot{m}$, $\dot{m}_{air}$, p_{in}, T_{amb}, input sources Φ_{in}, respectively $T_{g,in}$ (relation to the state variables), parameters

treated as constants M_{mix}, R_{id}, V_{cc}, HV, ΔH_R, A_{kin}, k_{loss}, $a^{cc}_{V,loss}$, E_a, broken rational functions $c_g(T_g)$, $c_{g,m}(T_{g,in})$ and quite important, the manipulated variable $\dot{m}_{fuel}$ for control of T_g.

$$\begin{aligned}\frac{dT_g}{dt} = \frac{1}{c_g(T_g)}\Bigg(&\left(\frac{|\dot{m}| + \dot{m}_{air}}{p_{in}}\right)\left(\frac{R_{id}}{V_{cc}M_{mix}}\right)\Big(T_g\big[c_{g,m}(T_{g,in})T_{g,in} - c_{g,m}(T_g)T_g\big]\Big) \\ &- \frac{1}{p_{in}}\left(\frac{R_{id}\,k_{loss}\,a^{cc}_{V,loss}}{M_{mix}}\right)T_g(T_g - T_{amb}) - \frac{\Delta H_R A_{kin}}{M_{mix}}\,\Phi\exp\left(\frac{-E_a}{R_{id}T_g}\right)\Bigg) \\ &+ \frac{1}{p_{in}}\left(\frac{HVR_{id}}{V_{cc}M_{fuel}M_{mix}}\right)\frac{T_g}{c_g(T_g)}\,\dot{m}_{fuel} \end{aligned} \tag{5.1.1a}$$

$$\frac{d\Phi}{dt} = \frac{|\dot{m}|}{p_{in}}\left(\frac{R_{id}}{V_{cc}M_{mix}}\right)T_g(\Phi_{in} - \Phi) - A_{kin}\,\Phi\exp\left(\frac{-E_a}{R_{id}T_g}\right) \tag{5.1.1b}$$

This ordinary differential equation delivers on the one hand a *single input single output* (SISO) and very interesting on the other hand an *affine input* (AI) system, although the actual goal will be to minimize the volume fraction Φ of a single material of *volatile organic compounds*, representative for the entire mixture of VOCs. This is one decisive disadvantage of all mathematical models in this thesis as actually one specific material of VOCs is considered as a reason of the *Arrhenius* law

$$r_g = -\frac{p_{in}}{R_{id}T_g}\Phi\,A_{kin}\exp\left(\frac{-E_a}{R_{id}T_g}\right)$$

adjusting the reaction rate r_g to one material by A_{kin} and E_a (as well as ΔH_R). At this point there already exist implemented models in *Matlab*, which consider up to ten different materials for reaction [2]. The high computational effort has to be remembered (see section 3.6), which will increase at least linearly with the number of coupled partial differential equations. The extension of this model by further chemical reactions for control remains open for future developments.

Equation (5.1.1) basically describes the temperature of the leaving gas, as well as the leaving volume fraction of VOCs from the combustion chamber, whereas the reduction from PDEs to ODEs comes along with the loss of location awareness. Let one assume that the mass flow enters the plant in side A and leaves in side B and then connect points in space of the combustion chamber to these sides, $x_{cc} = 0 \overset{\text{to}}{\rightarrow}$ A and $x_{cc} = L_{cc} \overset{\text{to}}{\rightarrow}$ B. Once the RTO switches its (half) cycle this connection still holds, although the mass flow enters in side B. Whereas the ordinary differential equations (5.1.1) are facing a problem, since former input values $T_{g,in}$ and Φ_{in} now become values of the state variables T_g and Φ for the moment in time when switching $\dot{m} \to 0$.

According to equations (5.1.1) it is worth mentioning that the rational function of the heat capacity c_g, as well as the one of the mean heat capacity $c_{g,m}$ do not have pole or zero points in a physically relevant range. The same applies to the absolute incoming pressure p_{in}, which also appears in the dominator.

For further considerations, constant and input parameters (not input sources) are com-

bined to coefficients

$$
\begin{aligned}
c_1 &:= \frac{(|\dot{m}| + \dot{m}_{air})R_{id}}{p_{in}M_{mix}V_{cc}} & c_4 &:= \frac{HVR_{id}}{p_{in}V_{cc}M_{fuel}M_{mix}} \\
c_2 &:= \frac{k_{loss}a^{cc}_{V,loss}R_{id}}{p_{in}M_{mix}} & c_5 &:= \frac{|\dot{m}|R_{id}}{p_{in}V_{cc}M_{mix}} \\
c_3 &:= \frac{\Delta H_R A_{kin}}{M_{mix}}
\end{aligned}
\tag{5.1.2}
$$

by being well aware that they will change over time (except c_3) in the simulation, although they can/will not considered to be explicit time functions. Now the two dimensional model

$$
\frac{d}{dt}\begin{bmatrix} T_g \\ \Phi \end{bmatrix} = \overbrace{\begin{bmatrix} \frac{1}{c_g(T_g)}\left(c_1 T_g\left[c_{g,m}(T_{g,in})T_{g,in} - c_{g,m}(T_g)T_g\right] - c_2 T_g(T_g - T_{amb}) - c_3\Phi\exp\left(\frac{-E_a}{R_{id}T_g}\right)\right) \\ c_5 T_g(\Phi_{in} - \Phi) - \Phi A_{kin}\exp\left(\frac{-E_a}{R_{id}T_g}\right) \end{bmatrix}}^{=:\mathbf{a}(T_g,\Phi)} + \underbrace{\begin{bmatrix} c_4\frac{T_g}{c_g(T_g)} \\ 0 \end{bmatrix}}_{=:\mathbf{b}(T_g)}\dot{m}_{fuel} \tag{5.1.3}
$$

which presents the basis for the control design, can be obtained. Thanks to the specific form of equation (5.1.3), input/output linearization will help to retain nonlinearities in the control law. One has to keep in mind that the reaction enthalpy ΔH_R is negative and thus the chemical reaction will certainly lead to an increase of the gas temperature.

5.2 Definitions

For ongoing operations one needs to define the *Lie* derivative of a scalar function $h(\mathbf{x})$, $h : \mathbb{R}^n \to \mathbb{R}$ along the vector field $\mathbf{f}(\mathbf{x})$, $\mathbf{f} : \mathbb{R}^n \to \mathbb{R}^n$

$$
L_{\mathbf{f}}(h) := \frac{\partial h}{\partial \mathbf{x}}\mathbf{f} = L^1_{\mathbf{f}}(h) \tag{5.2.1}
$$

and to extend this definition by the recursion

$$
\begin{aligned}
L^0_{\mathbf{f}}(h) &:= h \\
L^i_{\mathbf{f}}(h) &:= L_{\mathbf{f}}\left(L^{i-1}_{\mathbf{f}}(h)\right)
\end{aligned}
\tag{5.2.2}
$$

introducing the derivative of the scalar function $h(\mathbf{x})$ along the vector $\mathbf{x} = \begin{bmatrix} x_1 & \dots & x_n \end{bmatrix}^T$

$$
\frac{\partial h}{\partial \mathbf{x}} := \begin{bmatrix} \frac{\partial h}{\partial x_1} & \frac{\partial h}{\partial x_2} & \dots & \frac{\partial h}{\partial x_n} \end{bmatrix} \tag{5.2.3}
$$

and the derivative of the vector field $\mathbf{f}(\mathbf{x}) = \begin{bmatrix} f_1(\mathbf{x}) & \dots & f_n(\mathbf{x}) \end{bmatrix}^T$ along the vector $\mathbf{x}$

$$
\frac{\partial \mathbf{f}(\mathbf{x})}{\partial \mathbf{x}} := \begin{bmatrix} \frac{\partial f_1(\mathbf{x})}{\partial x_1} & \frac{\partial f_1(\mathbf{x})}{\partial x_2} & \dots & \frac{\partial f_1(\mathbf{x})}{\partial x_n} \\ \frac{\partial f_2(\mathbf{x})}{\partial x_1} & \frac{\partial f_2(\mathbf{x})}{\partial x_2} & \dots & \frac{\partial f_2(\mathbf{x})}{\partial x_n} \\ \vdots & \vdots & & \vdots \\ \frac{\partial f_n(\mathbf{x})}{\partial x_1} & \frac{\partial f_n(\mathbf{x})}{\partial x_2} & \dots & \frac{\partial f_n(\mathbf{x})}{\partial x_n} \end{bmatrix} \tag{5.2.4}
$$

which results in the Jacobian matrix. One will also take advantage of the *Lie bracket* of vector fields $\mathbf{g}(\mathbf{x})$, $\mathbf{g} : \mathbb{R}^n \to \mathbb{R}^n$ and $\mathbf{f}(\mathbf{x})$

$$\mathrm{ad}^1_{\mathbf{f}}(\mathbf{g}) \coloneqq \frac{\partial \mathbf{g}}{\partial \mathbf{x}}\mathbf{f} - \frac{\partial \mathbf{f}}{\partial \mathbf{x}}\mathbf{g} =: \big[\mathbf{f}(\mathbf{x}), \mathbf{g}(\mathbf{x})\big] \tag{5.2.5}$$

with the recursion

$$\begin{aligned} \mathrm{ad}^0_{\mathbf{f}}(\mathbf{g}) &\coloneqq \mathbf{g} \\ \mathrm{ad}^i_{\mathbf{f}}(\mathbf{g}) &\coloneqq \mathrm{ad}_{\mathbf{f}}\left(\mathrm{ad}^{i-1}_{\mathbf{f}}(\mathbf{g})\right). \end{aligned} \tag{5.2.6}$$

5.3 Analysis on a Full-State Feedback Linearization

The following consideration requires the vector fields $\mathbf{a}(\mathbf{x})$ and $\mathbf{b}(x_1)$ to be smooth, which is the case (cf. equation (5.1.3)). By introducing the state variable vector

$$\mathbf{x} = \begin{bmatrix} T_g \\ \Phi \end{bmatrix} = \begin{bmatrix} x_1 \\ x_2 \end{bmatrix} \tag{5.3.1}$$

and the manipulated variable $u = \dot{m}_{fuel}$, the aim to transform the AI system $\frac{d\mathbf{x}}{dt} = \mathbf{a}(\mathbf{x}) + \mathbf{b}(x_1)u$ into a chain of integrators

$$\dot{\mathbf{z}} = \frac{\partial \boldsymbol{\varphi}}{\partial \mathbf{x}}\big(\mathbf{a}(\mathbf{x}) + \mathbf{b}(x_1)u(\mathbf{x}, v)\big) = \begin{bmatrix} 0 & 1 \\ 0 & 0 \end{bmatrix}\mathbf{z} + \begin{bmatrix} 0 \\ 1 \end{bmatrix} v \tag{5.3.2}$$

by means of the transformation $\mathbf{z} = \boldsymbol{\varphi}(\mathbf{x})$ and the new input v, the new state variables $\mathbf{z}$ need to satisfy the conditions

$$\mathbf{z} = \begin{bmatrix} \varphi_1(\mathbf{x}) \\ L_{\mathbf{a}}(\varphi_1(\mathbf{x})) \\ L^2_{\mathbf{a}}(\varphi_1(\mathbf{x})) \\ \vdots \\ L^{n-1}_{\mathbf{a}}(\varphi_1(\mathbf{x})) \end{bmatrix} = \begin{bmatrix} \varphi_1(\mathbf{x}) \\ L_{\mathbf{a}}(\varphi_1(\mathbf{x})) \end{bmatrix} \qquad \begin{bmatrix} \varphi_1(\mathbf{x}) \\ L_{\mathbf{b}}(\varphi_1(\mathbf{x})) \\ L_{\mathbf{b}}L_{\mathbf{a}}(\varphi_1(\mathbf{x})) \\ \vdots \\ L_{\mathbf{b}}L^{n-2}_{\mathbf{a}}(\varphi_1(\mathbf{x})) \end{bmatrix} = \begin{bmatrix} \varphi_1(\mathbf{x}) \\ L_{\mathbf{b}}(\varphi_1(\mathbf{x})) \end{bmatrix} = \underline{0} \tag{5.3.3}$$

which would result in a system of first order partial differential equations

$$\frac{\partial \varphi_1}{\partial \mathbf{x}}\Big[\mathrm{ad}^0_{\mathbf{a}}(\mathbf{b}) \quad \mathrm{ad}_{\mathbf{a}}(\mathbf{b}) \quad \dots \quad \mathrm{ad}^{n-1}_{\mathbf{a}}(\mathbf{b})\Big] = \frac{\partial \varphi_1}{\partial \mathbf{x}}\Big[\mathbf{b} \quad \mathrm{ad}_{\mathbf{a}}(\mathbf{b})\Big] \overset{!}{=} \big[0 \quad \kappa(\mathbf{x}) \neq 0\big] \tag{5.3.4}$$

to solve. (Remark: Function $\kappa(\mathbf{x})$ can be considered arbitrary.) This would accomplish a full-state feedback linearization and simultaneously the ability to control not only the gas temperature, but also the concentration of the VOCs (respectively Φ) in the gas mixture. Though a different approach is taken in this thesis, **controllability** was analyzed.

5.3.1 Controllability in terms of a Full-State Feedback Linearization

Referring to a full-state feedback linearization the condition for controllability is equivalent with the existence of the transformation $\boldsymbol{\varphi}(\mathbf{x})$ [19], whereas the vectors $\mathbf{b}$ and $\mathrm{ad}_{\mathbf{a}}(\mathbf{b})$ need to be linearly independent, which is equivalent with the request for regularity of the controllability matrix

$$\mathbf{S}_u = \Big[\mathrm{ad}_{\mathbf{a}}^0(\mathbf{b}) \quad \dots \quad \mathrm{ad}_{\mathbf{a}}^{n-1}(\mathbf{b})\Big] = \Big[\mathbf{b} \quad \mathrm{ad}_{\mathbf{a}}(\mathbf{b})\Big]. \tag{5.3.5}$$

The *Lie* bracket of vector fields $\mathbf{a}$ and $\mathbf{b}$

$$\mathrm{ad}_{\mathbf{a}}(\mathbf{b}) = \frac{\partial \mathbf{b}}{\partial \mathbf{x}}\mathbf{a} - \frac{\partial \mathbf{a}}{\partial \mathbf{x}}\mathbf{b} \tag{5.3.6}$$

can be readily calculated by hand, but the determinant of $\mathbf{S}_u$ demands quite a lot computation steps. The computer algebra program *Mathematica* was used to determine the determinant

$$\det(\mathbf{S}_u) = \frac{1}{p_{in}^2}\left(\frac{HV^2\,R_{id}A_{kin}E_a}{V_{cc}^2 M_{fuel}^2 M_{mix}^2}\right)\frac{\Phi}{c_g(T_g)^2}\exp\left(\frac{-E_a}{R_{id}T_g}\right) - \frac{|\dot{m}|}{p_{in}^3}\left(\frac{HV^2\,R_{id}^3}{V_{cc}^3\,M_{fuel}^2\,M_{mix}^3}\right)\frac{T_g^2\,(\Phi_{in}-\Phi)}{c_g(T_g)^2} \neq 0 \tag{5.3.7}$$

which leads to the condition

$$p_{in}\big(V_{cc}M_{mix}A_{kin}E_a\big)\Phi\exp\left(\frac{-E_a}{R_{id}T_g}\right) - \dot{m}\,R_{id}^2\,T_g^2(\Phi_{in}-\Phi) \neq 0 \tag{5.3.8}$$

to be satisfied. It is quite interesting and intuitive that the concentration, respectively the volume fraction of VOCs can only be controlled when the incoming quantity Φ_{in} or/and the locally present Φ is greater zero (negative values do not have physical relevance). This result should on the one hand demonstrate the physical reference to control theory, on the other hand that the portion of harmful substances in the gas mixture could not only be minimized if there are sufficient high temperatures, but specific concentrations could be potentially targeted during run time. This certainly assumes that the transformation $\mathbf{z} = \boldsymbol{\varphi}(\mathbf{x})$ exists, whereas the system of partial differential equations needs to be solved analytically.

5.3.2 Existence of the Transformation

With the analysis of the solvability of first order homogenous partial differential equations, *G. Frobenius* argues with an *integrability* condition for differential systems, which leads to the **involution** of vector fields [21] [22] [23].

Definition: Distribution of Vector Fields. *The set of vector fields*

$$\boldsymbol{F}_d(\boldsymbol{x}) = \Big[\boldsymbol{f}_0(\boldsymbol{x}), \boldsymbol{f}_1(\boldsymbol{x}), \dots, \boldsymbol{f}_{n-2}\Big], \quad \operatorname{rank}\boldsymbol{F}_d = d, \quad \boldsymbol{x} \in \mathbb{R}^n$$

spans the distribution $\Delta_d(\boldsymbol{x})$ *of dimension* $d = \dim \Delta_d(\boldsymbol{x}) = \operatorname{rank} \boldsymbol{F}_d(\boldsymbol{x})$

$$\Delta_d(\boldsymbol{x}) = \operatorname{span}\{\boldsymbol{f}_0(\boldsymbol{x}), \boldsymbol{f}_1(\boldsymbol{x}), \ldots, \boldsymbol{f}_{n-2}\}, \quad \dim(\Delta_d) = d, \quad \boldsymbol{x} \in \mathbb{R}^n$$

which defines a d-dimensional vector space.

Definition: Involution. *The set of d linear independent vector fields* $\boldsymbol{f}_i(\boldsymbol{x}), i = 0, \ldots, d-1$*, respectively the corresponding distribution* $\Delta_d(\boldsymbol{x})$ *is called involutive if the Lie bracket of two vector fields can be represented as linear combination of vector fields of the distribution*

$$\left[\boldsymbol{f}_i(\boldsymbol{x}), \boldsymbol{f}_j(\boldsymbol{x})\right] = \sum_{k=0}^{n-2} \alpha_k(\boldsymbol{x}) \boldsymbol{f}_k(\boldsymbol{x}) \quad \forall i, j \tag{5.3.9}$$

considering linear coefficients α_k*, which can also be functions of state variables* $\boldsymbol{x}$*. The condition*

$$\operatorname{rank}\left\{\boldsymbol{F}_d(\boldsymbol{x}), \left[\boldsymbol{f}_i(\boldsymbol{x}), \boldsymbol{f}_j(\boldsymbol{x})\right]\right\} \stackrel{!}{=} \operatorname{rank} \boldsymbol{F}_d(\boldsymbol{x}) \quad \forall i, j \tag{5.3.10}$$

serves for the verification of the involution property.

The vector fields in matrix $\mathbf{F}_d$ can be replaced by the *Lie brackets* of smooth $\mathbf{a}(\mathbf{x})$ and $\mathbf{b}(x_1)$

$$\mathbf{f}_k = \operatorname{ad}_{\mathbf{a}}^k(\mathbf{b}) \quad \text{for} \quad k = 0, \ldots, n-2 \tag{5.3.11}$$

in conditions (5.3.9) and (5.3.10), which lead to a trivial condition to check for the model in equation (5.1.3) as the single vector $\mathbf{b}(x_1)$ is always involutive. However, this property guarantees the existence of a solution for the system of first order PDEs, which results out of equation (5.3.4).

5.3.3 Summary

The analysis on the possibility of applying a full-state feedback linearization shows that not only the gas temperature can be controlled, but also the volume fraction of at least one specific material of VOCs, which will be considered in the model for control purposes (5.1.3) if and only if the controllability condition (5.3.8) is satisfied.
As the currently installed sensors in the RTO completely lack any information about Φ, the focus is put on the control of T_g, whereas the solving of the PDEs out of equation (5.3.4) presents a quite demanding issue itself. The use of observers for obtaining information about Φ will be covered in the following sections, although the (currently) unknown input source Φ_{in} will cause serious problems.

5.4 Input/Output Linearization

In this section one will provide the linearization of the nonlinear system model in equation (5.1.3) by considering stable zero dynamics of an intern unobservable state (referring to Φ). This method demands the selection of an explicit output quantity, which certainly will be

$$y = T_g = x_1 = c(\mathbf{x}). \tag{5.4.1}$$

5.4.1 Relative Degree

One is searching for the lowest order derivative of y providing influence of the manipulated variable $u = \dot{m}_{fuel}$, which can be obtained by

$$\dot{y} = \dot{x}_1 = a_1(\mathbf{x}) + b_1(x_1)u \tag{5.4.2}$$

whereas the notation

$$\mathbf{a}(\mathbf{x}) = \begin{bmatrix} a_1(\mathbf{x}) \\ a_2(\mathbf{x}) \end{bmatrix} \qquad \mathbf{b}(x_1) = \begin{bmatrix} b_1(x_1) \\ 0 \end{bmatrix} \tag{5.4.3}$$

in reference to equation (5.1.3) was applied. Since $b_1 \neq 0$ for all reasonable x_1 the relative degree

$$r = 1 \tag{5.4.4}$$

can be specified, which will lead to an internal dynamic of degree $n - r = 1$ to be analyzed.

5.4.2 Diffeomorphism

The desired transformation $\begin{bmatrix} \mathbf{z} & \mathbf{w} \end{bmatrix}^T = \boldsymbol{\varphi}(\mathbf{x})$ with unobservable states $\mathbf{w} \in \mathbb{R}^{n-r}$ can be accomplished by the *Diffeomorphism*

$$\boldsymbol{\varphi}(\mathbf{x}) = \begin{bmatrix} c(\mathbf{x}) \\ L_{\mathbf{a}}(c(\mathbf{x})) \\ \vdots \\ L_{\mathbf{a}}^{r-1}(c(\mathbf{x})) \\ \hline \varphi_{r+1}(\mathbf{x}) \\ \vdots \\ \varphi_n(\mathbf{x}) \end{bmatrix} = \begin{bmatrix} x_1 \\ \varphi_2(\mathbf{x}) \end{bmatrix} = \begin{bmatrix} z_1 \\ w_1 \end{bmatrix} \tag{5.4.5}$$

whereas the determination of $\varphi_2(\mathbf{x})$ comes along with the condition for the Jacobian matrix

$$\frac{\partial \boldsymbol{\varphi}}{\partial \mathbf{x}} = \begin{bmatrix} 1 & 0 \\ \frac{\partial \varphi_2}{\partial x_1} & \frac{\partial \varphi_2}{\partial x_2} \end{bmatrix} \quad \curvearrowright \quad \frac{\partial \varphi_2}{\partial x_2} \overset{!}{\neq} 0 \tag{5.4.6}$$

to be regular. Furthermore, one will also make sure that the internal dynamic is independent from the manipulated variable.

$$\begin{aligned} L_{\mathbf{b}}(\varphi_2(\mathbf{x})) \overset{!}{=} 0 \quad &\curvearrowright \quad \frac{\partial \varphi_2}{\partial \mathbf{x}} \mathbf{b}(\mathbf{x}) = \begin{bmatrix} \frac{\partial \varphi_2}{\partial x_1} & \frac{\partial \varphi_2}{\partial x_2} \end{bmatrix} \begin{bmatrix} c_4 \frac{x_1}{c_g(x_1)} \\ 0 \end{bmatrix} \\ &\curvearrowright \quad \frac{\partial \varphi_2}{\partial x_1} c_4 \frac{x_1}{c_g(x_1)} \overset{!}{=} 0 \end{aligned} \tag{5.4.7}$$

One intuitively selects

$$\varphi_2(\mathbf{x}) = x_2 \tag{5.4.8}$$

which facilitates the interpretation of transformed states

$$\boldsymbol{\varphi} = \begin{bmatrix} \mathbf{z} \\ \mathbf{w} \end{bmatrix} = \begin{bmatrix} x_1 \\ x_2 \end{bmatrix} \tag{5.4.9}$$

as they are identical to the original states $\mathbf{x}$. If further materials of VOCs for reaction are considered, the model (5.1.3) needs to be extended by further states, e.g. Φ_A and Φ_B. As a result, the transformation leads to transformed states, which presumably will not equal to the original ones, thus the determination of $\mathbf{w} = \begin{bmatrix} \varphi_{r+1} & \dots & \varphi_n \end{bmatrix}^T$ will be presumably complicated as well.

5.4.3 Internal Dynamics

For controlling the gas temperature by taking advantage of the input/output linearized model, it is required that the internal dynamics are stable. Considering

$$\begin{aligned} \dot{w}_1 = \frac{d\Phi}{dt} &= c_5 x_1(\Phi_{in} - x_2) - x_2 A_{kin} \exp\left(\frac{-E_a}{R_{id} x_1}\right) \\ &= c_5 z_1(\Phi_{in} - w_1) - w_1 A_{kin} \exp\left(\frac{-E_a}{R_{id} z_1}\right) \end{aligned} \tag{5.4.10}$$

the dynamic of the unobservable (in terms of the linearization) state Φ, the exponential term of the *Arrenhius* law with negative sign represents a dominant part in favor of stability. However, the zero dynamics

$$\dot{\mathbf{w}}(\mathbf{z} = \underline{0}, \mathbf{w}) = \dot{w}_1(z_1 = 0, w_1) \to 0 \tag{5.4.11}$$

give less information on stability. One needs to shift the zero point of the state $z_1 = x_1 = T_g$ for more consequent arguments, since the aim to target $T_g = 0\text{K}$ is rather absurd. The usual reference temperatures in the combustion chamber are by about $850°\text{C} = 1123\text{K}$. The shifting will be achieved by the substitution of the transformed state z_1 with $\tilde{z}_1$ considering the initially unspecified temperature $T_0 > 273.15\text{K}$

$$\tilde{z}_1 = z_1 - T_0 \tag{5.4.12}$$

in order to aim $\tilde{z}_1 \to 0$. Consequentially, one obtains

$$\dot{w}_1 = c_5(\tilde{z}_1 + T_0)(\Phi_{in} - w_1) - w_1 A_{kin} \exp\left(\frac{-E_a}{R_{id}(\tilde{z}_1 + T_0)}\right) \tag{5.4.13}$$

which leads to the modified zero dynamic (note: $c_5 \geq 0, A_{kin} \ggg 0$)

$$\dot{w}_1(\tilde{z}_1 = 0, w_1) = -\left(c_5 T_0 + A_{kin} \exp\left(\frac{-E_a}{R_{id} T_0}\right)\right) w_1 + c_5 T_0 \Phi_{in}. \tag{5.4.14}$$

The condition

$$\Phi\left(c_5 T_0 + A_{kin} \exp\left(\frac{-E_a}{R_{id} T_0}\right)\right) \overset{!}{>} c_5 T_0 \Phi_{in} \tag{5.4.15}$$

reveals the good-natured character of the internal dynamic, since for all reasonable parameter values and T_0 the condition (5.4.15) holds and therefore guarantees stability. The result seems obvious as the portion of reactive substances will certainly decrease with the growing gas temperature. It might be reasonably assumed that in case of the consideration of further volume fractions of volatile organic compounds in the model (5.1.3) (e.g. $\Phi_A, \Phi_B, \ldots$), the internal dynamics remain stable, although the relative degree r will not change.

5.4.4 Linearized Model and State Feedback

By means of the input/output linearization the r^{th} order derivative of the chosen output $y = T_g$

$$\frac{d^r y}{dt^r} = L_{\mathbf{a}}^r(c(\mathbf{x})) + L_{\mathbf{b}} L_{\mathbf{a}}^{r-1}(c(\mathbf{x}))u = a_1(\mathbf{x}) + b_1(x_1)u = v \tag{5.4.16}$$

is set to be the new input v of the linearized model

$$\dot{z}_1 = v \tag{5.4.17}$$

with the transformed state $z_1 = T_g$ and thereby provides the law

$$u = \frac{v - a_1(\mathbf{x})}{b_1(x_1)} \tag{5.4.18}$$

for transformation of model (5.1.3) to model (5.4.17) by considering the stable internal dynamic in equation (5.4.10). To establish a control, the reference temperature T_{target} and the feedback of (one of) the measured gas temperature appear in the new input variable v

$$v = -kz_1 + V_{ref} T_{target} \tag{5.4.19}$$

considering the eigenvalue $-k$ of the linearized model, which needs to be chosen and a proportionality factor V_{ref}. This raises the question how to choose V_{ref} so that the output $y = T_g$ follows the reference T_{target} at least in steady state ($t \to \infty$). Initially assuming that T_{target} is constant, the demand

$$\lim_{t \to \infty} y(t) \stackrel{!}{=} T_{target} \tag{5.4.20}$$

leads to (notation: $\mathscr{L}\{y(t)\} = Y(s)$)

$$\lim_{s \to 0} sY(s) = \lim_{s \to 0} \frac{V_{ref}}{s + k} T_{target} \stackrel{!}{=} T_{target} \quad \curvearrowright \quad V_{ref} = k \tag{5.4.21}$$

the solution in the $\mathscr{L}$aplace domain.

5.5 Control Law

The first approach of the control law (note: $x_1 = T_g$ and $x_2 = \Phi$)

$$\boxed{\begin{aligned}\dot{m}_{fuel}(\mathbf{x}, T_{target}) = \frac{c_g(x_1)}{c_4 x_1} k(x_1 - T_{target}) + \frac{c_1}{c_4}\Big(c_{g,m}(x_1)x_1 - c_{g,m}(T_{g,in})T_{g,in}\Big) \\ + \frac{c_2}{c_4}(x_1 - T_{amb}) + \frac{c_3}{c_4}\left(\frac{x_2}{x_1}\right)\exp\left(\frac{-E_a}{R_{id}x_1}\right)\end{aligned}} \tag{5.5.1}$$

can be finally summarized, but it will undergo further processing in order to gain maximal performance. For example the eigenvalue

$$-k = -1.6 \tag{5.5.2}$$

has achieved quite good results in the simulation, at least when testing on the model (5.1.3) in steady state of the plant. The control law (5.5.1) can not only be considered to be a function of $\mathbf{x}$ and T_{target}, but also of all input parameters such as $\dot{m}, p_{in}, T_{amb}$ appearing in the coefficients c_1 to c_5 and in particular of the input source $T_{g,in}$. Besides, the dependency on the composition of the gas could be considered, as broken rational functions like c_g and $c_{g,m}$, as well as the molar mass M_{mix} depend on this composition (see section 2.1), which would require the knowledge of the exact amount of portions in the gas mixture. Although there might be an upgrade of existing plants by the equipment of additional sensors, this information presumably can not be entirely provided. As a consequence, these parameters are adapted to the main components of air (see table 6.1.1 and 6.1.2) assuming small portions of *volatile organic compounds* in the contaminated gas.

5.5.1 Consideration of a Time Variant Mass Flow

Simulation results have shown that the system is very sensitive during the RTO half cycle switches, causing the mass flow to change its direction through the plant, which provokes the change of the sign of $\dot{m}$. The problem is that the temperature sensors are such inert, so that they do not notice the rapid increase of T_g when the mass flow decreases and stops at the moment when switching $\dot{m} \to 0$, which should lead to the immediate decrease of the injected fuel substance $\dot{m}_{fuel}$. At the moment when switching the entire heat from the side of the combustion chamber, which was effected by the burner flame in the previous half cycle (subspace $\mathbb{B}$, see section 2.5.2), is transported to the other side of the combustion chamber causing far too high temperatures.
Although section 4.1.2 clearly describes the determination of the real gas temperature providing an explicit solution, the sampled approximation of the derivatives also leads to a significant delay in the restored T_g assuming a sample time of $t_s = 1s$ and a transition time of $t_{\text{trans}} = 3\text{s}$ between half cycles.

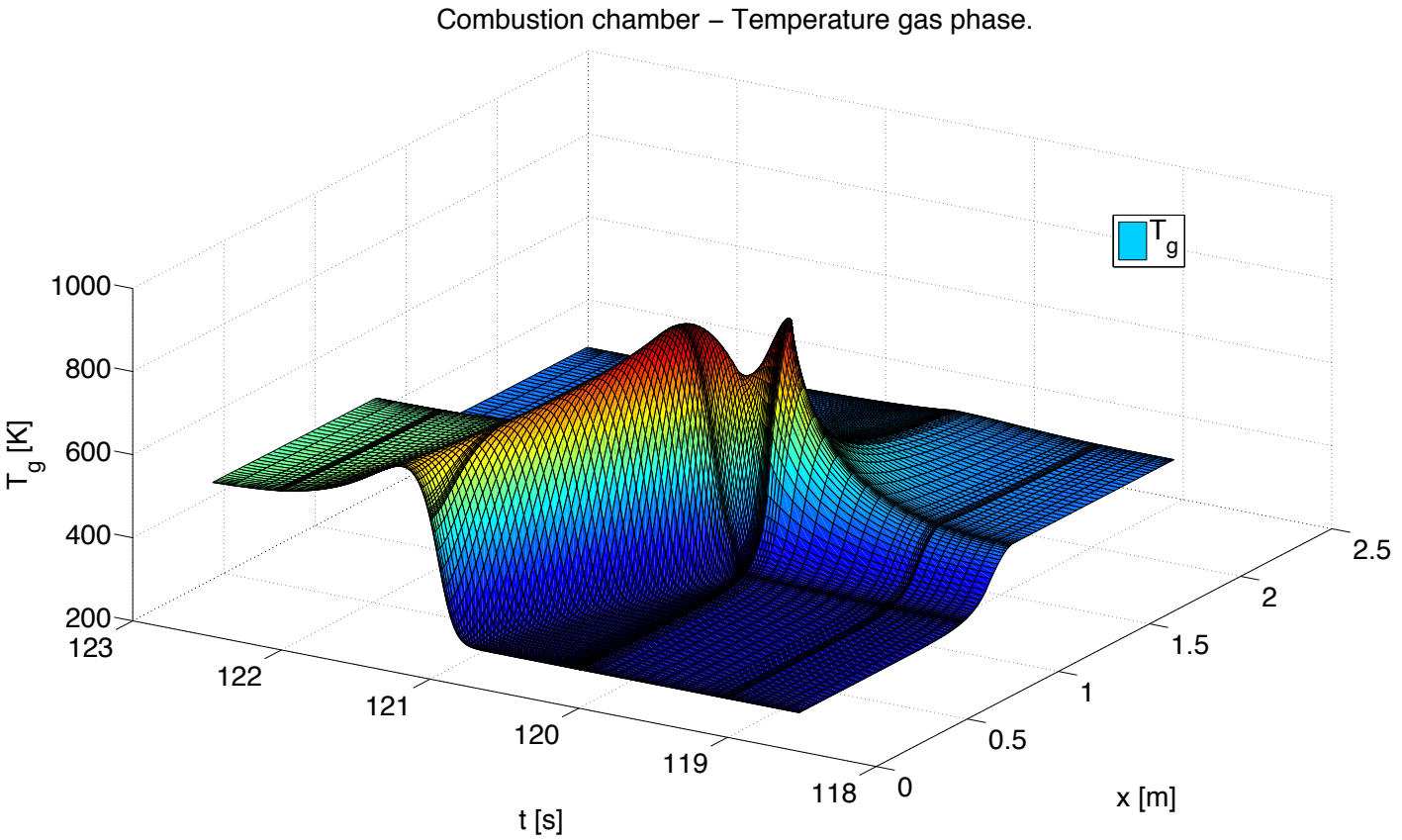

Figure 5.5.1: Distribution of T_g in the combustion chamber monitoring a RTO half cycle switch by applying the maximal amount fuel $u = \max\{\dot{m}_{fuel}\}$.

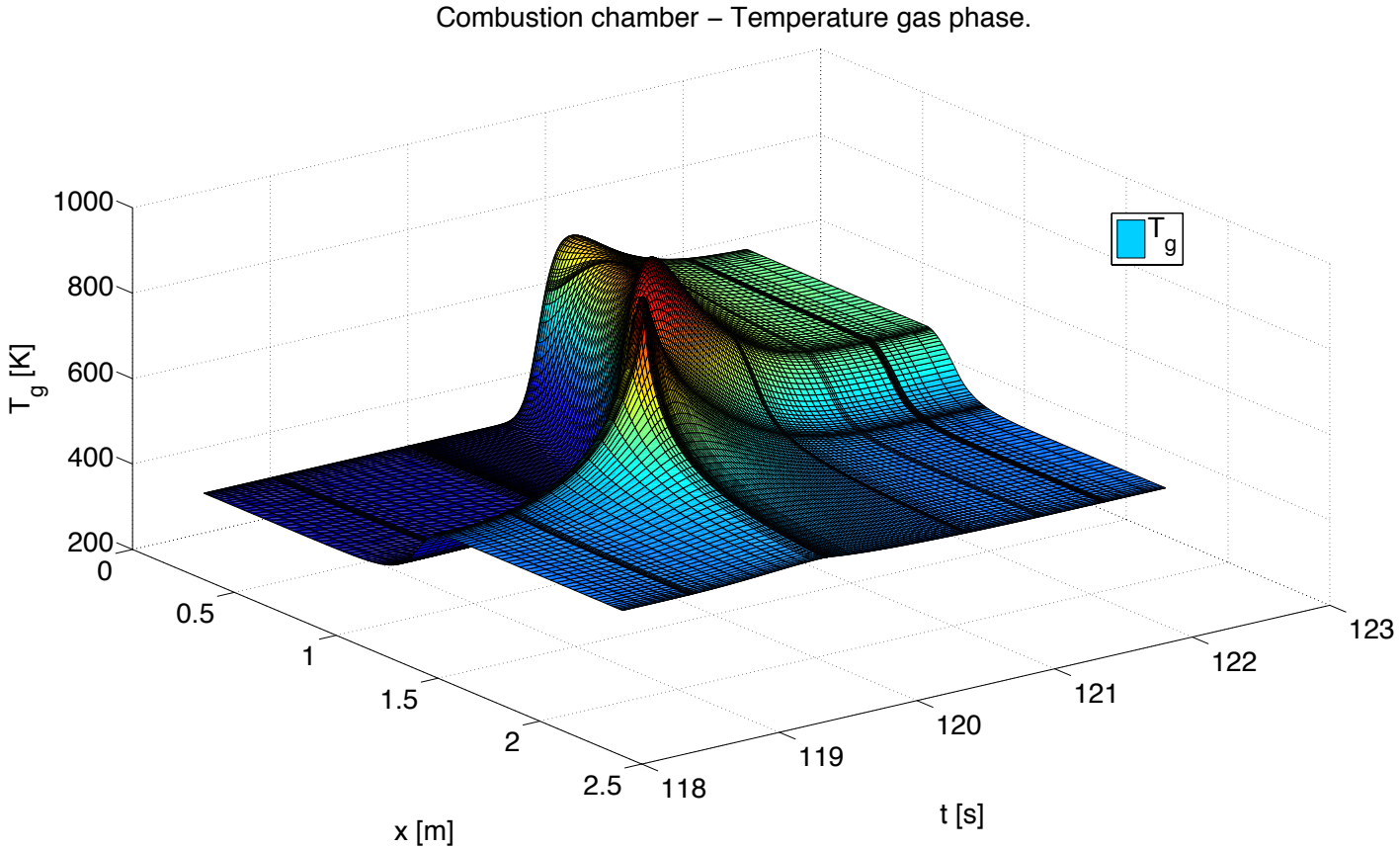

Figure 5.5.2: Different view of figure 5.5.1.

Figures 5.5.1 and 5.5.2 demonstrate the unpleasant effects in the solution T_g in the initially cold (at $t = 0$) combustion chamber while permanently feeding the maximal amount of fuel $\max\{\dot{m}_{fuel}\}$ to the burner during the transition in between RTO half cycles (switch at $t = 120$s). These effects have negative impact on the simulation time due to the significant change of values in a very small time window, which forces the solver algorithm to tighten step sizes. These overshooting will also occur when the reference temperature in the combustion chamber is already reached and then triggers unnecessary fuel consumption and consequentially causes the exceeding of desired temperatures, which can not be measured or restored out of sensor data in time. The kind of odd distribution of T_g at $t = 120$s displayed in figure 5.5.1 can be attributed to the fact that some inputs of the system are sampled, which also explains the small step sizes at every full second in simulation time.
In order to suppress these effects it will not be sufficient to consider only the time variant decrease of the mass flow during the transition in between RTO half cycles (appearing in the coefficients c_1 and c_5) in the control law, therefore a different approach has to be made. Intuitively, the decrease of the mass flow during switches according to section 3.5

$$\dot{m} = \dot{m}_{abs}\dot{m}_{switch}(t)$$

corresponding with

$$\tilde{t}(t,\tau) \coloneqq \left(t + \frac{t_{\text{trans}}}{2}\right) \pmod{\tau} \tag{5.5.3}$$

$$s(t,\tau) \coloneqq \operatorname{sign}\left(\sin\left(\frac{\pi}{\tau}t\right)\right) \tag{5.5.4}$$

$$\dot{m}_{switch}(t,\tau) = \begin{cases} s\left(t+\frac{t_{\text{trans}}}{2},\tau\right) p_{\dot{m}}(\tilde{t}) & \text{for} \quad 0 \le \tilde{t} < t_{\text{trans}} \\ s(t,\tau) & \text{for} \quad \frac{t_{\text{trans}}}{2} \le t \pmod{\tau} < \tau - \frac{t_{\text{trans}}}{2} \end{cases} \tag{5.5.5}$$

the polynomial $p_{\dot{m}}$ for transition (which should be replaced by a function based on measurements), the transition time t_{trans}, the period of half cycles τ and the new modified input $\dot{m}_{abs}$ are considered in the control law. $\dot{m}_{abs}$ should actually be replaced by sensor information assuming positive values (same applies for $\dot{m}_{air}$ and $\dot{m}_{fuel}$).

$$|\dot{m}| = \dot{m}_{abs}|\dot{m}_{switch}(t,\tau)|$$

The problem is that the polynomial $p_{\dot{m}}$ is only active in a small time window $t_{\text{trans}} \le 3$s and consequentially can not be accurately displayed in the manipulated variable with a sampling time of $t_s = 1$s. Since the fuel injection will be controlled by a valve, which can only change its position with a naturally continuous motion, it is assumed that $p_{\dot{m}}$ can be imprinted to the valve in charge of the fuel injection somehow. This presents again an issue demanding for more attention.
At least in the simulation the simple action (cf. figures 5.5.3 and 5.5.4)

$$u(\mathbf{x}, T_{target}, t, \tau) = \dot{m}_{fuel}(\mathbf{x}, T_{target})|\dot{m}_{switch}(t,\tau)| \tag{5.5.6}$$

successfully suppresses these unpleasant effects.

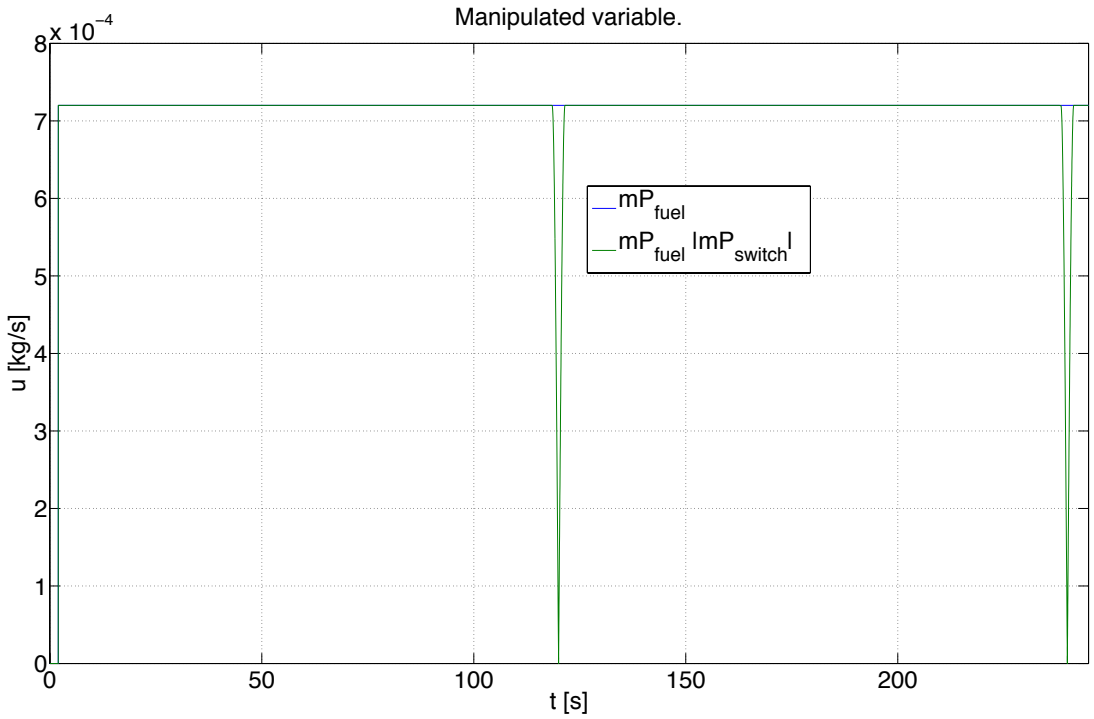

Figure 5.5.3: Choice of the manipulated variable to suppress unpleasant effects in the solution during RTO half cycle switches.

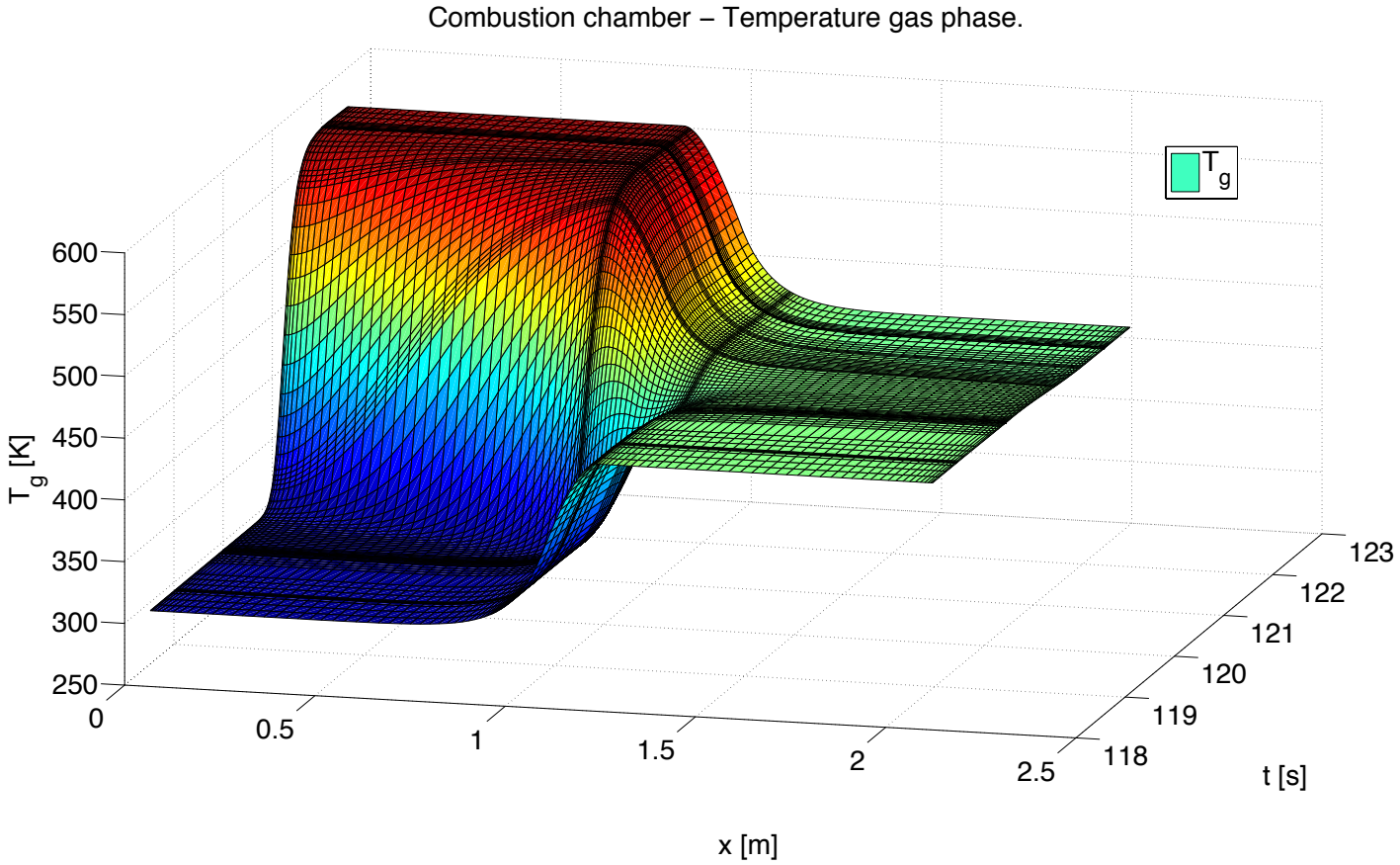

Figure 5.5.4: Heating of the combustion chamber in start-up phase considering a modified fuel injection $u = \dot{m}_{fuel}|\dot{m}_{switch}|$ during RTO half cycle switches (cf. figure 5.5.3).

Comparing figures 5.5.1 and 5.5.2 with figure 5.5.4 it can be seen that one should take advantage of the knowledge that unintended high temperatures occur during switches in the combustion chamber, which can not be measured in time, and use this information for modifying the control of the valve in charge of the fuel injection in order to save fuel. Due to time and resource constraints the inner control loop of this valve aiming to feed the desired fuel mass flow (given by the outer control law in equation 5.5.1) is not covered in this thesis.

5.5.2 Installation of an Integrator

Due to the simplification of the more accurate combustion chamber model (2.4.1) the simulation shows that there would remain an error between T_{target} and the measured (and restored) temperature(s) used as output value y for control when applying the control law in equation (5.5.1). The extension of x_1 by the state

$$\tilde{x} = \int_t (T_{target} - x_1)\, dt \tag{5.5.7}$$

aiming asymptotic stability

$$\dot{\tilde{x}} = T_{target} - x_1 \to 0 \tag{5.5.8}$$

by means of the linear state feedback $-kx_1 + \tilde{k}\tilde{x}$ (be aware $z_1 = x_1$) in equation (5.5.1), applying another proportionality factor $\tilde{k}$, will help to reduce this error. Since the linearized system (see section 5.4.4) describes

$$\begin{aligned} \dot{z}_1 &= v \\ \dot{x}_1 &= -kx_1 + kT_{target} + \tilde{k}\tilde{x} \end{aligned} \tag{5.5.9}$$

one obtains the following linear differential equation.

$$\begin{aligned} \frac{d}{dt}\begin{bmatrix} x_1 \\ \tilde{x} \end{bmatrix} &= \begin{bmatrix} -k & \tilde{k} \\ -1 & 0 \end{bmatrix}\begin{bmatrix} x_1 \\ \tilde{x} \end{bmatrix} + \begin{bmatrix} k \\ 1 \end{bmatrix} T_{target} \\ y &= x_1 \end{aligned} \tag{5.5.10}$$

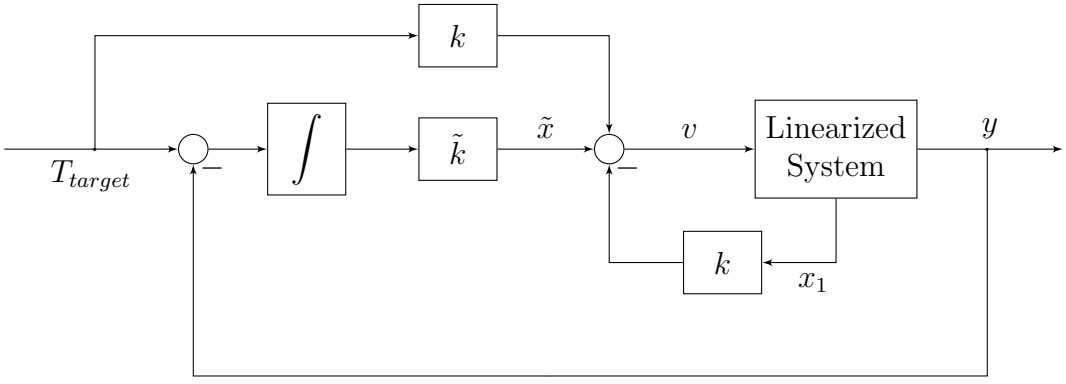

Figure 5.5.5: Block diagram of the linear control part.

The extended linear system can be written as follows

$$\begin{aligned}\frac{d}{dt}\begin{bmatrix}x_1\\ \tilde{x}\end{bmatrix} &= \left(\underbrace{\begin{bmatrix}0 & 0\\ -1 & 0\end{bmatrix}}_{=:\overline{\mathbf{A}}} + \underbrace{\begin{bmatrix}1\\ 0\end{bmatrix}}_{=:\overline{\mathbf{b}}}\underbrace{\begin{bmatrix}-k & \tilde{k}\end{bmatrix}}_{=:\overline{\mathbf{k}}^T}\right)\begin{bmatrix}x_1\\ \tilde{x}\end{bmatrix} + \begin{bmatrix}k\\ 1\end{bmatrix}T_{target}\\ y &= \begin{bmatrix}1 & 0\end{bmatrix}\begin{bmatrix}x_1\\ \tilde{x}\end{bmatrix}\end{aligned} \tag{5.5.11}$$

whereas the row vector $\overline{\mathbf{k}}^T$ serves for adjusting the eigenvalues of that system. Applying the determinant on the dynamic matrix of the closed loop in the $\mathscr{L}$aplace domain, the characteristic polynomial

$$\det\left(s\mathbf{I} - (\overline{\mathbf{A}} + \overline{\mathbf{b}}\overline{\mathbf{k}}^T)\right) = s(s+k) + \tilde{k} \tag{5.5.12}$$

delivers

$$s_{1,2} = -\frac{k}{2} \pm \sqrt{\left(\frac{k}{2}\right)^2 - \tilde{k}} \tag{5.5.13}$$

with the possibility not only to explicitly specify the eigenvalue s_1 of the dynamic of x_1, but the eigenvalue s_2 (or vice versa) of the error dynamic between the reference value T_{target} and x_1. For example $\overline{\mathbf{k}}$ can be specified using the *Matlab* command: $-\overline{\mathbf{k}}^T = \text{acker}\left(\overline{\mathbf{A}}, \overline{\mathbf{b}}, \begin{bmatrix}s_1 & s_2\end{bmatrix}\right)$. Simulation showed that with the chosen values

$$\overline{\mathbf{k}}^T = \begin{bmatrix}1.6 & 0.5\end{bmatrix} \tag{5.5.14}$$

corresponding with the eigenvalues

$$s_1 = -1.1742 \qquad s_2 = -0.4258 \tag{5.5.15}$$

quite good results could be accomplished in steady state of the RTO.

5.5.3 Anti Wind-Up Method

The application of the method in section 5.5.2 to the control law (5.5.1) comes along with the drawback that in case the manipulated variable reaches its saturation $u \in [u_{min}, u_{max}]$, the error between reference T_{target} and state x_1 keeps being integrated. After u would have to leave this saturation due to the reduction of $e = T_{target} - x_1$, or even the change of the sign of $T_{target} - x_1$ (overshooting), the integrated error first needs to be decreased by integrating towards zero. In particular during the start-up phase of the plant (thinking of a step response from $y = 20°\text{C}$ to $y = 850°\text{C}$) this would cause uncontrollable overshooting of the gas temperature and as a consequence the complete unnecessary consumption of fuel. Using the values in equation (5.5.14) for control, it turned out that they lead to a quite aggressive reaction in the manipulated variable in case $y \neq T_{target}$. Furthermore, it highlighted that the control would have to distinguish between the different half cycles, so the integrated error in the first half cycle should/must not be used for the second one and vice versa!

It is preferable to completely suppress every form of wind-up by enabling the integrator of state $\tilde{x}$ only when the manipulated variable is not in saturation $u \neq u_{min} = 0$ kg/s or $u \neq u_{max} = 7.2 \cdot 10^{-4}$ kg/s and to simultaneously reset the integrator at the **falling edge** when reaching one of these limitations.
The link of the connection between the saturation of u and the ports of the integrator would provoke the occurrence of an algebraic loop, which was suppressed by simple placing a delay element in between. See figure 5.8.1, which properly demonstrates the applied methods in order to control the gas temperature in the combustion chamber.

5.6 Selection of the Control Variable

Current plants of CTP with two, or more bed configurations are equipped with two temperature sensors (see chapter 4) next to the burner in the combustion chamber. The actual aim of the control is to establish a stable average, respectively mean gas temperature over the space of the combustion chamber to guarantee a certain amount of decomposition of VOCs. A single burner in the center of the combustion chamber in reference to the pilot plant is in charge of the desired heating.
There is the problem that only one part (one half) of the combustion chamber can be heated in the appropriate half cycle as the mass flow $\dot{m}$ determines the direction of the burner flame according to its flow (cf. figure 5.5.4), which means that the gas temperature of the other half of the combustion chamber will be mainly affected by the ceramic temperature at the top of the bed, which heats the incoming gas of the RTO. The gas temperature in that half of the combustion chamber will certainly decrease almost linearly as a consequence of the cooling of the ceramic bed for the half cycle period.
Furthermore, the consideration of a combustion chamber model consisting of ODEs (5.1.3) comes along with the loss of location awareness as explained in section 5.1.1, which would require the compensation of the error in integrator states after switching, especially in the observer (see section 5.7).

5.6.1 Mean Gas Temperature

In order to overcome the issue concerning integrator states one could aim to control the real mean gas temperature in the combustion chamber

$$\overline{T}_{g,cc} = \frac{1}{L_{cc}} \int_{x_{cc}=0}^{L_{cc}} T_g(x_{cc}, t) dx \tag{5.6.1}$$

in both half cycles of the two-bed RTO, which would demand its estimation from the two processed sensor signals. Simulation results show (see section 6) that the linear average

$$y = \overline{T}_{g,cc} \approx \frac{T_{ss,0} + T_{ss,L}}{2} \tag{5.6.2}$$

of the two processed temperature sensor signals $T_{ss,0}$ and $T_{ss,L}$ (in the way that the original gas temperatures $T_{g,1}$ and $T_{g,2}$ at the location of the sensors are restored of

thermocouple temperatures $T_{\mathrm{Se},1}$ and $T_{\mathrm{Se},2}$) by taking advantage of the sensor model in equation (4.1.17) (see section 4.1.2), represent a sufficiently accurate value for the real integral quantity $\overline{T}_{g,cc}$, which was already discussed in the introduction of chapter 5.
As the model applied for control (5.1.3) describes the leaving gas temperature $y = T_g(x_{cc} = L_{cc}, t)$ (or $y = T_g(x_{cc} = 0, t)$, depending on the half cycle) of the combustion chamber and not the mean value $\overline{T}_{g,cc}$, the reference quantity T_{target} would have to be adjusted. So in case one aims to establish e.g. $\overline{T}_{g,cc} = 850°\mathrm{C}$ by applying

$$\overline{T}_{g,cc} = \frac{T_{g,in} + T_{target}}{2} \tag{5.6.3}$$

to the permanently changing reference

$$T_{target} = 2\overline{T}_{g,cc} - T_{g,in} \tag{5.6.4}$$

the request on the control concept is very high and consequentially results in a strong change of the manipulated variable. It is worth mentioning that the incoming gas temperature $T_{g,in}$ as well as y (as output quantity of the closed control loop) need to be switched between the processed sensor signals $T_{ss,0}$ and $T_{ss,L}$ corresponding with the sign of the mass flow $\dot{m}$, respectively with the RTO half cycles. For example, assuming the sensors with corresponding values $T_{ss,0}$ at $x_{cc} = 0$ and $T_{ss,L}$ at $x_{cc} = L_{cc}$ the definition

$\dot{m} > 0$	$\dot{m} < 0$
$y = T_{g,out} = T_{ss,L}$	$y = T_{g,out} = T_{ss,0}$
$T_{g,in} = T_{ss,0}$	$T_{g,in} = T_{ss,L}$

Table 5.6.1: Definition of the input source and the output considered for control.

holds. One should be aware that the cooling of the unaffected half of the combustion chamber by the burner will cause the related heating of the other half of the combustion chamber by the increase of T_{target} as an effect of the dropping input source $T_{g,in}$ (inside of one half cycle of the RTO).

5.6.2 Output Temperature of the Combustion Chamber

One should also consider being content with the control of the temperature of one half of the combustion chamber, tolerating the slow cooling of $\overline{T}_{g,cc}$ inside of one RTO half cycle as a consequence of the cooling of the ceramic bed. This concept demands less from the control method and does not provoke such a strong change of the manipulated variable. This would allow the reference e.g.

$$T_{target} = 850°\mathrm{C} \tag{5.6.5}$$

to remain constant (in case of a step response), whereas y and $T_{g,in}$ need to be switched according to table 5.6.1. Nevertheless, the issue with wrong integrator states at RTO half cycle switches (mentioned in the introduction of section 5.6) takes place when applying this concept.

5.7 Observer

The plants are currently not equipped with any sensors measuring the portion of VOCs in the gas mixture, whereas the simulation (see chapter 6) demonstrates that this knowledge could substantially improve the control of *Regenerative Thermal Oxidizers*. Although there might be an upgrade of sensor systems in future developments, it is very unlikely that such sensors will be placed in the combustion chamber or at the top of the ceramic beds.
For that reason there is no way to avoid the application of an observer (or estimator), estimating one or more appropriate concentrations, or volume fractions of VOCs at the location of the combustion chamber based on the measured temperatures in that area. By analyzing the model (5.1.3) it can be recognized that the still unknown input source Φ_{in} will cause the major problem in this approach. In this thesis it has to be assumed that either plants will be equipped with the appropriate sensors or that the dynamic behavior of the temperatures in the area of the ceramic bed (already available) could give information of Φ_{in}, whereas the combination of both concepts would certainly deliver the most reliable information. Due to the intensive effort for the other aspects in this thesis, there was no time left to occupy with this subject.

5.7.1 Observability

The existence of the invertibility of transformation

$$\mathbf{z} = \mathbf{q}(\mathbf{x}, u) = \begin{bmatrix} y \\ \dot{y} \\ \vdots \\ y^{(n-1)} \end{bmatrix} = \begin{bmatrix} x_1 \\ a_1(\mathbf{x}) + b(x_1)u \end{bmatrix} = \begin{bmatrix} z_1 \\ z_2 \end{bmatrix} \tag{5.7.1}$$

so that the state variable vector can be expressed by transformed states and the manipulated variable (and its derivatives in case $n > 2$)

$$\mathbf{x} = \mathbf{q}^{-1}(\mathbf{z}, u) \tag{5.7.2}$$

guarantees global observability [20] in the domain $\mathbf{x} \in D_{\mathbf{x}}$ and $u \in D_{\mathbf{u}}$ (satisfying the invertibility), assuming real numbers for $\mathbf{x} \in \mathbb{R}^n$ and $u \in \mathbb{R}$. Obtaining

$$\mathbf{x} = \begin{bmatrix} z_1 \\ \frac{1}{c_3} \exp\left(\frac{E_a}{R_{id} z_1}\right) \left(c_1 z_1 \left[c_{g,m}(T_{g,in}) T_{g,in} - c_{g,m}(z_1) z_1 \right] - c_2 z_1 (z_1 - T_{amb}) - c_g(z_1) z_2 + c_4 z_1 u \right) \end{bmatrix} \tag{5.7.3}$$

it becomes evident that the leaving Φ of the combustion chamber can be theoretically determined in the entire relevant range, despite using initially unspecified functions $c_g(T_g)$ and $c_{g,m}(T_g)$ (see section 2.1) and even if the manipulated variable equals zero $u = 0$. This is a remarkable result and can be presumably also accomplished when using more state variables $\Phi_A, \Phi_B, \ldots$ as a reason of the linearity in Φ, although the appearance of derivatives of u in $\mathbf{z} = \mathbf{q}(\mathbf{x}, u, \dot{u}, \ldots, u^{(n-1)})$ would significantly aggravate the determination of $\mathbf{x} = \mathbf{q}^{-1}(\mathbf{x}, u, \dot{u}, \ldots, u^{(n-1)})$.

5.7.2 Normal Form of the Nonlinear Observer

The transformation to the normal form for nonlinear observers

$$\begin{aligned}\dot{\mathbf{z}} = \begin{bmatrix} z_2 \\ \varphi\left(\mathbf{z}, u, \dot{u}\right) \end{bmatrix} &= \underbrace{\begin{bmatrix} 0 & 1 \\ 0 & 0 \end{bmatrix}}_{=:\hat{\mathbf{A}}} \mathbf{z} + \underbrace{\begin{bmatrix} 0 \\ 1 \end{bmatrix}}_{=:\hat{\mathbf{b}}} \varphi\left(\mathbf{z}, u, \dot{u}\right) \\ y = z_1 &= \underbrace{\begin{bmatrix} 1 & 0 \end{bmatrix}}_{=:\hat{\mathbf{c}}^T} \mathbf{z}\end{aligned} \tag{5.7.4}$$

aims a system basically consisting of a chain of integrators, whereas the nonlinearities of the original system are gathered in function

$$\begin{aligned}\varphi(\mathbf{x}, u, \dot{u}) = \dot{z}_2 = \frac{\partial(a_1(\mathbf{x}) + b_1(x_1)u)}{\partial \mathbf{x}}(\mathbf{a}(\mathbf{x}) + \mathbf{b}(x_1)u) + \frac{\partial b_1(x_1)}{\partial \mathbf{x}}\dot{u} \\ \varphi(\mathbf{z}, u, \dot{u}) = \varphi\left(\mathbf{q}^{-1}(\mathbf{z}, u), u, \dot{u}\right)\end{aligned} \tag{5.7.5}$$

appearing at the end of that chain. Thanks to the structure of the normal form in equation (5.7.4) and the output value $y = x_1 = z_1$, this system is always observable [20]. The existence of the invertibility of the transformation in equation (5.7.3) is therefore sufficient for the proof of global observability. The retransformation of the system in equation (5.7.4) to the original one makes it possible to avoid the computation of function $\varphi(\mathbf{z}, u, \dot{u})$.

5.7.3 High-Gain Feedback

In the first step one provides a copy of the transformed system

$$\dot{\hat{\mathbf{z}}} = \hat{\mathbf{A}}\hat{\mathbf{z}} + \hat{\mathbf{b}}\varphi\left(\hat{\mathbf{z}}, u, \dot{u}\right) \tag{5.7.6}$$

and ensures that the copy will follow the real (transformed) system by applying the feedback of the error between the real output $y = x_1 = z_1$ and the copy

$$\dot{\hat{\mathbf{z}}} = \hat{\mathbf{A}}\hat{\mathbf{z}} + \hat{\mathbf{b}}\varphi\left(\hat{\mathbf{z}}, u, \dot{u}\right) + \boldsymbol{\ell}(\epsilon)(y - \hat{\mathbf{c}}^T\hat{\mathbf{z}}) \tag{5.7.7}$$

considering the vector

$$\boldsymbol{\ell}(\epsilon) = \begin{bmatrix} \epsilon^{-1} & 0 \\ 0 & \epsilon^{-2} \end{bmatrix} \begin{bmatrix} l_1 \\ l_2 \end{bmatrix} = \mathbf{D}^{-1}(\epsilon)\mathbf{l} \tag{5.7.8}$$

with the parameter ϵ, which should be adjusted to the noise of the (restored) sensor signal. When analyzing the dynamic of the error

$$\dot{\mathbf{e}} = \dot{\mathbf{z}} - \dot{\hat{\mathbf{z}}} \tag{5.7.9}$$

after applying their system definitions in equation (5.7.4) and (5.7.7)

$$\dot{\mathbf{e}} = \left(\hat{\mathbf{A}} - \boldsymbol{\ell}(\epsilon)\hat{\mathbf{c}}^T\right)\mathbf{e} + \hat{\mathbf{b}}(\varphi\left(\mathbf{z}, u, \dot{u}\right) - \varphi\left(\hat{\mathbf{z}}, u, \dot{u}\right)) \tag{5.7.10}$$

one puts focus on the dynamic matrix of the linear part in the first place, which can be written as follows:

$$\hat{\mathbf{A}} - \mathbf{D}^{-1}(\epsilon)\mathbf{l}\hat{\mathbf{c}}^T = \begin{bmatrix} -l_1\epsilon^{-1} & 1 \\ -l_2\epsilon^{-2} & 0 \end{bmatrix} \tag{5.7.11}$$

The characteristic polynomial of this matrix

$$\det\left(s\mathbf{I} - (\hat{\mathbf{A}} - \mathbf{D}^{-1}(\epsilon)\mathbf{l}\hat{\mathbf{c}}^T)\right) = s^2 + \frac{l_1}{\epsilon}s + \frac{l_2}{\epsilon^2} \tag{5.7.12}$$

leads to the transformed eigenvalues (notation: $\lambda \coloneqq \epsilon s$)

$$\lambda_{1,2} = -\frac{l_1}{2} \pm \sqrt{\left(\frac{l_1}{2}\right)^2 - l_2}. \tag{5.7.13}$$

of the linear part of the dynamic matrix of the observer error. Finally one can see that this part is asymptotically stable in case the chosen eigenvalues $\lambda_{1,2}$ have a negative real part. It is shown on pages 540 to 542 in [21] that the error made by the nonlinear part

$$\hat{\mathbf{b}}(\varphi(\mathbf{z}, u, \dot{u}) - \varphi(\hat{\mathbf{z}}, u, \dot{u})) \tag{5.7.14}$$

of the dynamic $\dot{\mathbf{e}}$ in the observer rapidly decays with growing ϵ.

5.7.4 Transformation to Original States

The aim in this subsection is to obtain an observer estimating the original states, which receive the notation $\hat{\mathbf{x}}$. Therefore one recapitulates, the *Diffeomorphism* (achieved by the equations (5.7.1) to (5.7.3))

$$\hat{\mathbf{z}} = \mathbf{q}(\hat{\mathbf{x}}, u) \quad \text{and} \quad \hat{\mathbf{x}} = \mathbf{q}^{-1}(\hat{\mathbf{z}}, u) \tag{5.7.15}$$

provided the system transformation

$$\dot{\hat{\mathbf{z}}} = \frac{d\mathbf{q}(\hat{\mathbf{z}}, u)}{dt} = \frac{\partial \mathbf{q}}{\partial \hat{\mathbf{x}}}\dot{\hat{\mathbf{x}}} + \frac{\partial \mathbf{q}}{\partial u}\dot{u} \stackrel{!}{=} \hat{\mathbf{A}}\hat{\mathbf{z}} + \hat{\mathbf{b}}\varphi(\hat{\mathbf{z}}, u, \dot{u}) + \boldsymbol{\ell}(\epsilon)(y - \hat{\mathbf{c}}^T\hat{\mathbf{z}}) \tag{5.7.16}$$

into a chain of integrators. When manipulating the second and third expression on the right hand side of equation (5.7.17) the left part of formulation

$$\dot{\hat{\mathbf{x}}} = \left(\frac{\partial \mathbf{q}}{\partial \hat{\mathbf{x}}}\right)^{-1}\left(\hat{\mathbf{A}}\hat{\mathbf{z}} + \hat{\mathbf{b}}\varphi(\hat{\mathbf{z}}, u, \dot{u}) - \frac{\partial \mathbf{q}}{\partial u}\dot{u}\right) + \left(\frac{\partial \mathbf{q}}{\partial \hat{\mathbf{x}}}\right)^{-1}\boldsymbol{\ell}(\epsilon)(y - \hat{\mathbf{c}}^T\hat{\mathbf{z}}) \tag{5.7.17}$$

leads to the original system.

$$\left(\frac{\partial \mathbf{q}}{\partial \hat{\mathbf{x}}}\right)^{-1}\left(\hat{\mathbf{A}}\hat{\mathbf{z}} + \hat{\mathbf{b}}\varphi(\hat{\mathbf{z}}, u, \dot{u}) - \frac{\partial \mathbf{q}}{\partial u}\dot{u}\right) = \mathbf{a}(\mathbf{x}) + \mathbf{b}(x_1)u \tag{5.7.18}$$

Consequentially, one finally obtains the *High-Gain Observer* for the original AI system.

$$\boxed{\dot{\hat{\mathbf{x}}} = \mathbf{a}(\hat{\mathbf{x}}) + \mathbf{b}(\hat{x}_1)u + \left(\frac{\partial \mathbf{q}(\hat{\mathbf{x}}, u)}{\partial \hat{\mathbf{x}}}\right)^{-1}\boldsymbol{\ell}(\epsilon)(y - \hat{y})} \tag{5.7.19}$$

As shown in equation (5.7.19), the desired estimation of states can be achieved by providing the following partial derivatives

$$\left(\frac{\partial \mathbf{q}(\mathbf{x},u)}{\partial \mathbf{x}}\right)^{-1} = \begin{bmatrix} 1 & 0 \\ \frac{\partial q_2}{\partial x_1} & \frac{\partial q_2}{\partial x_2} \end{bmatrix}^{-1} = \begin{bmatrix} 1 & 0 \\ -\frac{\partial q_2}{\partial x_1}\left(\frac{\partial q_2}{\partial x_2}\right)^{-1} & \left(\frac{\partial q_2}{\partial x_2}\right)^{-1} \end{bmatrix} \tag{5.7.20}$$

in the inverted Jacobian matrix of the transformation directive $\mathbf{q}(\mathbf{x},u)$. One obtains the expressions

$$\begin{aligned} \frac{\partial q_2}{\partial x_1} = \frac{1}{c_g(x_1)}\Bigg(c_1\left(c_{g,m}(T_{g,in})T_{g,in} - 2x_1 c_{g,m}(x_1) - x_1^2\frac{dc_{g,m}(x_1)}{dx_1}\right) + c_2(T_{amb} - 2x_1) - \\ c_3\frac{E_a}{R_{id}}\frac{x_2}{x_1^2}\exp\left(\frac{-E_a}{R_{id}x_1}\right) + c_4 u - \frac{dc_g(x_1)}{dx_1}(a_1(\mathbf{x}) + b_1(x_1)u)\Bigg) \end{aligned} \tag{5.7.21}$$

$$\frac{\partial q_2}{\partial x_2} = -\frac{c_3}{c_g(x_1)}\exp\left(\frac{-E_a}{R_{id}x_1}\right) \tag{5.7.22}$$

consisting of the derivatives

$$c_g'(x_1) = \frac{dc_g(x_1)}{dx_1} \quad \text{and} \quad c_{g,m}'(x_1) = \frac{dc_{g,m}(x_1)}{dx_1}$$

which can be explicitly provided easily (see section 2.1).

5.7.5 Configuration

In the simulation the values

$$\lambda_1 = -70 \qquad \lambda_2 = -70 \qquad \epsilon = 0.5 \tag{5.7.23}$$

delivered quite good results, whereas the parameter ϵ should be adjusted to the background noise of the (restored - see chapter 4) sensor signal $y = x_1$. It turned out that the observer is very sensitive by compensating the error made by wrong initial states of $\hat{x}_2 = \hat{\Phi}$. It may occur that the integrator state of $\hat{x}_2$ becomes tremendously big before decaying to the real value. This phenomenon might be attributed to the fact that the exponential term

$$\exp\left(\frac{E_a}{R_{id}T_g}\right)$$

appears in the expression $\hat{\mathbf{x}} = \mathbf{q}^{-1}(\mathbf{z},u)$ in equation (5.7.3) and in the inversion of $\frac{\partial q_2(\mathbf{x})}{\partial x_2}$, which directly affects the observer in equation (5.7.19). This term literally explodes in case the gas temperature is too small. Hence, this observer state (respectively the entire observer) should only be activated if the gas has already reached a certain temperature range

$$x_1 > 650°\mathrm{C} = T_{enable}$$

which was considered in the simulation (see chapter 6). Due to the fact that the composition of VOCs starts at higher temperatures anyway, the error when setting $\hat{x_2} = \hat{\Phi} = 0$

for temperatures smaller than $x_1 \leq T_{enable}$ in the control law (5.5.1) is negligible as a result of the weak reaction heat. The interaction of all methods applied for control should become more comprehensible when analyzing figure 5.8.1.

In addition to these settings, the application of a factor α_Φ (see section 3.4) for reducing and preventing numerical issues, which will occur due to the high range difference between temperatures and volume gas portions, is highly recommended. It significantly supports convergence and accuracy of the algorithm solving the dynamic system (in equation (5.7.19)) of the observer.

5.8 Structural Overview

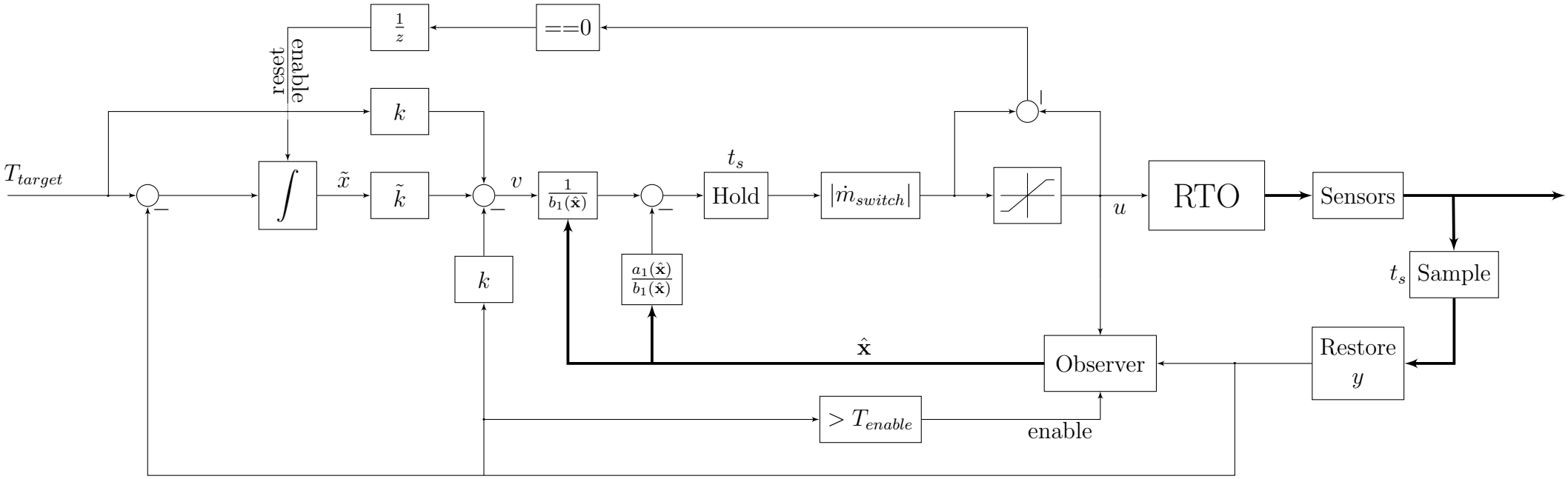

Figure 5.8.1: Block diagram of the loop controlling the gas temperature in the combustion chamber, whereas the potential measurement of further quantities (e.g. $\dot{m}, p, T_{amb}, T_{g,in} \ldots$), which should also be applied in the control loop, is not displayed. The processing of the output quantity y for control (cf. table 5.6.1) considering different sensor signals and the recalculation of original gas temperatures (according to section 4.1.2) are combined in the block *Restore y*.

5.9 Résumé

As shown in chapter 6, the applied methods deliver promising results in the simulation compared to the former PID controller, whose parameters are not based on the mathematical modelling of the plant and controls the gas temperature by means of the real sensor signals T_{Se} (of the thermocouples), which presumably cause serious sustained deviations from the real reference temperatures in the combustion chamber (cf. section 4.1.3). The concept can be considered to be the first sophisticated model based approach for a highly accurate temperature control. Due to the lack of time and resources this thesis does not occupy with measurements and test phases on the plant. However, it needs to be mentioned that the verification of the models in chapter 2, which presents the basis for the control design, was already done by *Thomas Rieger* [1] [2], at least partially.

The valve in charge of the injection of the desired fuel mass flow $\dot{m}_{fuel}$, which serves as the manipulated variable in the developed control concept, certainly demands the modelling of an additional system to be installed in the simulation. This system presumably features some sort of low-pass behavior, which filters the sampled value for the manipulated variable (cf. figure 5.8.1). Section 5.5.1 illustrates that the inner control loop should be equipped with the appropriate method to prevent that the desired temperatures in the combustion chamber exceed at half cycle switches, which inevitably leads to unnecessary consumption of fuel. This would require a time variant, considerably faster control and consequentially much faster sampling.

If it is decided to apply this concept to the plants of CTP, it is advisable to optimize the eigenvalues of the linearized system in the state feedback by means of a LQR - Linear Quadratic Regulator and to do further analysis on the parameters, respectively on the eigenvalues (see equation (5.7.23)) of the observer. There may be a possibility to exploit the observer for estimating the error between the control variable y and the reference T_{target} and one could consequentially leave the integrator (see section 5.5.2) and the anti wind-up method from the concept.

Furthermore, I believe that the concept could be extended by additional materials for reaction, which would lead to the consideration of further state variables $\Phi_A, \Phi_B, \ldots$ in the model for control purposes (5.1.3). This paper includes comments on used methods with the aim to provide additional information for a potential application in future developments.

6 Simulation

The simulation on the simplified model of the combustion chamber in equation (5.1.3) and on the entire system including all complex models in chapter 2 serves for the evaluation of the control methods presented in chapter 5.

6.1 General Configuration

6.1.1 System

The **composition of the gas** is adapted to the main components of air

Volume Fraction	Value	Component
x_{O2}	0.21	oxygen
x_{N2}	0.78	nitrogen
x_{Ar}	0.01	argon

Table 6.1.1: Volume fractions.

Mass Fraction	Value	Component
w_{O2}	0.232	oxygen
w_{N2}	0.7542	nitrogen
w_{Ar}	0.0138	argon

Table 6.1.2: Mass fractions.

for the parameters M_{mix}, η_g, λ_g, c_g, $c_{g,m}$ and consequentially for ρ_g (see section 2.1) during simulation. All **initial states** at $t_0 = 0$s of RTO components, as well as of the two temperature sensors and the observer

Valve Boxes	
$T_g(t_0)$	20°C
$\Phi(t_0)$	0

Ceramic Beds	
$T_s(t_0, x_l)$	20°C $\forall l$
$T_g(t_0, x_l)$	20°C $\forall l$
$\Phi(t_0, x_l)$	0 $\forall l$

Combustion Chamber	
$T_g(t_0, x_l)$	20°C $\forall l$
$\Phi(t_0, x_l)$	0 $\forall l$

Temperature Sensors	
$T_{\mathrm{ST}}(t_0)$	20°C
$T_{\mathrm{Se}}(t_0)$	20°C

Observer	
$\hat{T}_g(t_0)$	20°C
$\hat{\Phi}(t_0)$	0
T_{enable}	650°C
$\hat{\Phi}(\hat{T}_g < T_{enable})$	0

Table 6.1.3: Initial states and configuration of components.

are adapted to ambient conditions. The input parameters, reference quantities and design parameters

Parameter	**Value**	**Description**
T_{target}	850°C	reference temperature of the combustion chamber in the area of the burner
$\overline{T}_{g,cc}$	850°C	reference mean gas temperature of the combustion chamber over space
T_{amb}	20°C	ambient temperature
p_{in}	101325Pa	absolute input pressure of the RTO/CC
$T_{g,in}$	60°C	temperature of the incoming raw gas of the RTO/CC
Φ_{in}	$5 \cdot 10^{-4}$	incoming volume fraction of VOCs of the RTO/CC
τ	120s	RTO half cycle period
$\dot{m}_{air}$	0.0124kg/s	portion of air added to the fuel mass flow
$\dot{m}_{abs} = \dot{m}_{max}$	0.2383kg/s	incoming raw gas flow of the RTO/CC
t_{trans}	3s	transition time between RTO half cycle switches
t_s	1s	sample time
u_{max}	$7.2 \cdot 10^{-4}$kg/s	upper limit of the fuel mass flow
u_{min}	0kg/s	lower limit of the fuel mass flow

Table 6.1.4: Input, reference and design parameters of the RTO.

are held constant unless otherwise stated. The switching in between **RTO half cycles** was simulated by the time variant decrease of the mass flow $\dot{m} = \dot{m}_{abs}\dot{m}_{switch}$ according to the method described in section 3.5 (cf. figure 3.5.1).

Furthermore, the location points of the two considered **temperature sensors**

$$x_{cc} = 0 \qquad \text{and} \qquad x_{cc} = L_{cc}$$

in the combustion chamber were assumed when dealing with the PDEs (2.4.1). When simulating the combustion chamber by means of the simplified model for control purposes (equation (5.1.1)) in section 6.2, only one sensor model (according to equation (4.1.17)) for the output gas temperature $T_{g,out}$ is used in the feedback loop.

6.1.2 Control

The consideration of a time variant mass flow in the control concept according to section 5.5.1 was a bit modified as the multiplication with $|\dot{m}_{switch}(t,\tau)|$ (see equation (5.5.6)) would demand the complete, sharp turn off of fuel, respectively of the manipulated variable u at t (mod τ). This causes the burner flame to go out and as a consequence the ignition of the burner would be required after each half cycle switch. In order to avoid this effect the decrease of the absolute value of the considered polynomial (according to the definition in equations (5.5.3) to (5.5.5))

$$|\dot{m}_{switch}| \overset{!}{\geq} 0.25 \tag{6.1.1}$$

is being held when it reaches 25%. This means that only a quarter of the calculated $\dot{m}_{fuel}$ in the control law (cf. equation (5.5.1) including the integrator, introduced in section 5.5.2) will be fed to the burner shortly before and after half cycle switches. Compare figures 6.1.1 and 5.5.3.

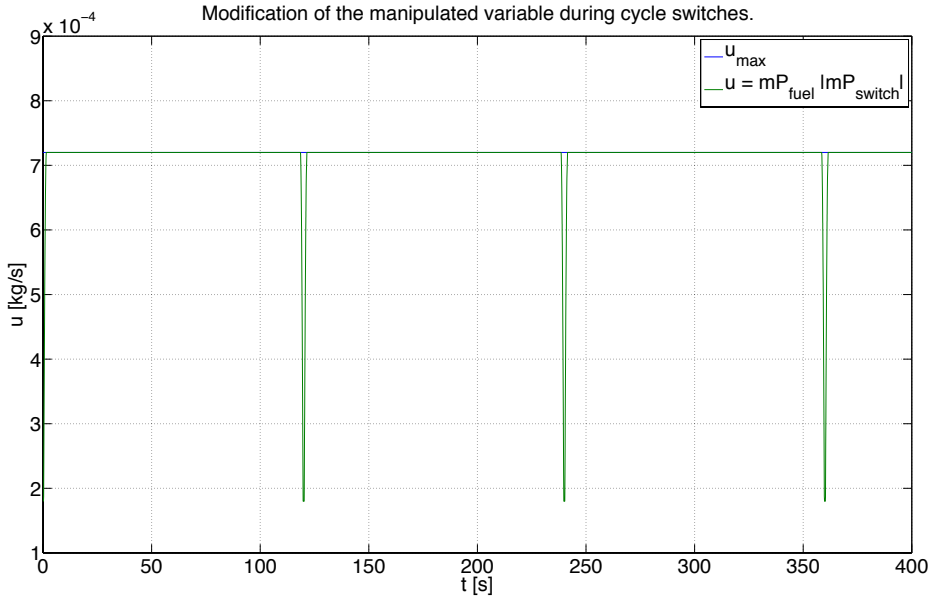

Figure 6.1.1: Modification of $\dot{m}_{switch}$.

It is preferable to distinguish between start-up and steady state of the plant, when dealing with the **eigenvalues** s_1 and s_2 of the **linearized system**, which can be adjusted by the vector $\overline{\mathbf{k}}^T = \begin{bmatrix} k & \tilde{k} \end{bmatrix}$ (see section 5.5.2). The values

$$\overline{\mathbf{k}}^T = \begin{cases} \begin{bmatrix} 0.6 & 0.1 \end{bmatrix} & \text{for} \quad y < 700°\text{C} \\ \begin{bmatrix} 1.6 & 0.5 \end{bmatrix} & \text{for} \quad y \geq 700°\text{C} \end{cases} \tag{6.1.2}$$

have delivered quite good results when aiming to establish the temperature $T_{target} = 850°\text{C}$. In reference to the **observer** (introduced in section 5.7) the following values are used.

$$\lambda_1 = -70 \qquad \lambda_2 = -70 \qquad \epsilon = 0.5 \tag{6.1.3}$$

6.2 Simplified Model of the Combustion Chamber

This section presents results of the simulation on the temperature control of the stirring-tank reactor model (5.1.1), which should reflect the combustion chamber.
As no other components of the plant are part of this simulation, the incoming gas temperature $T_{g,in}$ has to be somehow increased over time, when one wants to reach $T_{target} = 850°C$ in the combustion chamber model. The ceramic beds actually undertake the task of gradually increasing the incoming gas temperature to the combustion chamber. In the start-up phase of the plant the reference T_{target} will be increased linearly with a slope of five degrees per minute $\frac{5}{60}$ [K/s], which should prevent the ceramic beds to be harmed by a too rapid rise of temperatures.
To simplify matters, it is assumed that the incoming gas temperature rises linearly from $T_{g,in} = 20°C$ to $T_{g,in} = 750°C$ with the same slope of $\frac{5}{60}$ [K/s] and a time delay of $10\tau = 1200s$ to T_{target}. This produces a permanent distance of 100K (for $t > 1200s$) between $T_{g,in}$ and T_{target} to be compensated by the burner.

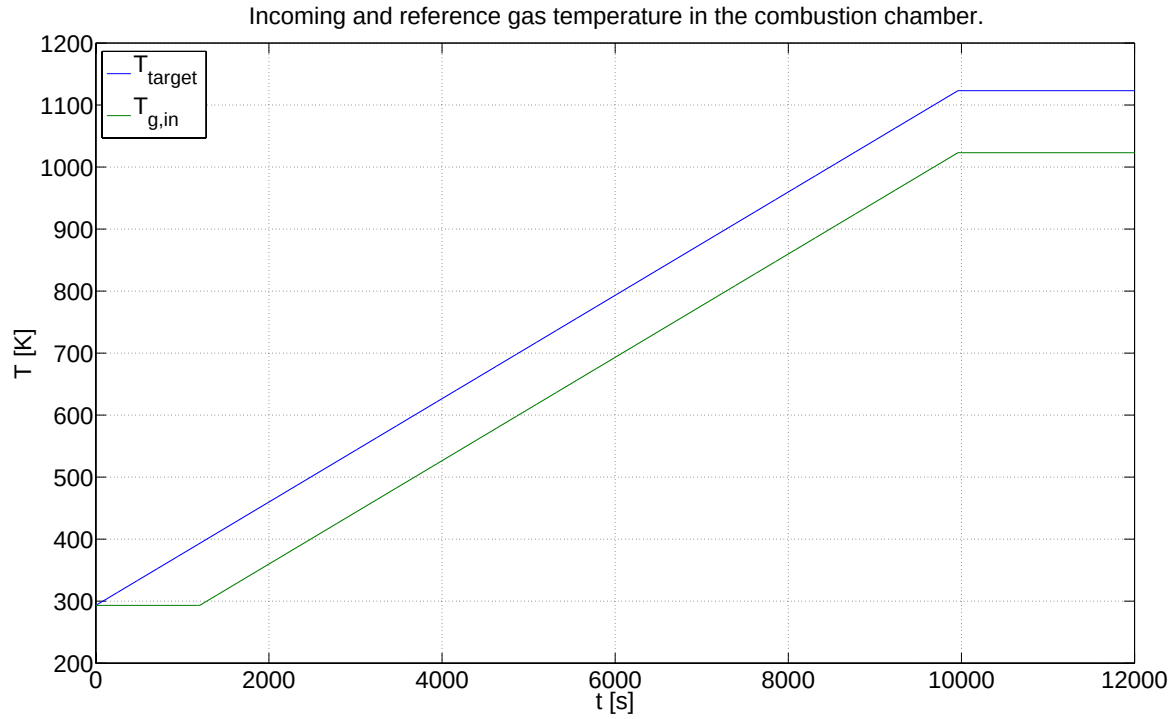

Figure 6.2.1: Incoming and reference gas temperature.

Due to time constraints this section exclusively deals with the control of the output gas temperature $T_{g,out}$ of the combustion chamber according to section 5.6.2. This temperature represents a proper estimate for the distribution of the temperature over the space between subspace $\mathbb{B}$ (equation (2.5.3)) and the end of the combustion chamber ($x_{cc} = 0$ if $\dot{m} < 0$ and $x_{cc} = L_{cc}$ if $\dot{m} > 0$) - see figure 6.3.10.
To visualize the effect of the **observer** estimating Φ (respectively Φ_{out}), it will be activated earlier when reaching $y \geq 400°C$, although $T_{enable} = 650°C$ remains the recommended value (cf. table 6.1.4).

6.2.1 Constant Input Parameters

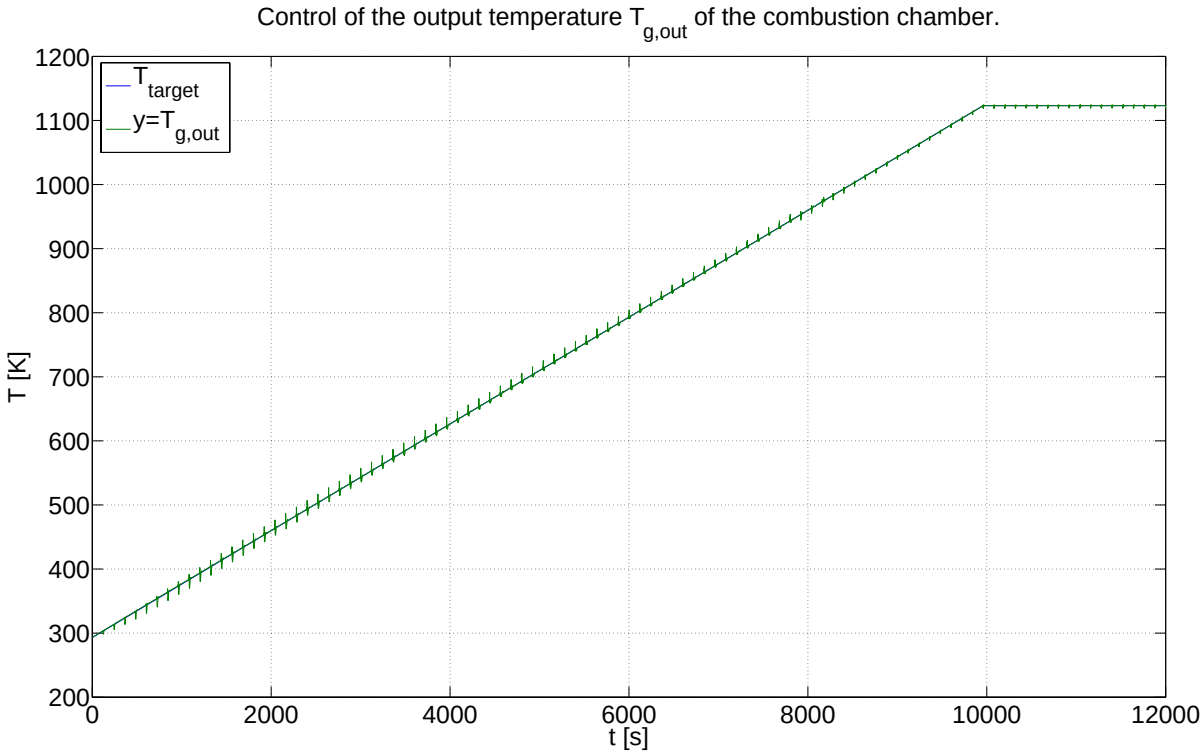

Figure 6.2.2: Distribution of the control variable.

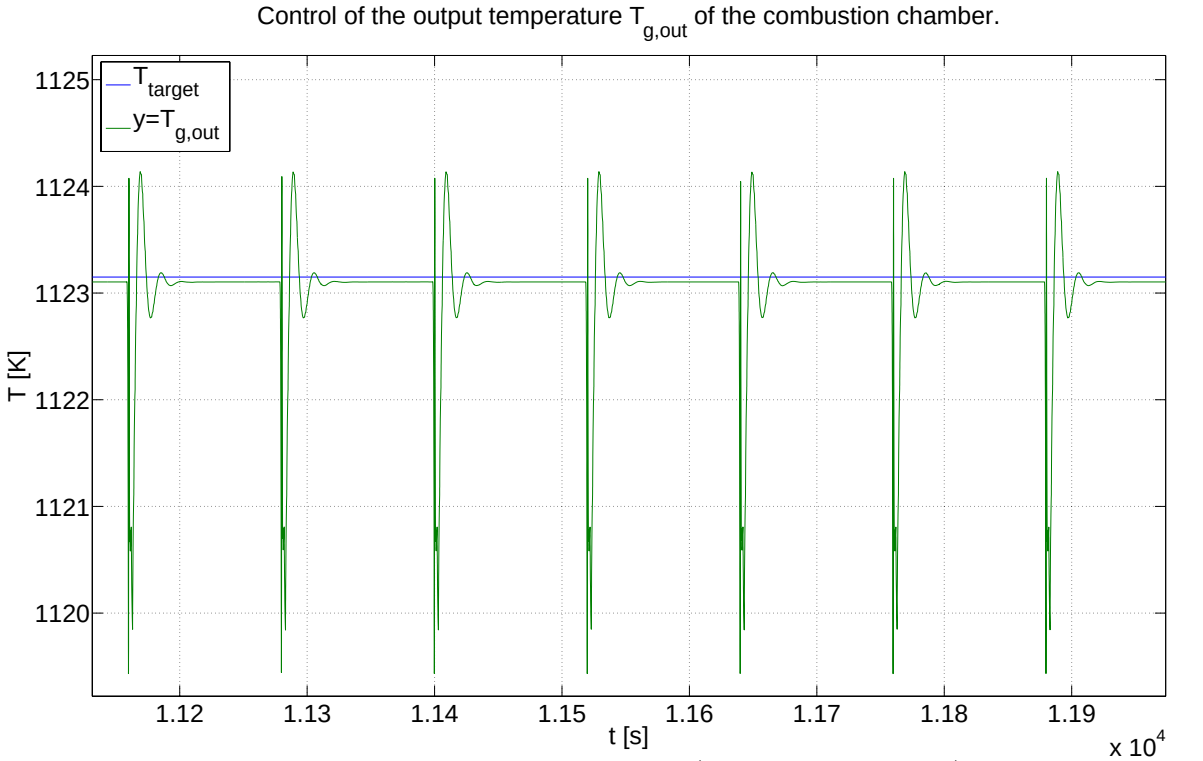

Figure 6.2.3: Zoom in figure 6.2.2 (steady state phase).

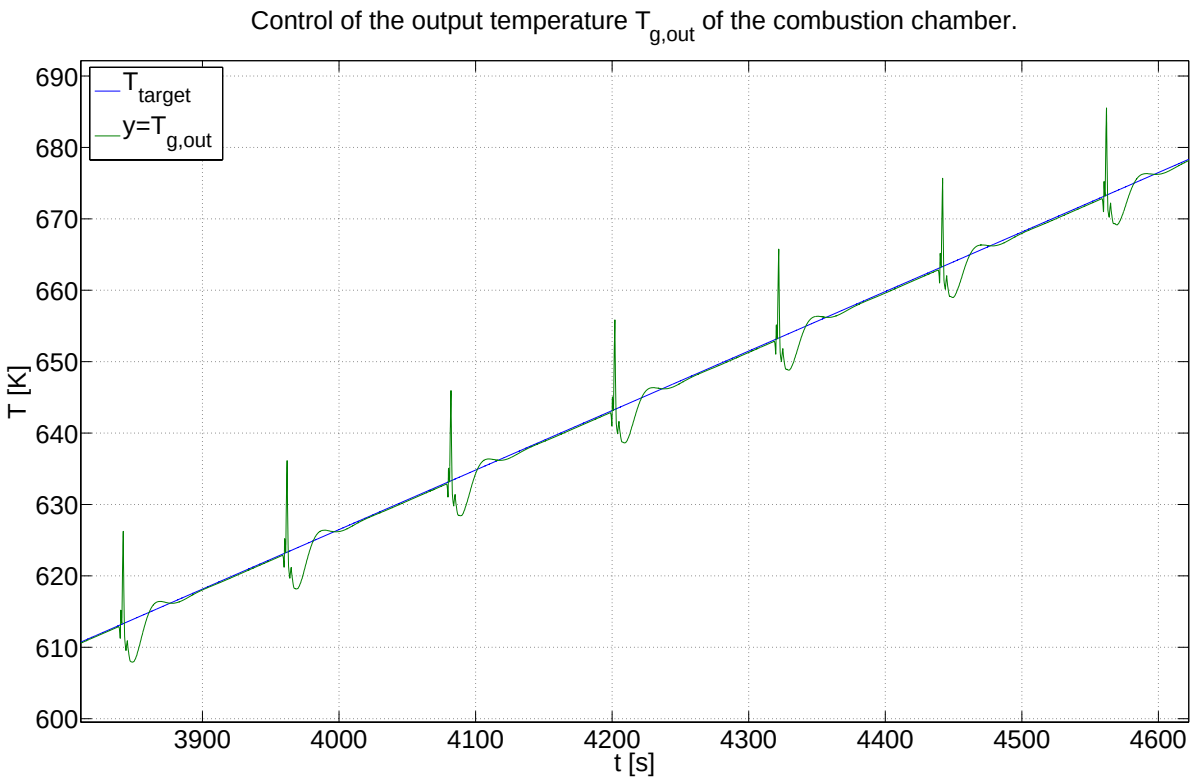

Figure 6.2.4: Zoom in figure 6.2.2 (start-up phase).

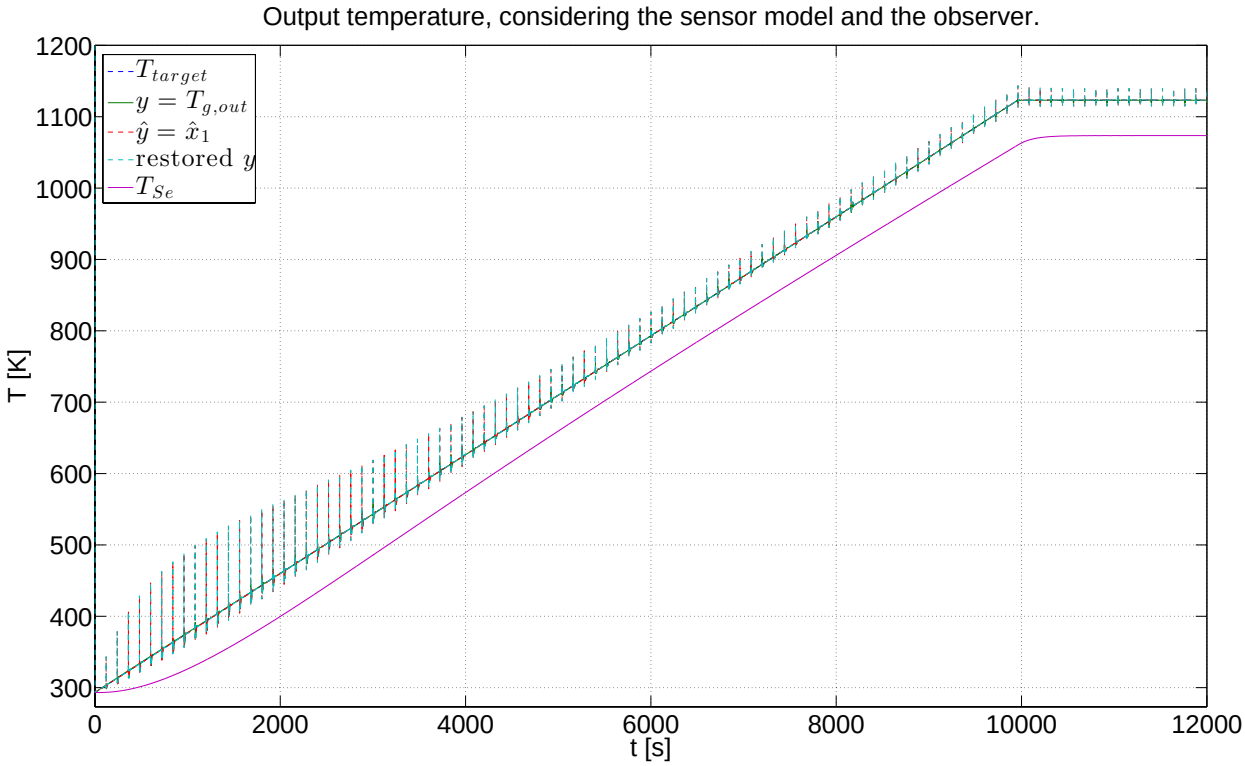

Figure 6.2.5: Displaying of the restored gas temperature (cyan) used for the control feedback and the temperature of the thermocouple (magenta).

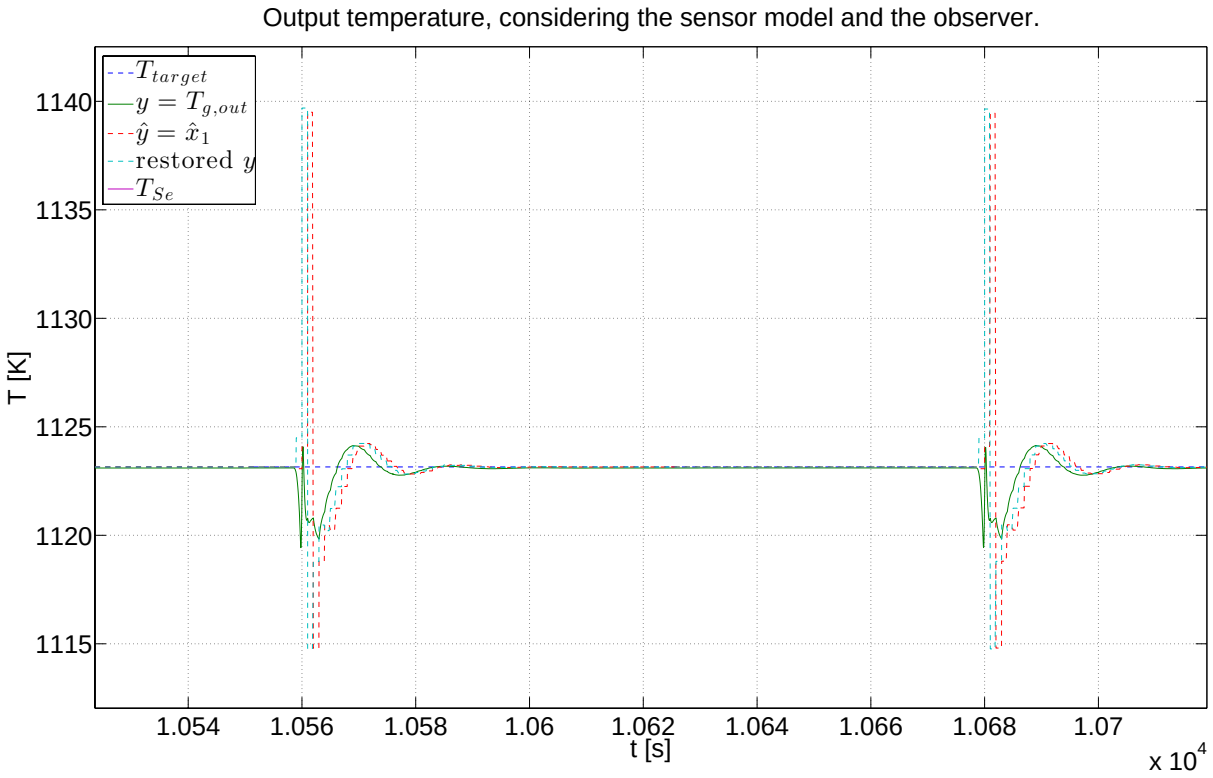

Figure 6.2.6: Zoom in figure 6.2.5 (steady state phase), displaying two half cycle switches.

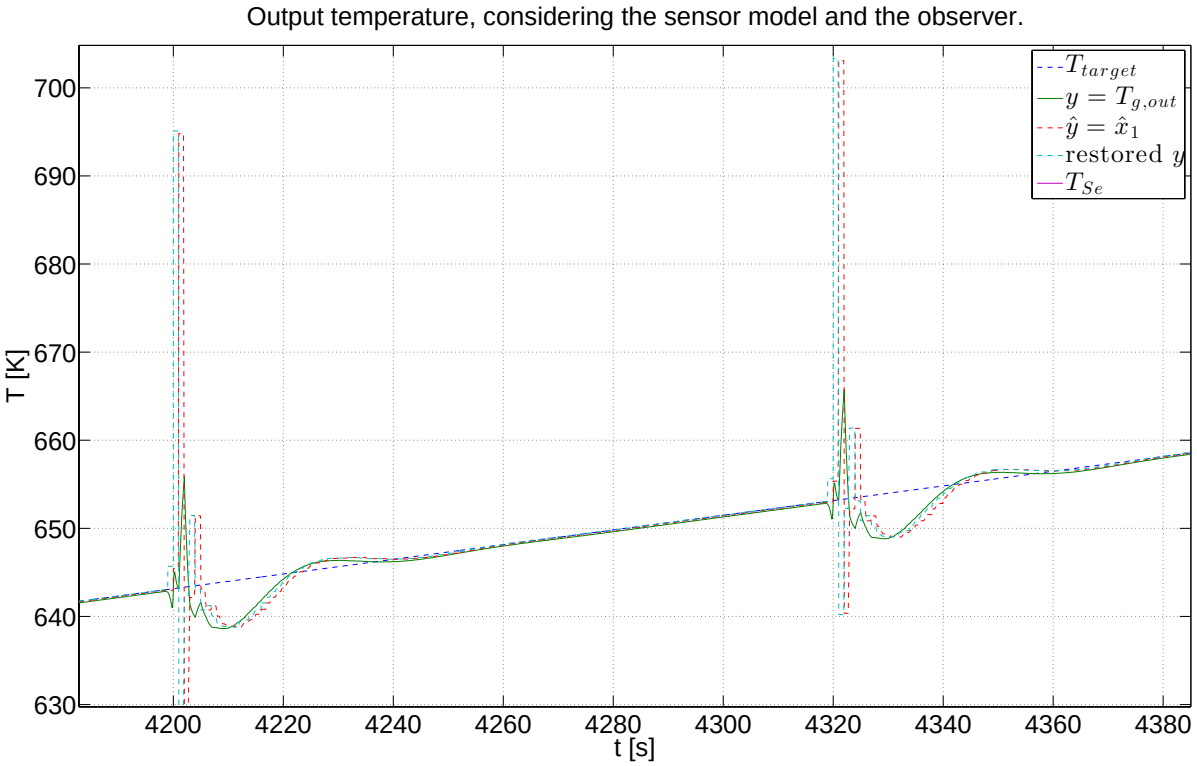

Figure 6.2.7: Zoom in figure 6.2.5 (start-up state phase), displaying two half cycle switches.

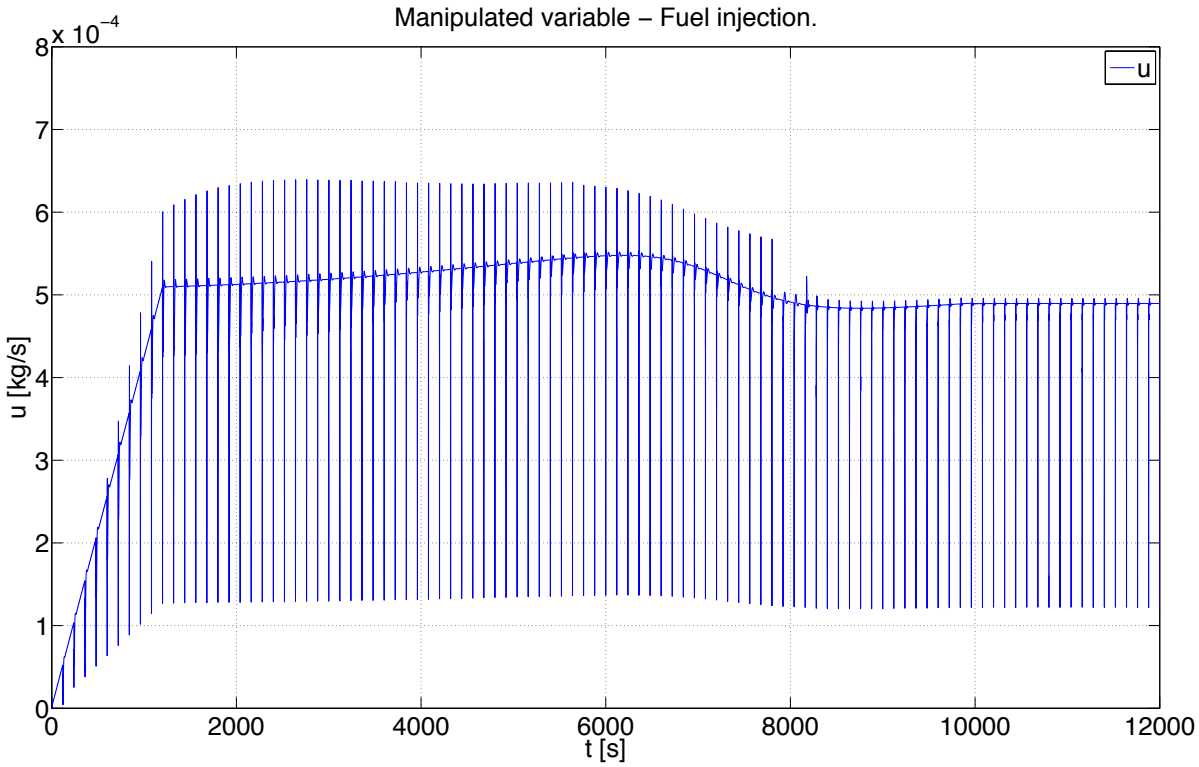

Figure 6.2.8: Manipulated variable.

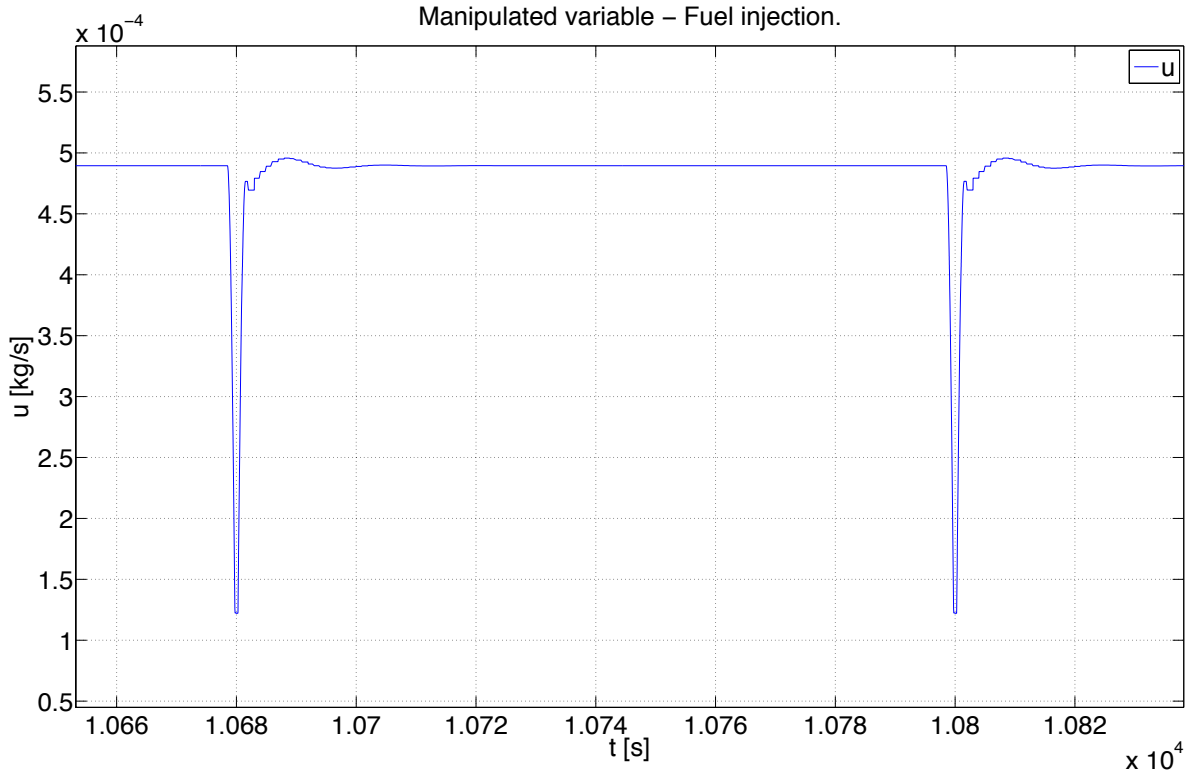

Figure 6.2.9: Manipulated variable according to figure 6.2.6.

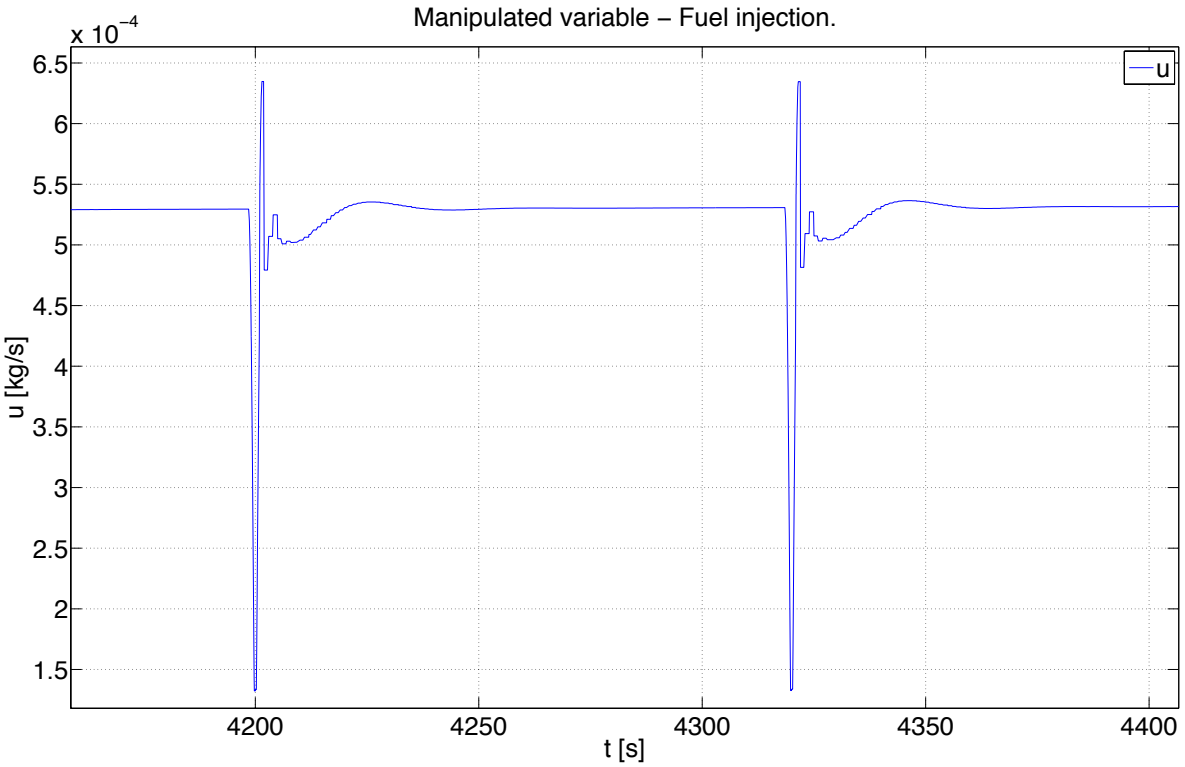

Figure 6.2.10: Manipulated variable according to figure 6.2.7.

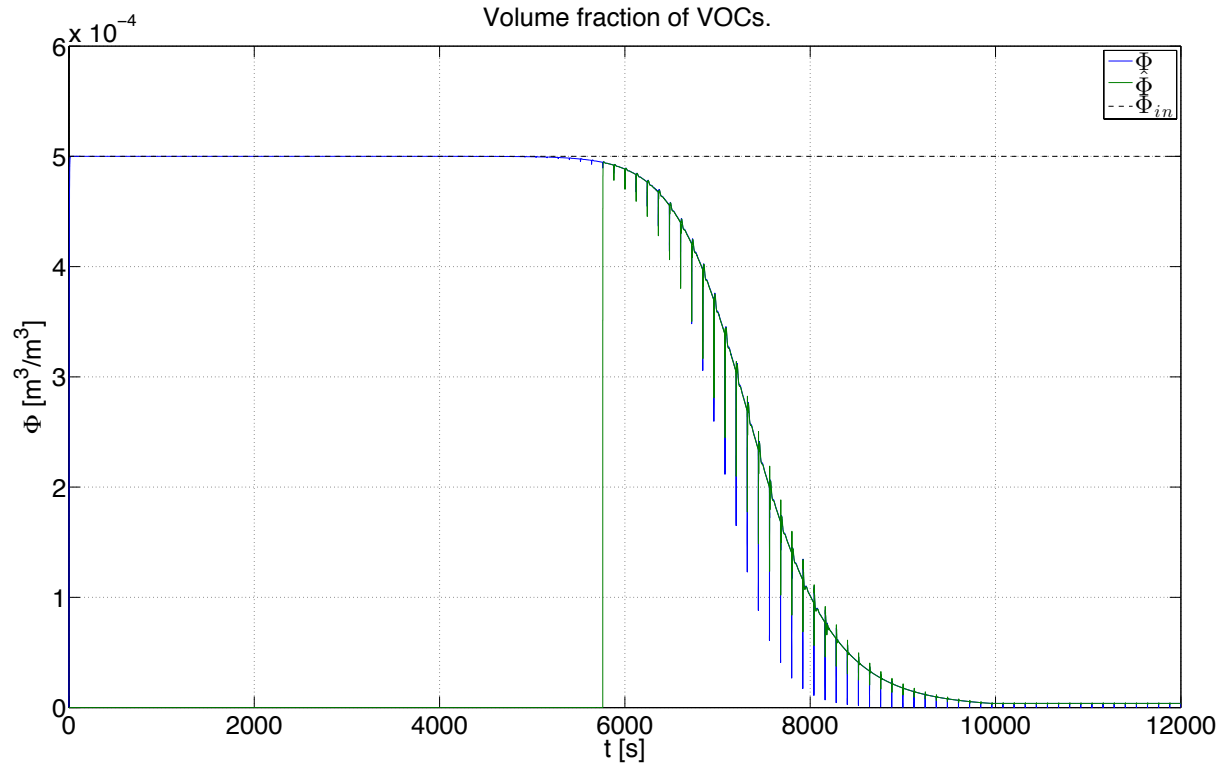

Figure 6.2.11: Distribution of the state variable Φ (blue) and its estimated value $\hat{\Phi}$ (green) of the observer.

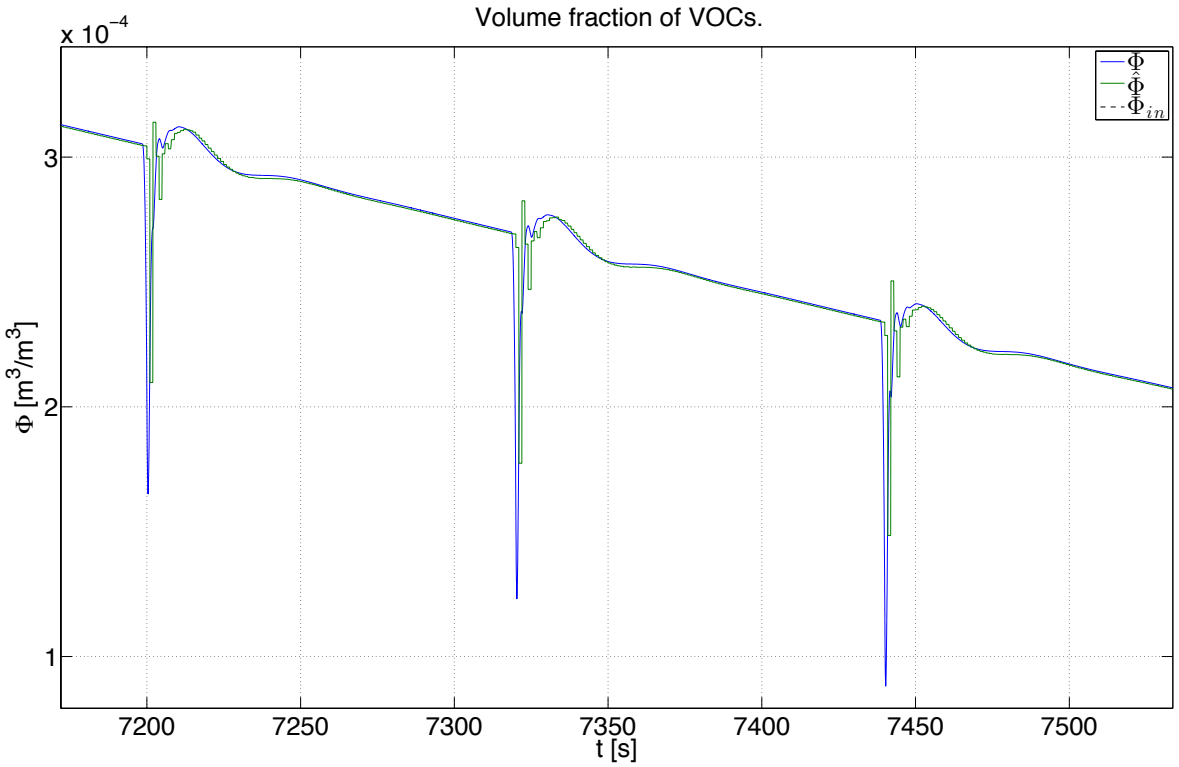

Figure 6.2.12: Zoom in figure 6.2.11.

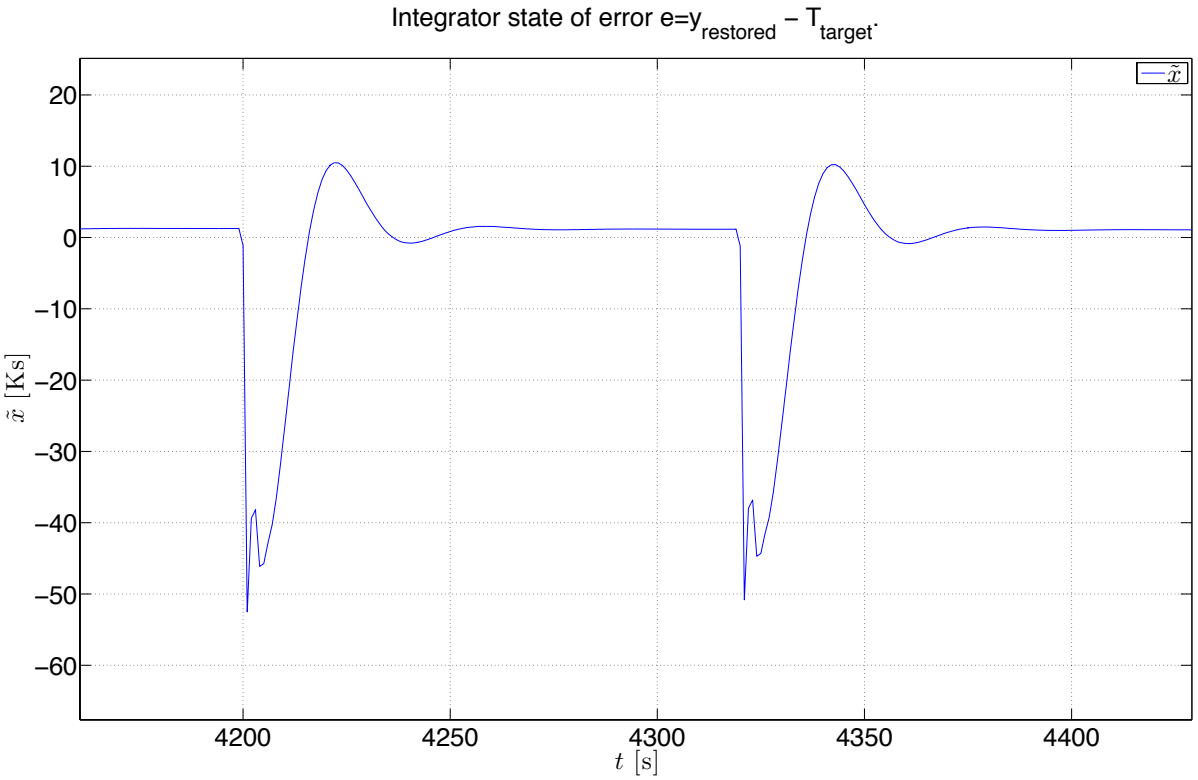

Figure 6.2.13: Integrator state of the error between restored y and T_{target} according to figure 6.2.7 and 6.2.10.

The simulation results illustrate that the half cycle switches of the RTO have tremendous effects on state variables and this consequentially leads to a very challenging task for the control concept. Figure 6.2.5 again demonstrates that the temperature of the thermocouple T_{Se} of the sensor features a significant response time and delivers far too low temperatures as a reason of thermal radiation.
The restoring of the original gas temperature (see section 4.1.2) produces a relatively large error at the time when switching as shown in figures 6.2.6 and 6.2.7. This causes unpleasant effects in the control, since the applied integrator (see section 5.5.2) accidentally integrates a nonexistent error between y and T_{target} (see figure 6.2.13), which produces slight oscillations (also shown in figure 6.2.6). This issue could be presumably fixed when using a better approximation of the derivative of T_{Se} (see section 4.1.2.4).
The change of the eigenvalues for control (see 3$^{\mathrm{rd}}$ paragraph in section 5.9) according to equation (6.1.2) can be clearly recognized in the manipulated variable at $t \approx 7600$s in figure 6.2.8. The decrease of the fuel injection in $t \in [6000, 8000]$s in figure 6.2.8 can be attributed to the growing reaction heat (cf. figure 6.2.11), which can be accurately considered in the control thanks to the observer. Referring to figure 6.2.11, the estimation of state Φ by the observer for $y > T_{enable} = 400°\mathrm{C}$ delivered reliable values, and therefore facilitates the consideration of the reaction heat in the control law without the need for compensation by the integrator.
Despite some negative effects, figure 6.2.2 shows that the reference (output) gas temperature can be properly established over the entire time interval.

6.2.2 Fluctuating Input Parameters

Although the application of the integrator in the control concepts might cause troubles at cycle switches and when the manipulated variable reaches its saturation, it becomes essential when important parameters such as the mass flow $\dot{m}_{abs}$ (appearing in the coefficients c_1 and c_2 of the control law (5.5.1)) and the incoming volume fraction of VOCs Φ_{in} (considered in the observer for obtaining information about the state variable Φ) are uncertain and differ from the real values.
As the current plants of CTP lack sensors measuring the mass flow $\dot{m}_{abs}$ and any portions, or concentration of VOCs, simulation with fluctuating $\dot{m}_{abs}$ and Φ_{in} should clarify the impact when considering wrong values in the control.
For demonstration purposes, it is assumed that the mass flow $\dot{m}_{abs}$ oscillates with a period of 250s, an amplitude of 20% of $\dot{m}_{max} = 0.2383$kg/s and a mean value of $0.8\dot{m}_{max}$, whereas the value 0.2383kg/s is considered in the control concept including the observer and the restoring of the original gas temperature. Φ_{in} oscillates with a period of 200s with an amplitude of $0.4 \cdot 5 \cdot 10^{-4}$ and a mean value of $5 \cdot 10^{-4}$, whereas this value is also used in the observer.
This produces a maximal deviation of 40% from the real values in the parameters $\dot{m}$ and Φ_{in} considered in control, in the method of restoring the original output gas temperature and in the observer (cf. figure 5.8.1).

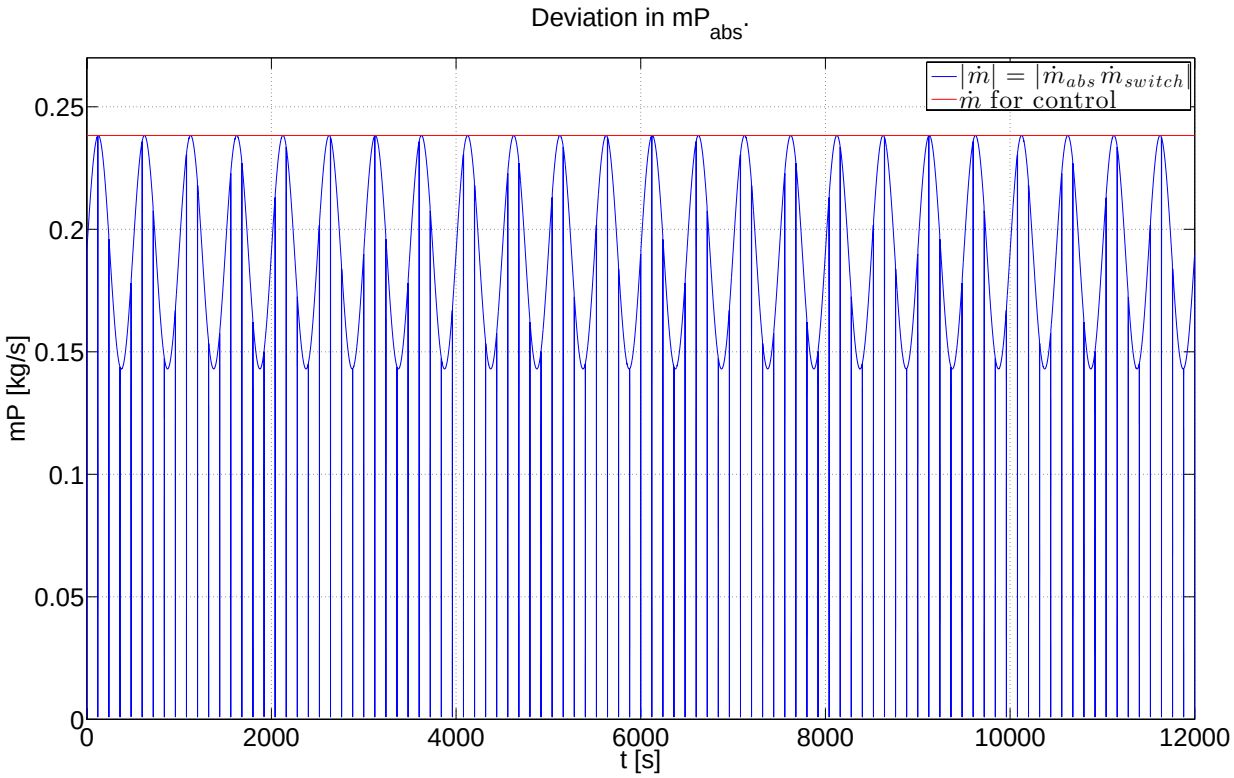

Figure 6.2.14: Deviation in the mass flow.

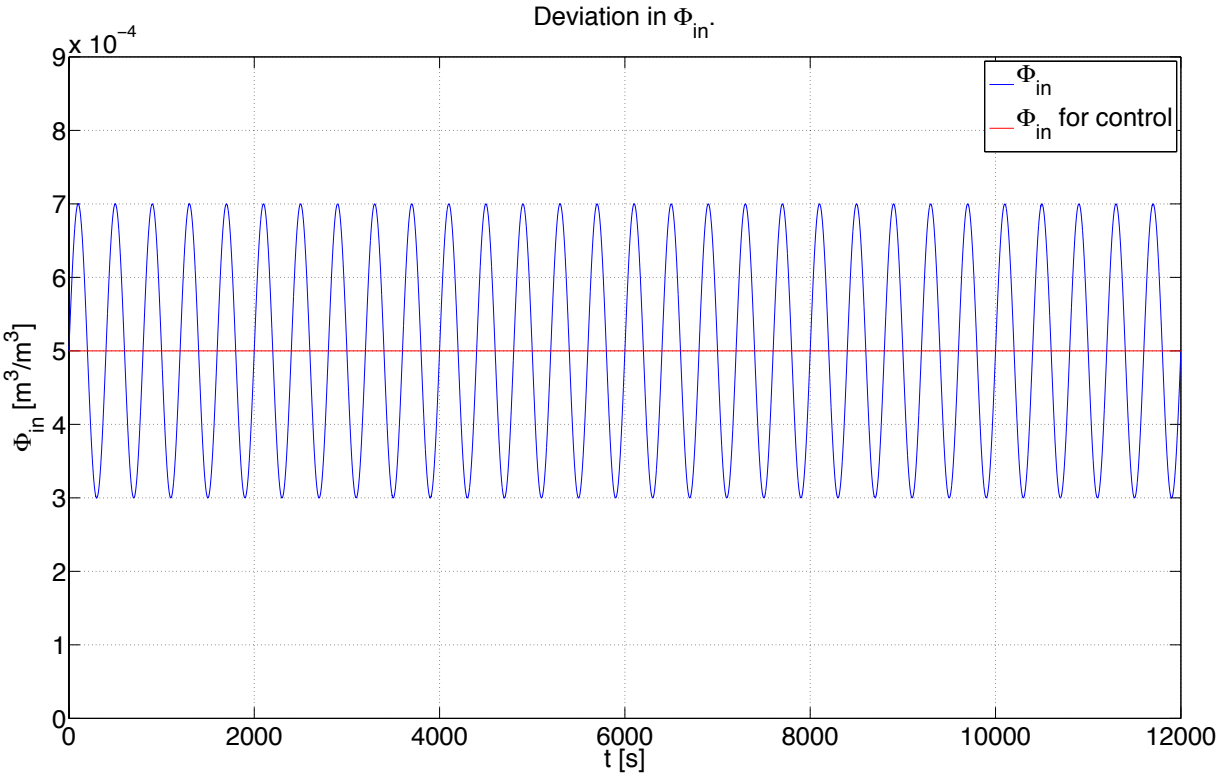

Figure 6.2.15: Deviation in the incoming volume fraction of VOCs.

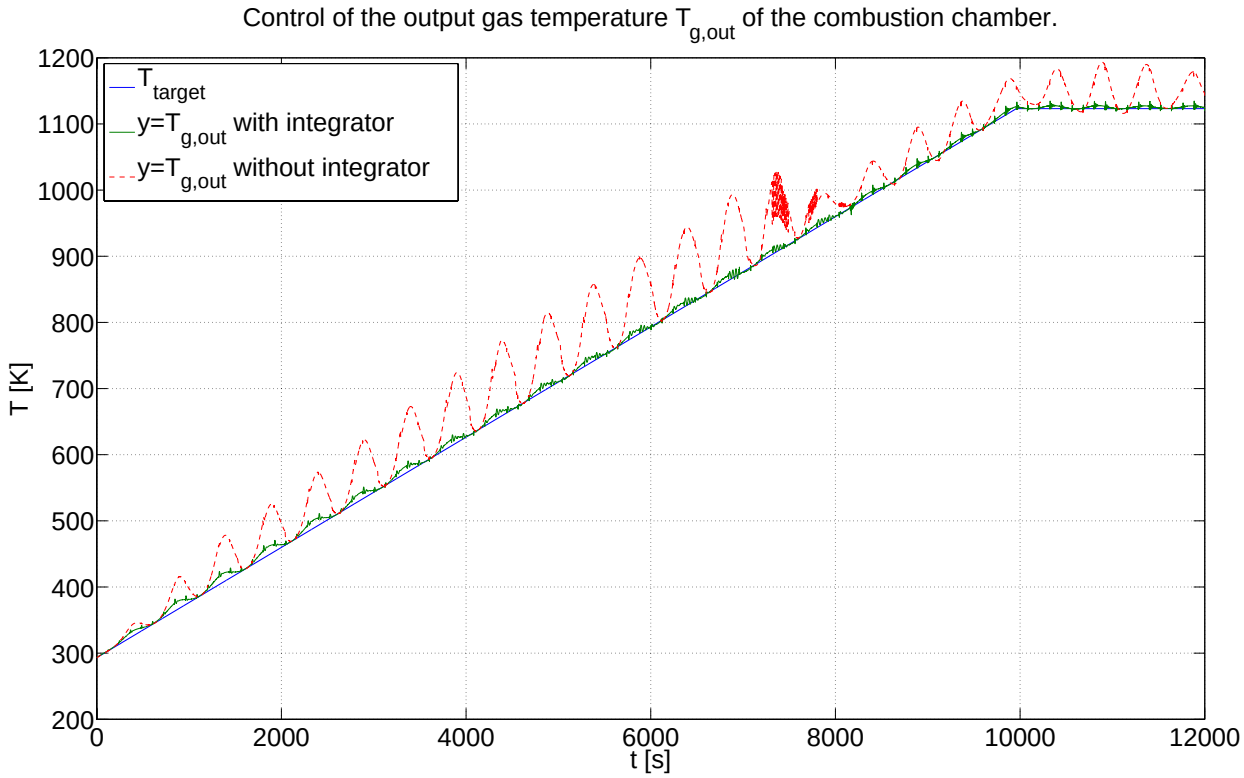

Figure 6.2.16: Comparing the impact of deviations in $\dot{m}$ and Φ_{in} in the control of $y = T_{g,out}$ when applying the integrator in the control concept (cf. figure 5.8.1).

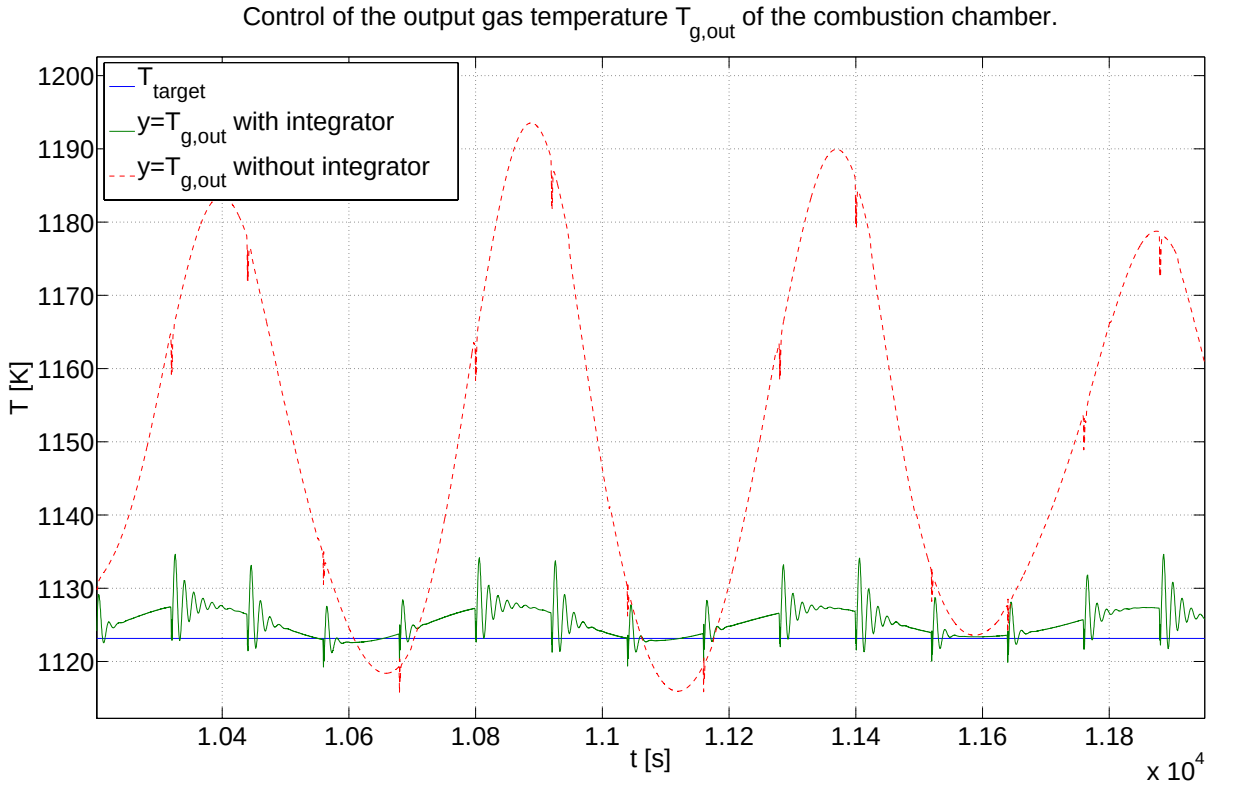

Figure 6.2.17: Zoom in figure 6.2.16 (steady state phase).

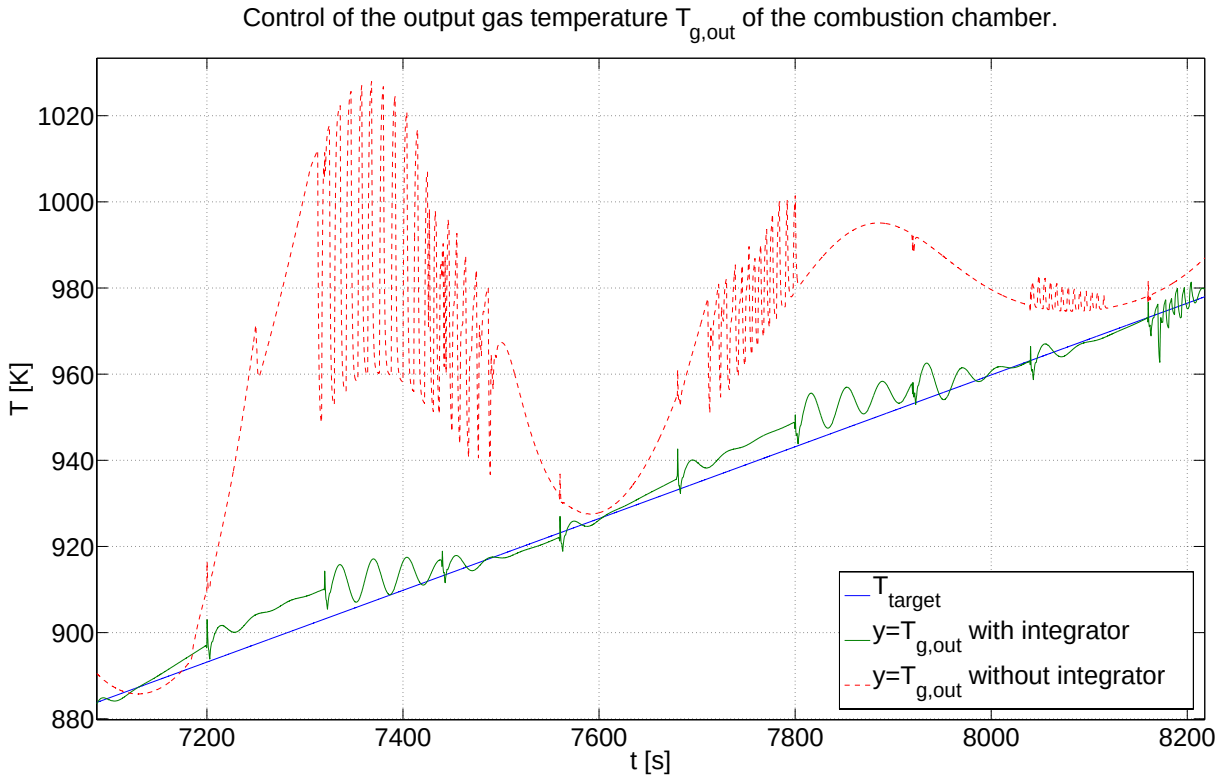

Figure 6.2.18: Zoom in figure 6.2.16 (start-up phase), displaying the change in eigenvalues when reaching $y > 973.15$K according to equation (6.1.2).

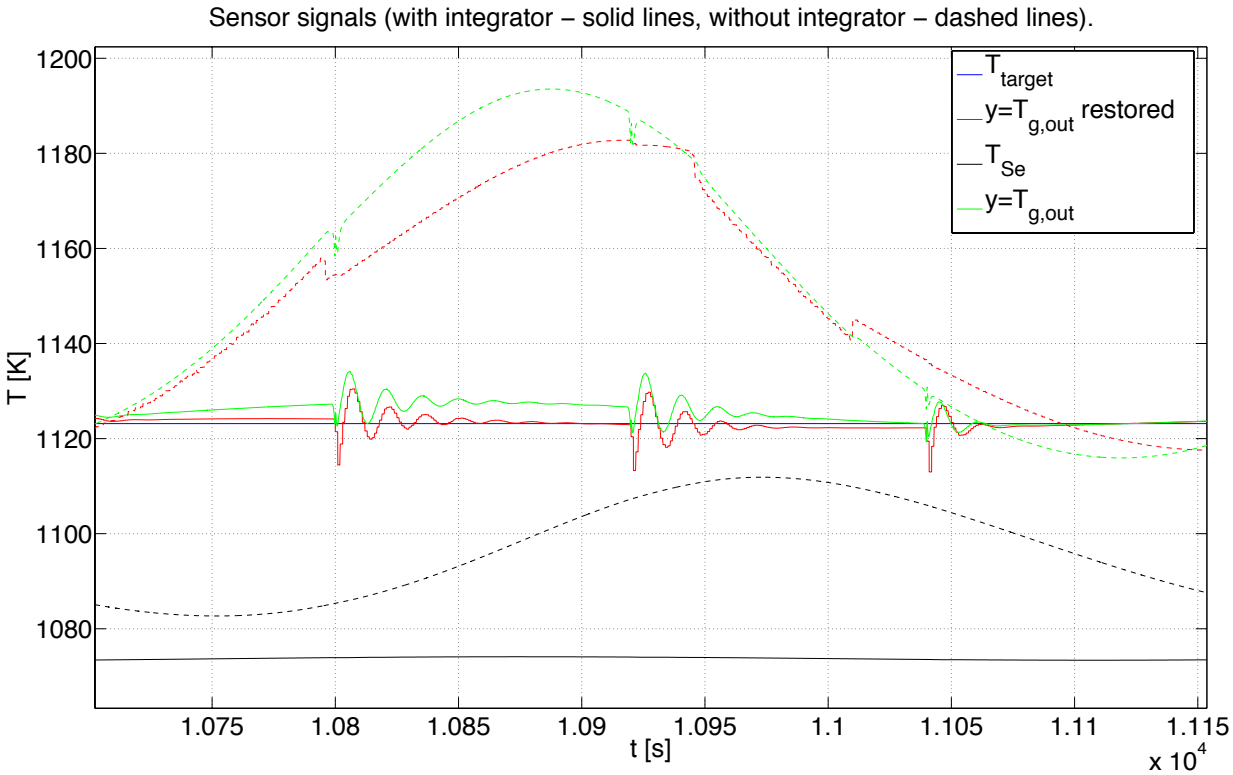

Figure 6.2.19: Displaying of the restored gas temperature in steady state phase with (solid lines) and without (dashed lines) the application of the integrator in the control concept.

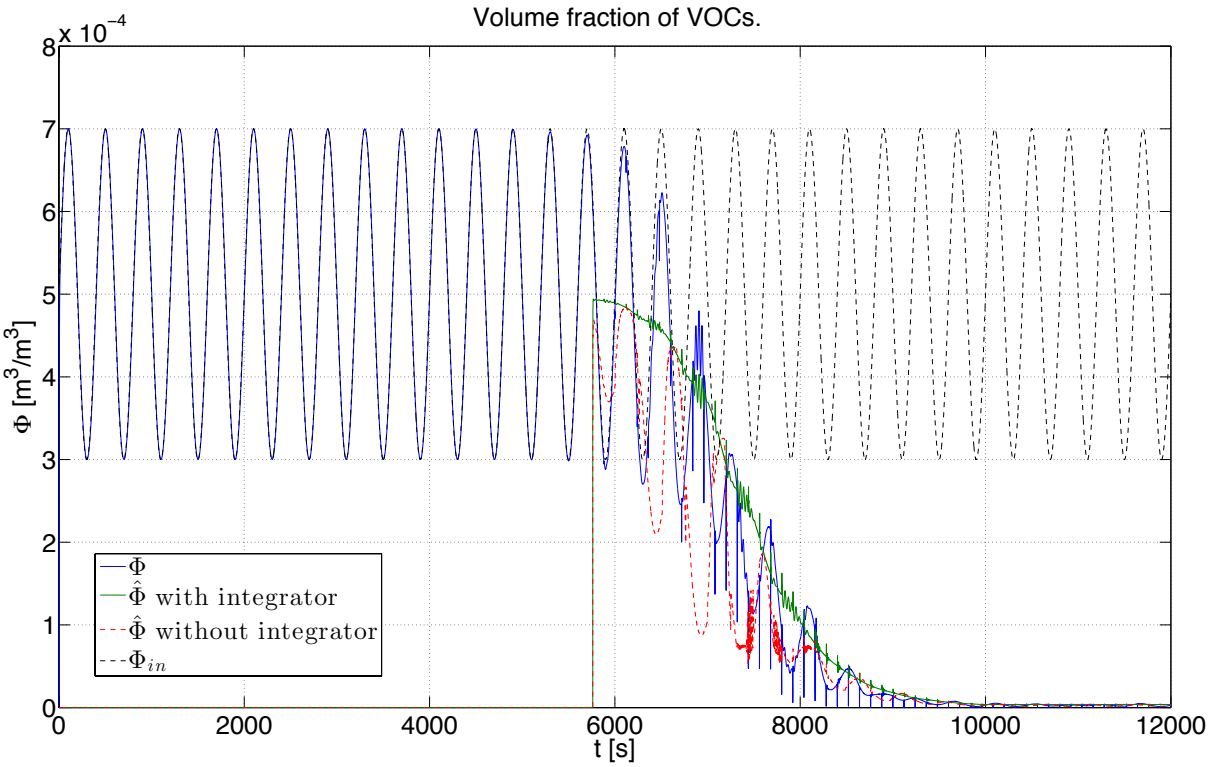

Figure 6.2.20: Distribution of the state variable Φ (blue) and its estimated value $\hat{\Phi}$ of the observer with (green solid) and without (red dashed) applied integrator.

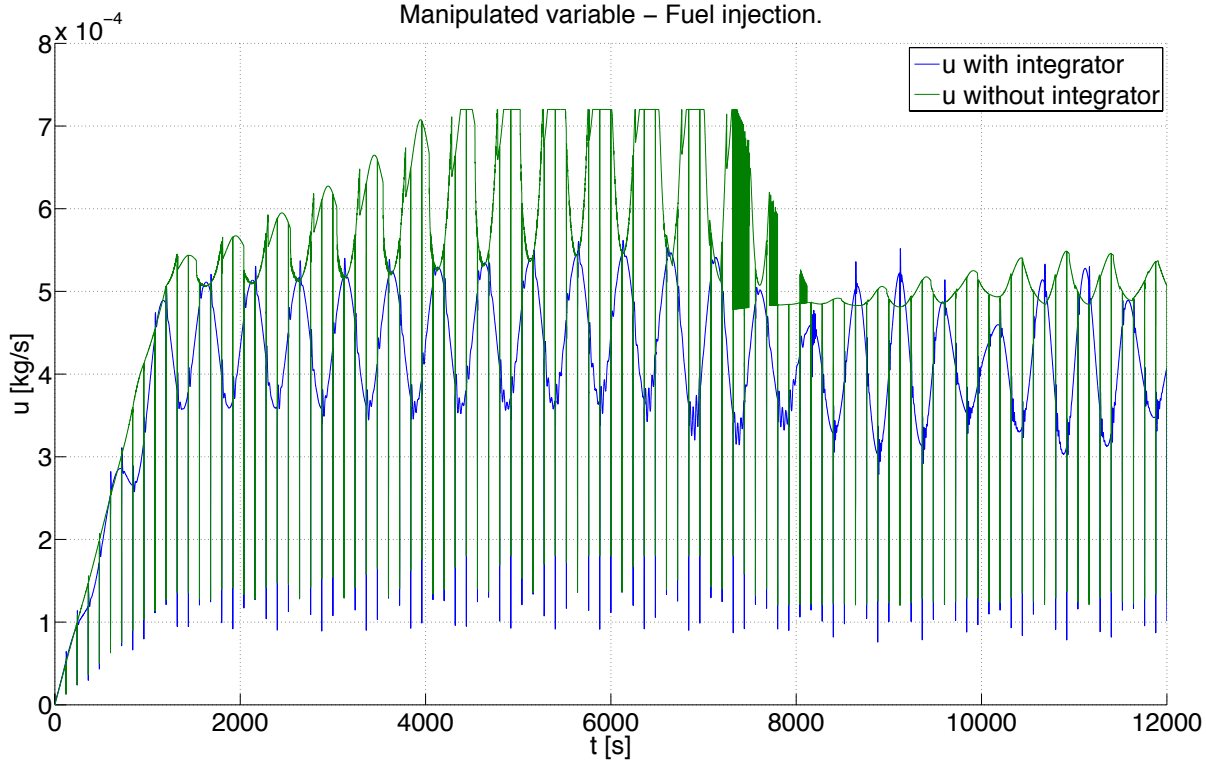

Figure 6.2.21: The manipulated variable with (blue) and without (green) applied integrator.

It is evident that the developed control concept is capable to overcome relatively large errors in system parameters, even if they rapidly change over time (see figure 6.2.16).

6.2.3 Short Comparison to Applied PID Controllers

Within the scope of this thesis the initial aim was to demonstrate that a model based approach of the temperature control can significantly outperform the currently applied PID controller. Beforehand, one must not forget that the model of the combustion chamber using the ODEs (5.5.1) represents reality substantially simplified.
Results are alarming when testing the actually applied (according to the information received) PID, respectively the PI controller

$$C(s) = 0.8\left(1 + \frac{1}{180s}\right) = K_p\left(1 + \frac{1}{T_i s}\right) \tag{6.2.1}$$

for the pilot plant, considering the illustrated potential in this simulation. This can not only be attributed to the fact that the temperature of the thermocouple (sensor) serves as input of the control, but the relatively aggressive values $K_p = 0.8$ and $T_i = 180$ for a maximal value of $u_{max} = 7.2 \cdot 10^{-4}$ lead to a toggling manipulated variable, comparable to the results of a *bang-bang* control. The thermocouples of the sensors are such inert, that they will not recognize the jumps in the distribution of the gas temperatures and consequentially follow the reference quantity, although the real gas temperatures are very far from target values (see figure 6.2.23).

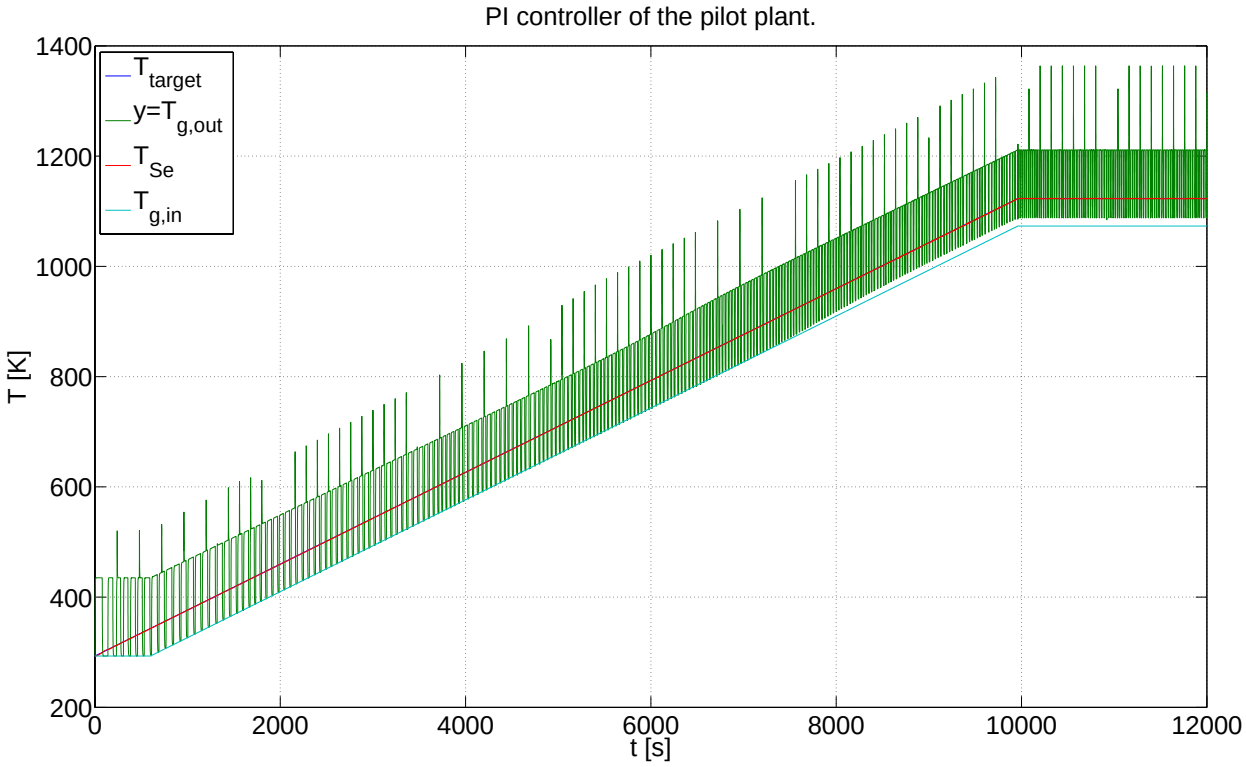

Figure 6.2.22: Results of applying the PI controller of the pilot plant.

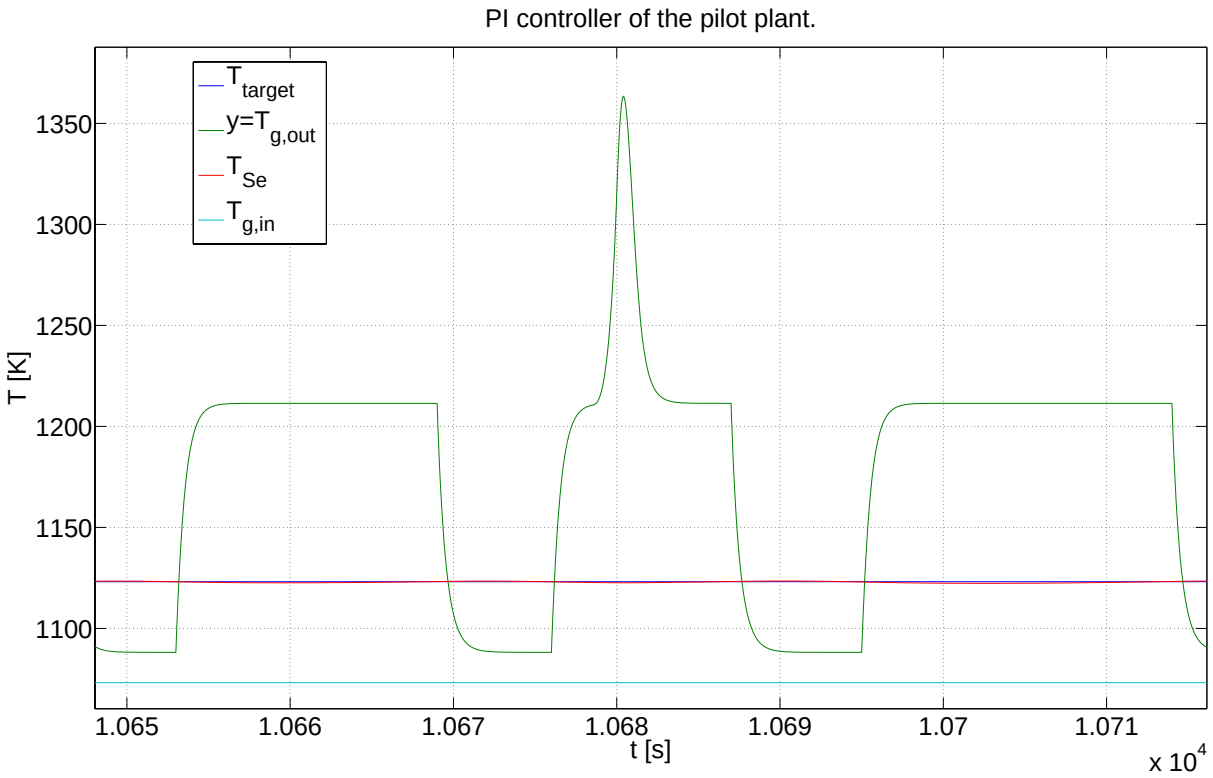

Figure 6.2.23: Zoom in figure 6.2.22 (steady state phase).

Except of the chosen input temperature $T_{g,in}$ (see figure 6.2.22), which produces a permanent distance of only 50°C to be compensated by the burner, the input parameters are held constant according to table 6.1.4 (compare with the results in section 6.2.1).

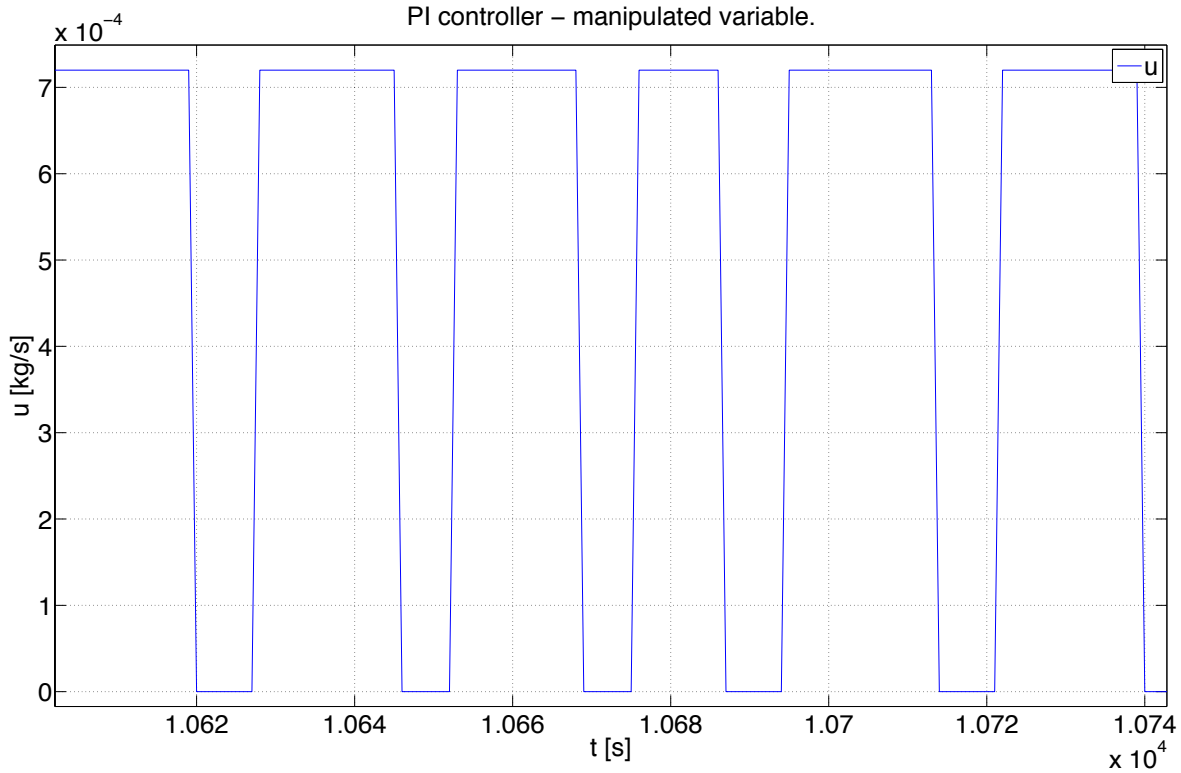

Figure 6.2.24: Manipulated variable according to figure 6.2.23.

6.3 Simulation including all Components

The simulation results of the entire plant, including two valve boxes (2.2.1), two ceramic beds (2.3.1), the combustion chamber (2.4.1) and the two temperature sensors (4.1.17) according to the methods in chapter 3 applying the control concepts of chapter 5 and the restoring of the original gas temperature (section 4.1.2) are finally presented.

The control of the output gas temperature of the combustion chamber only (analogous to section 5.6.2) is focused due to time constraints, whereas constant input parameters regarding table 6.1.4 were used. The reference quantity T_{target} is raised linearly with a slope of $\frac{5}{60}$ [K/s] (see figure 6.2.1) to imitate the real start-up process of the plant. As in section 6.2, the restored gas temperature serves as input of the control concept (cf. figure 5.8.1). Furthermore, it needs to be mentioned that the control law compensates the error made in the inlet pressure p_{in} (see equation (5.1.1)) as it is fed with $p_{in,control} = 101325$Pa. The input pressure in the combustion chamber will be certainly lower due to the pressure drop in one of the ceramic beds (section 2.3.2) and in one of the valve boxes (section 2.2.1).

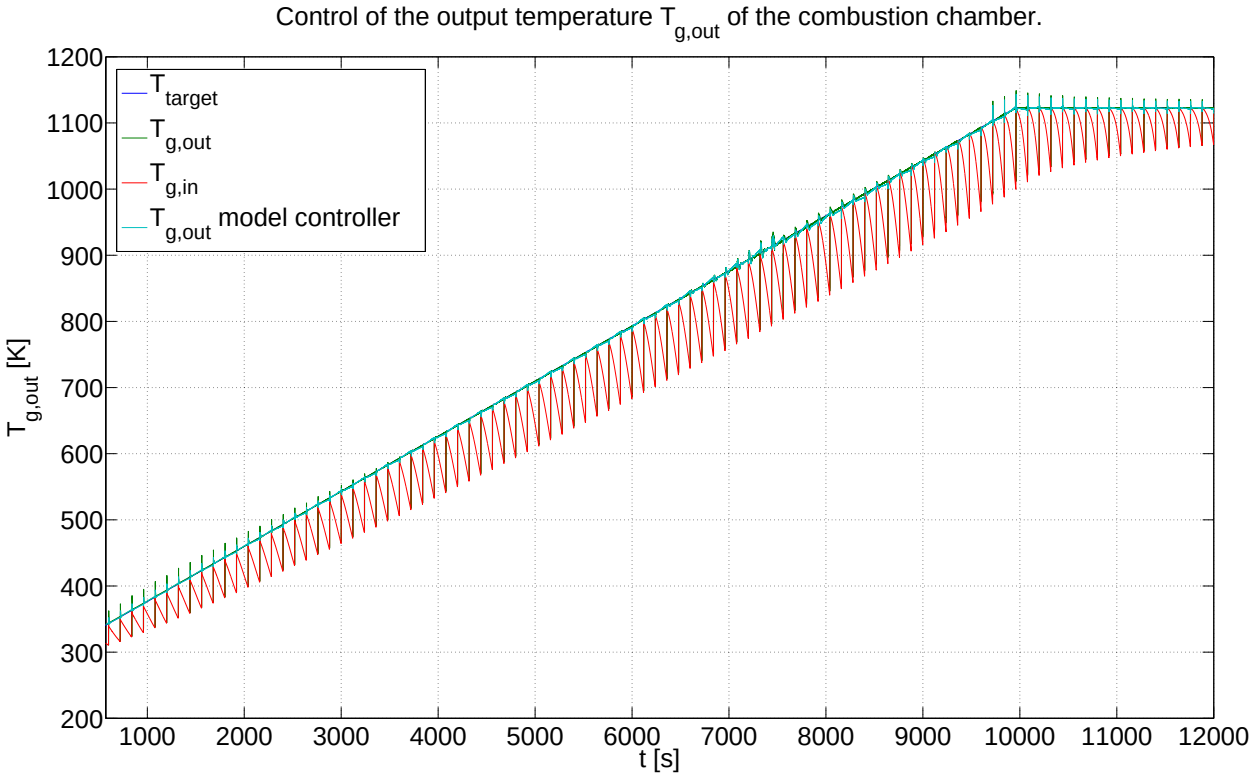

Figure 6.3.1: Distribution of the control variable $T_{g,out}$ and comparison to the value when feeding the same inputs to the simplified model of the combustion chamber according to equation (5.1.1).

It is remarkable that the simplified model of the combustion chamber delivers almost identical results as the complex model consisting of PDEs when feeding same inputs (referring to figure 6.3.1).

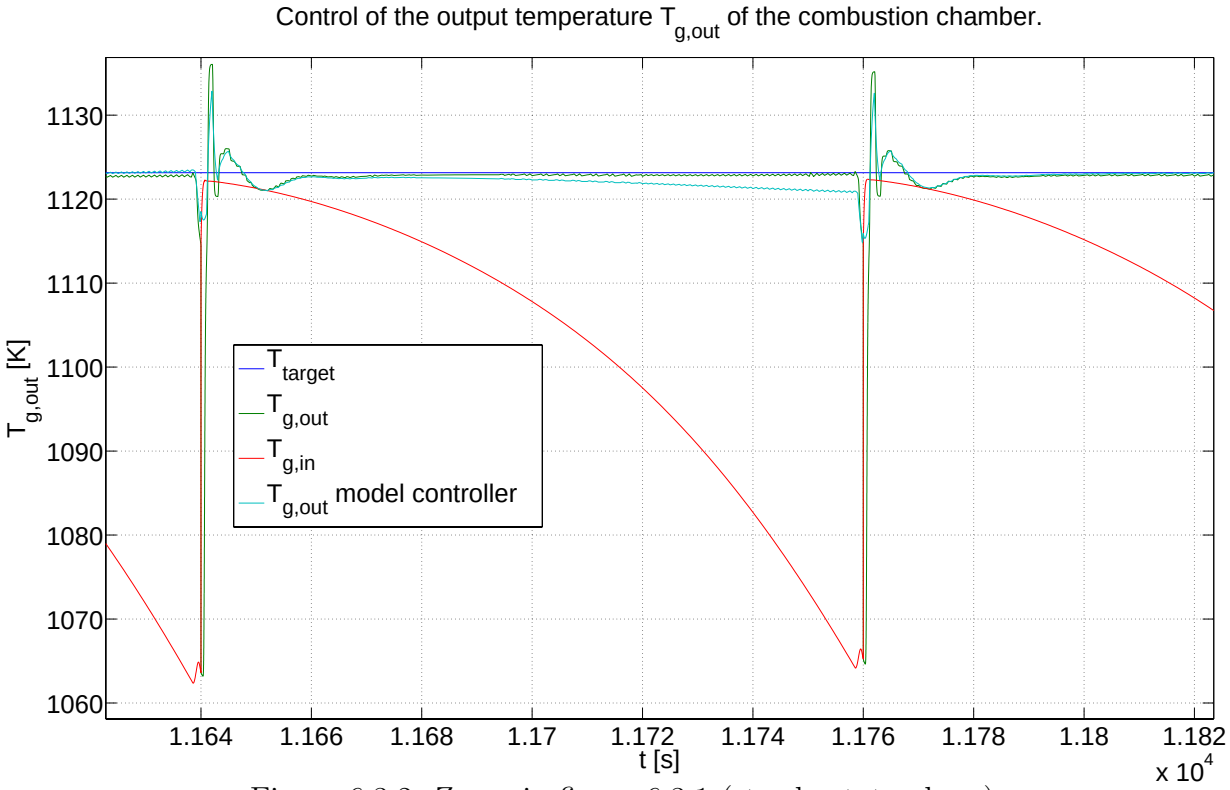

Figure 6.3.2: Zoom in figure 6.3.1 (steady state phase).

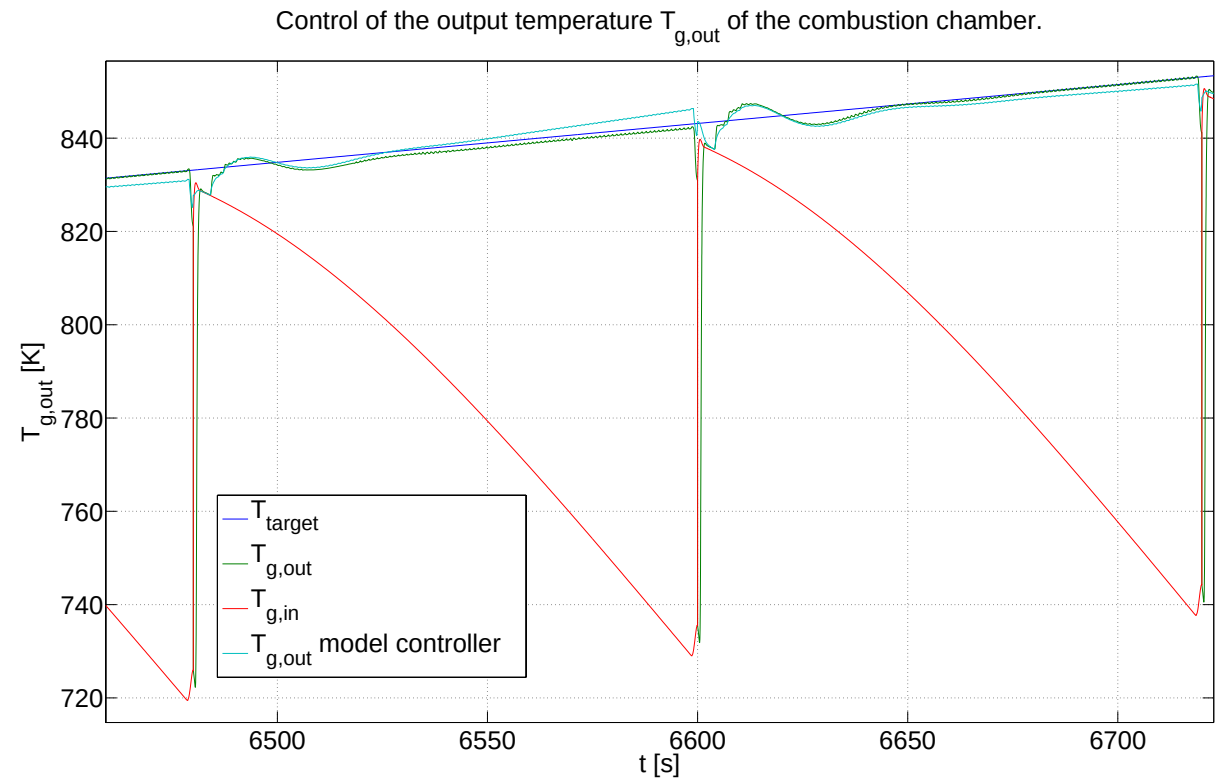

Figure 6.3.3: Zoom in figure 6.3.1 (start-up phase).

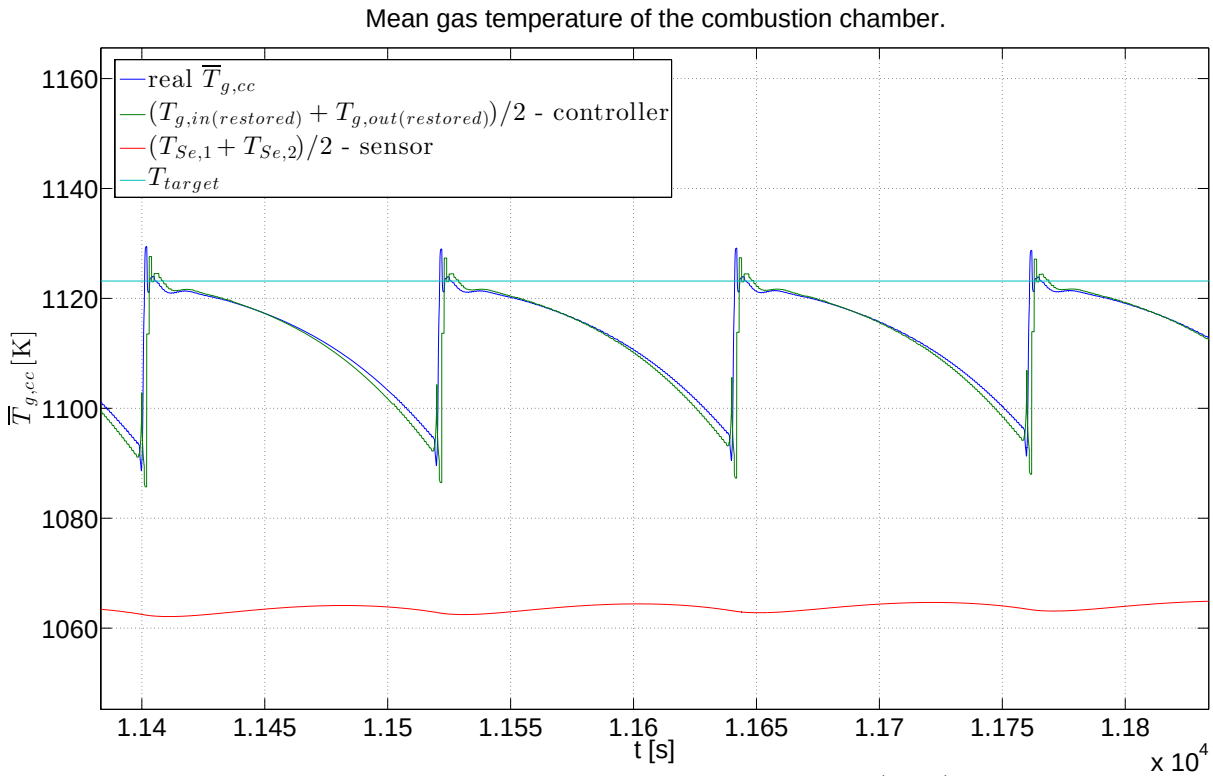

Figure 6.3.4: Comparison of the real mean gas temperature (blue) of the combustion chamber with the average of the restored input $T_{g,in(restored)}$ and output $T_{g,out(restored)}$ temperature, as well as the average of the temperature of the thermocouples $T_{Se,1}$ and $T_{Se,2}$ in steady state of the plant (cf. figure 6.3.2).

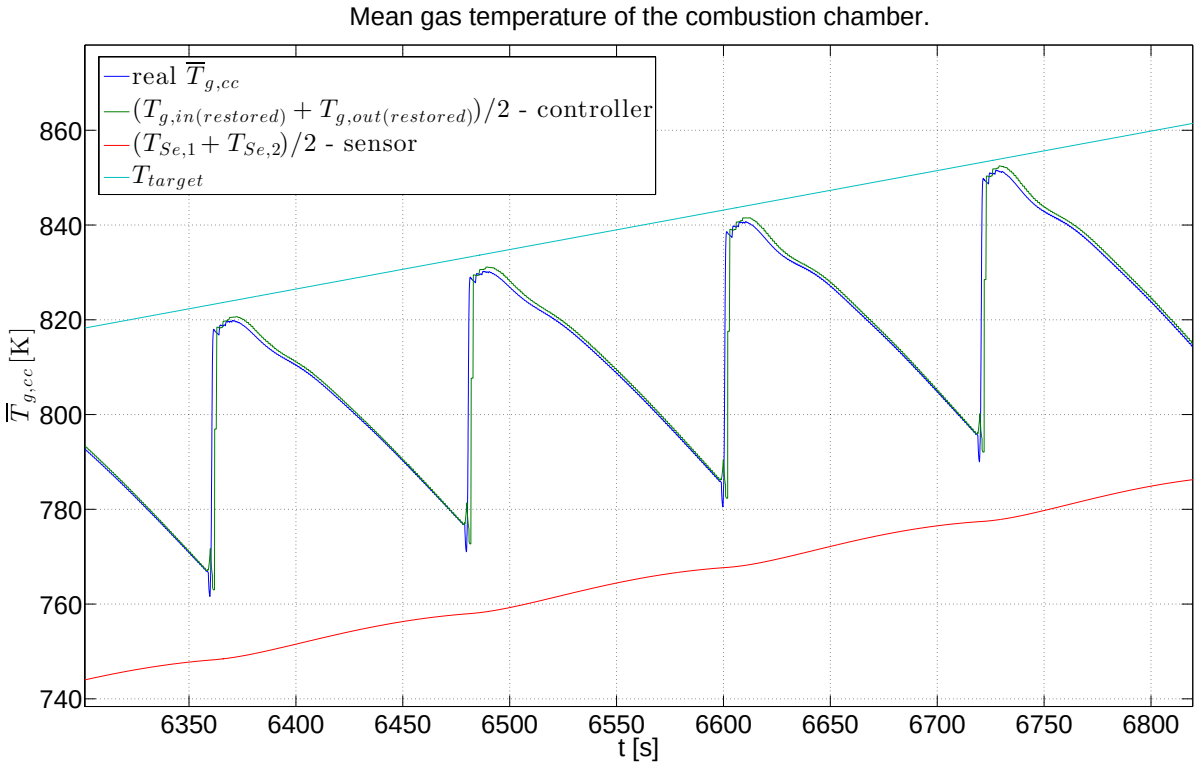

Figure 6.3.5: Start-up phase of figure 6.3.4 (cf. figure 6.3.3).

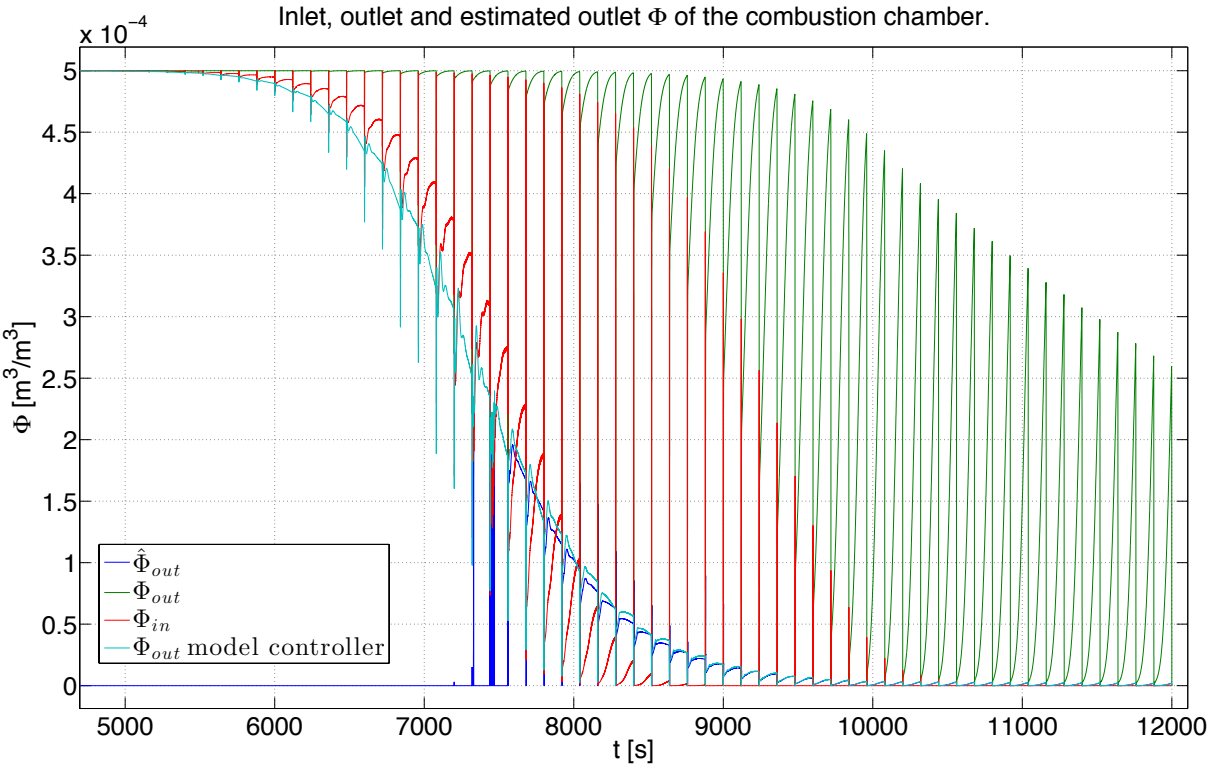

Figure 6.3.6: Inlet (green), outlet (red) and estimated outlet (blue) volume fraction of VOCs of the combustion chamber, displaying deviations to Φ_{out} (cyan) in the simplified model (equation 5.1.1) when feeding same inputs.

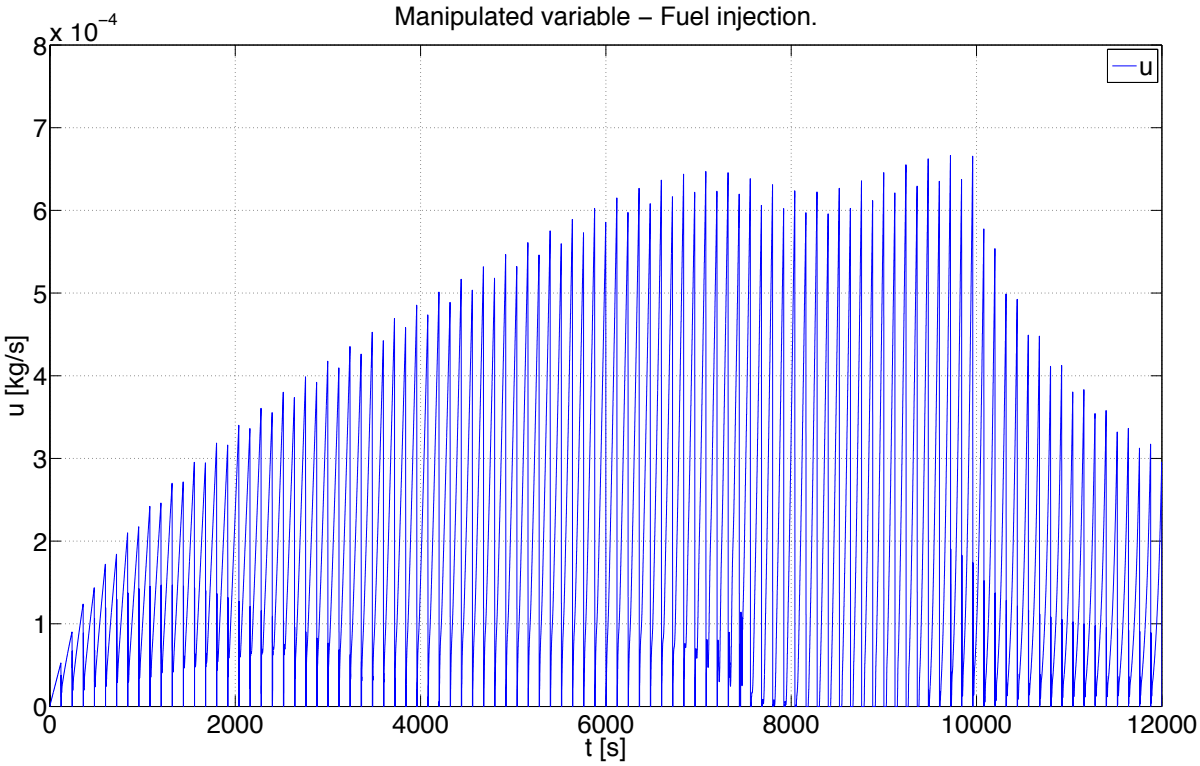

Figure 6.3.7: Distribution of the fuel mass flow.

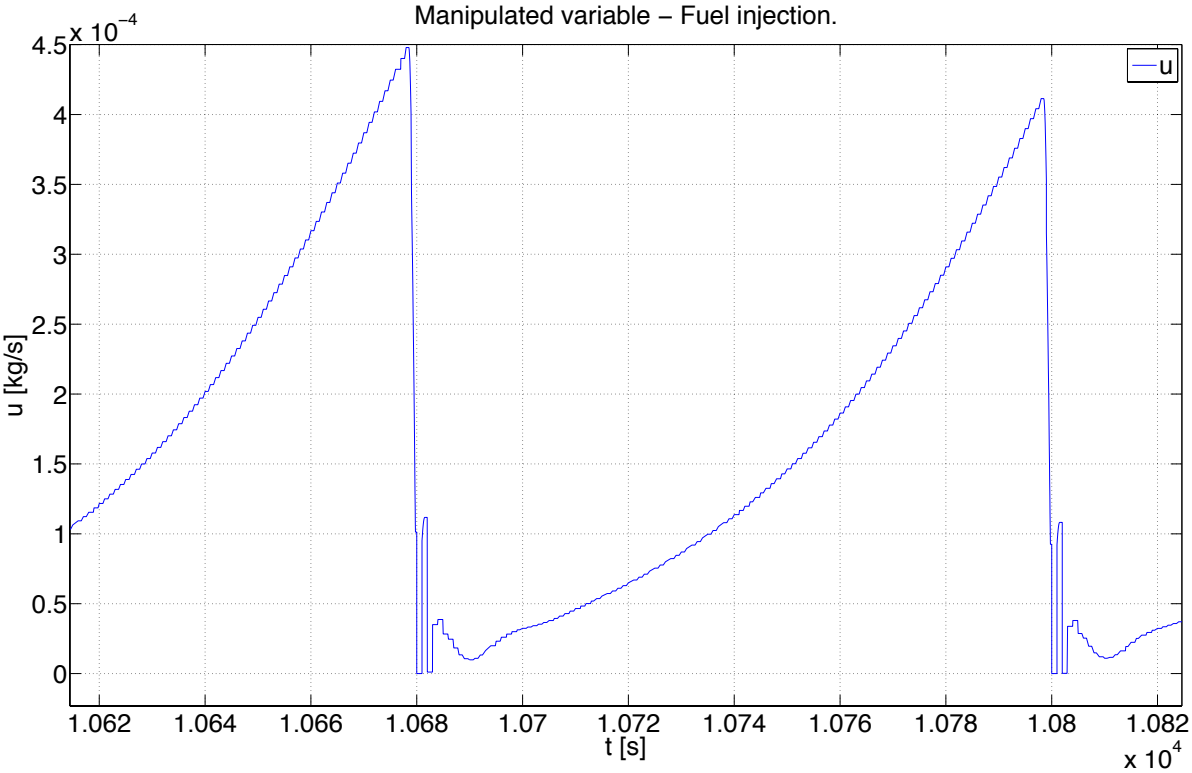

Figure 6.3.8: Manipulated variable according to figure 6.3.2.

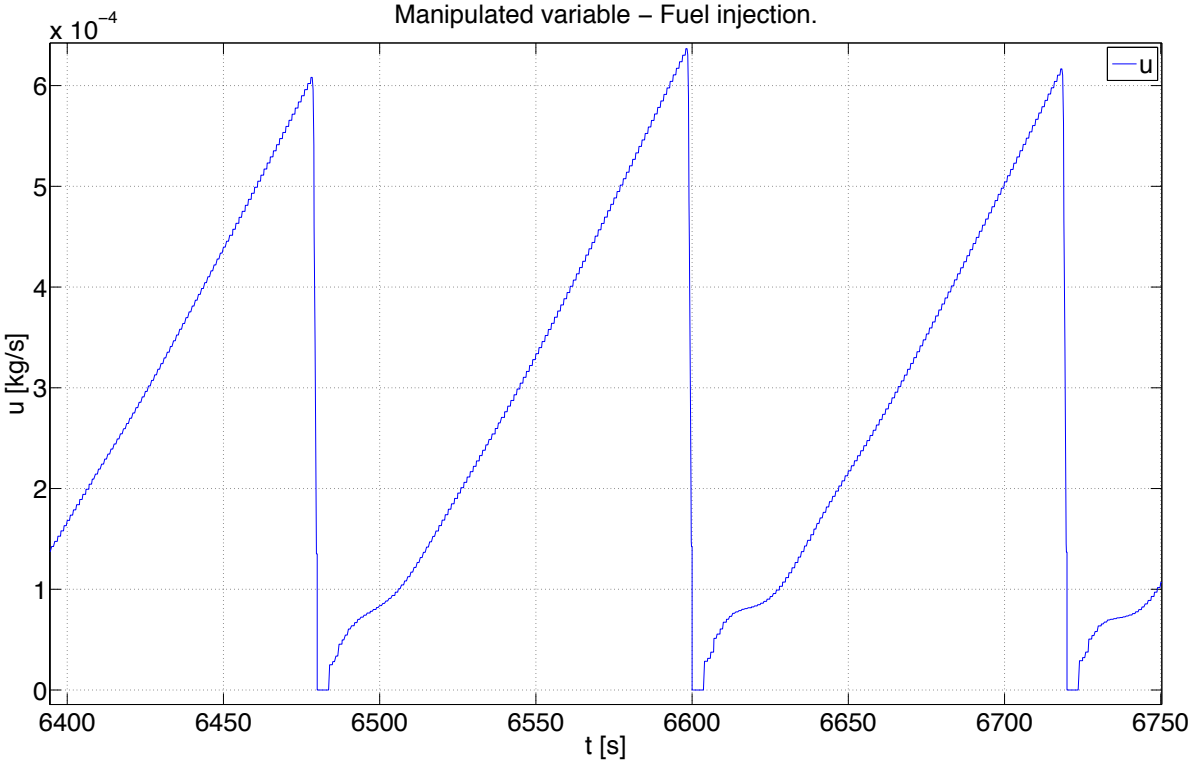

Figure 6.3.9: Manipulated variable according to figure 6.3.3.

6.3.1 Combustion Chamber

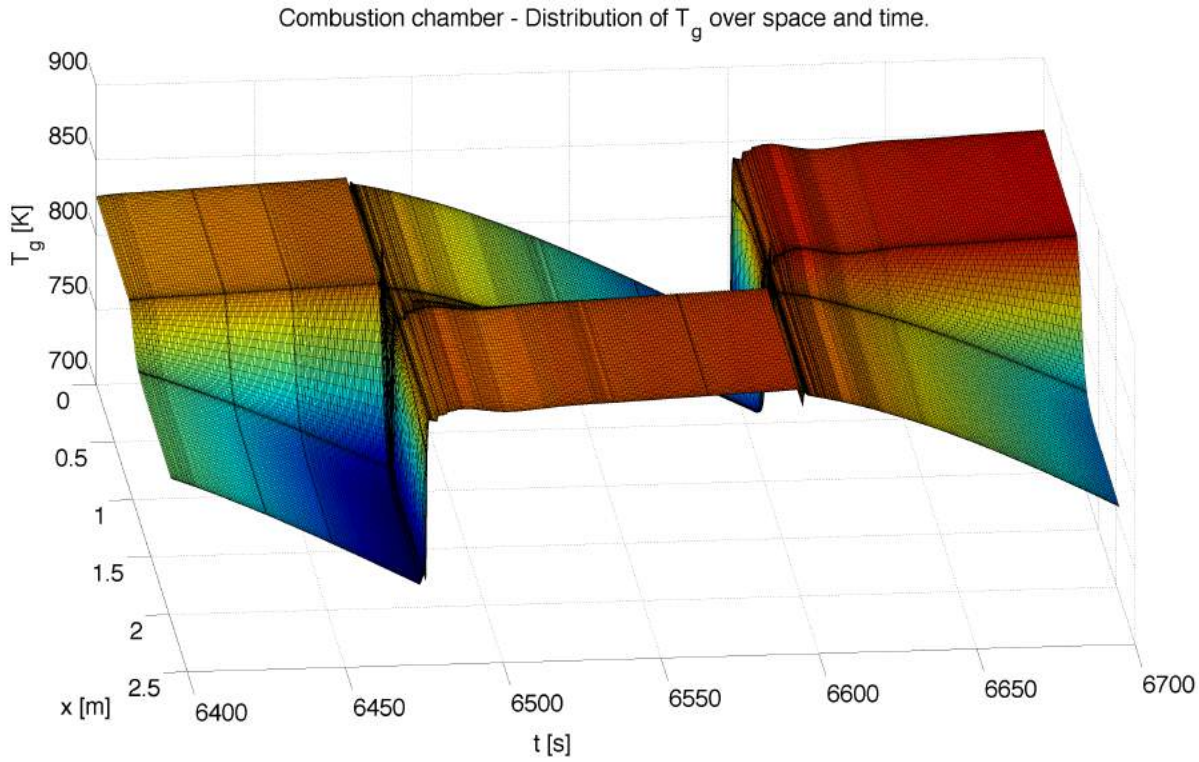

Figure 6.3.10: Distribution of T_g according to figure 6.3.3.

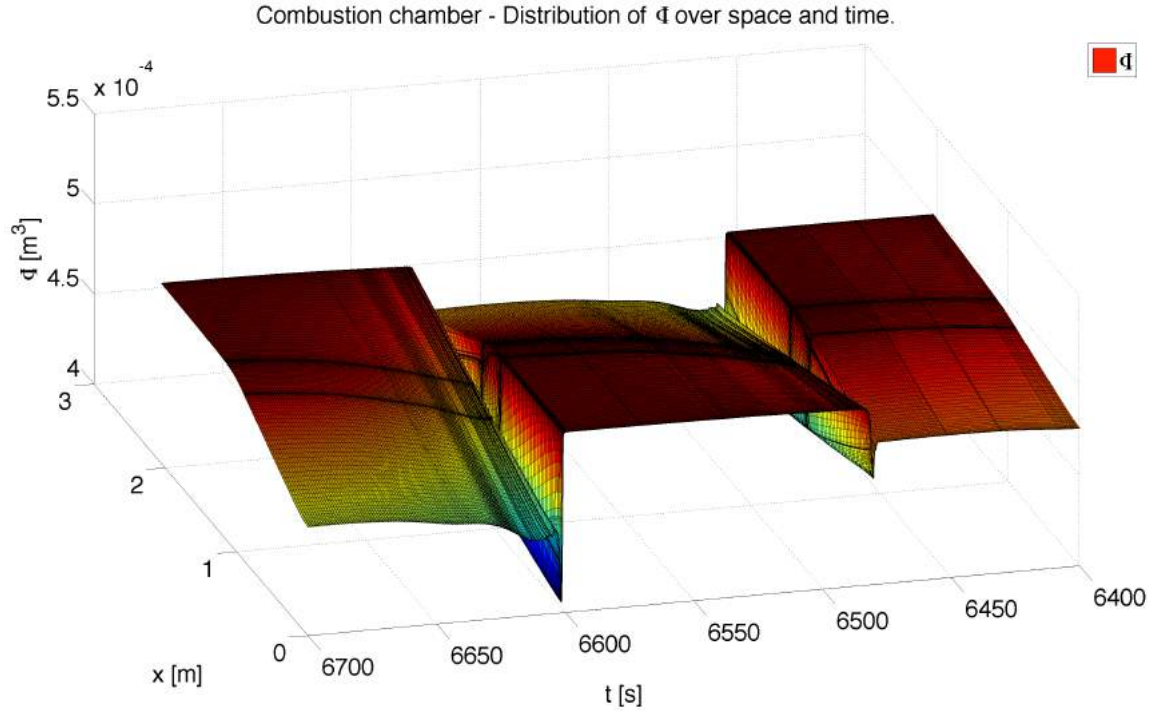

Figure 6.3.11: Distribution of Φ according to figure 6.3.3.

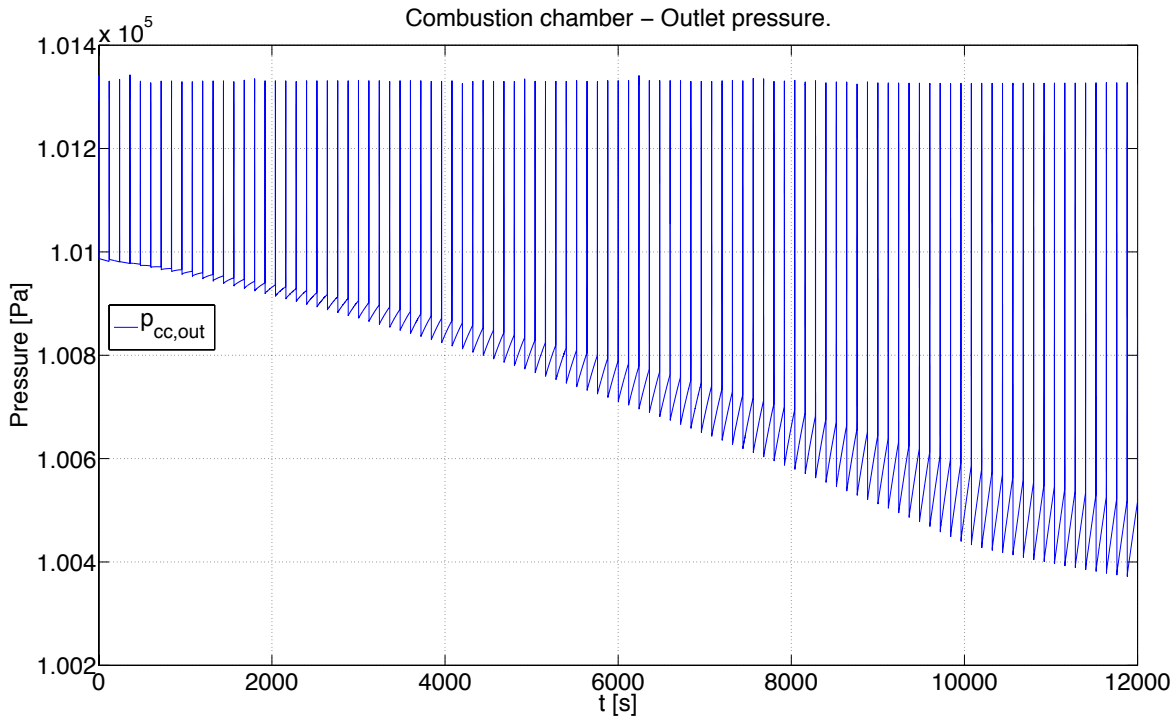

Figure 6.3.12: Outlet pressure of the combustion chamber and thereby input pressure of the appropriate ceramic bed per RTO half cycle.

6.3.2 Ceramic Bed A

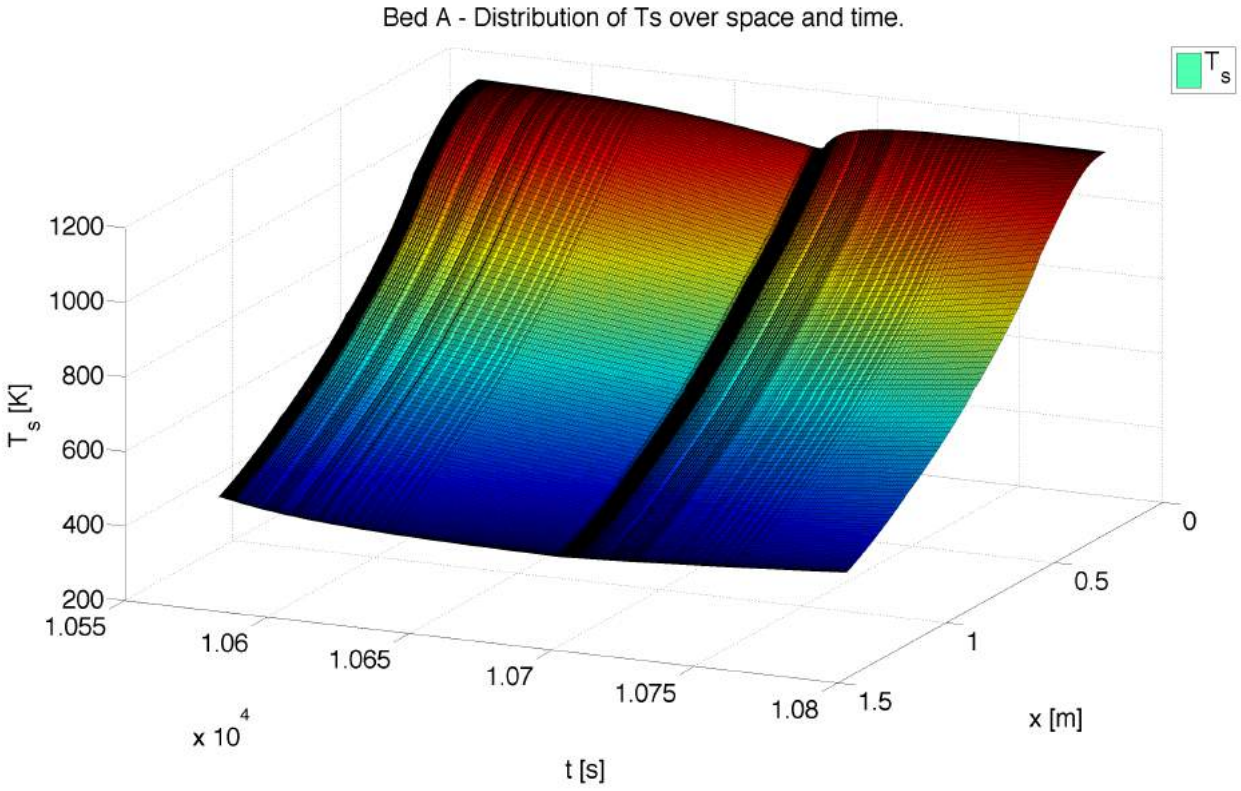

Figure 6.3.13: Distribution of T_s in ceramic bed A according to figure 6.3.2.

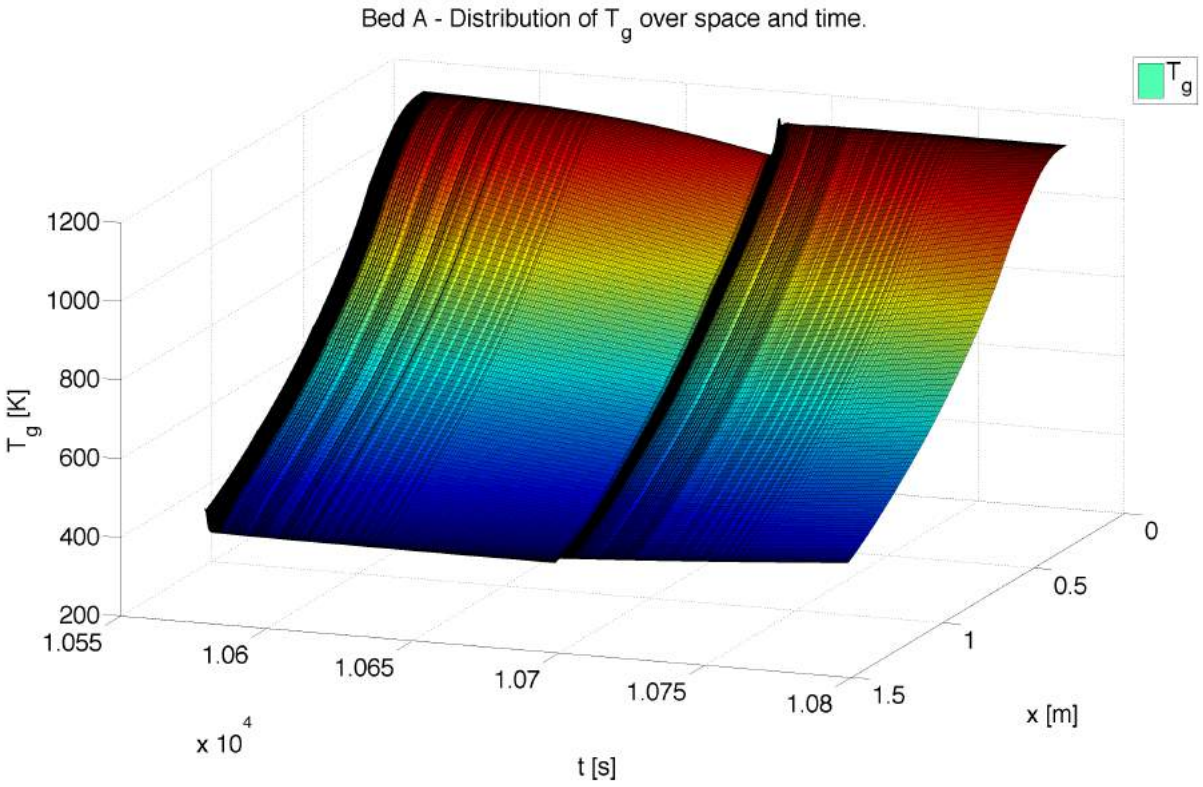

Figure 6.3.14: Distribution of T_g in ceramic bed A according to figure 6.3.2.

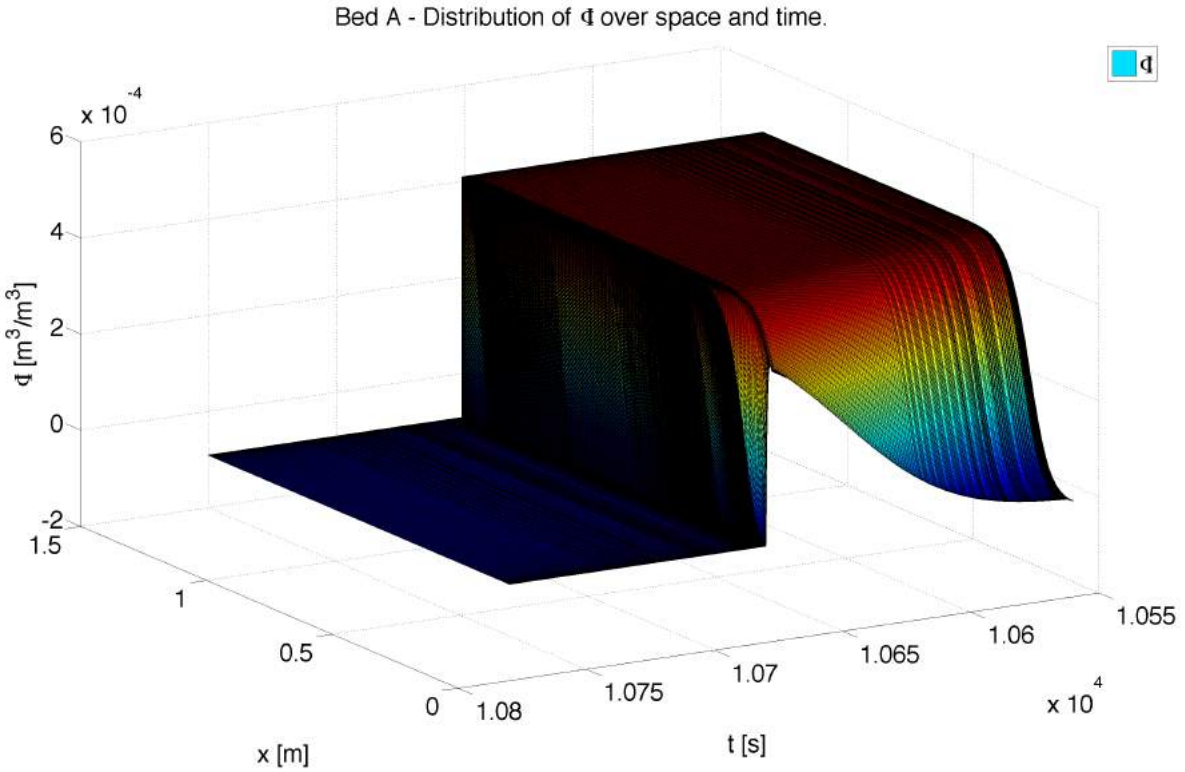

Figure 6.3.15: Distribution of Φ in ceramic bed A according to figure 6.3.2.

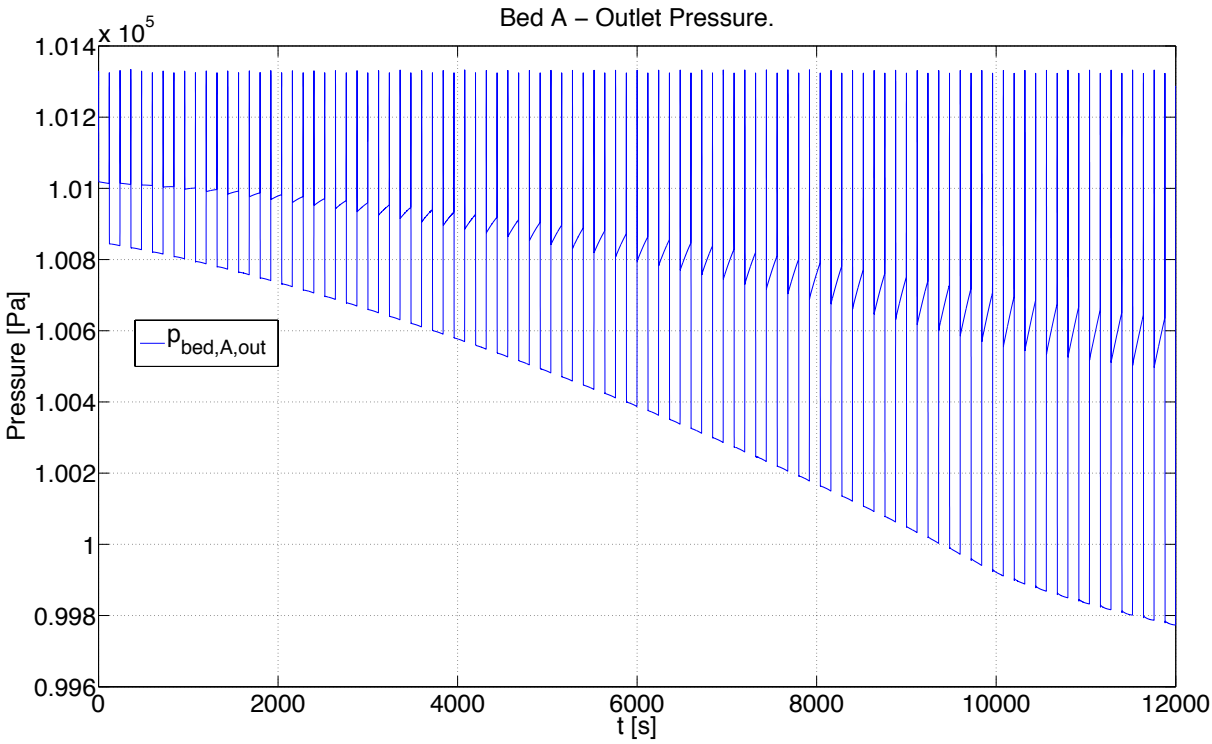

Figure 6.3.16: Outlet pressure of the ceramic bed A and thereby input pressure of the combustion chamber or valve box A depending on the RTO half cycle.

6.3.3 Valve Box A

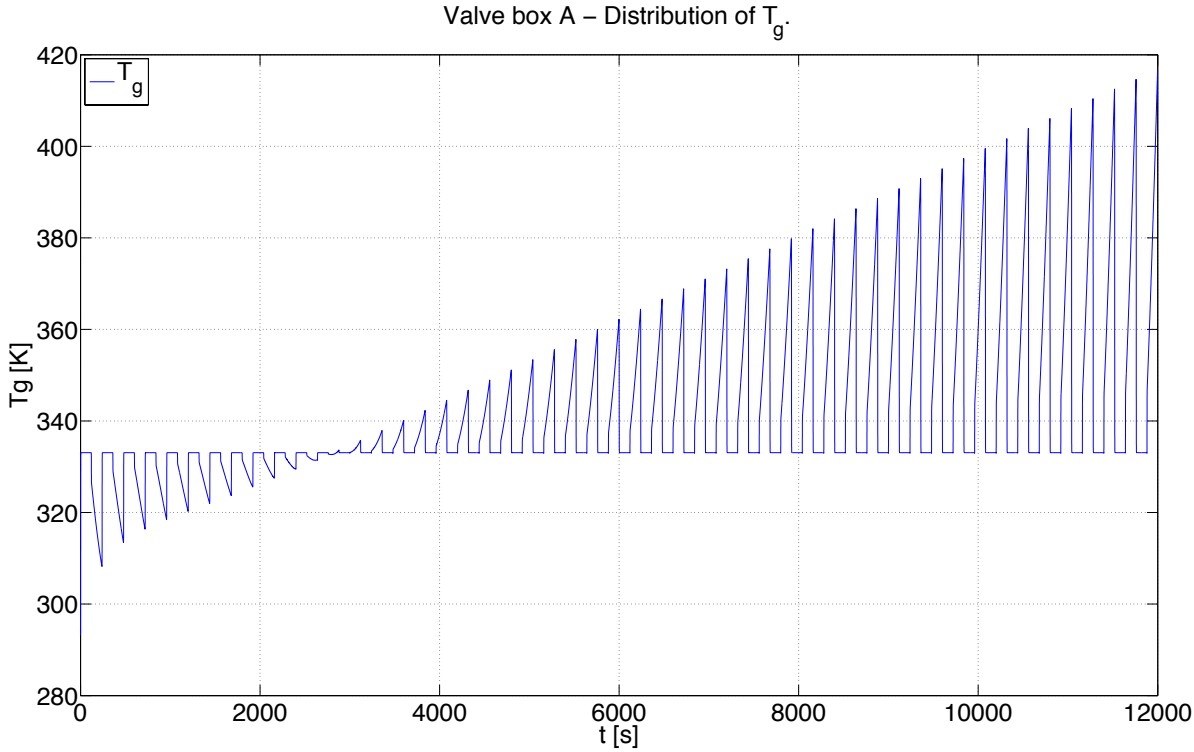

Figure 6.3.17: Distribution of T_g in the valve box A, switching between RTO in- and outputs.

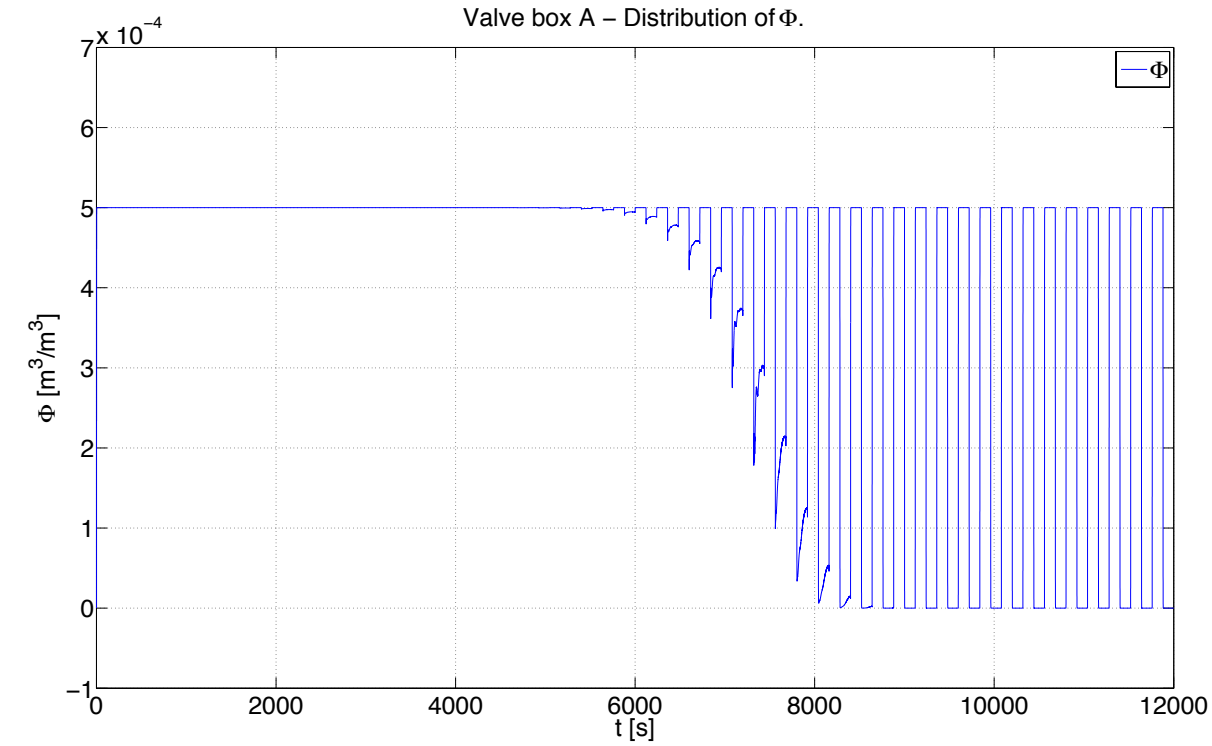

Figure 6.3.18: Distribution of Φ in the valve box A, switching between RTO in- and outputs.

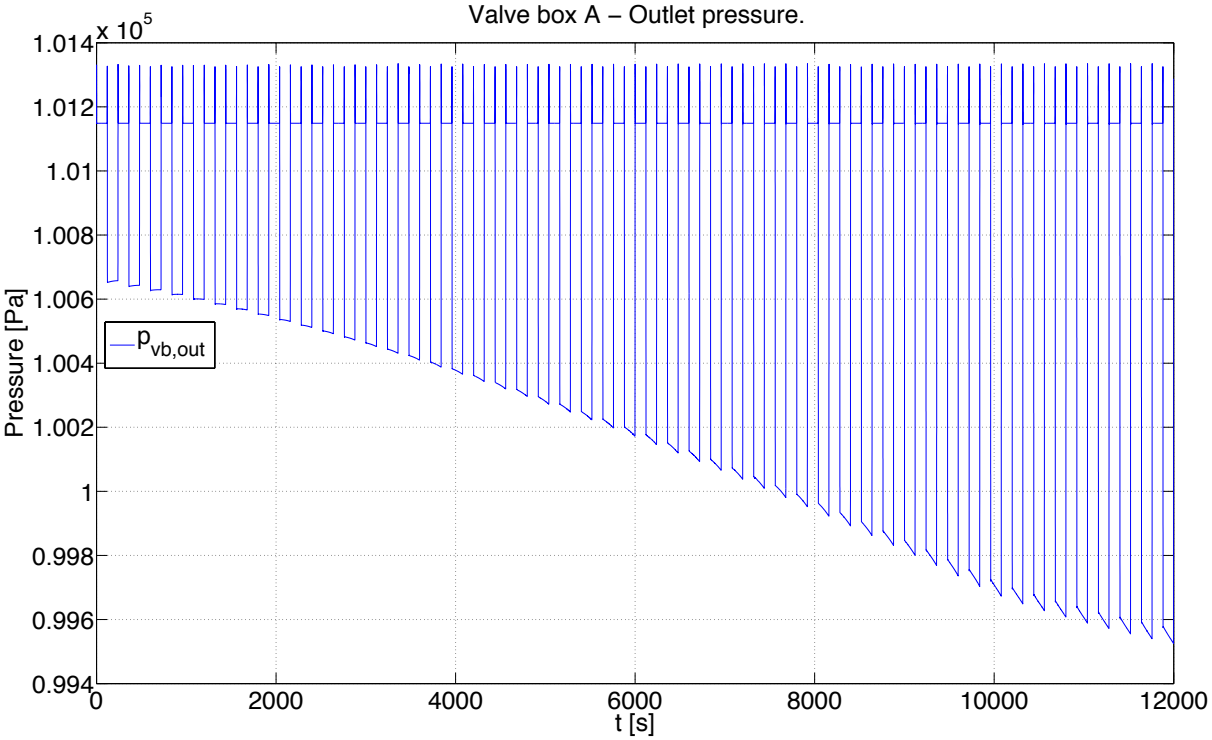

Figure 6.3.19: Outlet pressure of the valve box A and thereby input pressure of the ceramic bed A or outlet pressure of the RTO depending on the half cycle.

6.3.4 Chimney Outlet

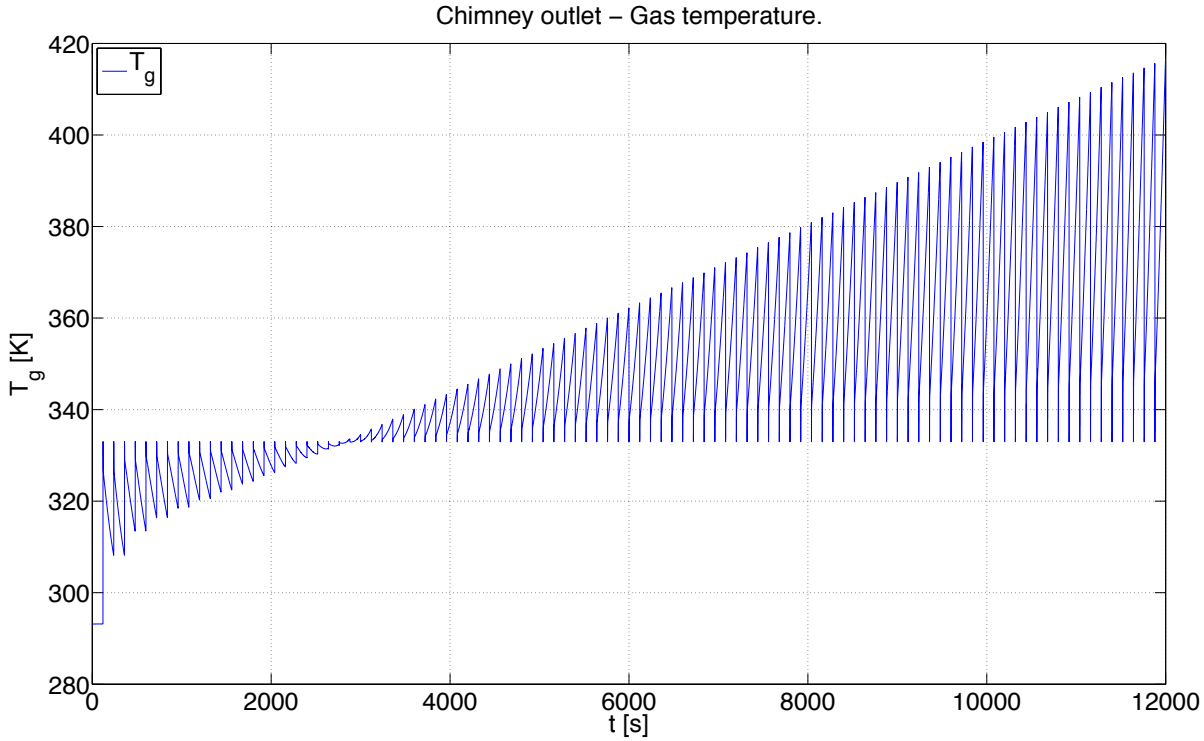

Figure 6.3.20: Leaving gas temperature of the RTO.

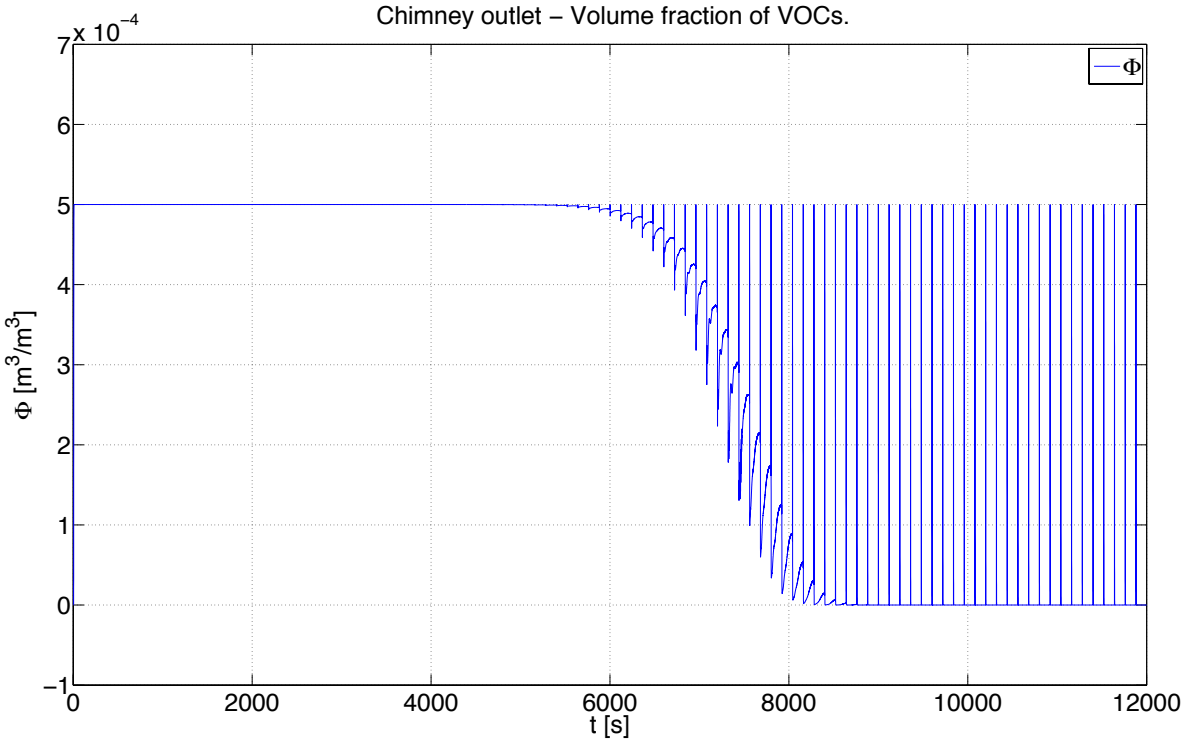

Figure 6.3.21: Leaving volume fraction of VOCs of the RTO.

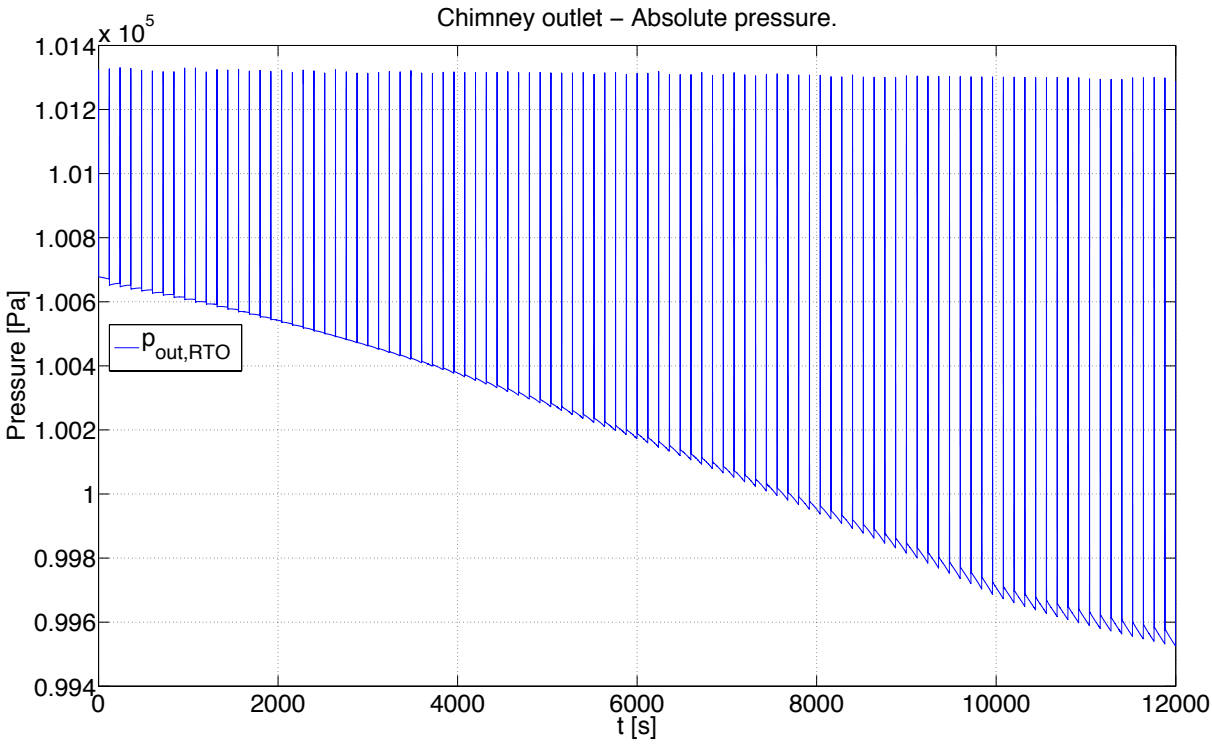

Figure 6.3.22: Outlet pressure of the RTO.

7 Conclusion and Outlook

Outlook

The design of the control concept was guided by the criteria of reproducing realistic conditions as far as possible, which motivated the description of plant components by sophisticated models. In the very first step the verification of these models by measurement data needs to be done, starting with the temperature sensors in the combustion chamber. After one made sure that real gas temperatures can be reproduced, the comparison between measured (then restored) and calculated temperatures will clarify the quality of applied models.

Before testing on the real plant, the control of the valve responsible for feeding the appropriate amount of fuel to the burner (provided by the developed concept) has to be (re)designed, whereas a time variant approach (see section 5.5.1) and faster sampling ($\ll 1$s) have to be taken into account.

Unless plants will be equipped with sensors measuring the inlet volume fraction of VOCs Φ_{in} to the combustion chamber, the possibility to exploit the signals of the temperature sensors in the area of the ceramic bed in order to find a reasonable estimate for Φ_{in} will be worth analyzing, if one wants to consider the reaction heat in the control without the need for compensation by the integrator.

Summary

(I) Measurements
  (i) Temperature sensors in the combustion chamber
  (ii) Approximation of derivatives of sensor signals (see section 4.1.2.4)
  (iii) Optimization of parameters (also see section 4.2)
  (iv) Verification of models

(II) Inner control loop of the valve in charge of the fuel injection
  (i) Modelling and integration in simulation
  (ii) Consideration of a time variant mass flow (see section 5.5.1 and 6.1.2)
  (iii) Sampling

(III) Additional sensors
  (i) Mass flow $\dot{m}_{abs}$
  (ii) Inlet volume fraction of VOCs Φ_{in} in the combustion chamber

(IV) Accurate consideration of the reaction heat in the control
  (i) By measuring Φ_{in}
  (ii) And/Or estimating Φ_{in} by exploiting temperature signals (see section 5.7)

Conclusion
The more research and mathematical modelling of effects and components are considered in the control of the gas temperature in the combustion chamber, the more it becomes evident that the applied PID controllers waste fossil fuels and that on a large scale.

Within the scope of this thesis it has been mathematically demonstrated that an appropriate model based control can not only save fuel, but even improve purification performance of contaminated raw gas. In view of the consumption level of natural gas for industrial purposes there is a huge potential to reduce costs and thereby increase the attractiveness of manufactured plants by CTP and the business dealing with *Regenerative Thermal Oxidizers* in general. The developed concept is not only restricted to a two-bed configuration, but it can be applied to all kinds of RTOs with various bed configurations and other materials than ceramic to buffer the enthalpy stream, leaving the combustion chamber.

Personally, I have not primarily focused on cost saving potential, but with the perspective of a more sensitive environmental consciousness I do feel responsible for topics like the waste of natural resources and the corresponding greenhouse effect, which subsequently leads to the fight for natural resources and very often legitimizes military operations. While this statement may be considered excessively dramatic, it should underline the importance of a conscious handling with all forms of energy.

Since we already have the technical capacities and the required expertise, it is in our responsibility to support research and development in order to minimize emissions. In this process we are not only capable to improve efficiency, but also to reduce expenses.

Bibliography

[1] Rieger T., Master's Thesis (2014), Wärmetransportvorgänge in regenerativen oxidativen Abgasreinigungsanlagen

[2] Rieger T. (Status: November 2015), Dokumentation des Modells zur verfahrenstechnischen Prozesssimulation - SIM10C, CTP GmbH - Air Pollution Control

[3] Stephan P. (2013), Berechnungsvorgänge für Wärmeleitung, konvektiven Wärmeübergang und Wärmestrahlung, VDI-Wärmeatlas (11. August). Berlin Heidelberg: Springer Verlag

[4] Kleiber M. & Joh R. (2013). Flüssigkeiten und Gase. In V.D. VDI-GVC (Hrsg.), VDI-Wärmeatlas (11. August). Berlin Heidelberg: Springer Verlag

[5] Frigerio S., Mehl M., Ranzi E., Schweiger D. & Schedler J. (2007). Improve efficiency of thermal regenerators and VOCs abatements systems: An experimental and modelling study. Experimental Thermal and Fluid Science, 31, page 403-411

[6] Stephan, Kabelac, Kind, Martin, Mewes & Schaber (2013) *Physical Properties Data Service* - equation. In V.D. VDI-GVC (Hrsg.), VDI-Wärmeatlas (11.August). Berlin Heidelberg: Springer Verlag

[7] Mzychka Y. & Yovanovich M. (1998). Modeling Nusselt numbers for thermally developing laminar flow in non circular ducts. *AIAA Paper*, page 98-2586

[8] Kast W. & Nirschl H. (2013). Druckverlust in einphasigen Strömungen. In V.D. VDI-GVC (Hrsg.), *VDI Wärmeatlas* (11. August page 1221-1237). Berlin Heidelberg: Springer Verlag

[9] Bodeau J., Riboulet G. & Roncalli T., Non uniform grids for PDE in finance (2000). Groupe de Recherche Operationnelle Credit Lyonnais, France. The finite difference method, 2.1, page 2-4

[10] Million E., The Hadamard Product (2007), accessed October 28 2015, http://buzzard.ups.edu/courses/2007spring/projects/million-paper.pdf

[11] Jung M., Langer U., Methode der finiten Differenzen für Ingenieure: Eine Einführung in die numerischen Grundlagen und Computersimulation, Springer Vieweg Verlag, 2. Auflage (2013)

[12] Steinbach O., Partielle Differentialgleichungen und Numerik, Berichte aus dem Institut für numerische Mathematik, Technische Universität Graz, Vorlesungsskript (2015)

[13] MATLAB Central Newsgroup (2009), accessed October 28 2015, http://www.mathworks.com/matlabcentral/newsreader/view_thread/243990

[14] Bauer R., Gölles M., Brunner T., Dourdoumas N. & Obernberger I. (2007), What Is Really Measured by Temperature Sensors in a Biomass Furnace ?

[15] Brookfield G. (2007). "Factoring quartic polynomials: A lost art". Mathematics Magazine 80 (1), page 67–70.

[16] D'Errico J. (2012), MATLAB Central File Exchange, accessed 28 October 2015, http://www.mathworks.com/matlabcentral/fileexchange/34765-polyfitn

[17] Alten H.-W., Naini A.D., Folkerts M., Schlosser H., Schlote K.-H., Wußing H.: 4000 Jahre Algebra. Geschichte, Kulturen, Menschen. Springer-Verlag Berlin Heidelberg, 2003.

[18] Christofides P.D., Nonlinear and robust control of PDE systems. Applications to transport-reaction processes, Springer (2001)

[19] Deutscher J. (2012), Zustandsregelung verteilt-parametrischer Systeme, Springer-Verlag Berlin Heidelberg

[20] Deutscher J. (2012), Zustandsregelung verteilt-parametrischer Systeme, Springer-Verlag Berlin Heidelberg, page 511-552

[21] J. Adamy, Nichtlineare Systeme und Regelungen, Springer-Verlag Berlin Heidelberg , 2. Auflage (2014)

[22] J.–J. E. Slotine, W. Li: Applied Nonlinear Control. Prentice–Hall 1991, page 230–233

[23] A. Isidori: Nonlinear Control Systems (2nd Edition). Springer–Verlag 1989, page 23–36

Nomenclature

Latin Letter	Units	Description
A	m^2	cross section area
A_{kin}	s^{-1}	pre-exponential, kinetic factor in the Arrhenius law
a_{eff}	$\mathrm{m}^2\,\mathrm{s}^{-1}$	dispersion coefficient of the gas phase
$a_{V(x)}$	$\mathrm{m}^2\,\mathrm{m}^{-3}$	specific surface of the ceramic beds, depending on space x
$a_{V,loss}$	$\mathrm{m}^2\,\mathrm{m}^{-3}$	specific surface considered for ambient loss
C	$\mathrm{kmol}\,\mathrm{m}^{-3}$	concentration
c	$\mathrm{J}\,\mathrm{kg}^{-1}\,\mathrm{K}^{-1}$	heat capacity
d_h	m	hydraulic diameter
D_{abs}	$\mathrm{m}^2\,\mathrm{s}^{-1}$	absolute or effective diffusion (ceramic beds)
D_{ax}	$\mathrm{m}^2\,\mathrm{s}^{-1}$	axial dispersion (ceramic beds)
E_a	$\mathrm{J}\,\mathrm{kmol}^{-1}$	activation energy in the Arrhenius law
H	m	height
HV	$\mathrm{J}\,\mathrm{kmol}^{-1}$	heating or calorific value
h	$\mathrm{W}\,\mathrm{m}^{-2}\,\mathrm{K}^{-1}$	heat transfer coefficient
$\mathbf{I}$	–	identity matrix
k_{loss}	$\mathrm{W}\,\mathrm{m}^{-2}\,\mathrm{K}^{-1}$	coefficient for ambient loss
L	m	length
L_{flame}	m	length of the burner flame in the combustion chamber
m	kg	mass
$\dot{m}$	$\mathrm{kg}\,\mathrm{s}^{-1}$	mass flow
$\dot{m}_{fuel}$	$\mathrm{kg}\,\mathrm{s}^{-1}$	mass flow of pure fuel substance added through the burner
M	$\mathrm{kg}\,\mathrm{kmol}^{-1}$	molar mass
M_{mix}	$\mathrm{kg}\,\mathrm{kmol}^{-1}$	molar mass of the gas mixture in the plant
N_{iter}	–	number of iterations
N_l	–	number of ceramic layers in the ceramic beds
N_x	–	number of grid points of discretized space
Nu	–	Nusselt number
p	Pa	absolute pressure
$p_{\dot{m}}$	–	polynomial approach for RTO cycle switches
Pr	–	Prandtl number
$\dot{Q}$	$\mathrm{kg}\,\mathrm{m}^2\,\mathrm{s}^{-3}$	heat flow
r_g	$\mathrm{kmol}\,\mathrm{s}^{-1}\,\mathrm{m}^{-3}$	reaction rate
Re	–	Reynolds number
R_{id}	$\mathrm{J}\,\mathrm{kmol}^{-1}\,\mathrm{K}^{-1}$	ideal gas constant

$R_{s,k}$	$\mathrm{J\,kmol^{-1}\,K^{-1}}$	specific gas constant of the gas component k
t	s	time
t_s	s	sampling time
T	K	temperature
T_{amb}	K	ambient temperature
T_{target}	K	reference temperature in the combustion chamber
$\overline{T}_{g,cc}$	K	mean gas temperature over space x_{cc}
V	$\mathrm{m^3}$	volume
w_k	–	mass fraction of the gas component k
x	m	general expression for space
x_k	–	molar volume fraction of the gas component k
y	–	general expression for solutions

Greek Letter	**Units**	**Description**
$\alpha_{cc,\mathrm{wall}}$	–	linear parameter for the temperature of the inner surface of the combustion chamber
α_Φ	–	numerical coefficient, appearing at Φ
ΔH_R	$\mathrm{J\,kmol^{-1}}$	enthalpy of reaction
Δp	Pa	differential pressure
ΔT	K	differential temperature
ϵ	–	emissivity
ϵ_R	–	infinitesimal bound
$\epsilon_{B(x)}$	–	porosity depending on space x in the ceramic beds
ζ	–	general coefficient for pressure drop
η	Pa s	dynamic viscosity
λ	$\mathrm{W\,m^{-1}\,K^{-1}}$	heat conductivity
$\lambda_{\text{af-ratio}}$	–	air-fuel equivalence ratio
ρ	$\mathrm{kg\,m^{-3}}$	density
σ	$\mathrm{W\,m^{-2}\,K^{-4}}$	Stefan-Boltzmann constant
τ	s	RTO half cycle period
Φ	$\mathrm{m^3\,m^{-3}}$	volume fraction of *volatile organic compound*(s)
φ_{shape}	–	shape coefficient for pressure drop

Superscripted Index	**Units**	**Description**
bed	–	ceramic bed
cc	–	combustion chamber
in	–	inlet
out	–	outlet
vb	–	valve box

Subscripted Index	Units	Description
ax	–	axial
$basis$	–	basis of the cross section area in reference to the mass flow
bed	–	ceramic bed
cc	–	combustion chamber
cc,wall	–	inner surface of the combustion chamber
Ce	–	ceramic tube in reference to the temperature sensor
eff	–	effective
$fuel$	–	indication of the fuel of the burner
g	–	gas phase
g, m	–	gas phase, mean value
i	–	running index, used for the ceramic layers in the bed
id	–	ideal
in	–	indication of incoming parameter
k	–	running index, used for different gas components
l, j	–	general running index
loss	–	parameter in terms of ambient loss
mix	–	mixture
out	–	indication of outlet parameter
ref	–	reference
s	–	solid phase
Se	–	thermocouple in reference to the temperature sensor
ss	–	temperature sensor
ST	–	protective steel tube in reference to the temperature sensor
vb	–	valve box

Abbreviations	Units	Description
AI	–	affine input
BED	–	ceramic bed
CC	–	combustion chamber
CTP	–	Chemisch Thermische Prozesstechnik GmbH
ICDQ	–	interpolated central differential quotient
ODEs	–	ordinary differential equations
PDDS	–	physical properties data service
PDEs	–	partial differential equations
PID	–	proportional–integral–derivative
PLC	–	programmable logic controller
PT1	–	proportional time (first order)
RTO	–	Regenerative Thermal Oxidizer
SISO	–	single output single input
VB	–	valve box
VOCs	–	volatile organic compounds

Appendix

General Parameters

Molar Mass [kg/kmol]				
Oxygen	Nitrogen	Water	Carbon Dioxide	Argon
32	28.01	18.015	44.01	39.948

Molar masses of materials.

Dynamic Viscosity [Pa s]					
Material	$A_\eta \cdot 10^5$	$B_\eta \cdot 10^7$	$C_\eta \cdot 10^{10}$	$D_\eta \cdot 10^{12}$	$E_\eta \cdot 10^{15}$
Oxygen	−0.10257	0.92625	−0.80657	0.05113	−0.01295
Nitrogen	−0.01020	0.74785	−0.59037	0.03230	−0.00673
Water	0.64966	−0.15102	1.15935	−0.10080	0.03100
Carbon Dioxide	−0.18024	0.65989	−0.37108	0.01586	−0.00300
Argon	0.16196	0.81279	−0.41263	0.01668	−0.00276

Coefficients for the dynamic viscosity of pure gases.

Heat Conductivity [$\mathrm{W\,m^{-1}\,K^{-1}}$]					
Material	$A_\lambda \cdot 10^3$	$B_\lambda \cdot 10^3$	$C_\lambda \cdot 10^6$	$D_\lambda \cdot 10^9$	$E_\lambda \cdot 10^{12}$
Oxygen	−1.285	0.10655	−0.052630	0.025680	−0.005040
Nitrogen	−0.133	0.10149	−0.060650	0.033610	−0.007100
Water	13.918	−0.04699	0.256066	−0.183149	−0.055092
Carbon Dioxide	−3.882	0.052839	0.071460	−0.070310	0.018090
Argon	4.303	0.04728	−0.007780	0	0

Coefficients for the heat conductivity of pure gases.

Heat Capacity Gas Phase $[\mathrm{J\,kg^{-1}\,K^{-1}}]$							
Material	A_{c_g}	B_{c_g}	C_{c_g}	D_{c_g}	E_{c_g}	F_{c_g}	G_{c_g}
Oxygen	2122.2098	3.5302	−7.1076	−1.4541	30.6057	−83.6686	79.4375
Nitrogen	432.2027	3.5160	2.8021	−4.1924	42.0453	−114.250	111.1019
Water	706.3032	5.1703	−6.0865	−6.0611	36.2423	−63.0965	56.2085
Carbon Dioxide	514.5073	3.4923	−0.9306	−6.0861	54.1586	−97.5157	70.9687
Argon	0	2.5	2.5	0	0	0	0

Coefficients for the heat capacity of pure gases.

Heat Capacity Solid Phase $[\mathrm{W\,m^{-1}\,K^{-1}}]$				
Layer i	$A_{c_s,i}$	$B_{c_s,i}$	$C_{c_s,i} \cdot 10^3$	$D_{c_s,i} \cdot 10^7$
1	753.76	1.298	−1.5	6.5
2-4	767.57	1.2869	−1.5	7

Coefficients for the heat conductivity of pure gases.

Specific Gas Constant $[\mathrm{J\,kmol^{-1}\,K^{-1}}]$				
Oxygen	Nitrogen	Water	Argon	Carbon Dioxide
259.8270	296.8390	461.4010	208.1321	188.9220

Specific gas constants of materials.

Chemical Reaction and Reaction Enthalpy			
Material	A_{kin}	E_a	ΔH_R
Ethanol	$5.37 \cdot 10^{11}$	$2.0135 \cdot 10^8$	$-1.24 \cdot 10^9$

Parameters considered for reaction.

Valve Boxes

Valve Boxes					
A_{vb}	V_{vb}	k_{loss}	$a^{vb}_{V,loss}$	A_{basis}	ζ_{vb}
0.1871	0.0918	0.55	9.2467	0.18	213

Parameters of the valve boxes.

Ceramic Beds

Beds					
A_{bed}	$a_{V,loss}^{\text{bed}}$	k_{loss}	ζ_{in}	φ_{shape}	ζ_{out}
0.18	6.6667	0.55	0.67	0.89	1.08

Parameters of the ceramic beds.

Ceramic Layers						
Layer i	$\lambda_{s,i}$	$\rho_{s,i}$	$a_{V,i}$	$\epsilon_{B,i}$	$d_{h,i}$	H_i
1	1.9	2100	847.64	0.6315	$3 \cdot 10^{-3}$	0.3
2	2.1	2700	847.64	0.6315	$3 \cdot 10^{-3}$	0.6
3	2.1	2700	847.64	0.6315	$3 \cdot 10^{-3}$	0.9
4	2.1	2700	847.64	0.6315	$3 \cdot 10^{-3}$	1.2

Parameters of the ceramic layers in the beds.

Combustion Chamber and Burner

Combustion Chamber					
A_{cc}	L_{cc}	$a_{V,loss}^{cc}$	k_{loss}	A_{basis}	ζ_{cc}
0.21	2.056	3.581307803	0.55	0.18	43

Parameters of the combustion chamber.

Burner				
L_{flame}	M_{fuel}	HV	$\max\{\dot{m}_{fuel}\}$	$\min\{\dot{m}_{fuel}\}$
0.15	16	$8.04 \cdot 10^8$	$7.2 \cdot 10^{-4}$	0

Parameters of the burner and the supplied fuel (natural gas).

Temperature Sensors

Sensor Components						
Component	A	m	c	ϵ	d_h	h
Steel Tube (ST)	0.0104	0.1407	661	0.25	0.0346	eq. (4.1.6)
Ceramic (Ce)	0.0075	0.0488	1148	0.9	–	70

Parameters of sensor components.

Sensors		
$\alpha_{cc,wall}$	$k_{ss,loss}$	σ
10	0.93	$5.670373 \cdot 10^{-8}$

Parameters considered in model of the temperature sensors.

List of Figures

List of Tables